The Effects of Magnetic Fields on Rolling Contact Fatigue Wear

By

Yusuke Iida

A thesis submitted for the degree of
Doctor of Philosophy

Mechanical Engineering
School of Engineering and Design
Brunel University
January 2007

Abstract

The thesis describes the effects of the magnetic field in rolling contact tests of steel by using a two-disc machine and the investigation of its mechanism from contact stress analysis by using FEM and the magnetisation of a ferromagnetic substance.

In the tests, two contact kinematic conditions, that is pure rolling and 10% rolling with sliding together with 1.1 and 0.4T [Tesla] of horizontal static magnetic fields created by permanent magnets were applied. The results of optical and scanning electron microscopy observations show that finer wear particles and smoother worn surfaces are produced in the presence of the magnetic field. For the generation of the finer wear particles, it is considered necessary that the subsurface crack initiation point is moved towards the surface due to the magnetic field.

Wear amounts of the discs are lowered in the magnetic fields under the pure rolling conditions. However, at 10% rolling with sliding, the wear amounts are increased in the magnetic fields even though finer particles and smoother surfaces are observed. Both tendencies are unified by calculating the number of cycles required to generate wear particles, which are reduced due to the magnetic field's presence.

For these mechanisms, it is considered that domain walls near the contact region are caught by dislocations when the specimen is magnetised and part of the energy for magnetisation activates the dislocation movement resulting in crack initiation.

Acknowledgements

My deepest appreciation to my supervisor Professor T. A. Stolarski and Dr. K. Sato, for giving me the opportunity of this exciting study and for the guidance, encouragement and patience which made the completion of this thesis possible.

I would like to extend my gratitude to all the technical staff and those involved in the modification of the test apparatus especially Mr. Keith Withers, Mr. Len Soans and Mr. Clive Barrett.

I would also like to thank the staff at the Experimental Techniques Centre for the use of the equipment and the time of their technical staff, especially Mita.

My acknowledgements also extend to some fellow students, for the endless discussions on their work, many of which are a source of motivation. To name a few, Duc Nhin Ha, Pratip Vongbandit, Masaaki,Yamane, Vincent Anjorin, Aziz, Giorgio Mustafaraj, Yousof Jadran and Ahmed Maki.

Special thanks for my parents, Mr. and Mrs. Kimura, Mr. Shichiro Kamio, Mrs. Hiroko Sakata, Ms. Mitsuko Sato, Tokuo, Mio, Yota and Yuto for their support.

Finally, I am grateful to Noriko for her cooperation and encouragement. Without them, this thesis could not have been completed.

Table of Contents

List of Figures

Chapter 1 Introduction

Chapter 2 Mechanisms of Rolling Contacts

Chapter 3 Magnetisation of Ferromagnetic Substances

Chapter 4 Rolling Contact Tests in Magnetic Fields

Chapter 5 Experimental Results

Chapter 6 Discussion

List of Tables

Chapter 4 Rolling Contact Tests in Magnetic Fields

Chapter 6 Discussion

Nomenclature

Chapter 2 Mechanisms of Rolling Contacts

a	Half width of contact
b	Burgers vector
E	Young's modulus
E'	Effective Young's modulus
ΔE_e	Free energy for an edge dislocation
ΔE_s	Free energy for a spiral dislocation
f_e	External force
G	Shear modulus
K	Boltzmann constant
P	Force per unit length
R	Radius of cylinder
R'	Mutual radius of curvature
r_0	Core radius
r_1	Effective radius
T	Absolute temperature
U_0	Resistance energy
x	Position of any point within the contact
μ	Friction coefficient
σ_Y	Yield stress
τ_e	Shear stress
$\tau_{zx,max}$	Maximum shear stress for plane strain condition
$\tau_{R,max}$	Maximum value of von Mises' stress
$\tau_{R,Y}$	Von Mises' shear strain-energy criterion to yield (=k)
ν	Poisson's ratio

Chapter 3 Magnetisation of Ferromagnetic Substances

a	Lattice constant
d	Thickness of domain
e	Total energy
e_m	Magnetostatic energy
e_{ex}	Exchange energy

e_a	Anisotropy energy
H	Magnetic field
H_d	Demagnetising field
I_s	Saturation magnetisation
J	Exchange integral
K	Anisotropy constant
l	Thickness of the crystal
N	Number of atoms in a domain wall
N	Demagnetising factor (dimensionless quantity), $0 \leq N \leq 1$
S	Total spin quantum number
ΔU_m	Energy for magnetisation
U_{mag}	Magnetostatic energy
θ	Angle of directions between magnetic field and easy direction
μ_0	Permeability of vacuum

Chapter 4 Rolling Contact Tests in Magnetic Fields

$a`$	Contact ellipse major semi-axis.
b	Contact ellipse minor semi-axis.
C_f	Coefficient decided from the value A/B (2)
E	Young's modulus
$f_{z_{\max}}$	Maximum compressive or Hertzian stress
K	Material constant
P	Applied load
q_{max}	Maximum sub- surface shear stress
$\bar{q}_{\max}$	Coefficient decided from the value A/B (2)
$W``$	Calculation parameter
$Z_{q_{\max}}$	Depth of maximum shear stress
$\left(\frac{Z}{b}\right)_{q_{\max}}$	Coefficient decided from the value A/B (2)
β	Ellipse semi-axes ratio, given by b/a
δ	Decrease in separation between two points on axis of symmetry.
ν	Poisson's ratio

Chapter 6 Discussion

a	Lattice constant
d	Thickness of domain
e	Total energy
e_m	Magnetostatic energy
e_{ex}	Exchange energy
e_a	Anisotropy energy
H	Magnetic field
I_s	Saturation magnetisation
J	Exchange integral
K	Anisotropy constant
l	Thickness of the crystal
N	Number of atoms in a domain wall
n	Number of cycles to detach one layer
S	Total spins quantum number
t	Thickness of wear particle
ΔU_m	Energy for magnetisation
W	Wear amount
θ	Angle of directions between magnetic field and easy direction
μ_0	Permeability of vacuum $(=4\pi x10^{7})$
ρ	Specific gravity of the disc

Chapter 1 Introduction

1.1 Introduction

The phenomenon of friction and wear is common in daily life. Various measures have been taken to combat it. In recent years, the study of friction and wear, known as 'tribology', and the understanding of underlying mechanisms involved are improving. However, there are still many unsolved problems.

Rolling contact fatigue, one of the causes of wear, also involves unsolved problems although it has been studied in a variety of ways in order to prevent damage and to extend the life of machine elements. Rolling contact fatigue is a fracture phenomenon taking place at the interface of rolling contacts such as roller bearings and gears. Wear particles, in the form of flakes, are usually generated within the contact zone. At the subsurface of contacting bodies, strain is stored up due to the cyclic nature of contact loading. In addition to loading conditions, many other factors such as, for example, the dynamics of the contact and lubrication affect rolling contact fatigue.

A recent trend in engineering is to combine traditional mechanical engineering with well-established electrical and electronic engineering in order to develop many new electromechanical products that are used in everyday life. When designing such products, it is necessary to consider the effect of new factors that have not been taken into account before. The magnetic field is such a new factor.

Magnetic fields are generated in various mechanical and electronic devices such as motors, power generators, etc. It is important to consider the tribology of their constitutive components and to understand the influence of the magnetic field on their performance in order to prevent premature failure and to achieve higher energy efficiency.

The main objective of this study is to investigate the effects and mechanisms by which the magnetic field affects the operation of a model rolling contact. Another objective is to evaluate the mechanism of crack propagation under the influence of the magnetic field. These objectives are accomplished by using contact mechanics theory, magnetism theory, and surface and sub-surface observations with the aid of an optical and scanning electron microscope.

1.2 Background

The effect of the magnetic field on friction and wear processes has been studied, experimentally and theoretically, by a number of researchers. A summary of the history in the study is shown in Appendix A. In 1970s, Muju (1) (2) (3) (4) was possibly the first to observe the magnetic field's effects on wear by carrying out pin-on-cylinder tests on various ferromagnetic and non-magnetic materials with different sliding velocities. From the results, as shown in Figures 1.1 and 1.2, the effects of magnetic fields on adhesive wear are determined in terms of hardness of rubbing surfaces, sliding velocity, and magnetic permeability. He pointed out that dislocation mobility in ferromagnetic materials is affected by magnetic fields and residual stress is relaxed. To give an example of the residual stress relaxation, he showed the decline of yield stress of mild steel in magnetic fields as seen in Figure 1.3.

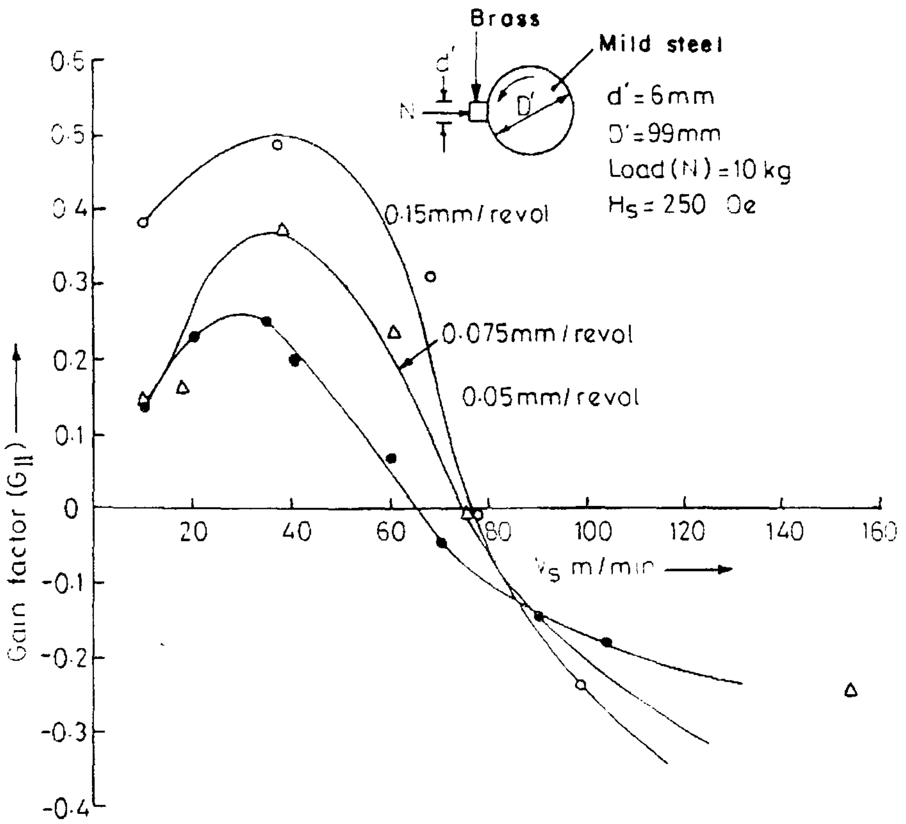

$$\text{Gain factor}=\frac{\text{(wear without magnetic field)- (wear with magnetic field)}}{\text{(wear without magnetic field)}}$$

Figure 1.1 Variation of gain factor with velocity and feed rate $^{(2)}$

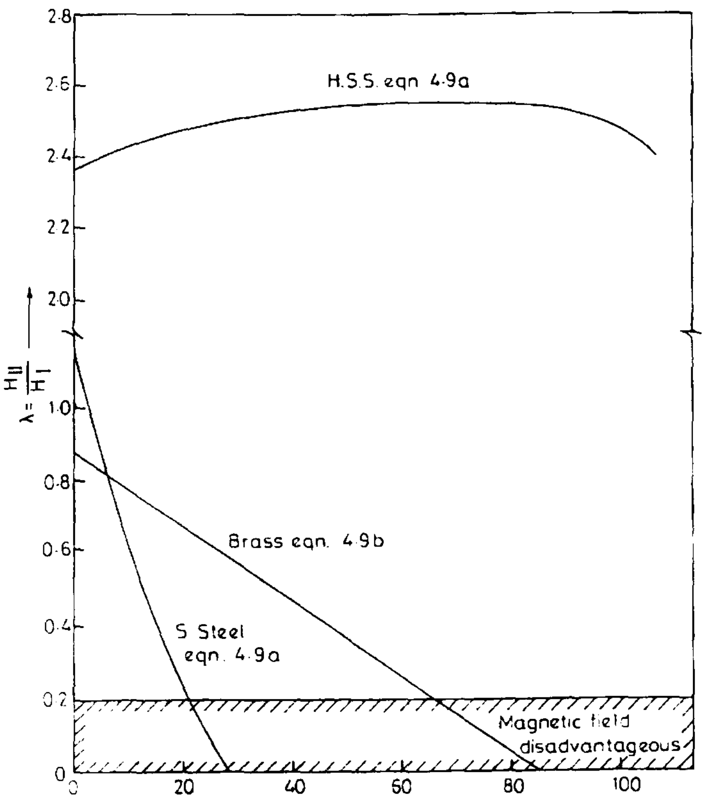

Sliding velocity [m/min]

λ: Hardness ratio (=Higher magnetic permeability [H_I] / Lower magnetic permeability[H_{II}])

Figure 1.2 Variation of hardness ratio with velocity $^{(3)}$

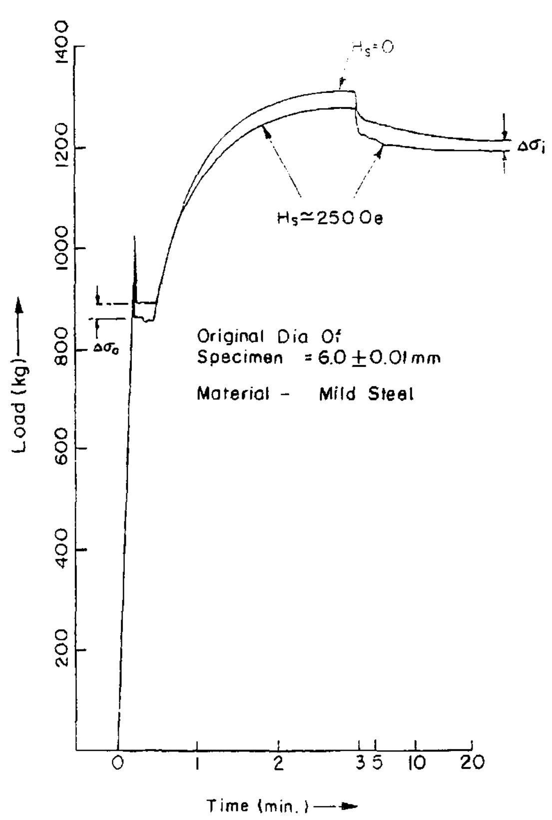

Figure 1.3 Stress relaxations in mild steel (1)

The effect of magnetic field is connected with the atmosphere around the rubbing surface due to the paramagnetism of oxygen, which is weakly magnetised by magnetic fields and it sometimes make a contribution to wear. Hiratsuka and Sasada (5) observed severe-mild wear transition and reduction in wear and the friction coefficient in air due to magnetic field during pin on disc experiments carried out for Ni-Ni and Fe-Fe contacts. In contrast with that, as shown in Figure 1.4, in Ar and N_2 gas atmosphere conditions, severe-mild wear transition did not occur. The results are interpreted in terms of accelerated oxidation of debris and their fine size. A similar trend in wear rate was also observed for Cu-Fe and Zn-Fe contacts (6).

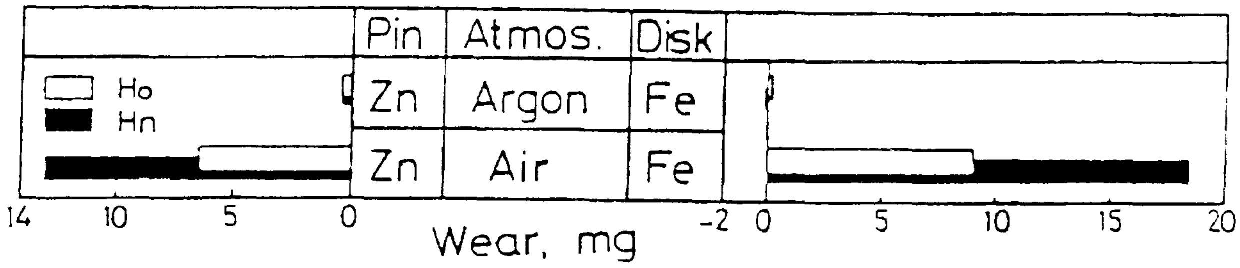

Figure 1.4 Comparison of magnetic effect on wear of Zn/Fe in air and in Ar gas; H_n=3700[Oe]; H_0=0.5[Oe] (6)

Kumagai (7) also examined the reasons for reduction of wear of Ni-steel contacts in the magnetic field. The lubrication effect of very fine particles was put forward as an explanation for the observed reduction in wear rates. From the observation, the size of fine particles was found to be 5-10μm in diameter as shown in Figure 1.5. Zaidi (8) (9) (10) (11) found an increase in micro-hardness of the interface. Also, accelerated oxidation and diminution of wear debris were observed.

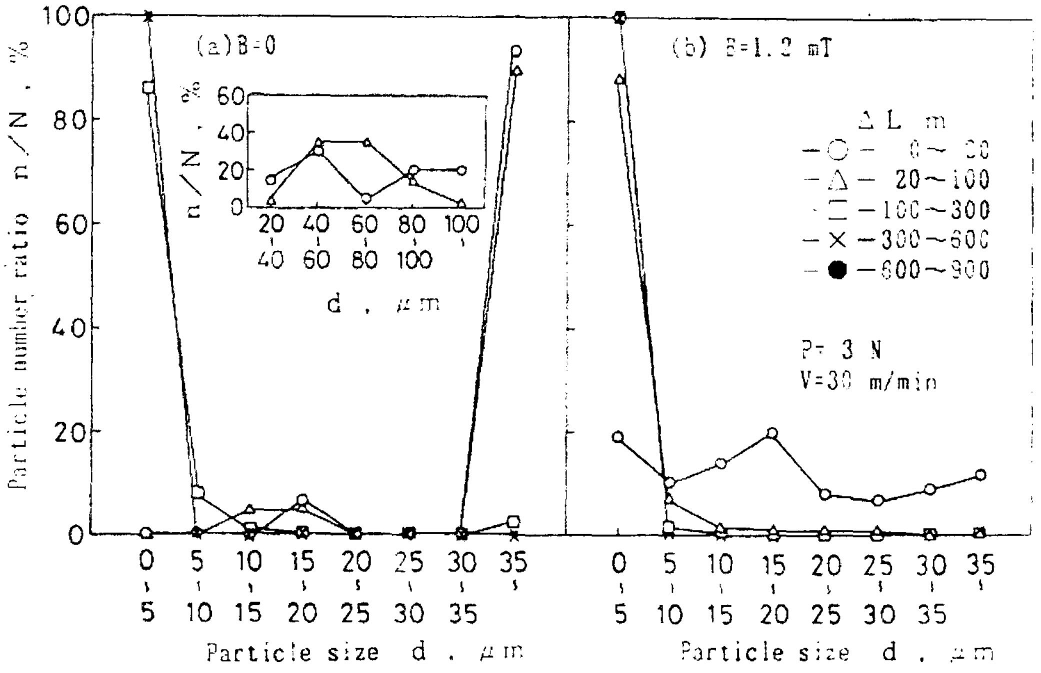

Figure 1.5 Magnetic effect on the particle size distribution for each sliding interval (7)

As a factor of atmospheres, polarity of lubricants is also affected by magnetic fields. Yamamoto (12) found a change in surface contact potential under boundary lubrication conditions with oils containing fatty acids in a ball-on-disc contact tested in magnetic fields. The results indicate that polar substances in the oil raise the critical temperature of the friction coefficient.

On the other hand, alternation of wear condition in the same contact state due to the magnetic field is reported. Mansoli (13) (14) (15) (16) (17) (18) observed the transformation in tool wear tests with the magnetic field. Abrasive wear without magnetic fields is transformed, in the presence of the magnetic field, to fracture due to the shift of shear stress to the subsurface region. Also, a decrease in wear, a lower friction coefficient, an increase of hardness of magnetised steel surface and a rise in temperature of rubbing surfaces were observed. Moreover, an irregular shape of cutting chips was observed when the magnetic fields were applied. Cracks in the subsurface region, seen in Figure 1.6, were observed by Zaidi and Chin. (8) (10) (11) (19) (20) They also observed a reduction in wear, stabilisation in friction coefficient, and the formation of an oxide layer on the rubbing surface with the magnetic fields. In addition, they pointed out that these effects are pronounced beyond 2000 A/m of the magnetic field around the specimens. Increase in specimens' temperature due to magnetic fields was reported by Bataineh (21) who performed FEM analysis. According to him, surface temperature of specimens is increased by approximately 17°C due to energy transformation delivered by magnetic pulse effect.

From fretting wear tests in magnetic fields, Sato (22) reported an increase in wear amount due to abrasive effect of oxidised wear particles as shown in Figure 1.7. Bhat (23) pointed out a drop in fatigue limit of mild steel in magnetic fields presence and concluded that the reason for the change is dislocation mobility alteration by magnetic fields as shown in Figure 1.8.

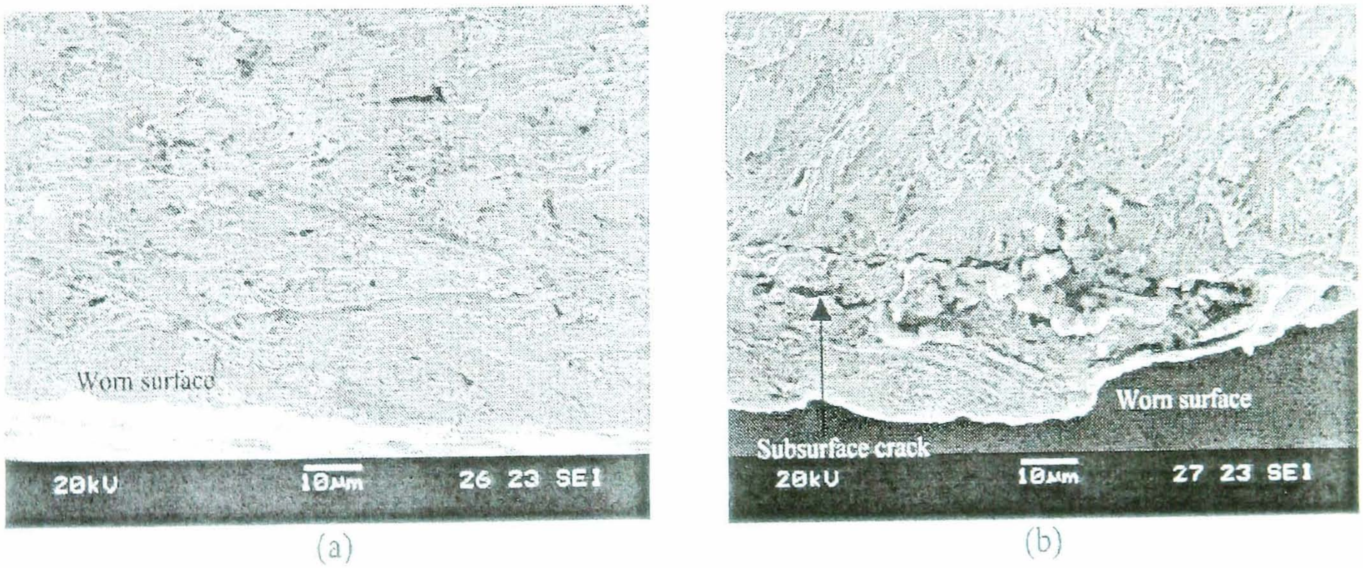

(a) (b)

Figure 1.6 Cross section of the tested steel pin; (a) without magnetic field and (b) magnetic field (H=6 kA/m) (19)

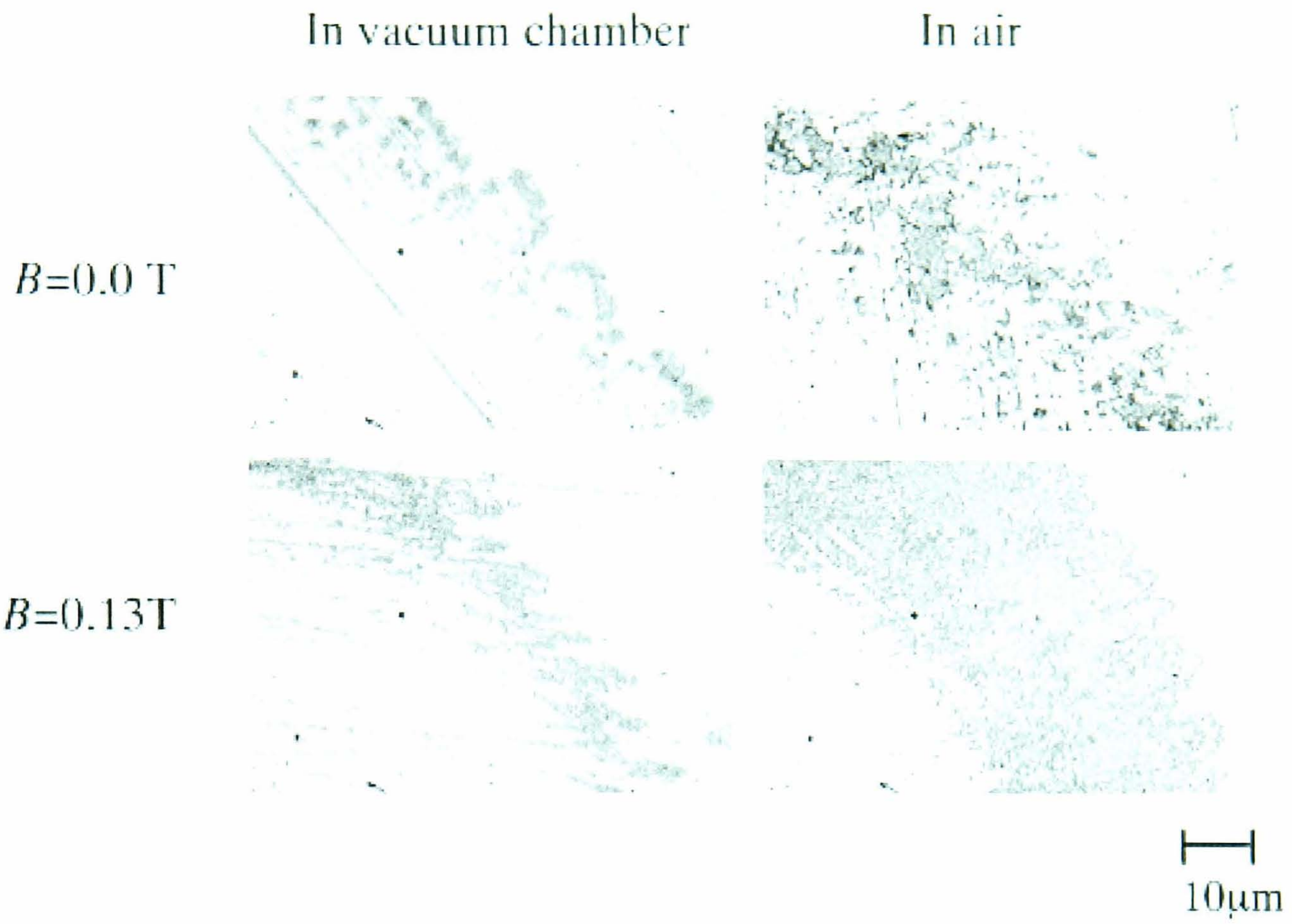

Figure 1.7 Photographs of wear scar on specimens fretted in vacuum and in air (22)

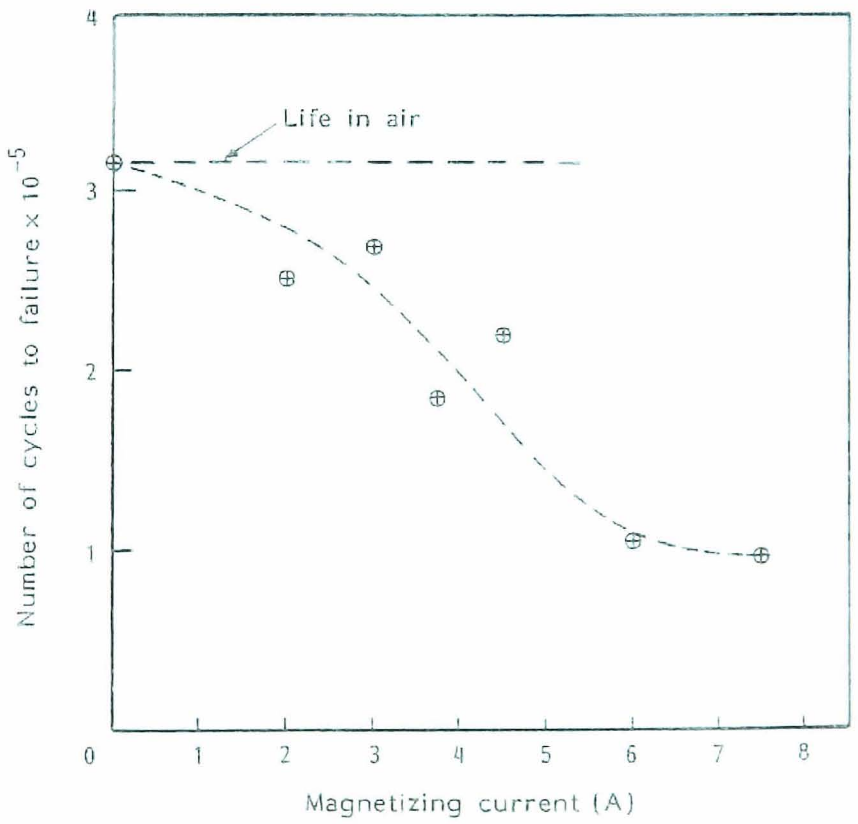

Figure 1.8 Effects of magnetic fields on fatigue of mild steel (23)

Previous studies of the mechanism of wear in magnetic fields point to a number of factors which should be considered:

1) Ferromagnetic wear particles behaviour due to magnetic force.
2) Accelerated oxidation of rubbing region due to paramagnetism of oxygen.
3) Alteration of material properties due to magnetisation.

Wear in magnetic fields is assumed to be influenced by these factors. Besides, various phenomena shown in the studies are linked in a complex way with these factors. Considering the factors individually, leads to the conclusion that behaviour and the role of ferromagnetic wear particles is the only simple phenomenon. However, in magnetic fields, oxidised wear particles will be more harmful for the contact due to paramagnetism of oxygen. Moreover, accelerated oxidation does not only affect wear particles but also rubbing surfaces. As a result, these phenomena make the mechanism complex. More specifically, highly oxidised wear particles, affected by a magnetic force operating between rubbing surfaces, act both as abrasive and lubricating agent depending on their conditions. Considering the effect from the property of ferromagnetic materials point of view, the relationship between the movement of domain walls in the magnetisation process and dislocation can be suggested. Ferromagnetic materials such as Fe and Ni have a domain structure composed of magnetic domains and domain walls. In the magnetic field, extending magnetic domains and aligning them with the field magnetise ferromagnetic materials. Simultaneously, other domains reduce their areas and the borders between domain walls move the during magnetisation process. Non-magnetic inclusion, such as dislocation, acts as resistance to the movement. It can be observed as Barkhausen noise (24) and utilized for a non destructive inspection. Additionally, Makar (25) (26) pointed out that a hysteresis loop of steel is changed by loading as shown in Figure 1.9. From these results, it is confirmed that magnetic fields affect mechanical properties of ferromagnetic materials.

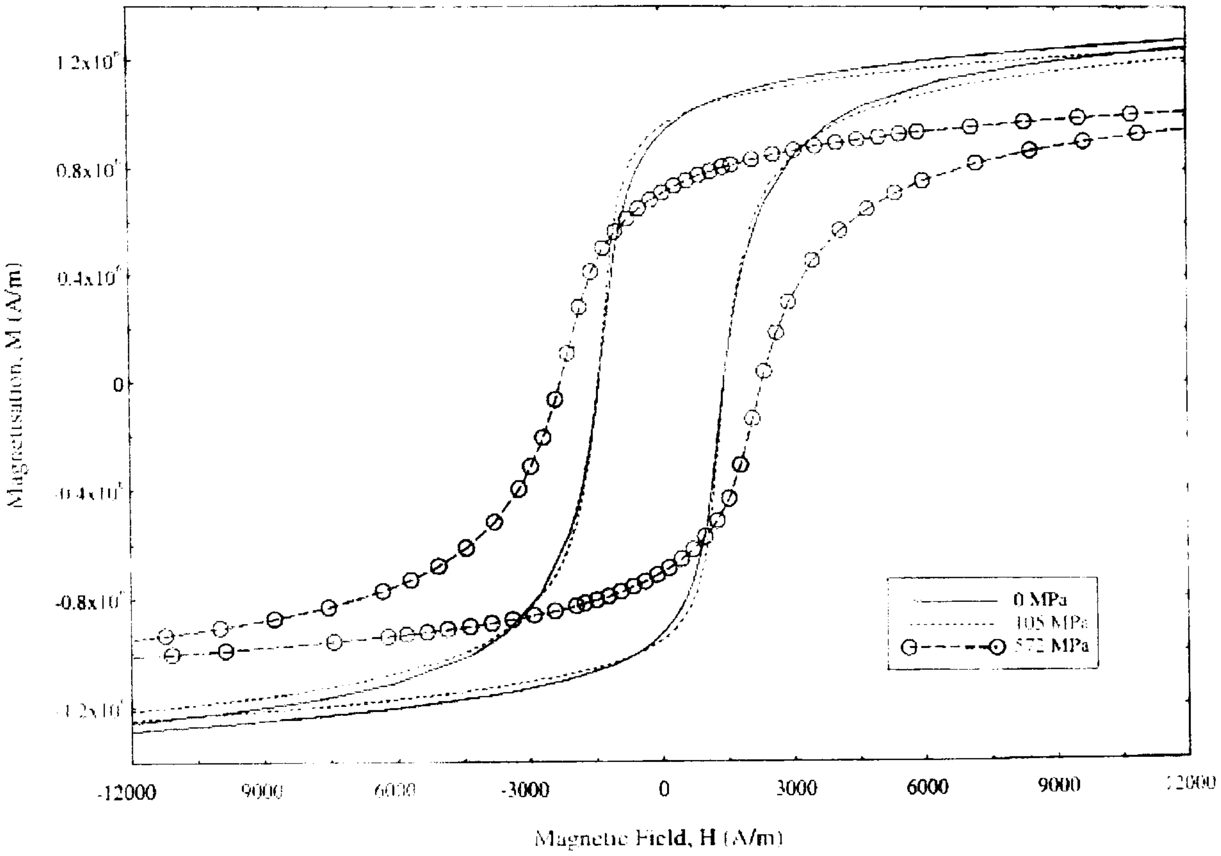

Figure 1.9 Effects of stress on hysteresis loop for carbon steels (25)

1.3 Research Objectives

The objective of this research project is to experimentally investigate the effect of magnetic fields on rolling contact operation and performance and to evaluate the mechanism involved. In order to accomplish the objective, rolling contact tests are carried out as a function of magnetic field density, direction of magnetic field and the speed under different contact conditions. For evaluation of the mechanism, contact mechanics theory and magnetism theory are used to explain the results.

1.4 Outline of Thesis

This thesis is presented in seven chapters, following the introduction in Chapter 1. Chapter 2 presents the general background information and previous experimental work related to the fatigue performance of rolling or rolling/sliding contact. This chapter is composed of three main sections. The second and third sections give a general background into the characteristic of rolling contact fatigue and theory of rolling contacts.

Chapter 3 introduces magnetisation of ferromagnetic substances, explaining domain structure of ferromagnetic substances and the magnetisation process under magnetic fields in connection with energy equilibrium. In addition, the connection between magnetic field and stress field is described.

Chapter 4 is concerned with the experimental set up and the main programme of experimental testing. Section two describes the mechanical and magnetic properties of specimens. Section three gives detailed description of the testing apparatus for pure rolling and rolling with sliding experiments. The test procedure is outlined in section four and five. Section six presents the wear measurements, optical and scanning electron microscope observations and surface roughness characterisation. Section seven gives results of mechanical and magnetic modelling using a finite element method.

Chapter 5 presents the experimental results obtained during pure rolling and rolling with sliding tests. The experimental results in pure rolling condition are presented in section two. In there, the effects of magnetic field in different magnetic densities, different rotational speeds of discs, different angles of magnetic fields, and the effect for non-magnetic substances are contained. Section three presents the effects of magnetic fields at rolling with sliding condition. In this section, the effects of the magnetic field in different magnetic densities, different angles of magnetic fields, and the effect for pure sliding condition are described.

Chapter 6 presents the discussion of the results. The effect of the magnetic field on contact performance is described in section two. The second section deals with contact conditions of the specimen without a magnetic field using ANSYS analysis. Rolling contact characteristics under the magnetic field is presented in the third section. And the fifth chapter suggests the Mechanisms of magnetic effect in rolling contact applying a magnetisation and crack initiation model with dislocation behaviour.

Chapter 7 presents the main conclusions of the study. A summary of the results and the contribution of the work, areas for further research and development are also outlined.

(1) M.K. Muju and A. Ghosh, "A model of adhesive wear in the presence of a magnetic field", Wear, Vol. 41, (1977), pp.103-116.

(2) M.K. Muju and A. Ghosh, "A model for cross diffusion across a sliding contact in the presence of a magnetic field", Wear, Vol. 53, (1979), pp. 35-42.

(3) M.K. Muju and A. Radhakrisna, "Wear of non-magnetic materials in the presence of a magnetic field", Wear, Vol. 58, (1980), pp. 49-58.

(4) M.K. Muju and A. Ghosh, "Effect of a magnetic field on the diffusive wear of cutting tools", Wear, Vol. 58, (1980), pp.137-145.

(5) K. Hiratsuka, T. Sasada and S. Norose, "The magnetic effect on the wear of metals", Wear, Vol.110, (1986), pp. 251-261.

(6) K. Hiratsuka and T. Sasada, "Wear of metals in a magnetic field", Wear, Vol. 160, (1993), pp. 119-123.

(7) K. Kumagai, K. Suzuki and O. Kamiya, "Study on reduction in wear due to magnetization", Wear, Vol. 162-164, (1993), pp. 196-201.

(8) H. Zaidi, L. Pan, D. Paulmier and F. Robert, "Influence of a magnetic field on the wear and friction behaviour of a nickel/XC 48 steel couple", Wear, Vol. 181-183, (1995), pp. 799-804.

(9) D. Paulmier, H. Zaidi, R. Bedri, E.K. Kadiri, L. Pan and Q. Jiang, "Steel surface modifications in magnetised sliding contact ", Surface and Coatings Technology, Vol. 76-77, (1995), pp. 583-588.

(10) H. Zaidi and A. Senoui, "Influence of magnetic field on surface modification and the friction behavior of sliding couple aluminium/XC 48 steel ", Surface and Coating Technology, Vol. 120-121, (1999), pp. 653-658.

(11) H. Zaidi, K.J. Chin and J. Frene, "Analysis of surface and subsurface of sliding electrical contact steel/steel in magnetic field", Surface and Coatings Technology, Vol. 148, (2001), pp. 241-250.

(12) Y. Yamamoto and S. Gondo, "Effect of a magnetic field on boundary lubrication", Tribology International, Vol. 20, (1987), pp. 342-346.

(13) M. El Mansori, H. Zaidi, E.K. Kardiri and D. Paulmier, "Surface modifications of a non-ferromagnetic copper/ferromagnetic steel XC48 couple in magnetized sliding contact", Surface and Coatings Technology, Vol. 86-67, (1996), pp. 511-515.

(14) M. El Mansori, M. Schmitt and D. Paulmier, "Role of transferred layers in friction and wear for magnetized dry frictional applications", Surface and Coatings Technology, Vol. 108-109, (1998), pp. 479-483.

(15) M. El Mansori, D. Paulmier, J. Ginsztler and M. Horvath, "Lubrication mechanisms of a sliding contact by simultaneous action of electric current and magnetic field", Wear, Vol. 225-229, (1999), pp. 1011-1016.

(16) M. El Mansori and D. Paulmier, "Effects of selective transfer on friction and wear of magnetised steel–graphite sliding couples", Applied Surface Science, Vol. 144-145, (1999), pp. 233-137.

(17) M. El Mansori, F. Pierron and D. Paulmier, "Reduction of tool wear in metal cutting using external electromotive sources", Surface and Coatings Technology, Vol. 163-164, (2003), pp. 472-477.

(18) M El Mansori, V. Iordache, P. Seitier and D. Paulmier, "Improving surface wearing of tools by magnetization when cutting dry", Surface and Coatings Technology, Vol. 188-189, (2004), pp. 566-571

(19) K.J. Chin, H. Zaidi, M.T. Nguyen and P.O. Renault, "Tribological behaviour and surface analysis of magnetized sliding contact XC 48 steel/XC 48 steel", Wear, Vol. 250, (2001), pp. 470-476.

(20) K.J. Chin, H. Zaidi, T. Mathia, "Oxide film formation in magnetized sliding steel / steel of the contact stress field and film failure mode", Wear, Vol. 259, (2005), pp. 477-481

(21) O. Bataineh, B. Klamecki and B.G. Koepke, "Effect of pulsed magnetic treatment on drill wear", Journal of Materials Processing Technology, Vol. 134, (2003), pp. 190-196.

(22) K. Sato, T.A. Stolarski and Y. Iida, "The effect of magnetic field on fretting wear", Wear, Vol. 241, (2000), pp. 99-108.

(23) I.K. Bhat, M.K. Muju and P.K. Mazumdar, "Possible effects of magnetic fields in fatigue", International Journal of Fatigue, Vol. 15, (1993), pp. 193-197.

(24) H. Barkhausen, Z. Phys., Vol. 20, (1919), pp. 401.

(25) J.M. Makar and B.K. Tanner, "The in situ measurement of the effect of plastic deformation on the magnetic properties of steel: Part I – Hysteresis loops and magnetostriction", Journal of Magnetism and Magnetic Materials, Vol. 184, (1998), pp. 193-208.

(26) J.M. Makar and B.K. Tanner, "The in situ measurement of the effect of plastic deformation on the magnetic properties of steel: Part II – Permeability curves", Journal of Magnetism and Magnetic Materials, Vol. 187, (1998), pp. 353-365.

Chapter 2 Mechanisms of Rolling Contact Fatigue Wear

2.1 Introduction

Rolling contact fatigue wear is one of wear phenomenon producing wear particles and surface damage called 'pitting', due to the cyclic nature of contact and friction loads. The particles are generated by cracks propagating on the surface or in the subsurface region of contacting materials. Thus, to consider the theory of rolling fatigue, an understanding of the mechanisms of crack initiation at rolling contacts is necessary. Although many researchers have studied it and many things have been clarified, some issues are still unresolved.

The objective of this chapter is to review current knowledge of rolling contacts and to provide some background for the various aspects involved.

2.2 Characteristic of Rolling Contact Fatigue Wear

Rolling contact fatigue wear is characterised by the formation of large wear fragments after a critical number of revolutions. Prior to this critical point, a negligible amount of wear takes place and a rolling contact will operate normally until the wear particles are detached, and the useful life of the contact is terminated. This is in marked contrast to the wear experienced in sliding contacts where, due to adhesion and abrasion, wear results in a gradual deterioration of contacting surfaces from the start of running. From this, it can be seen that the amount of material removed by fatigue wear in rolling contact is not a very useful parameter for performance assessment. Much more relevant is the useful life of a contact in terms of number revolutions or time at a given speed.

The definition of life of a bearing used by manufacturers is the number of revolutions which are reached or exceeded by 90 per cent of similar bearings and expressed by load conditions as main parameters. For the case of bearings, the equation for the lifetime is based on Palmgren's theory (1). It was adopted in 1962 as ISO R 281-1962 and is currently used with some modifications.

$$L = \left(\frac{C}{P}\right)^p \qquad (2.1)$$

where:
L - Rating life ($\times 10^6$ revolutions)
C - Static load rating
P - Dynamic equivalent load
p - 3 for ball bearings, 10/3 for roller bearings

As seen in Equation (2.1), the main factor to determine a bearing's life is mainly the load condition. However, many other parameters influence a bearing's life and their interaction makes rolling contact fatigue a complex matter.

Rolling contact fatigue wear is classified by origins of crack initiation. One is surface crack and the other is subsurface crack. The starting point of surface crack is thought to be due to surface roughness or contamination in lubricating medium. At a certain point, concentrated contact stress initiates a crack and the crack propagates to subsurface. When the crack grows to a certain length in the subsurface region it emerges on the surface again, and the wear particle is formed. In the case of surface crack, the shape of wear debris produced by it is shown in Figure 2.1 (a). It is arrowhead shaped and spread radially from the initiation point. Shape of its cross section depends on the initiation point and angle. On the other hand, wear particle produced by subsurface crack, shown in Figure 2.1 (b), has the bottom section flat shaped and parallel to the surface. It indicates that the subsurface crack is initiated and propagated by maximum shear stress parallel to the surface. Wear particles are formed by cracks emerging to the surface.

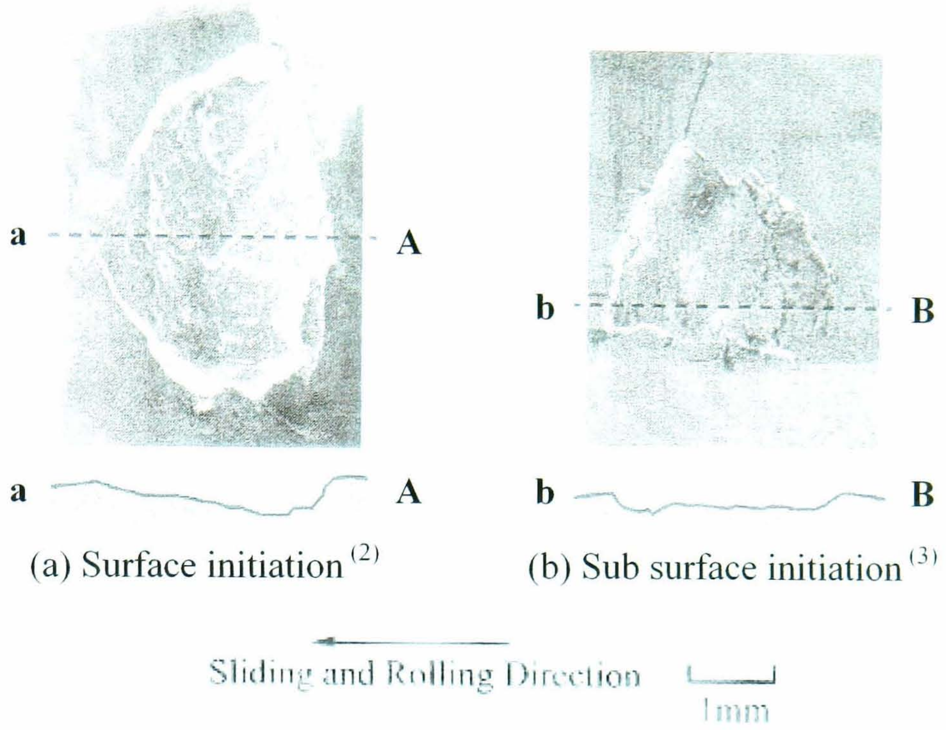

(a) Surface initiation (2)

(b) Sub surface initiation (3)

Figure 2.1 Surface photographs and section profiles of two pitting forms

2.3 Theory of Rolling Contact Fatigue Wear

2.3.1 Contact Stress Distribution within the Cylinders

As mentioned in previous section, the main factor in estimating rolling contact is the load condition. Due to the cyclic load applied to the contact region, a crack is initiated at the rolling contact fatigue. Therefore, to consider the crack initiation model, it is necessary to understand the distribution of the nearby contacting region.

Hertz (4) was the first to recognise that when non-conforming bodies contact, the stresses created could be analysed independently of the geometry and the state of stress in the bodies as a whole.

As shown in Figure 2.2 (5), when two cylindrical bodies with their axes both lying parallel to the y-axis in a coordinate system are pressed in contact by a force P per unit length, the problem becomes a two-dimensional one. They make contact over a long strip of width $2a$

lying parallel to the y-axis. The half width of contact a and the pressure distribution along the x-axis due to P is expressed by Equation (2.2) and (2.3) (6).

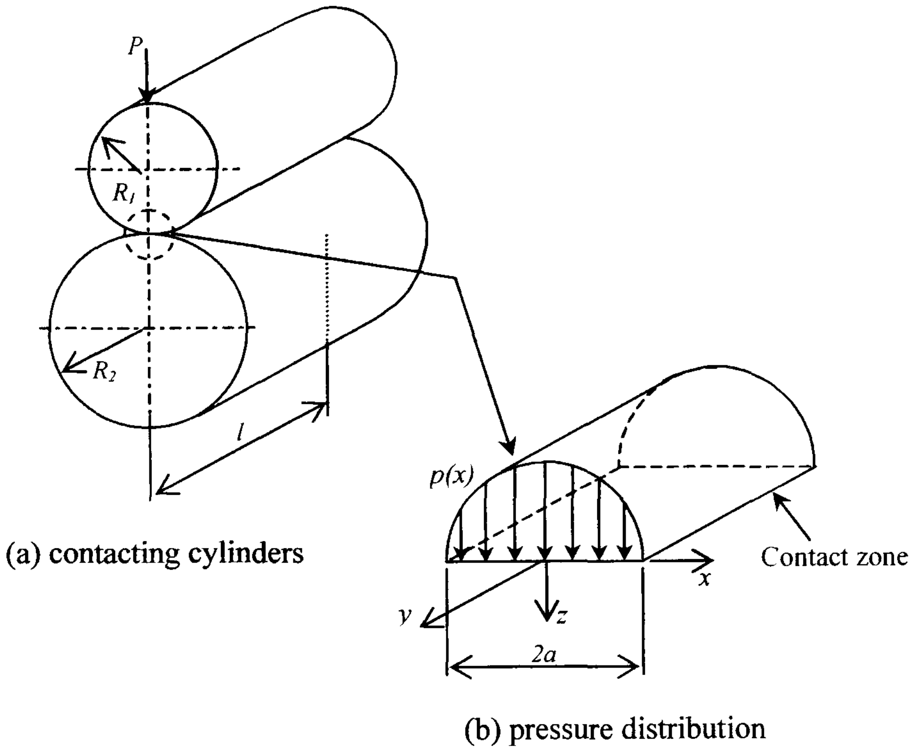

Figure 2.2 Pressure distribution of two cylinders (5)

$$a^2 = \frac{4PR'}{\pi E'} \qquad (2.2)$$

$$p(x) = \frac{2P}{\pi a^2}\left(a^2 - x^2\right)^{1/2} \qquad (2.3)$$

$$\frac{1}{E'} = \frac{1-\nu_1^2}{E_1} + \frac{1-\nu_2^2}{E_2}$$

$$\frac{1}{R'} = \frac{1}{R_1} + \frac{1}{R_2}$$

where:
a - Half width of contact
P - Force per unit length
R'- Mutual radius of curvature
R_1, R_2 - Radii of both cylinders
E'- Effective Young's modulus
E_1, E_2 - Young's moduli for both materials
ν_1, ν_2 - Poisson's ratio for both materials
x - Position of any point within the contact.

Maximum contact pressure is expressed by Equation (2.4)

$$p_0 = \frac{2P}{\pi a} = \left(\frac{PE'}{\pi R'} \right)^{1/2} \qquad (2.4)$$

The stress components within both the cylinders in a plane stress condition are given by Flamant (7) as shown in Equations (2.5).

$$\sigma_x = -\frac{2z}{\pi} \int_{-a}^{a} \frac{p(s)(x-s)^2 \, ds}{\left\{(x-s)^2 + z^2\right\}^2} - \frac{2}{\pi} \int_{-a}^{a} \frac{q(s)(x-s)^3 \, ds}{\left\{(x-s)^2 + z^2\right\}^2} \qquad (2.5a)$$

$$\sigma_z = -\frac{2z^3}{\pi} \int_{-a}^{a} \frac{p(s) \, ds}{\left\{(x-s)^2 + z^2\right\}^2} - \frac{2z^2}{\pi} \int_{-a}^{a} \frac{q(s)(x-s) \, ds}{\left\{(x-s)^2 + z^2\right\}^2} \qquad (2.5b)$$

$$\tau_{zx} = -\frac{2z^2}{\pi} \int_{-a}^{a} \frac{p(s)(x-s) \, ds}{\left\{(x-s)^2 + z^2\right\}^2} - \frac{2z}{\pi} \int_{-a}^{a} \frac{q(s)(x-s)^2 \, ds}{\left\{(x-s)^2 + z^2\right\}^2} \qquad (2.5c)$$

These integrals were evaluated by McEwan (8) and expressed by Equations (2.6).

$$\sigma_x = -\frac{p_0}{a}\left\{ m\left(1 + \frac{z^2 + n^2}{m^2 + n^2}\right) - 2z \right\} + \frac{q_0}{a}\left\{ n\left(2 - \frac{z^2 - m^2}{m^2 + n^2}\right) - 2x \right\} \qquad (2.6a)$$

$$\sigma_z = -\frac{p_0}{a} m\left(1 - \frac{z^2 + n^2}{m^2 + n^2}\right) - \frac{q_0}{a} n\left(\frac{m^2 - z^2}{m^2 + n^2}\right) \qquad (2.6b)$$

$$\left(\tau_{zx}\right)_q = -\frac{p_0}{a} n\left(1 - \frac{m^2 - z^2}{m^2 + n^2}\right) - \frac{q_0}{a}\left\{\left(1 + \frac{z^2 + n^2}{m^2 + n^2}\right) - 2z\right\} \qquad (2.6c)$$

$$m^2 = \frac{1}{2}\left[\left\{\left(a^2 - x^2 + z^2\right)^2 + 4x^2 z^2\right\}^{1/2} + \left(a^2 - x^2 + z^2\right)\right] \qquad (2.6d)$$

$$n^2 = \frac{1}{2}\left[\left\{\left(a^2 - x^2 + z^2\right)^2 + 4x^2 z^2\right\}^{1/2} - \left(a^2 - x^2 + z^2\right)\right] \qquad (2.6e)$$

Additionally, the maximum shear stress for the plane strain condition is given by the radius of the Mohr's stress circle, defined by Equation (2.7).

$$\tau_{zx,\max} = \left[\frac{\left(\sigma_x - \sigma_z\right)^2}{2} + \tau_{zx} \right]^{1/2} \qquad (2.7)$$

Stress distributions for the plane strain condition and the contour of maximum shear stress are presented in Figure 2.3. According to them, the greatest value of $\tau_{zx,\,max}$ is $0.30p_0$ and it occurs below the surface at a depth of $0.78a$. Therefore, yield is considered to occur at the depth and it suggests subsurface crack initiation.

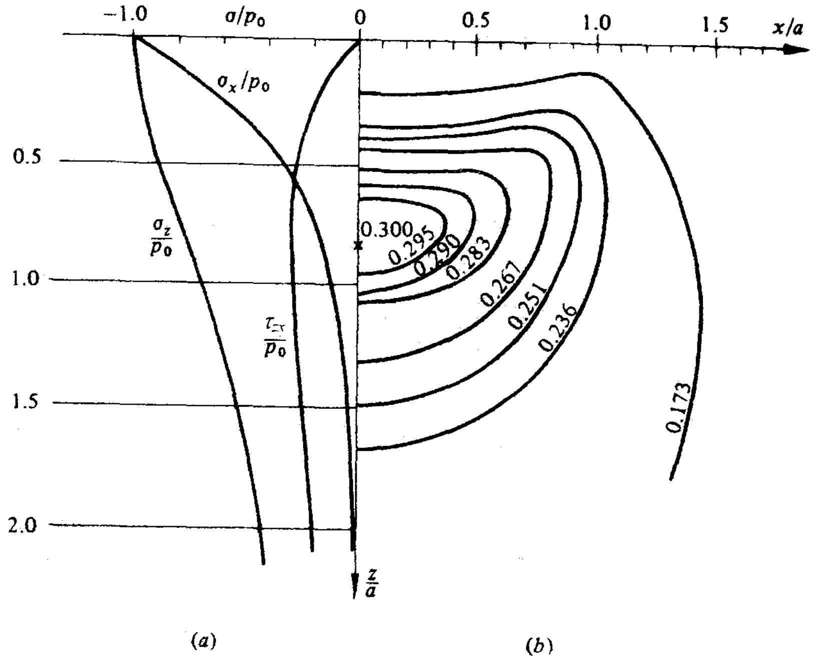

Figure 2.3 Distributions of contacting cylinders (a) subsurface stress along the axis of symmetry, (b) contours of maximum shear stress $\tau_{zx,max}$(6)

2.3.2 Slip at Surface Contact

The solution to the two-dimensional contact problem of rolling cylinders transmitting a tangential force was first presented by Carter(9) and discussed in more detail by Poritsky(10) in connection with the action of a locomotive driving wheel. The summary is presented in this section.

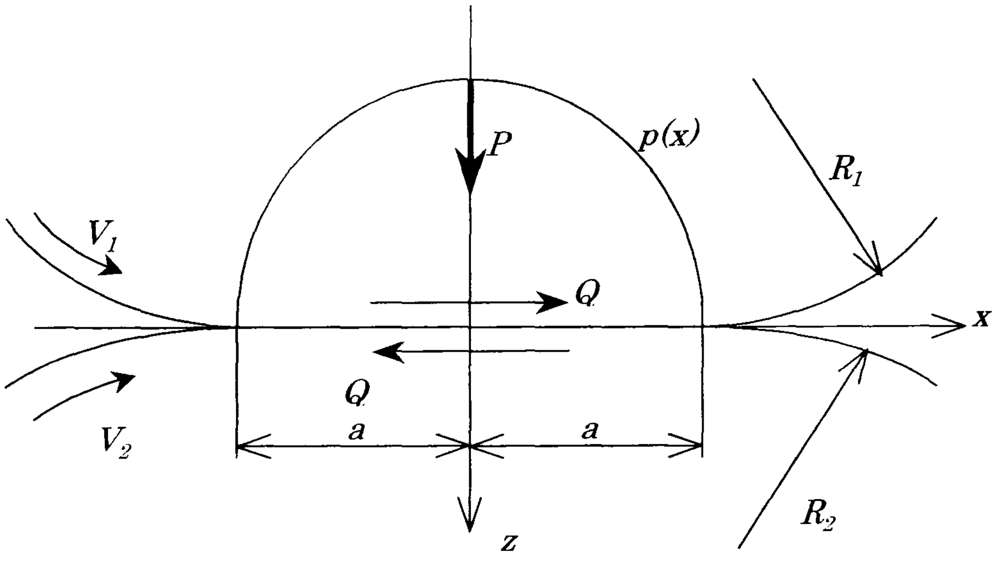

Figure 2.4 Rolling under the action of a tangential force(11)

As shown in Figure 2.4, a two-dimensional contact model, applying a tangential force Q upon the Hertzian contact is considered. In the condition, a slip in the surface contact region will occur due to the stress caused by tangential traction at rolling contact. The relationship between the tangential traction and the normal pressure in the contact is assumed to obey Amonton's law of sliding friction:

$$\frac{|Q|}{P} = \mu \tag{2.8}$$

If there were complete slip the tangential traction would be given by condition $|q(x)| = \mu p(x)$.

$$X' = q(x) = \mu p(x) = \frac{2\mu P}{\pi a}\sqrt{1 - \frac{x^2}{a^2}} \tag{2.9}$$

This traction produces tangential surface strains in the contact area given by

$$\frac{\partial u'}{\partial x} = -\frac{4\mu Pkx}{a^2} \tag{2.10}$$

where:

$$k = \frac{1 - \nu^2}{\pi E}$$

To obtain a region of no-slip a second tangential traction given by

$$X'' = -\left(\frac{a'}{a}\right)^2 \frac{2\mu P}{\pi a}\sqrt{1 - \frac{(x+c)^2}{a^2}} \tag{2.11}$$

Acting over the strip of width $2a'$ is added to X'. The strains due to X'', by analogy with Equation (2.10), are given by

$$\frac{\partial u''}{\partial x} = \left(\frac{a'}{a}\right)^2 \frac{4\mu Pk(x+c)}{a'^2} = \frac{4\mu Pk(x+c)}{a^2} \tag{2.12}$$

Thus the net strain within the inner band is

$$\frac{\partial u}{\partial x} = \frac{\partial u'}{\partial x} + \frac{\partial u''}{\partial x} = \frac{4\mu Pkc}{a^2} = const. \tag{2.13}$$

These distributions of traction and strain are illustrated in Figure 2.5.

Applying Equation (2.13) to each body in turn and remembering that the traction on the lower surface is opposite in sign to that on the upper produces,

$$\frac{\partial u_1}{\partial x}-\frac{\partial u_2}{\partial x}=\frac{4\mu P(k_1+k_2)c}{a^2}=const. \qquad (2.14)$$

This result establishes that there is no slip over the strip on which *X"* acts. The value of *a'* is determined by the equilibrium of the integrated traction *X* with the applied force *Q*, whence

$$\frac{a'}{a}=\sqrt{1-\frac{Q}{\mu P}} \qquad (2.15)$$

In his presentation of the theory, Poritsky was uncertain what factor controlled the position of the locked region specified by value of *c*. In the discussion, Cain(12) showed that the locked region coincided with the leading edge of the contact strip, whereby *c* had the value *a-a'*.

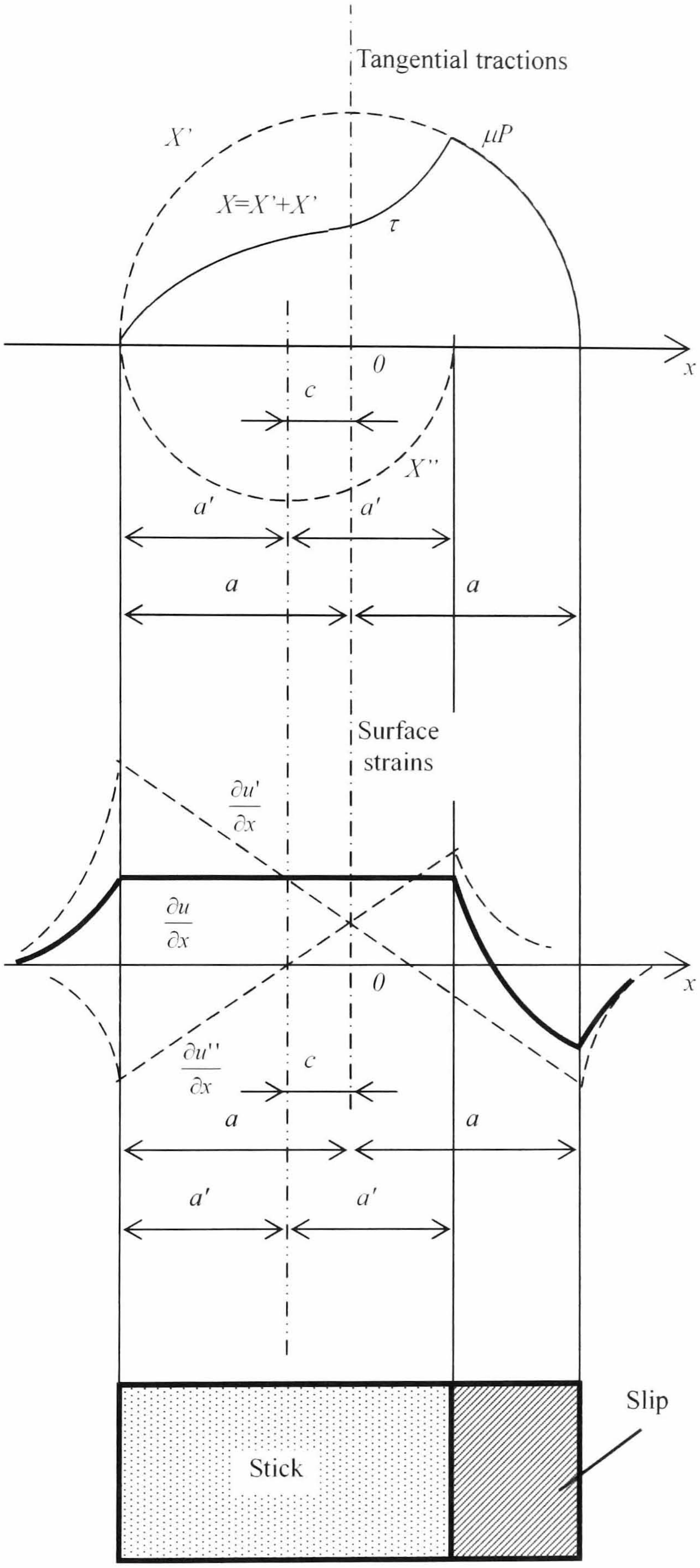

Figure 2.5 Carter-Poritsky theory of driving wheel; tangential tractions, surface strains and micro-slip in contact area (11)

2.3.3 Mechanisms of Crack Initiation in Rolling Contact Fatigue Wear

Merwin and Johnson (13) analysed plastic deformation at rolling contact theoretically and reported the behaviour of materials and their residual stresses under rolling contact. When a structure or mechanical component is subjected to repeated loading, its response depends upon the ratio of the amplitude of the maximum stress to the yield strength of the material.

Concerning these results to crack initiation, yield condition near the contact region is taken to be governed by von Mises' shear strain-energy criterion in the contact region, defined as Equation (2.16a).

$$k = \tau_{R,Y} = \left[\frac{1}{6}\left\{(\sigma_x - \sigma_y)^2 + (\sigma_y - \sigma_z)^2 + (\sigma_z - \sigma_x)^2 + (\tau_{xy}^2 + \tau_{yz}^2 + \tau_{zx}^2)\right\}\right]^{1/2} = \frac{\sigma_Y}{\sqrt{3}} \qquad (2.16a)$$

where:
$\tau_{R,Y}$- Von Mises' shear strain-energy criterion to yield
σ_Y- Yield stress

To simplify it, considering the model in plane stress condition, Equation (2.16a) can be expressed as (2.16b).

$$k = \tau_{R,Y} = \left[\frac{1}{6}\left\{(\sigma_x - \sigma_y)^2 + (\sigma_y - \sigma_z)^2 + (\sigma_z - \sigma_x)^2 + \tau_{zx}^2\right\}\right]^{1/2} = \frac{\sigma_Y}{\sqrt{3}} \qquad (2.16b)$$

where:
$\sigma_y = \nu\,(\sigma_x + \sigma_z)$
ν - Poisson's ratio (=0.3 for steel)

For example, as shown in Figure 2.6, at condition of μ=0, standing p_0 for the maximum contact pressure and a for the half width of contact, the maximum value of von Mises' stress takes $\tau_{R,max}$=0.322p_0 at depth e=0.705a (14). From these results, it can be suggested the first yield will occur at there and reach to subsurface crack initiation.

In addition, by applying friction force into the contact, the crack initiation point is moved to the surface. Specifically, at μ=0.05, $\tau_{R,max}$ is 0.323p_0 at the depth e=0.696a (15). On the other hand, maximum shear stress $\tau_{zx,max}$, obtained from Mohr's stress circle, defined by Equation

(2.7) also indicates a tendency to initiate crack at the subsurface, $\tau_{zx,max}=0.250p_0$ at $e=0.5a$(14) in the condition of $\mu=0$ and $\tau_{zx,max}=0.265p_0$ at $e=0.5a$ in the condition of $\mu=0.05$(15).

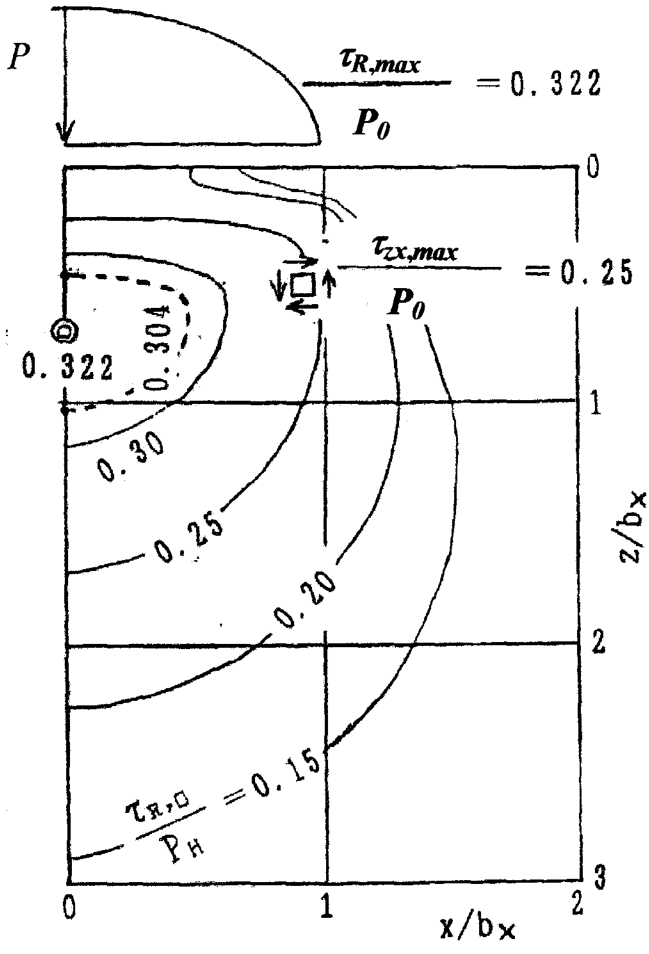

(a) $\mu=0$(14)

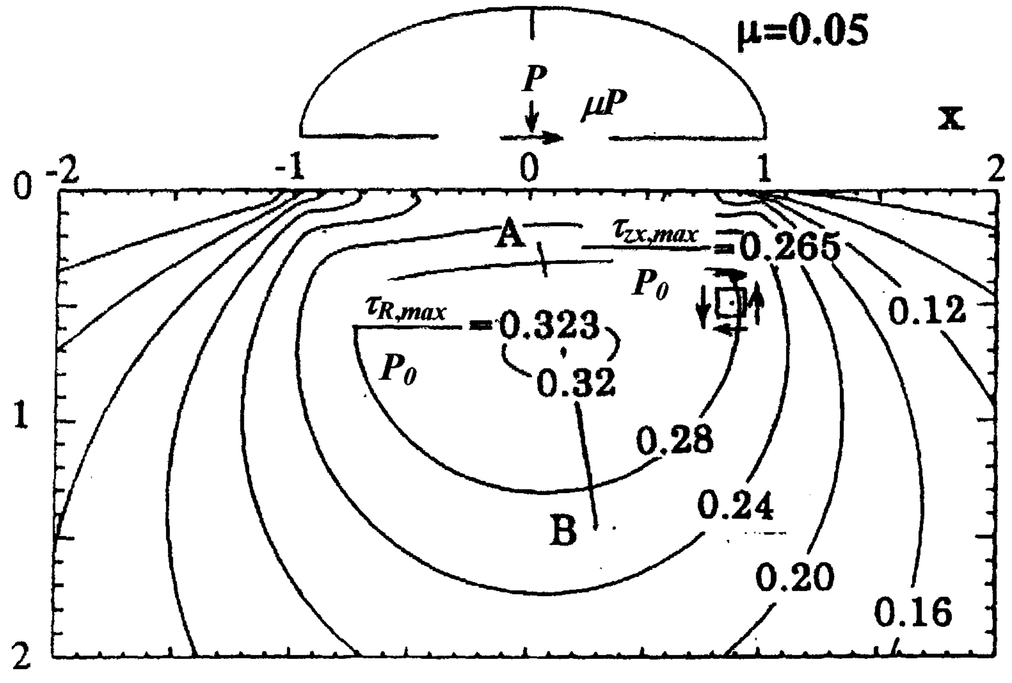

(b) $\mu=0.05$(15)

Figure 2.6 Distributions of τ_R/p_0 in $\mu=0$ and $\mu=0.05$

Considering the stress distributions, when μ=0, yield first occurs at a point beneath the surface where the maximum contact pressure p_0=1/0.322k=1.79σ_Y (the value of 1.79 depends on contact conditions such as geometry or yield conditions). Beyond the yield point, 'shakedown' under repeated loading will be happening when p_0=4k=2.31σ_Y. Under this condition, in the first pass of repeated loading, the elastic limit is exceeded and some plastic deformation will take place thereby introducing residual stress. In the second passage of the load, the material is subjected to the combined action of the contact stresses introduced in the previous pass. Generally speaking such residual stresses are protective in the sense that they make yielding less likely on the second pass. It is possible that after a few passes the residual stresses build up to such a value that subsequent passes of the load result in entirely elastic deformation.

When the load exceeds the shakedown limit, orthogonal plastic shear would occur in the subsurface elements *B* and *D* shown in Figure 2.7. According to experiments in free rolling condition by Crook (16) and Hamilton (17), these amounts are not the same. Permanent shear at element *D* was slightly larger than that of *B* and it causes cumulative deformation and forward displacement in the surface layers shown in Figure 2.8.

Although, the shakedown theorem is used as a tool for analysis of rolling contact, Miyoshi (18) pointed out that rolling fatigue occurred even if the amplitude of the maximum contact pressure was below the yield point. He proposed surface roughness as a reason for residual stress creation within the specimens. As a result, stress distribution in the contact region indicates the tendency to initiate a crack at subsurface. However, there is no indication of surface crack initiation from the stress distribution.

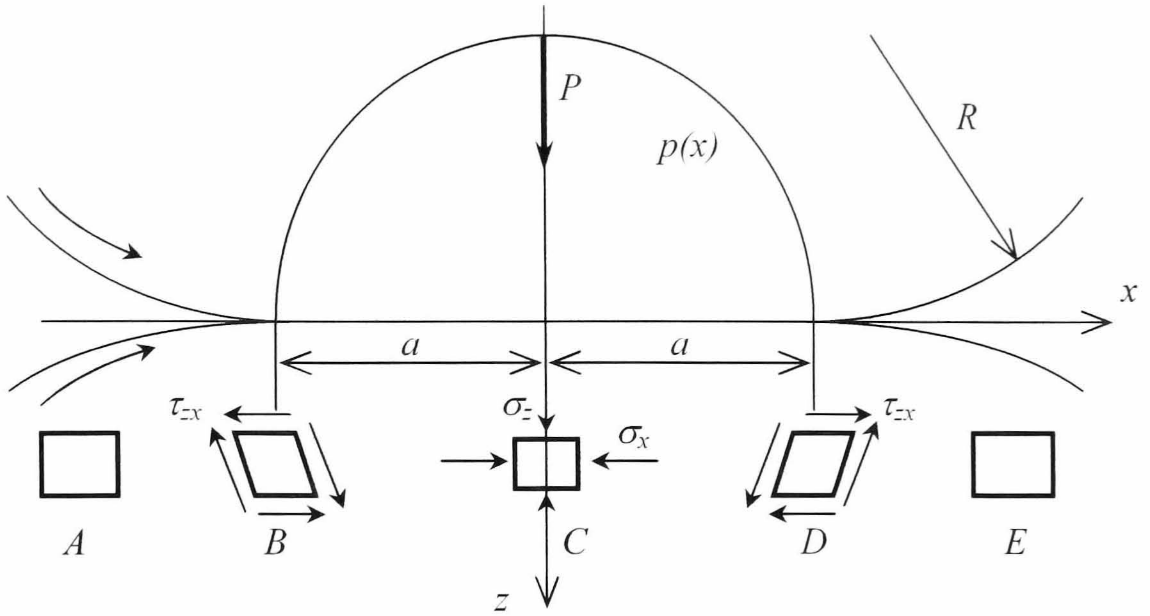

Figure 2.7 Deformation in rolling contact, an element of material experiences the cycle of reversed shear and compression *A-B-C-D-E* (6)

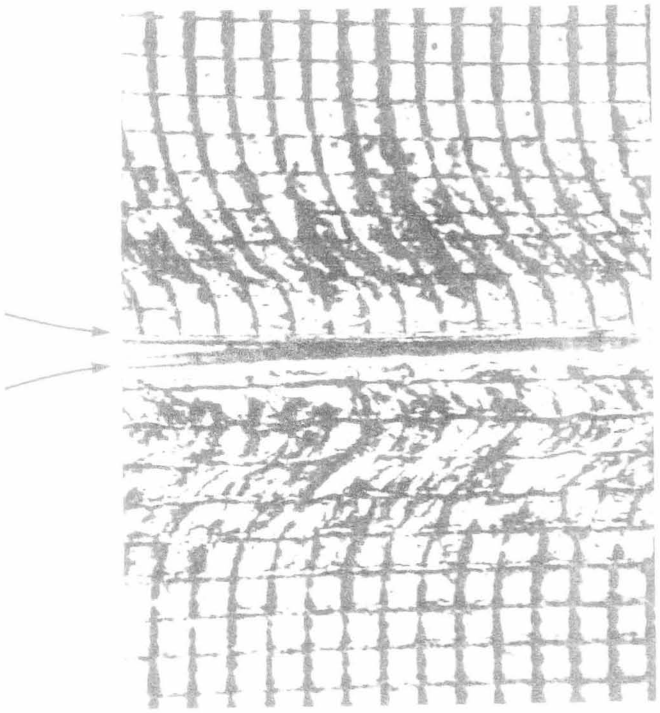

Figure 2.8 Plastic deformation in rolling contact (6)

On the other hand, several models of its mechanism are suggested for surface crack initiation. Chiu (19) observed the initiation point of surface crack in flaking failure due to contamination present between contacting bodies and the formation of stress concentration. Muro (20) studied residual stress in detail using his results of surface crack initiation and pointed out that there are residual tensile stresses just below the rolling contact surface. He also explained that crack initiation is due to the cyclic combination of residual stress and contact stress. Additionally, Miyoshi (21) put forward the mechanism of arrowhead shaped debris formation which is caused by cyclic surface asperity deformation and tensile strain.

2.3.4 Mechanisms of Crack Propagation in Rolling Contact Fatigue Wear

Many models put forward the mechanism of crack propagation, however they can be roughly classified into two types, that is, opening or tensile mode (mode I) and forward shear or edge sliding mode (mode II). Way (22) evaluated effects of lubricants and surface shape at rolling contact in two roller experiments and described the process from crack initiation to pitting. According to his observation, the crack was initiated from the surface, not at the point of maximum von Mises' shear strain-energy criterion in subsurface. He argued that contaminations at the contact area cause plane stress concentration on the surface and help to initiate surface crack. For the mechanisms of pitting under lubricating conditions, he explained that the surface crack is propagated in mode I by pressure produced by locked up lubricant in the crack. Therefore, high viscosity lubricant can prevent pitting because they cannot easily enter the crack. Muro (23) also estimated the crack propagation by mode I applying residual stress produced during shakedown process.

On the other hand, Otsuka (24) pointed out that cracks propagate in mode II under compressive stress created in a rolling contact.

Crack propagation mechanism in rolling contact is also analysed numerically using fracture mechanics. For instance, Keer and Bryant (25) (26) (27) evaluated stress intensity factor for surface and subsurface cracks using elastic analysis and explained the mechanism of pitting as mode II.

However, the mechanism is not yet fully elaborated. This is because: 1) contact stress distribution model with a crack cannot be classified as Hertzian contact; 2) crack surfaces have to be considered as a contact problem; 3) load due to friction at the surface has to be considered; 4) friction coefficient magnitude at crack surface is uncertain; 5) behaviour of a lubricant in the crack is not fully clarified.

2.4 Crack Initiation Mechanism Based on Dislocation Theory

2.4.1 Crack Initiation Model

In machine elements, such as bearings or gear wheels, all of the input power for the elements is not transmit as output work, and some of the power is dissipated. Energy can be dissipated due to (28);

(1) Formation of real area of contact in the contact region

(2) Works at contact region

- 1) Elastic deformation
- 2) Plastic deformation
- 3) Adhesion

(3) Dissipations of energy at contact area

- a) Deformation accumulation in the material
  - 1) Accumulation of strain energy
  - 2) Generation of dislocations or defects
- b) Heat radiation
- c) Other energy radiation
  - 1) Sound waves
  - 2) Photons
  - 3) Electrons

In this section, current studies of the relation between crack initiation, dislocation, and the energy dissipation are reviewed.

Initiation of fatigue cracks in a crystalline material is started with the nucleation and accumulation of dislocations. Due to these actions, specific slip markings consisting of extrusions and intrusions called persistent slip markings (PSM) or persistent slip bands (PSB) are created on the surface (29). The inside of the markings, accumulation of dislocations forms ladder structure shown in Figure 2.9.

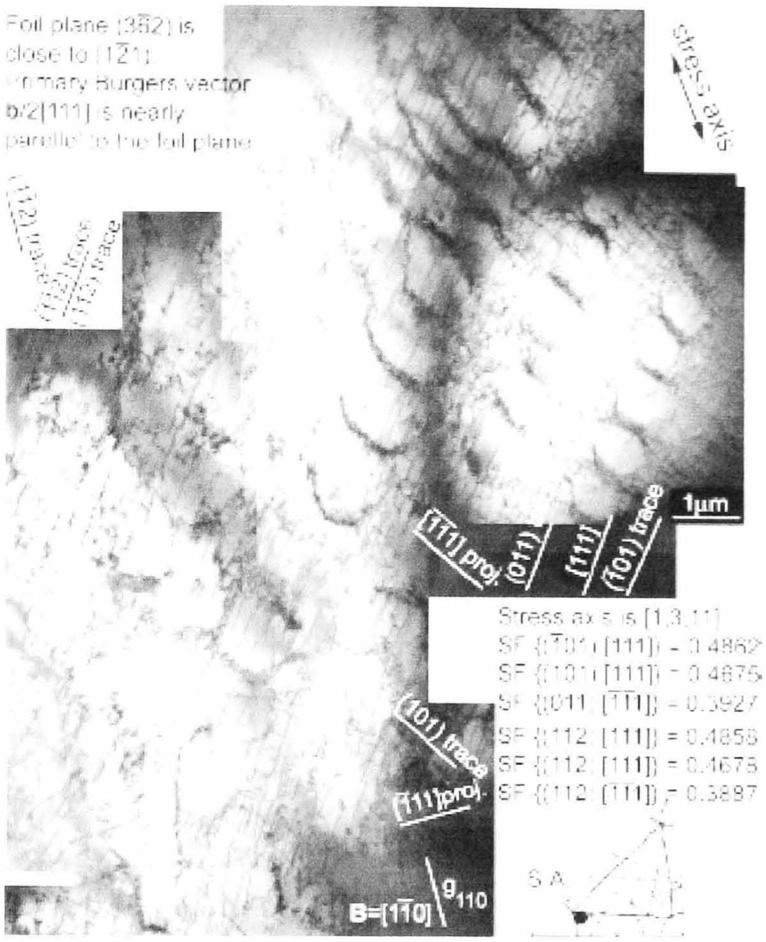

Figure 2.9 Ladder formed dislocation structure in the grain of fatigued steel (30)

In connection with the mechanism of wear process linked to fatigue, models based on dislocation theory are suggested. These mechanisms, originally for bulk materials, can be applied to regions close to surface (31). An example of wear mechanism based on dislocation, is that proposed by Suh (32). He reported the mechanism based on the behaviour of dislocations at the surface, sub-surface crack and void formation, and subsequent amalgamation of cracks by shear deformation of the surface.

For crack initiation nearby surface, mechanisms based on dislocation theory are also suggested by some researchers. Zener (33) presented the model shown in Figure 2.10 (a). In his model, dislocations were stopped by an obstacle where a crack is thus initiated to release high level energy accumulated in the dislocation pileup. Cottrel (34) explained that united dislocations along cleavage surface initiate the crack shown in Figure 2.10(b). Stroh (35) (36) proposed that crack initiates at tilt boundary as shown in Figure 2.10(c). In addition to the suggested mechanisms, obstacles such as oxides existing in the subsurface region can be the crack initiation source or cause of dislocation pileup.

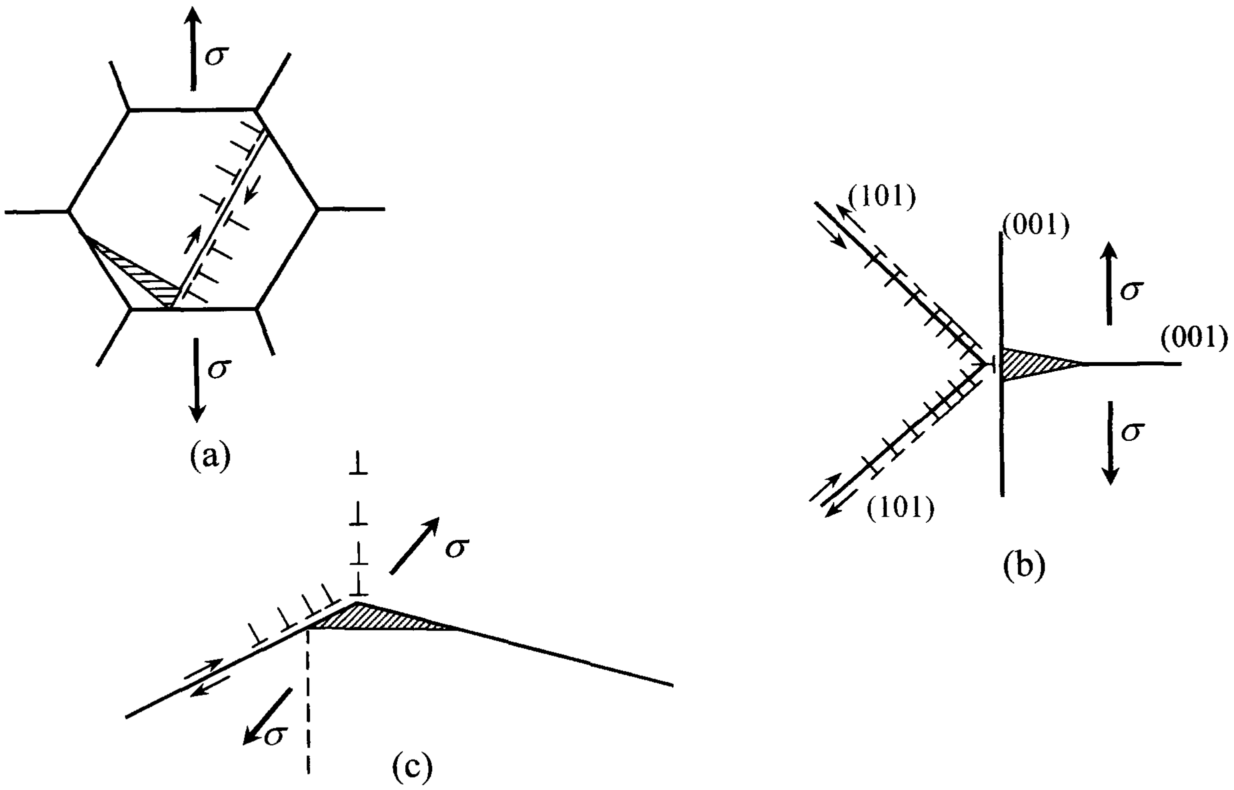

Figure 2.10 Crack initiation models (28)

2.4.2 Thermally Activated Process in Dislocation

For isotropic crystals, free energies per unit length of a dislocation are expressed by Equation (2.17) (37);

$$\Delta E_e = \frac{Gb^2}{4\pi(1-\nu)}\ln\frac{r_1}{r_0} \qquad (2.17a)$$

$$\Delta E_s = \frac{Gb^2}{4\pi}\ln\frac{r_1}{r_0} \qquad (2.17b)$$

where:
ΔE_e - Free energy for an edge dislocation
ΔE_s - Free energy for a spiral dislocation
G - Shear modulus
ν - Poisson's ratio
b - Burgers vector
r_0 - Core radius
r_1 - Effective radius

When these energies are assumed to correspond to strain energy at wear process, it is less than 1% of whole the energy dissipated at wear process and most of them are transformed to heat radiation (38).

To make a slip motion of a dislocation, activation energy that overcomes resistance for the dislocation is needed. Generally, the energy is supplied as external work. Additionally, the energy due to thermal vibration at lattice, called 'thermal fluctuation' can be provided as activation energy. The phenomenon is called "thermally activated process".

Illustration of resistance energy is schematically shown in Figure 2.11. When the resistance force is compared to the height l^* and the range affected is compared to width d^*, the resistance energy for dislocation corresponds to an area of mountain-shaped curve. When external force per unit length is applied to the dislocation in the slip direction, it is expressed by Equation (2.18).

$$f_e = \tau_e b \qquad (2.18)$$

where:
f_e - External force
τ_e - Shear stress
b - Burgers vector

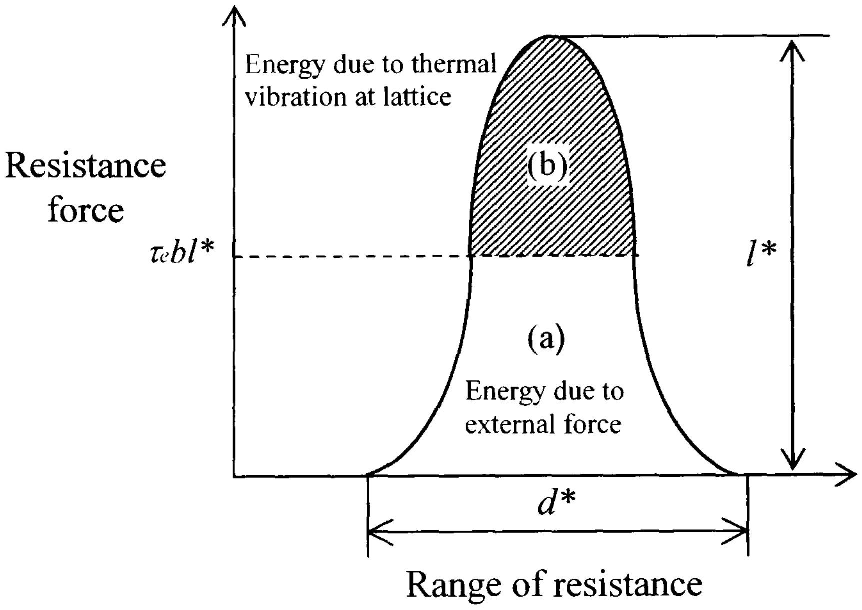

Figure 2.11 Resistance energy for dislocation (39)

The activation energy obtained from f_e is equal to (a) in Figure 2.11 and more energy, corresponding to (b), is needed to initiate slip. The energy due to thermally activated process satisfies the gap in a probability expressed by Equation (2.19) (39).

$$2\exp\left(-\frac{U_0}{kT}\right)\sinh\frac{\tau_e bl^* d^*}{kT} \qquad (2.19)$$

where:
U_0- Resistance energy
K - Boltzmann constant
T - Absolute temperature

The value of kT is about $4\text{x}10^{-21}$J in room temperature and $1.8\text{x}10^{-20}$J even if T=1300K (38). Thus, when dislocation is slipped due to thermally activated process, it is required that there is a certain activation energy due to external work and low resistance for the motion; for instance, low resistance force or small resistance range.

(1) A. Palmgren, “Ball and Roller Bearing Engineering”, (1945), S.H. Burbank & Co.

(2) Otsuka, Mori and Kawamura, JSME International Journal Series A, Vol.45-399, (1979), 1312.

(3) Murakami, Sakae, Ichimaru and Morita, JSME International Journal Series C, Vol. 62-594, (1996), 683.

(4) Hertz, “Uber die Beruhrung Fester Elastischer korper”, (1881), J.Reine and Math.

(5) T.A. Stolarski and S. Tobe, “Rolling Contacts”, (2000), J.W Arrowsmith Ltd, UK.

(6) K.L. Johnson, “Contact Mechanics”, (1985), Cambridge University Press.

(7) Flamant, Compt. Rendus, Vol. 114, (1892), pp. 1465 Paris.

(8) E. McEwan, “Stresses in elastic cylinders in contact along a generatrix”, Philosophical Magazine, Vol. 40, (1949), pp. 454.

(9) F.W. Carter, Proc. Roy. Soc. London, A 112, (1926), pp. 151.

(10) H. Poritsky, J. Appl. Mech., Vol. 72, (1950), pp. 101.

(11) Bidwell, “Rolling contact phenomena”, (1962), Elsevier publishing company.

(12) B. S. Cain, J. Appl. Mech., Vol. 72, (1950), pp. 465.

(13) J.E. Merwin and K.L. Johnson, “An Analysis of Plastic Deformation in Rolling Contact”, Proceedings of the Institution of Mechanical Engineers, Vol. 177, (1963), pp. 676-685.

(14) J.O. Smith and Ch.K. Liu, “Stresses due to tangential and normal loads on an elastic solid with application to some contact stresses problems”, J. Appl. Mech., Vol. 20, (1953), pp. 157

(15) M. Shima, K. Okada, K. Kimura and R. Yamamoto, Journal of Japan Society of Lubrication Engineers, Vol. 25, (1980), pp. 817

(16) A.W. Crook, “Simulated gear-tooth contacts: some experiments on their lubrication and subsurface deformation”, Proceedings, Institution of Mechanical Engineers, Vol. 171, (1957), pp. 187.

(17) G.M. Hamilton, “Plastic flow in rollers loaded above the yield point”, Proceedings, Institution of Mechanical Engineers, Vol. 177 (1963), pp. 667.

(18) H. Miyoshi, Journal of Japanese Society of Tribologists, Vol. 20, (1975), pp.843-851.

(19) Y.P. Chiu and J.Y. Liu, “An Analytical Study of the Stress Concentration around a Furrow Shaped Surface Defect in Rolling Contact”, Transactions of the ASME, Journal of Lubrication Technology, Vol. 92, (1970), pp. 258-263.

(20) H. Muro, T. Tsushima and M. Nagafuchi, “Initiation and Propagation of Surface Crack in Rolling Fatigue of High Hardness Steel”, Wear, Vol. 35, (1975), pp. 261-282.

(21) H. Miyoshi, Journal of Japanese Society of Tribologists, Vol. 39, (1994). pp. 678-684.

(22) S. Way, “Pitting Due to Rolling Contact”, Transactions of the ASME, Journal of Applied Mechanics, Vol. 2, (1935), pp.A49-58.

(23) Muro, Journal of Japanese Society of Tribologists, Vol. 39, (1994), pp.668-677.

(24) A. Otsuka, H. Sugawara and M. Shomura, “A Test Method For Mede II Fatigue Crack Growth Relating to a Model for Rolling Contact Fatigue”, Fatigue & fracture of engineering materials & structures, Vol. 19, (1996), pp.1265-1275.

(25) L.M. Keer, M.D. Bryant and G.K. Haritos, “Subsurface Cracking and Delamination”, ASME AMD, Vol. 39, (1980), pp.79-95.

(26) L.M. Keer, M.D. Bryant and G.K. Haritos, "Subsurface and Surface Cracking due to Hertzian Contact", Transactions of the ASME, Journal of Lubrication Technology, Vol. 104, (1982), pp.347-351.

(27) L.M. Keer and M.D. Bryant, "A Pitting Model for Rolling Contact Fatigue", Transactions of the ASME, Journal of Lubrication Technology, Vol. 105, (1983), pp.198-205.

(28) H. Czichos, "Tribology", (1978), Elsevier scientific publishing company

(29) H. Mughrabi, "Dislocations and Properties of Real Materials", The Institute of Metals, London, (1985), pp. 244–262.

(30) J. Polak, M. Petrenec and J. Man, "Dislocation structure and surface relief in fatigued metals", Materials Science and Engineering A, Vol. 400-401, (2005), pp. 405-408.

(31) D.H. Buckley, "Friction, Wear and lubrication in vacuum", (1971), NASA SP-277, Washington, pp.66.

(32) N.P. Suh, "The delamination theory of wear", Wear, Vol. 25, (1973), pp. 111-124.

(33) C. Zener, "The micro-mechanism of fracture", In: Fracturing of Metals. American Society of Metals, Cleveland, (1948), pp. 3-31.

(34) A.H. Cotterel, "Theory of brittle fracture in steel and similar metals", Transaction of the Metallurgical Society of the AIME, Vol. 212, (1958), 192-203.

(35) A.N. Stroh, "The Formation of cracks as a result of plastic flow, I", Proceedings of The Royal Society of London Series, Vol. A 223, (1954), pp. 404-414

(36) A.N. Stroh, "The Formation of cracks as a result of plastic flow, II", Proceedings of The Royal Society of London Series, Vol. A 232, (1955), 548-560

(37) G.E.R. Shultze, "Metallphysik", Akademie-Verlag, Berlin, (1967), pp. 217.

(38) N. Gane and J. Skinner, "The generation of dislocations in metals under a sliding contact and the dissipation of frictional energy", Wear, Vol. 25, (1973), pp. 381-384

(39) O. Izumi, "Atomism for material strength", (1985) The Japan Institute of Metals

Chapter 3 Magnetisation of Ferromagnetic Substances

3.1 Introduction

Ferromagnetic substances have domain structure, composed of magnetic domains and domain walls, and they are arranged to minimize the internal energy. Magnetisation is taking place due to an external magnetic field and reaches the saturation through two processes: domain wall displacement and rotation magnetisation. Properties of applied magnetic field and magnetism of ferromagnetic substances are expressed by hysteresis loop. It is known that the magnetic properties are affected by inclusion or mechanical conditions such as stresses.

The objective of this chapter is to review structure of ferromagnetic substances and its magnetisation process with its energy status and provide current knowledge of the relation between magnetisation and internal stress.

3.2 Structure of Ferromagnetic Substances

Ferromagnetic substances, such as Fe, Ni, etc., have spontaneous magnetisation below Curie temperature. As shown in Figure 3.1, magnetic moments in the substance are divided into a number of magnetic domains. Without external magnetic field magnetic domain structure is formed and a state of magnetic pole, as a whole, exists. Magnetic domains are distributed to cancel directions of magnetisation. The direction magnetic moments point to is parallel to an axis of easy magnetisation. For instance, in iron crystal the easy axes are [100], [010], and [001]. As seen in Figure 3.1, the boundaries between the domains are named 'domain wall'. Inside the domain wall, magnetic domains rotate gradually from one domain to the next. When the external magnetic field is applied parallel to the magnetisation of one domain, the moments inside both domains experience no torque resulting from the field. In contrast, moments inside the wall, which have some angle with the field direction, start to rotate toward the field direction. As a result of the rotation of the moment inside the wall, the centre of the wall should be displaced as seen in Figure 3.2, resulting in an increase in the volume of the domain that has its magnetisation parallel to the external field.

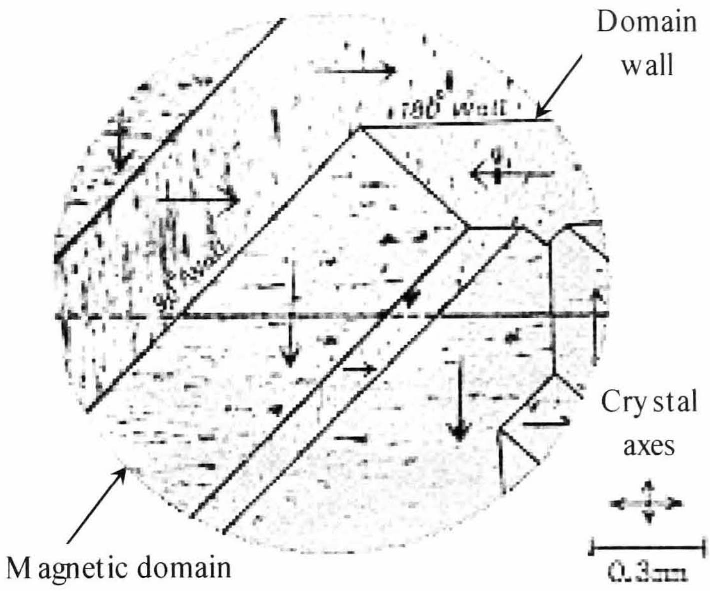

Figure 3.1 Domain pattern on a surface of 4% Si-Fe crystal (1)

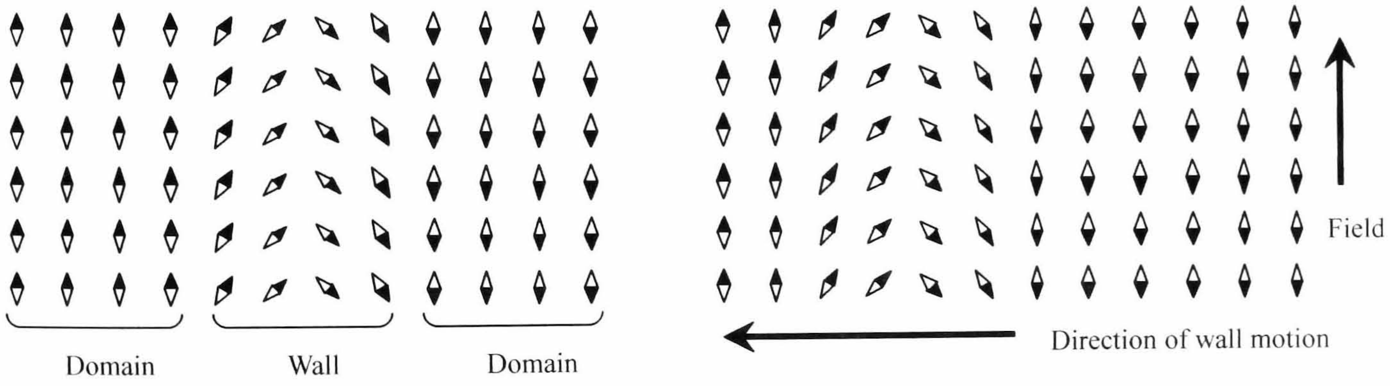

Figure 3.2 Schematic explanation of domain wall and its displacement (1)

When external magnetic field is not applied, stable domain structure, such as the size, the shape, is determined so as to minimize the total energy. Total energy is composed of:

1) Magnetostatic energy

   Associated with magnetisation in its own self-field. It increases when magnetic pole appears on the surface of ferromagnetic materials.

2) Exchange energy

   Associated with Pauli's exclusion principle among atomic moments and is required at forming domain wall to reduce magnetostatic energy.

3) Anisotropy energy

   Associated with tendency for the magnetic moments to align directions with an axis of easy magnetisation. It increases when the direction shifts due to external magnetic fields.

4) Magnetoelastic energy

   Associated with spontaneous deformation during magnetisation process.

From these energies, magnetostatic energy to form domains, exchange and anisotropy energies to form domain walls are main components when no external magnetic field exists. Specifically, magnetic domains have a tendency to be divided into many thin domains for the reason that magnetostatic energy increases in proportion with the width of domain. When the domains are divided into thin pieces, domain walls are created at these boundaries simultaneously. It means that exchange and anisotropy energies are increased whilst magnetostatic energy is decreased. Thus, the thickness of domains *d* is decided to minimize the total of these energies. Total energy per area is expressed below:

$$e = e_m + e_{ex} + e_a \qquad (3.1)$$

where:
e - Total energy
e_m- Magnetostatic energy
e_{ex}- Exchange energy
e_a- Anisotropy energy

$$e_m = \frac{2I_s^2 d}{\pi^2 \mu_0} \sum_{n=1}^{\infty} \frac{1}{n^2 d} \int_0^d \sin n\left(\frac{\pi}{d}\right) x dx \qquad (3.2)$$

$$e_{ex} + e_a = \frac{l}{d}\left(\frac{JS^2\pi^2}{a^2 N} + KNa\right) \qquad (3.3)$$

where:
I_s - Saturation magnetisation
d - Thickness of domain
μ_0- Permeability of vacuum
l - Thickness of the crystal
J - Exchange integral
S - Total spin quantum number
a - Lattice constant
N - Number of atoms in a domain wall
K - Anisotropy constant

For example, considering 180° wall of Fe, substitute I_s=2.15T, $\mu_0 = 4\pi x10^7$, l=0.01m, J=2.16x10^{-21}, S=1, N=150, K=4.2x10^4 into Equation (3.2) and (3.3), d=5.6x10^{-6}m and e=5.63J/m^2 will be obtained.

3.3 Magnetisation Process of Ferromagnetic Substances

One feature of ferromagnetic substances is that they exhibit a fairly complex change in magnetisation upon the application of a magnetic field. This behaviour can be described by an initial magnetisation curve (see Figure 3.3). Starting from a demagnetised state (I=H=0), the magnetisation increases with an increase of the field along the curve *OABC* and finally reaches the saturation magnetisation which is normally denoted by I_s. In the region *OA* the process of magnetisation is almost reversible; that is, the magnetisation comes back to zero upon removal of the field. Beyond this region the processes of magnetisation are no longer reversible. If the field is decreased from its value of at point *B*, the magnetisation comes back, not along *BAO*, but along the minor loops *BB'*. If the magnetic field is decreased from the saturated state *C*, the magnetisation I is gradually decreased along *CD*, not along *CBAO*, and at $H=0$ it reaches the finite value I_r ($=OD$), which is called the residual magnetisation or the remanence. Further increase of the magnetic field in a negative sense results in a continued decrease of the intensity of magnetisation, which finally falls to zero. The field at this point is called the coercive force H_c ($=OE$). This position, *DE*, of the magnetisation curve is often referred to as a demagnetising curve. Further increase of H in a negative sense results in an increase of the intensity of magnetisation in a negative sense and finally leads to a negative saturation magnetisation. If the field is then reversed to the positive sense, the magnetisation will change along *FGC*. The closed loop *CDEFGC* is called the hysteresis loop.

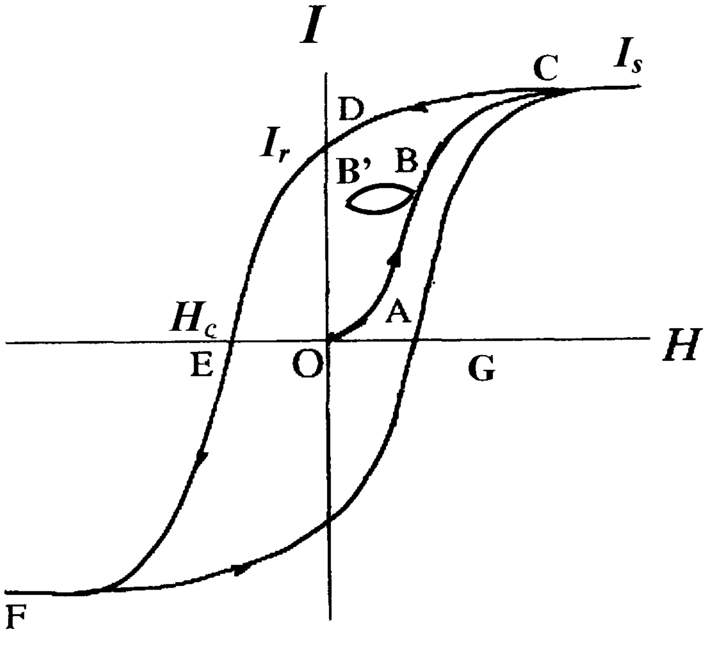

Figure 3.3 Initial magnetisation curve and hysteresis loop (1)

In magnetisation process *OABC*, the ferromagnetic substance takes two steps to saturation. When a magnetic field is applied, domains whose magnetisation directions are closest to the field direction increase their volume by domain wall displacement from in Figure 3.4 (a) to (b) and finally cover the whole volume of the specimen shown in Figure 3.4 (c). If the field is increased further, the magnetisations in each domain rotate from the easy directions toward the field direction, and finally the specimen reaches saturation magnetisation shown in Figure 3.4 (d). Details of each process are described below.

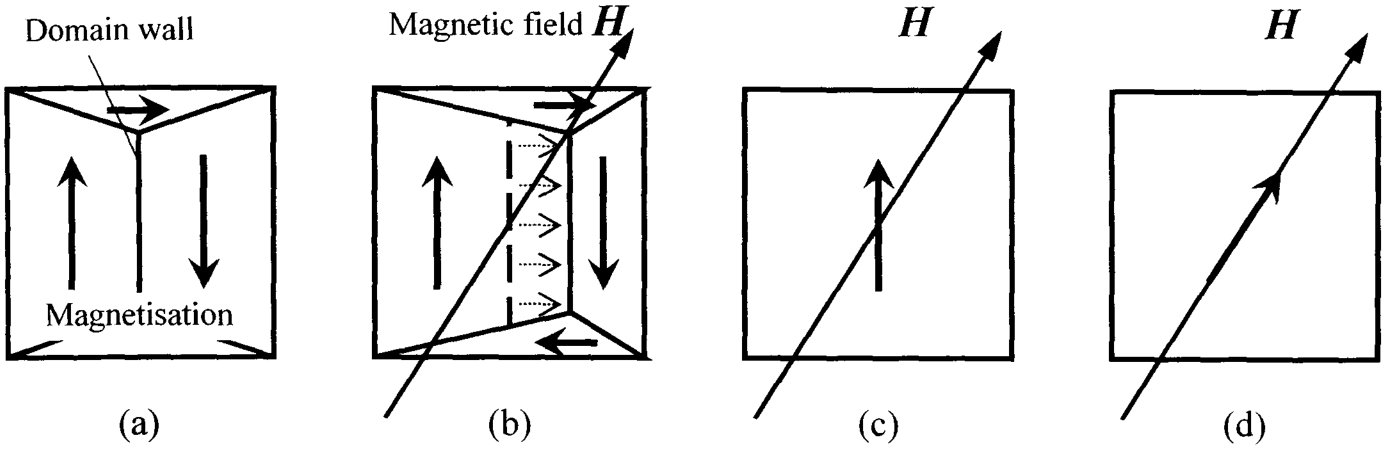

Figure 3.4 Magnetisation process of ferromagnetic materials

(1) Domain wall displacement

Magnetic domains inside of ferromagnetic substance tend to arrange in line along the easy directions. The domain walls, boundary between the domains, move during the domains are making uniform their directions. Thus, at the step, energy for magnetisation can be stated to spend for domain wall displacement. The energy is expressed as Equation (3.4).

$$\Delta U_m = 2I_s H \cos\theta \qquad (3.4)$$

where:
ΔU_m - Energy for magnetisation
I_s - Saturation magnetisation
H - Magnetic field
θ - Angle of directions between magnetic field and easy direction

However, there are foreign substances in domains such as inclusions or dislocations in particular, and they act as resistance against the domain wall displacement. These inclusions are dealt with as defects. Due to non-homogeneity, magnetic poles appear on the surface of the defect in a domain and magnetostatic energy is generated there. When a domain wall passes by the defect, magnetic poles on the surface are divided and the magnetostatic energy is reduced to half. Thus, inclusions or dislocations in a domain wall act as resistance so as to make it energy state stable. The effect of these defects during magnetisation is experimentally observed as Barkhausen noise (2) and utilized for a non destructive inspection. The magnetostatic energy U_{mag} generated due to a defect is expressed assuming the defect as a sphere in radius of r.

$$U_{mag} = \frac{1}{2} \cdot \frac{1}{2} \cdot \frac{I_s^2}{3\mu_0} \cdot \frac{4\pi r^3}{3} \approx 2.8 \times 10^5 I_s r^3 \qquad (3.5)$$

The value of magnetic field H_0 to separate domain wall from resistance of a defect is given below.

$$2I_s H_0 \cos\theta \cdot l^2 r > U_{mag} \qquad (3.6)$$

The value H_0, which satisfies Equation (3.6), is $H_0 > 3\times10^3$A/m for Fe. In magnetisation process, region below H_0 is called initial permeability range. In this region, due to the resistance against domain walls, increase of magnetisation is small. When the magnetic field is beyond H_o, domain walls can move freely from the resistance and magnetisation increases sharply. The region beyond H_0 is called range of irreversible magnetisation.

(2) Rotation magnetisation

When a further magnetic field is applied to, magnetic moments which completed domain wall displacement are turned to the same easy direction; domains rotate along direction of the field from the easy direction. At the rotation, energy for magnetisation is consumed against anisotropy energy. This region in magnetisation process is called range of rotation magnetisation. When the rotation is completed, magnetisation is saturated.

As magnetic fields are increased in this region, the shape of ferromagnetic specimen is deformed. The phenomenon is called magnetostriction and magnetoelastic energy is consumed during the process. The strain $\delta l/l$ due to magnetostriction is as small as 10^{-5} to 10^{-8}.

3.4 Demagnetising Factor

If a ferromagnetic body of finite size is magnetised, free magnetic poles are induced on both its ends. They raise a magnetic field in an opposite direction to the magnetisation. This field, called demagnetising field H_d, is proportional to magnetisation I and expressed as Equation (3.7).

$$H_d = \frac{NI}{\mu_0} \qquad (3.7)$$

where:
μ_0- Permeability of vacuum
N - Demagnetising factor (dimensionless quantity), $0 \leq N \leq 1$

The demagnetising factor N is function of the shape of specimen. When a long, thin specimen rod is magnetised along its long axis, N takes small value. In contrast, the factor takes larger for a short, thick specimen.

3.5 Relation between Magnetisation and Fracture of Materials

To understand the relation between magnetisation and deformation of ferromagnetic substances, many studies have been carried out. Characteristics of Barkhausen noise, that is the effect of defects observed in magnetisation process are clarified by Lomaev (3). According to him, the noise responds sensitively to material structure and stress status and it has been tried to be utilized for a non-destructive inspection by analysing grain sizes (4), inclusions (5), dislocations (6), and residual stresses (7).

For the behaviour of the hysteresis loop and magnetostrictive behaviour under elastic stress, Makar and Tanner (8) (9) observed that the magnetic properties of steels are varied by amount of C contents and applied stresses in the curves shown in Figure 3.5. They postulated that the inclusion in the steel and increase or motion of dislocation act as resistance against domain wall movement. Concerning the effect of magnetostriction, Asai (10) pointed out that magnetostriction is changed by stress direction and explained the reason as an issue of internal energy.

Concerning the effect of magnetostriction on mechanical properties, Tang (11) and Lu (12) reported that pulsed magnetic field decreases residual stress in low carbon steel as shown in Figure 3.6. Tang (13) explained the mechanism by postulating that pulsed magnetic process reduces dislocation density and makes rearrangement of dislocation in the specimens (see Figure 3.7).

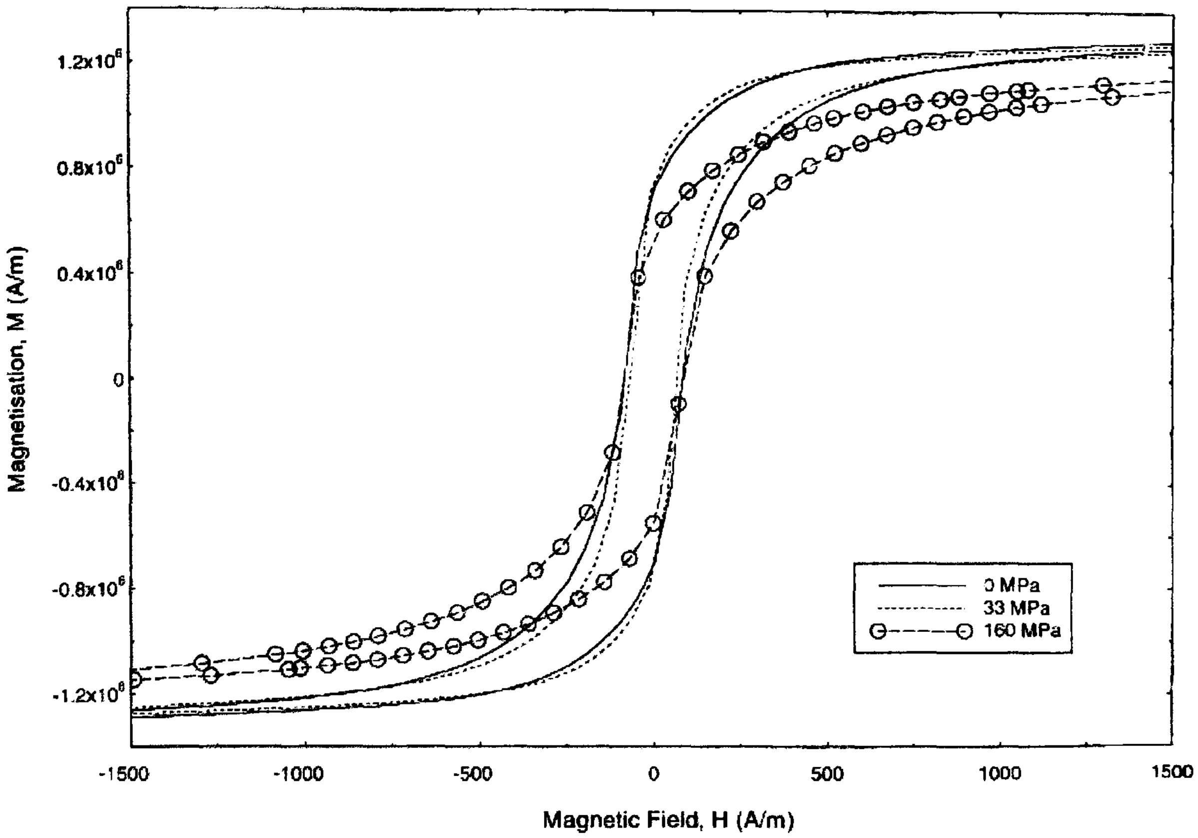

(a) 0.003 wt% C

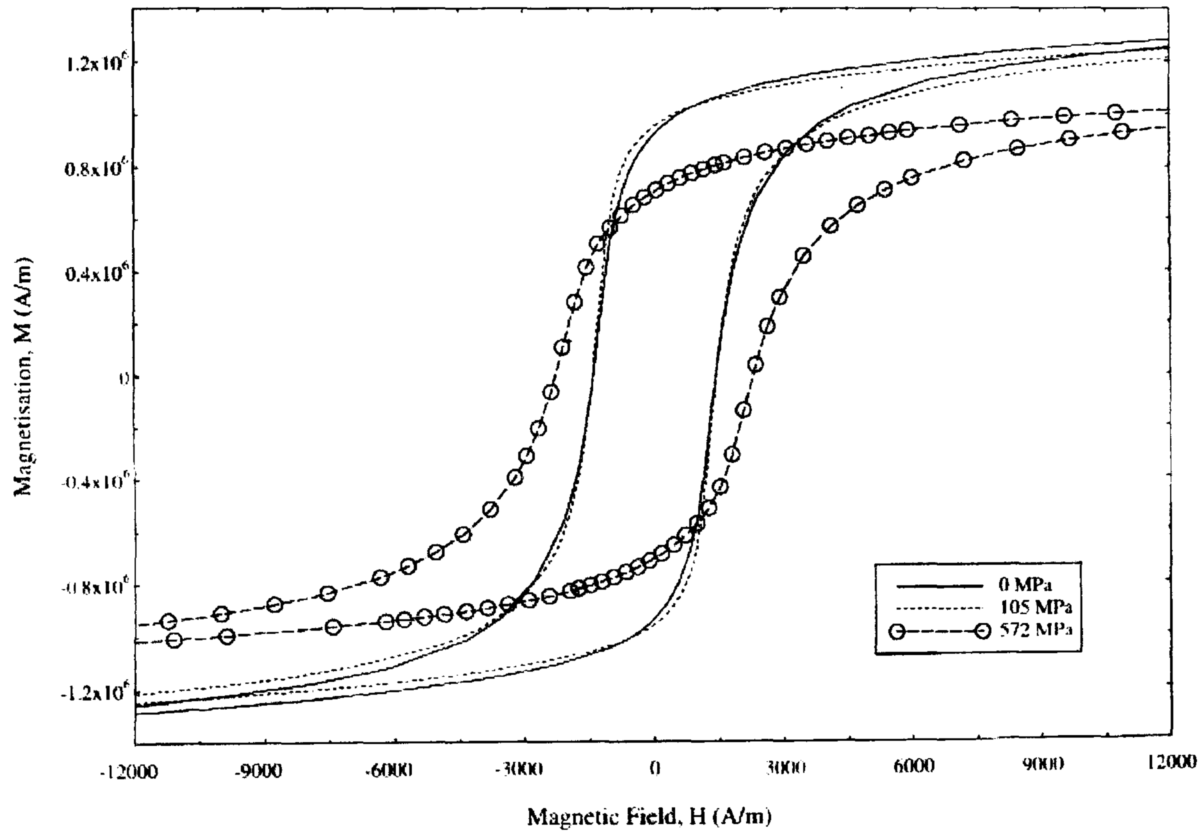

(b) 0.86 wt% C

Figure 3.5 Hysteresis loops for different stresses and amount of carbon (8)

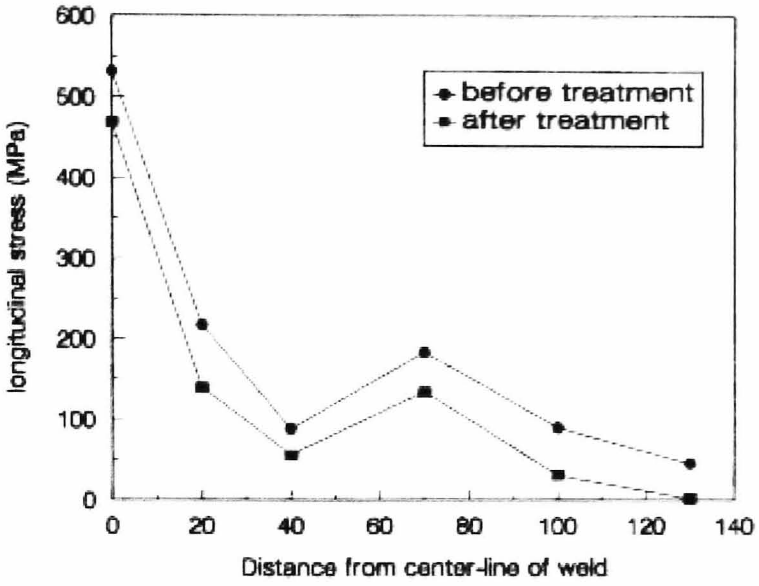

Figure 3.6 Residual stress distributions of before and after pulsed magnetic treatment (12)

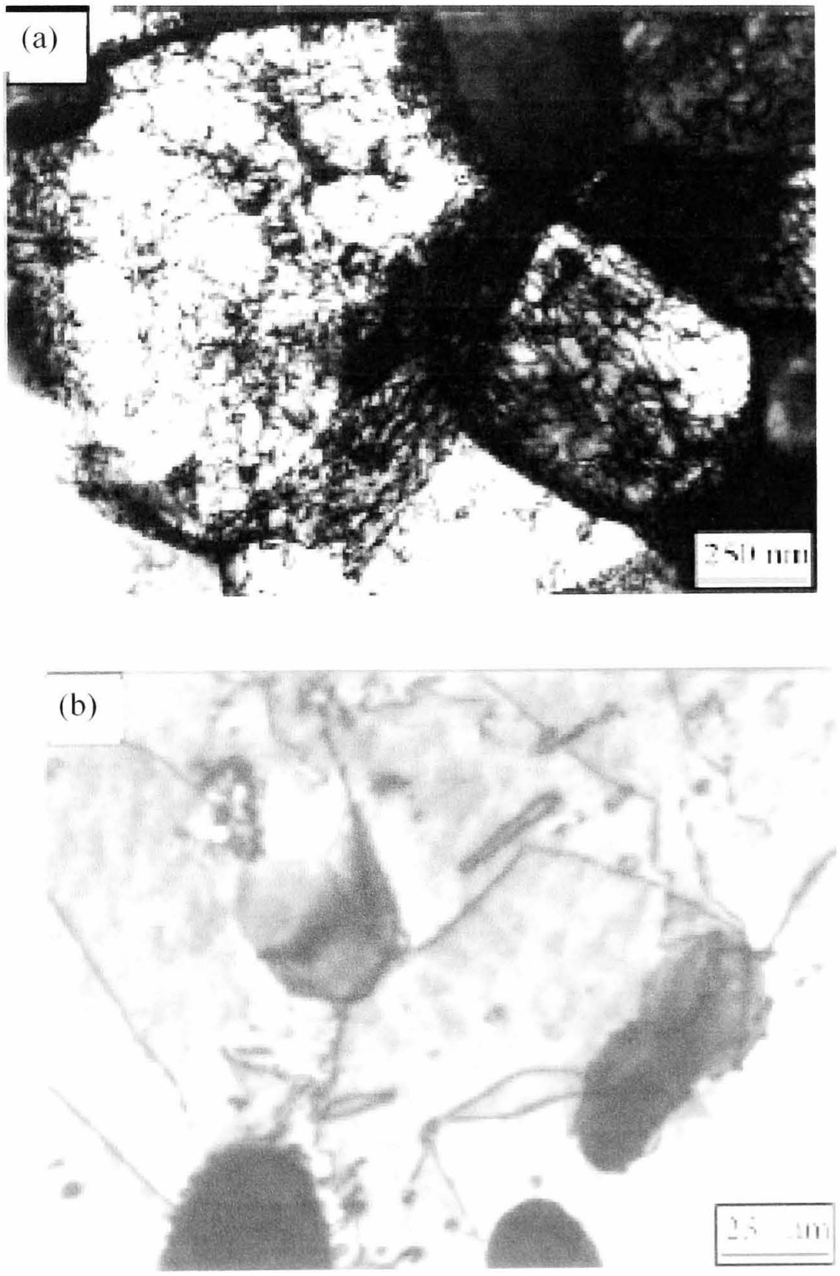

Figure 3.7 Dislocation structure in the deformed specimens (a) before pulsed magnetic treatment and (b) after pulsed magnetic treatment (13)

(1) S. Chikazumi, “Physics of magnetism”, John Wiley & Sons, Inc. (1964).

(2) H. Barkhausen, Phys. Zeitschrift, Vol. 20, (1919), pp. 201.

(3) G.V. Lomaev and V.S. Malyshev, Defectoskopia, Vol. 3, (1984), pp. 54.

(4) S. Saynajakangas, IEEE Trans. Magn., Vol. 10-1 (1974), pp. 39.

(5) D.E. Scherperel, L. Kazmerski and C.W. Allen, Metall, Trans., Vol. 1-2, (1970), pp. 179.

(6) H. Sakamoto, M. Okada and M. Homma, IEEE Trans. Magn., Vol. 23-5 (1987), pp. 2236.

(7) R.L. Pasley, Mater. Eval., Vol. 28-7, (1970), pp. 157.

(8) J.M. Makar and B.K. Tanner, “The in situ measurement of the effect of plastic deformation on the magnetic properties of steel: Part I – Hysteresis loops and magnetostriction”, Journal of Magnetism and Magnetic Materials, Vol. 184, (1998), pp. 193-208.

(9) J.M. Makar and B.K. Tanner, “The in situ measurement of the effect of plastic deformation on the magnetic properties of steel: Part II – Permeability curves”, Journal of Magnetism and Magnetic Materials, Vol. 187, (1998), pp. 353-365.

(10) K. Asai, E. Matsumoto and T. Shibata, “Effects of stress on magnetostriction and magnetisation curve of ferromagnetic materials”, JSME International Journal Series A, Vol.64-624, (1998), pp. 2183-2190.

(11) F. Tang, A.L. Lu, J. F. Mei, H. Z. Fang and X. J. Luo, “Research on residual stress reduction by a low frequency alternating magnetic field ”, Journal of Materials Processing Technology, Vol. 74, (1998), pp. 255-258.

(12) A. L. Lu, F. Tang, X. J. Luo, J. F. Mei and H. Z. Fang, “Research on residual-stress reduction by strong pulsed magnetic treatment”, Journal of Materials Processing Technology, Vol. 74 (1998), pp. 259-262.

(13) G. Tang, Z. Xu, M. Tang, X. Chen, H. Zhou and A. Lu, “Effect of a pulsed magnetic treatment on the dislocation substructure of a commercial high strength steel”, Materials Science and Engineering A Vol. 398, (2005), pp. 108-112.

iiwaneChapter 4 Rolling Contact Tests in Magnetic Fields

4.1 Introduction

Experiments in this study are carried out in two-disc rolling contact test apparatus shown in Figure 4.1. To investigate the effect of horizontal magnetic field on rolling contact fatigue, permanent magnets are attached to the equipment. In this chapter, the details of the apparatus and the experimental techniques are described.

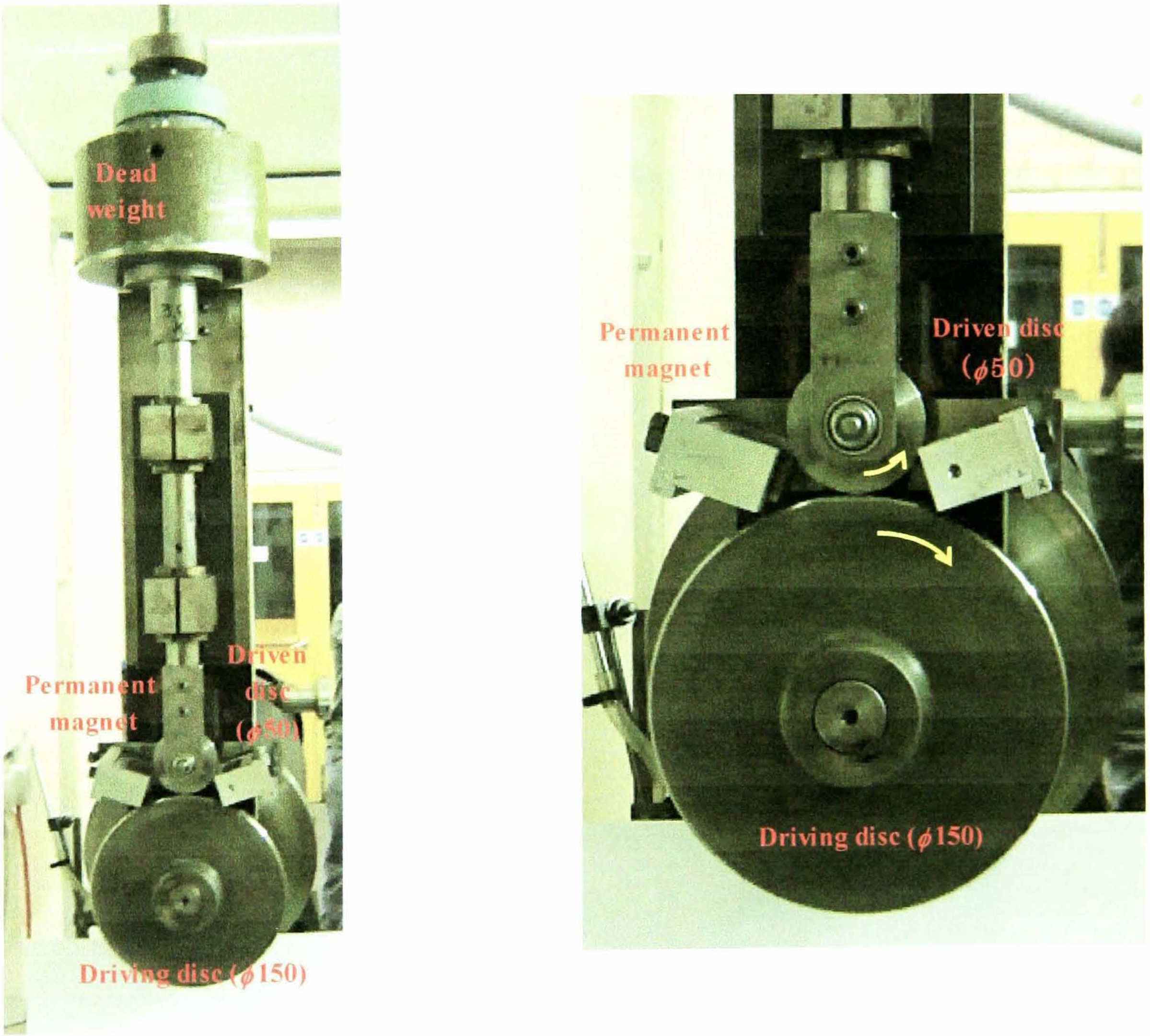

Figure 4.1 Two-disc rolling contact test apparatus

4.2 Experimental Technique and Equipment

4.2.1 Test apparatus

The two-disc rolling contact test apparatus used in this study is shown in Figure 4.2. The test disc is the driven disc and the driving disc is connected to the electric motor. For contact pressure, dead weight is loaded from the top of the test apparatus. Due to the load, deflection at the contact point in the test condition is less than 0.1μm and it can be neglected. The driven disc can be turned about its vertical axis in order to introduce a slip into the contact. By setting up permanent magnets in brackets, shown in Figure 4.2, the test apparatus is equipped to create a magnetic field. Changing the position of brackets can vary an angle between the plane in which rolling takes place and the magnetic field. Drawings of the brackets are shown in Appendix B.

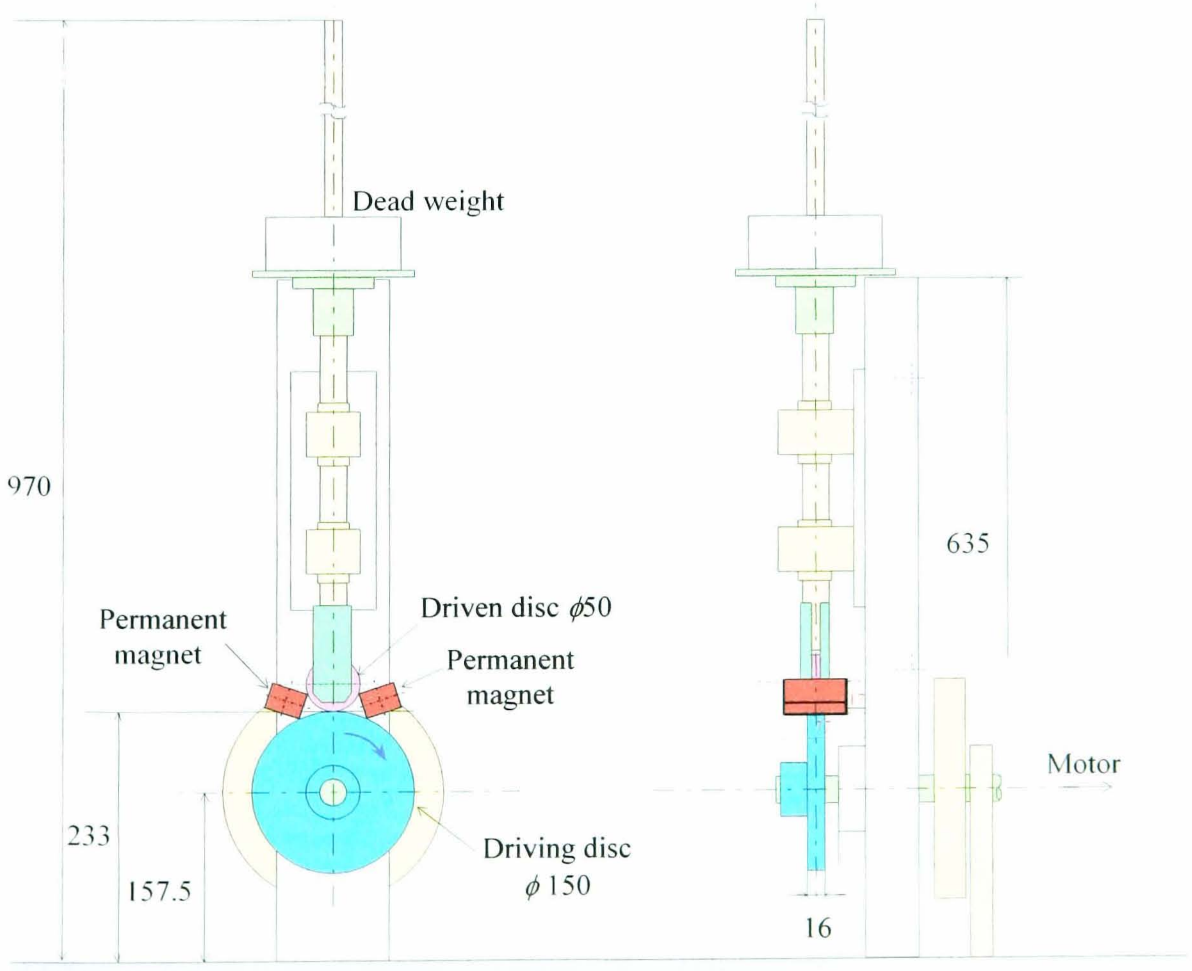

Figure 4.2 Dimensions of two-disc rolling contact test apparatus

4.2.2 Test Specimens

To evaluate the effect of the magnetic field on rolling contact fatigue, a disc with 50mm diameter and thickness of 4mm made of EN1A free cutting steel is used as the driven disc. Its hardness was about 160 HV (1) The driving disc has a 150mm diameter and 16mm thickness and is made of cylindrical ground hardened EN40B steel containing 3% wt% Cr. Its hardness was about 615 HV (1). Chemical composition and mechanical properties of both discs are shown in Table 4.1 and 4.2. All experiments were performed in unlubricated ambient conditions. Prior to any test, surface roughness measurements and optical microscopy observations were conducted and initial inspection of the surface was carried out. Before each test, the surface of the driving disc was finished with the abrasive paper (number 2400) and the surface of the driven disc was used as machined. The resulting roughnesses, R_a, of the driving and driven discs were about 0.08μm and 0.10μm respectively. Discs were cleaned with acetone before the tests. In addition, to evaluate the magnetic effect on non-magnetic materials, aluminium discs were also used.

Table 4.1 Composition of specimens [wt%] (1)

	C	Si	Mn	S	P	Ni	Cr	Mo
EN1A	0.05-0.15	0.10max	0.80-1.20	0.20-0.30	0.070max	-	-	-
EN40B	0.10-0.20	0.10-0.35	0.40-0.65	0.050max	0.050max	0.40max	2.90-3.50	0.40-0.70

Table 4.2 Mechanical properties of specimens (1)

	Young's modulus [GPa]	Poisson's ratio	Yield strength [MPa]	Tensile strength [MPa]
EN1A	203	0.28	243	394
EN40B	205	0.30	516	684
Al	70.3	0.345	110(*)	285

(*) 0.2% proof stress

4.2.3 Loading Conditions

The experiments were conducted under the normal and constant load of 150N by using dead weights. The width of the contact area a and the maximum contact pressure p_0 are obtained from Equations (2.2)-(2.4) and the values are 89.7μm and 266.3MPa respectively. In addition, at $\mu=0$, the maximum shear strain-energy, from Equation (2.16b), is 86.7MPa at the depth of 63.2μm. In order to evaluate stress status of the test specimen, ANSYS programme was used. To analyse the stresses in the rolling contact a three-dimensional model is constructed. The model, shown in Figure 4.3, represents contacting discs with the dimensions: 1mm x 2mm x 4mm for the driven disc and 1mm x 2mm x 6mm for the driving disc. Total number of the elements and nodes in the model are 13200 and 14432 respectively. The contour map for compressive and shear stresses at the middle of the width of the discs is shown in Figure 4.4. The maximum contact pressure p_0, the maximum shear strain-energy, and the depth at which it is located under the condition of Equation (2.16b) ($\mu=0$) obtained from ANSYS are 267MPa, 91.3MPa, and 76μm respectively. Differences between results from ANSYS analysis and Hertz's theory are: 0.3% in the maximum contact pressure and 5.3% in the maximum shear strain-energy. To estimate the stress status more realistically, tangential load Q is applied to the lower disc in the range of 0 to 75N.

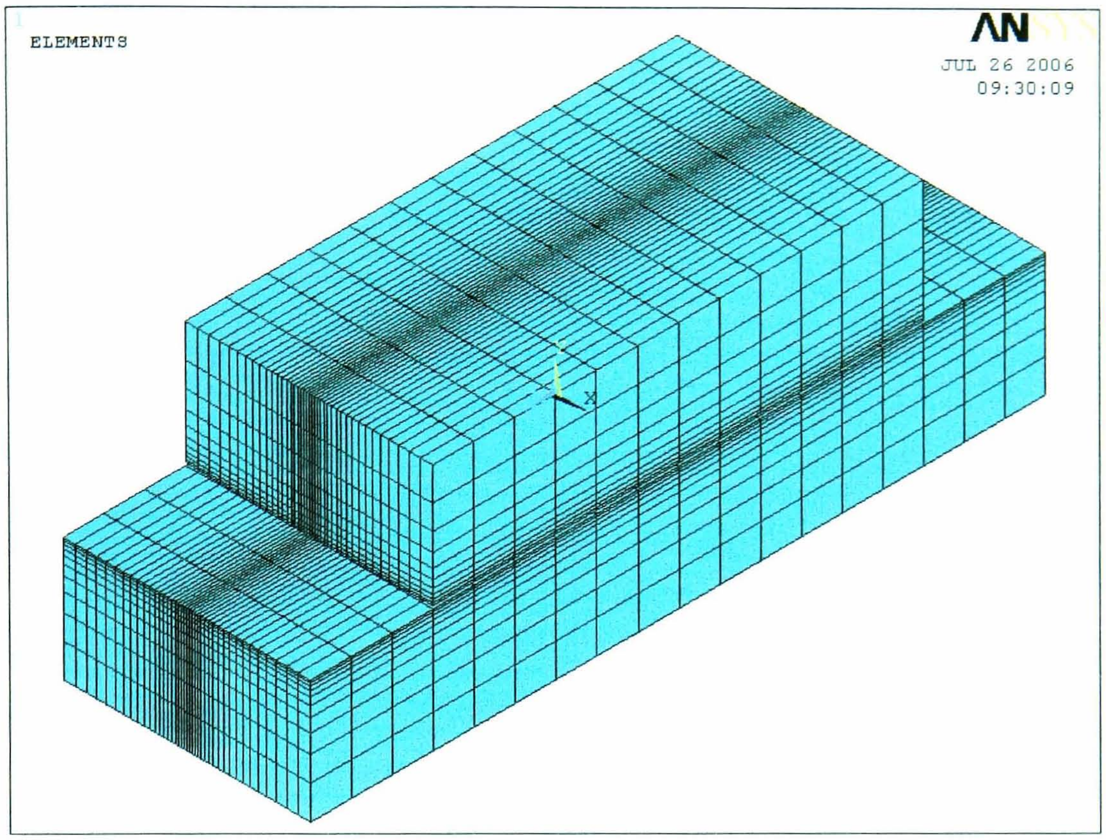

(a) Isometric view

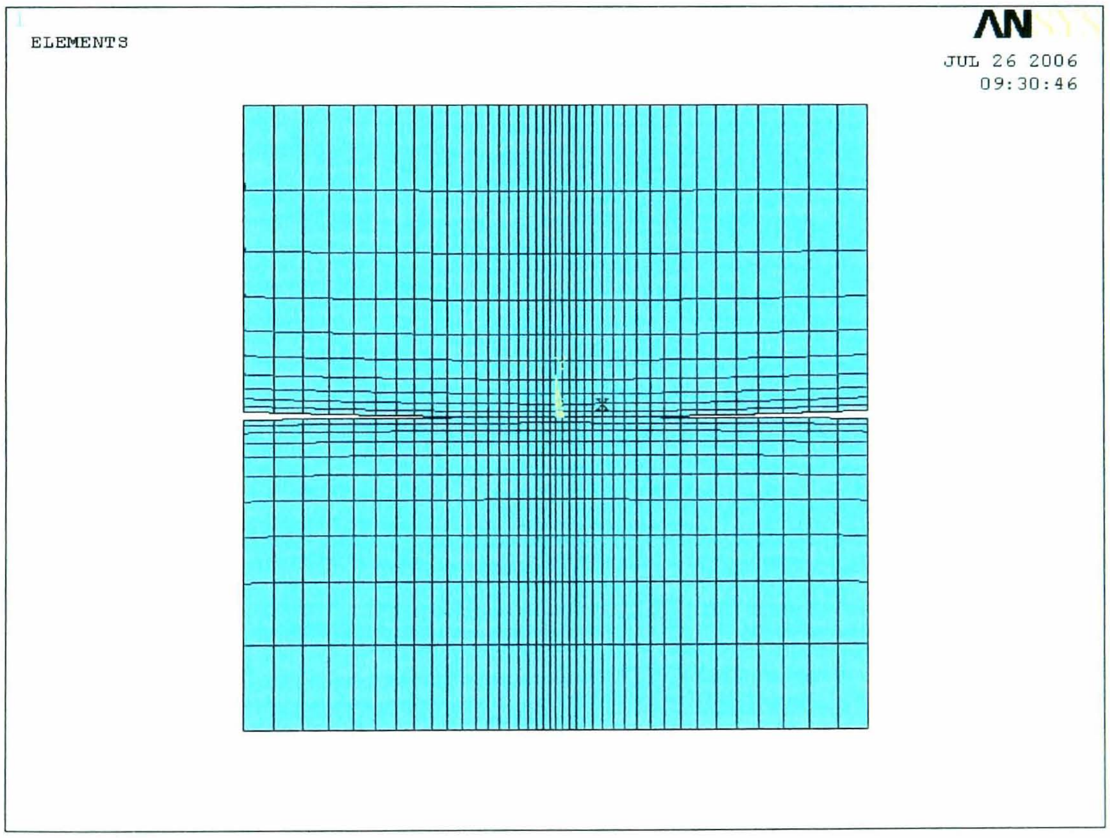

(b) Front view

Figure 4.3 FEM models of ANSYS stress analysis

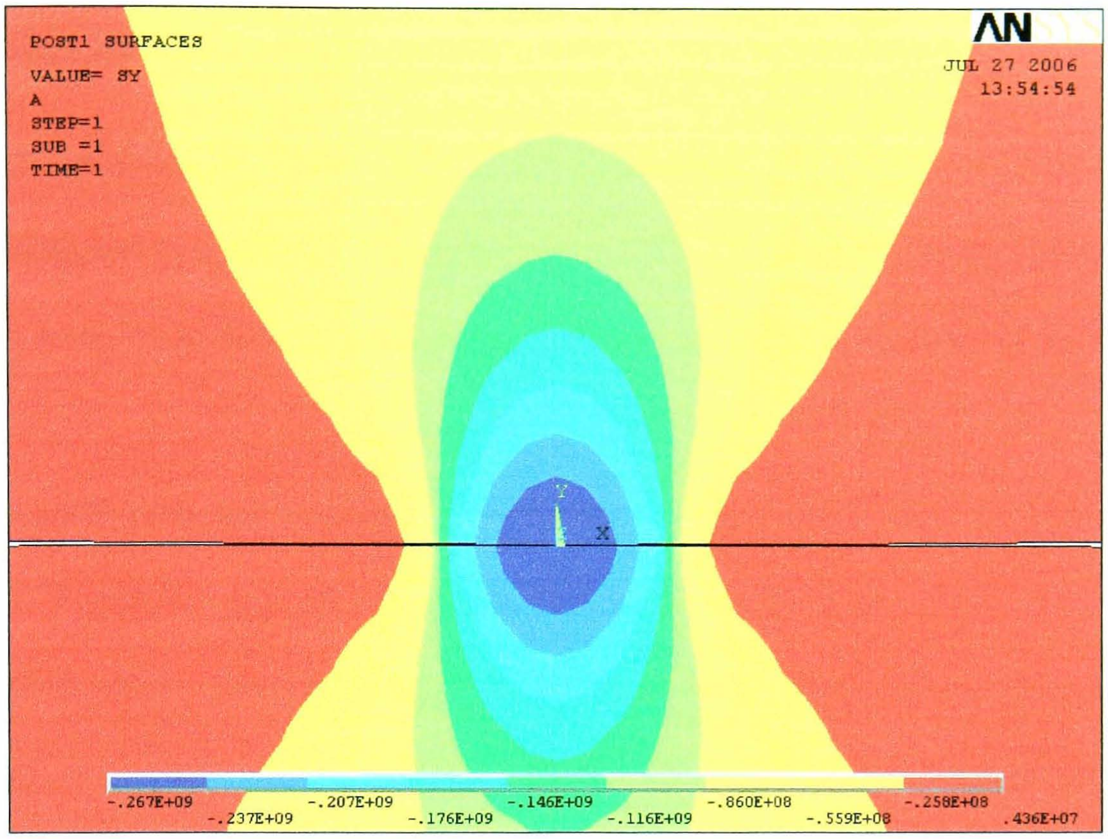

(a) Compressive stress

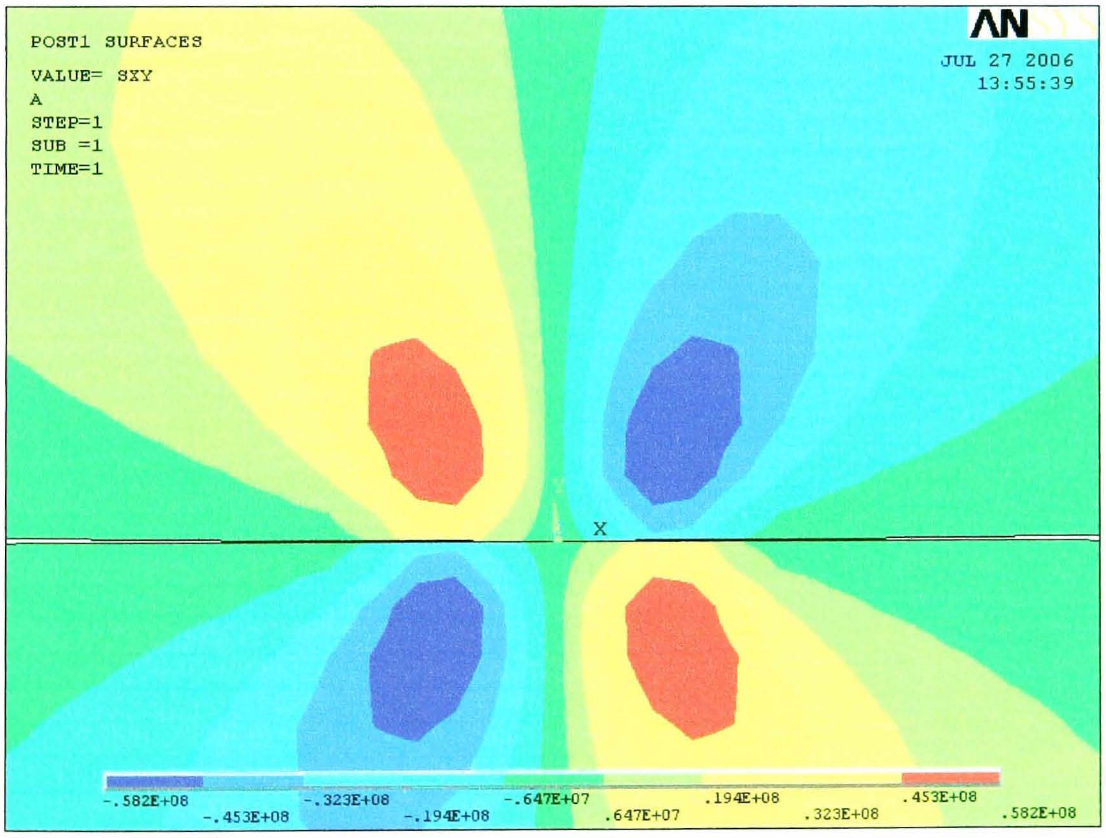

(b) Shear stress

Figure 4.4 Contour results of ANSYS stress analysis

4.2.4 Contact Kinematics

Rotational speed and the slip ratio were kept fixed during the duration of a test. The driving disc was connected to a variable speed electric motor via a coupling. Rotational speeds of the driven disc were set to 450 rpm and 180rpm so that the effect of rotational speed could be evaluated.

In order to add a slip into the contact, the driven disc was turned about its vertical axis disc as shown in Figure 4.5 (a). By doing that, rotating velocity of the driven disc, transmitted from the driving disc v_1, shown in Figure 4.5 (b), is divided into v_{21} and v_{22}. Assuming that the velocities are transmitted without loss, their relationships are expressed as follows:

$$v_1^2 = v_{21}^2 + v_{22}^2 \qquad (4.1) \qquad \text{and} \qquad {}^{v_{22}}\!\!/\!_{v_{21}} = \tan\phi \qquad (4.2)$$

By selecting the angle ϕ as $\tan^{-1}(1/10) = 5.71^\circ$, the 10% slip ratio was introduced into the contact. In the present study, the slip ratio was set to 0 (pure rolling) and 10% (rolling with sliding).

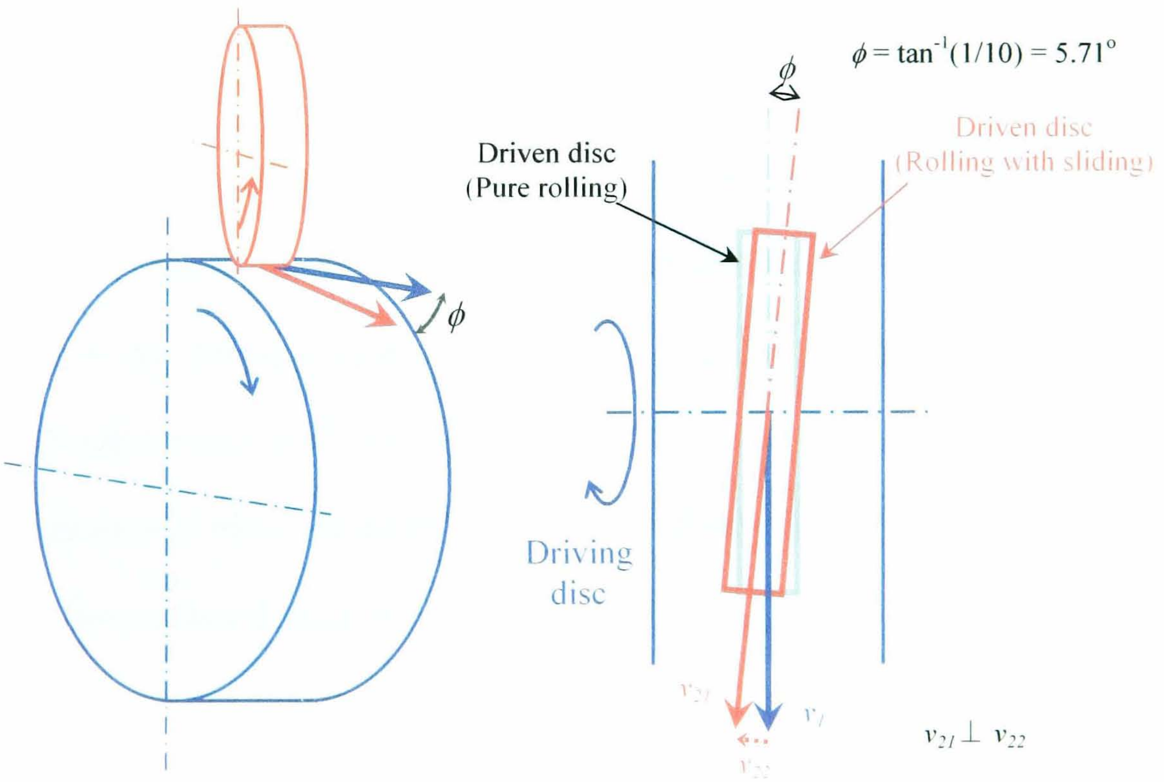

(a) (b)

Figure 4.5 Geometry of pure rolling and rolling with sliding

Addition of a tangential loading to normal loading can significantly alter the contact surface and sub-surface stress distributions. The distribution of pressure, *p*, over the contact area is represented by the ordinates of the semi-ellipsoid shown in Figure 4.6 constructed on the contact surface. The elliptical distributions in the x-z and y-z planes are sometimes referred to as the Hertzian distributions.

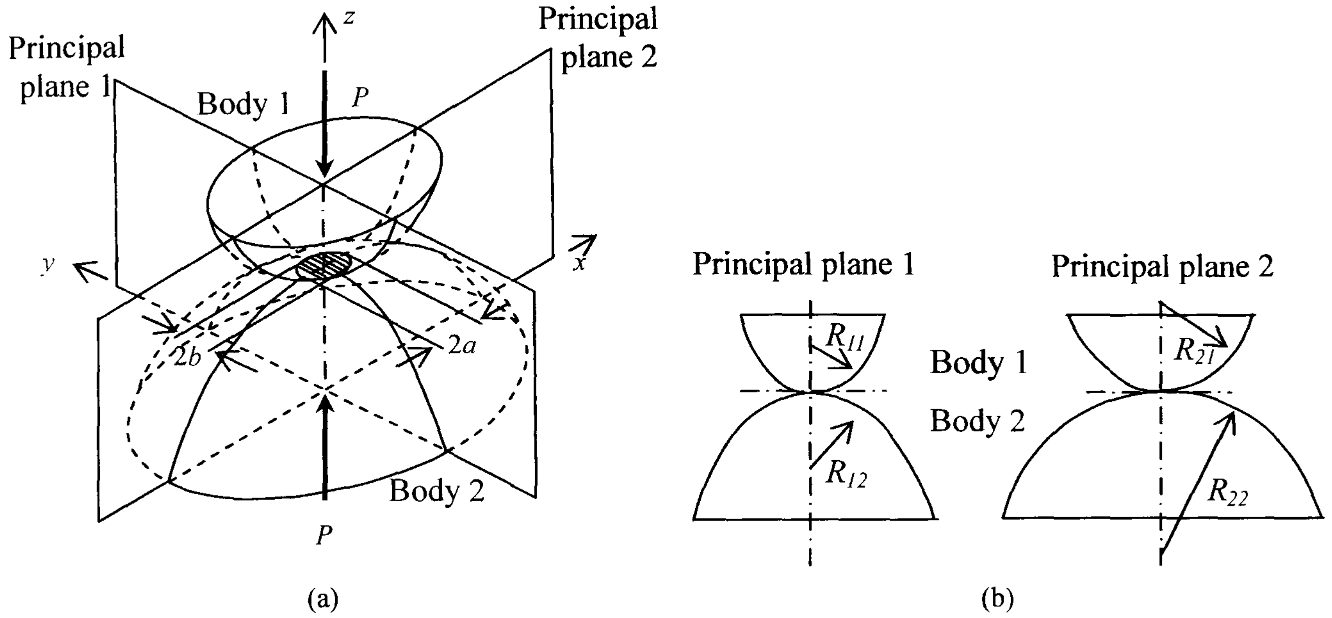

Figure 4.6 Contact of two bodies with curved surfaces and their principal planes of curvature (a) radii of curvature in the principal planes of the bodies with curved surfaces (b)

Each of the two bodies 1 and 2 is characterised by its curvatures in the principal plans, perpendicular to each other, in which the maximum and minimum curvatures are contained, as presented in Figure 4.6 (a). R_{11}, R_{12} are the principal radii of curvature of body (1 and 2) respectively in one principal plane of curvature. R_{21}, R_{22} are the principal radii of curvature in the other principal plane as shown in Figure 4.6 (b).

The reciprocals of these curvature radii are termed the principal curvatures. A and B are constants whose values depend on the magnitude of the principal curvatures and angle, ω, between the planes in which the principals curvatures

If the corresponding planes of curvature of the two bodies do not coincide, then

$$A=\frac{1}{4}\left\{\frac{1}{R_{11}}+\frac{1}{R_{12}}+\frac{1}{R_{21}}+\frac{1}{R_{22}}-\left[\left(\frac{1}{R_{11}}-\frac{1}{R_{12}}\right)^2+\left(\frac{1}{R_{21}}-\frac{1}{R_{22}}\right)^2+2\left(\frac{1}{R_{11}}-\frac{1}{R_{12}}\right)\left(\frac{1}{R_{21}}-\frac{1}{R_{22}}\right)\cos(2\omega)\right]^{1/2}\right\} \tag{4.3}$$

$$B=\frac{1}{4}\left\{\frac{1}{R_{11}}+\frac{1}{R_{12}}+\frac{1}{R_{21}}+\frac{1}{R_{22}}+\left[\left(\frac{1}{R_{11}}-\frac{1}{R_{12}}\right)^2+\left(\frac{1}{R_{21}}-\frac{1}{R_{22}}\right)^2+2\left(\frac{1}{R_{11}}-\frac{1}{R_{12}}\right)\left(\frac{1}{R_{21}}-\frac{1}{R_{22}}\right)\cos(2\omega)\right]^{1/2}\right\} \tag{4.4}$$

An elliptical contact occurs between two non- conforming cylinders when ω, is between 0° and 90° and $R_{11}\neq R_{22}$, $R_{12}=R_{22}=\infty$

For this investigation, ω=5.71 °, R_{11}=25x10^{-3}m and R_{21}=75x10^{-3}m are substitute for Equation (4.5) and (4.6).

$$A=\frac{1}{4}\left\{\frac{1}{25\times10^{-3}}+\frac{1}{\infty}+\frac{1}{75\times10^{-3}}+\frac{1}{\infty}-\left[\left(\frac{1}{25\times10^{-3}}-\frac{1}{\infty}\right)^2+\left(\frac{1}{75\times10^{-3}}-\frac{1}{\infty}\right)^2+2\left(\frac{1}{25\times10^{-3}}-\frac{1}{\infty}\right)\left(\frac{1}{75\times10^{-3}}-\frac{1}{\infty}\right)\cos(2\omega)\right]^{1/2}\right\} \tag{4.5}$$

$$B=\frac{1}{4}\left\{\frac{1}{25\times10^{-3}}+\frac{1}{\infty}+\frac{1}{75\times10^{-3}}+\frac{1}{\infty}+\left[\left(\frac{1}{25\times10^{-3}}-\frac{1}{\infty}\right)^2+\left(\frac{1}{75\times10^{-3}}-\frac{1}{\infty}\right)^2+2\left(\frac{1}{25\times10^{-3}}-\frac{1}{\infty}\right)\left(\frac{1}{75\times10^{-3}}-\frac{1}{\infty}\right)\cos(2\omega)\right]^{1/2}\right\} \tag{4.6}$$

$A+B$, A/B are then calculated, and are given in Table 4.3 for the three different angles

Table 4.3 Values of A, B, A/B and $A+B$ for ω=5.71°

ω	A	B	A/B	$A+B$
5.71	0.050	26.61	0.0019	26.66

The ellipse dimensions and their ratio, and the mutual approach of the bodies can be calculated from the following Equations.

$$W''=\left[\frac{3P\pi}{4}(K_1+K_2)(A+B)^2\right]^{1/3} \tag{4.7}$$

$$K=\frac{(1-\upsilon^2)}{\pi E} \tag{4.8}$$

$$a' = \frac{C_a W''}{(A+B)}\left(\frac{A}{B}\right)^{1/3} \qquad (4.9)$$

$$b = \frac{C_b W''}{(A+B)}\left(\frac{A}{B}\right)^{1/3} \qquad (4.10)$$

$$\beta = C_\beta\left(\frac{A}{B}\right)^{2/3} \qquad (4.11)$$

$$\delta = \frac{C_\delta W''^2}{(A+B)}\left(\frac{A}{B}\right)^{1/3} \qquad (4.12)$$

where:
W''-Calculation parameter
P - Applied load
K - Material constant
E - Young's modulus
ν - Poisson's ratio
$K_1 = 1.45\text{x}10^{-12}$ [m^2/N]
$K_2 = 1.41\text{x}10^{-12}$ [m^2/N]
a' - Contact ellipse major semi-axis
b - Contact ellipse minor semi-axis
β - Ellipse semi-axes ratio, given by b/a
δ - Decrease in separation between two points on axis of symmetry

The coefficients C_a, C_b, C_β, and C_δ are decided from the value A/B (2). The values for these coefficients in this investigation and the values of a, b, β, δ, and W'' obtained from Equations (4.7)-(4.12) are shown in Table 4.4.

Table 4.4 Values of C_a, C_b, C_β, and C_δ for A/B=0.00188 and a, b, β, δ, and W''

C_a	C_b	C_β	C_δ	W''	a [mm]	B [mm]	β	δ [µm]
1.4	1.95	1.39	2.4	0.0089	0.058	0.081	0.021	0.89

The distribution of pressure, p, over the contact area is represented by the semi-ellipsoid, constructed on the contact surface. The elliptical distributions are sometimes referred to as the Hertzian distribution. The maximum direct stress at the surface occurs at the centre of the ellipsoidal boundary and is given by

$$f_{z_{\max}} = -C_f \frac{2W}{\pi^2 (K_1 + K_2)} \tag{4.13}$$

$$p_o = \frac{1.5w}{\pi ab} = -f_{z_{\max}} \tag{4.14}$$

The maximum shear stress and the maximum depth of shear can be calculated as follows

$$q_{\max} = \bar{q}_{\max} f_{z_{\max}} \tag{4.15}$$

$$Z_{q_{\max}} = b \left(\frac{Z}{b} \right)_{q_{\max}} \tag{4.16}$$

where:

q_{max} - Maximum sub-surface shear stress
$Z_{q_{\max}}$ - Depth of maximum shear stress
$\bar{q}_{\max}$ - Coefficient decided from the value $A/B^{(2)}$
$f_{z_{\max}}$ - Maximum compressive or Hertzian stress
$\left(\frac{Z}{b} \right)_{q_{\max}}$ - Coefficient decided from the value $A/B^{(2)}$
C_f- Coefficient decided from the value $A/B^{(2)}$

The results of these calculations are shown in Table 4.5. As compared with that of ANSYS using the model shown in Figure 4.7, values of p_0 and q_{max} are 282MPa and -71.5MPa. The contour results of finite element analyses for compressive and shear stresses at the middle of the width of the discs are shown in Figure 4.8.

Table 4.5 Maximum contact pressure and depth of shear stress

ω	p_0 [MPa]	C_f	$(Z/b)_{qmax}$	$\bar{q}_{\max}$	q_{max} [MPa]	$Z_{q_{\max}}$ [mm]
5.71^{0}	241. 25	0.38	0.79	0.31	-74.79	0.063

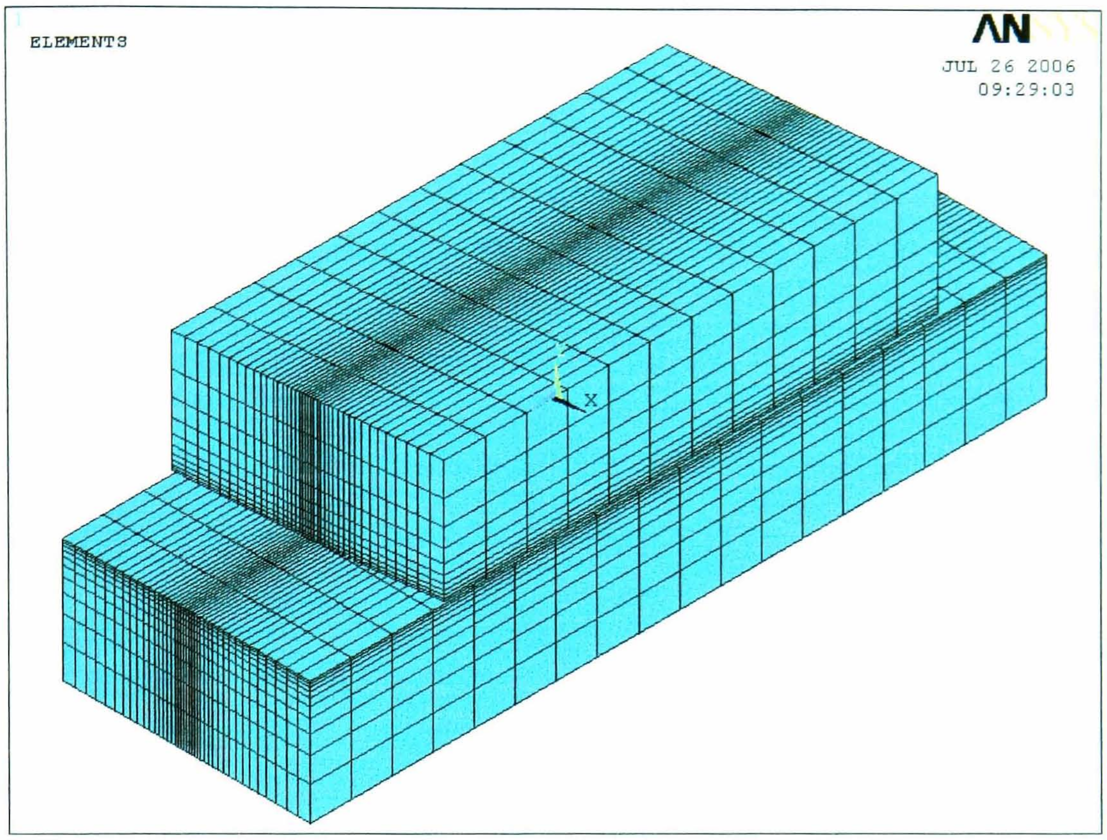

(a) Isometric view

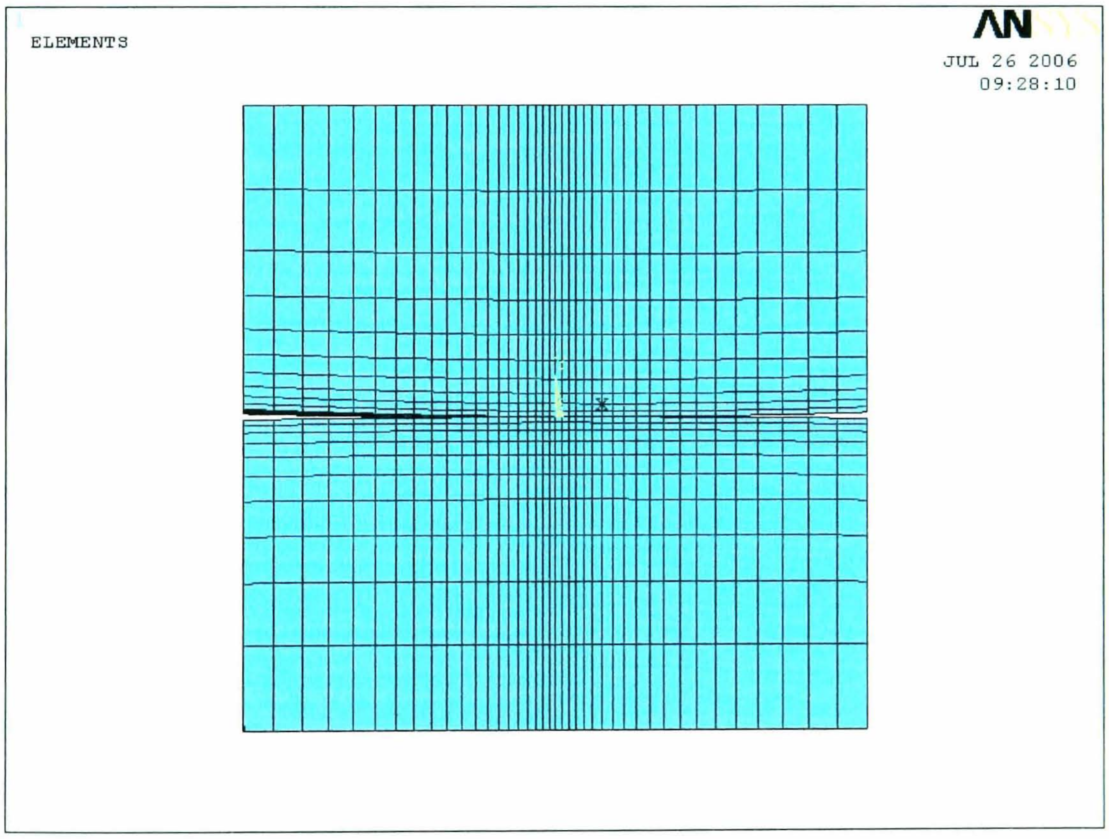

(b) Front view

Figure 4.7 FEM models of ANSYS stress analysis (Rolling with sliding)

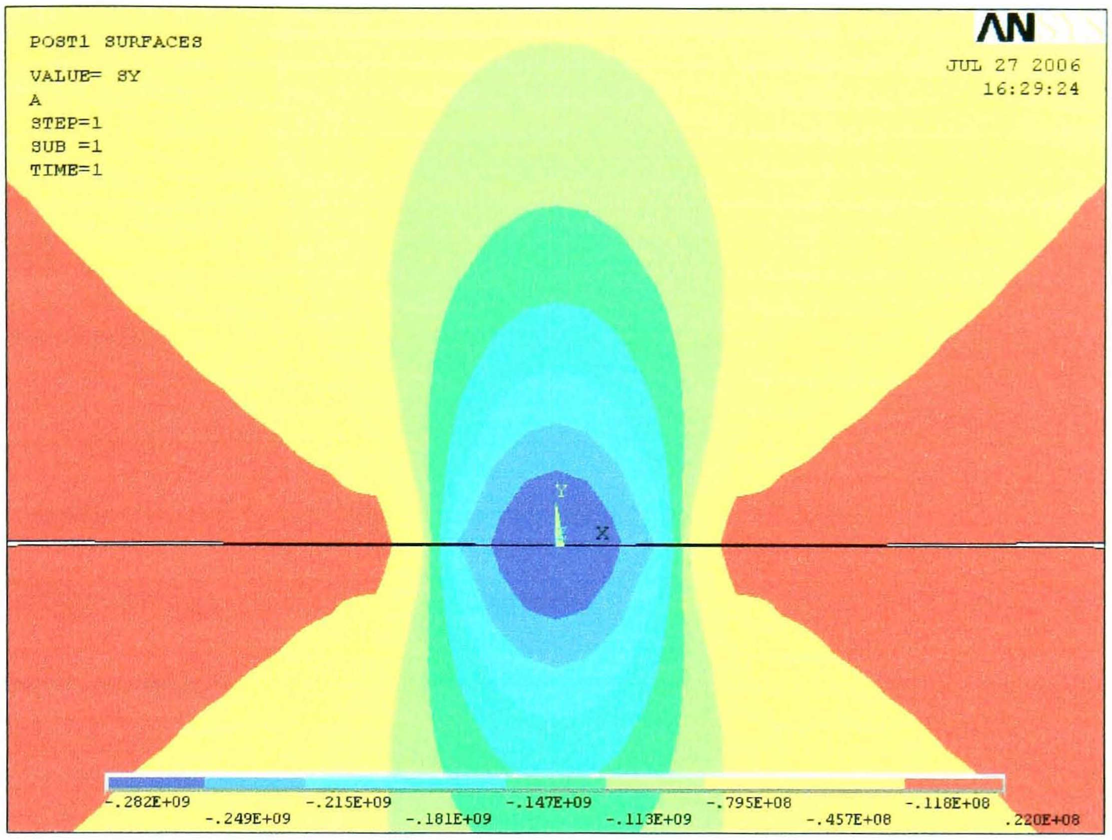

(a) Compressive stress

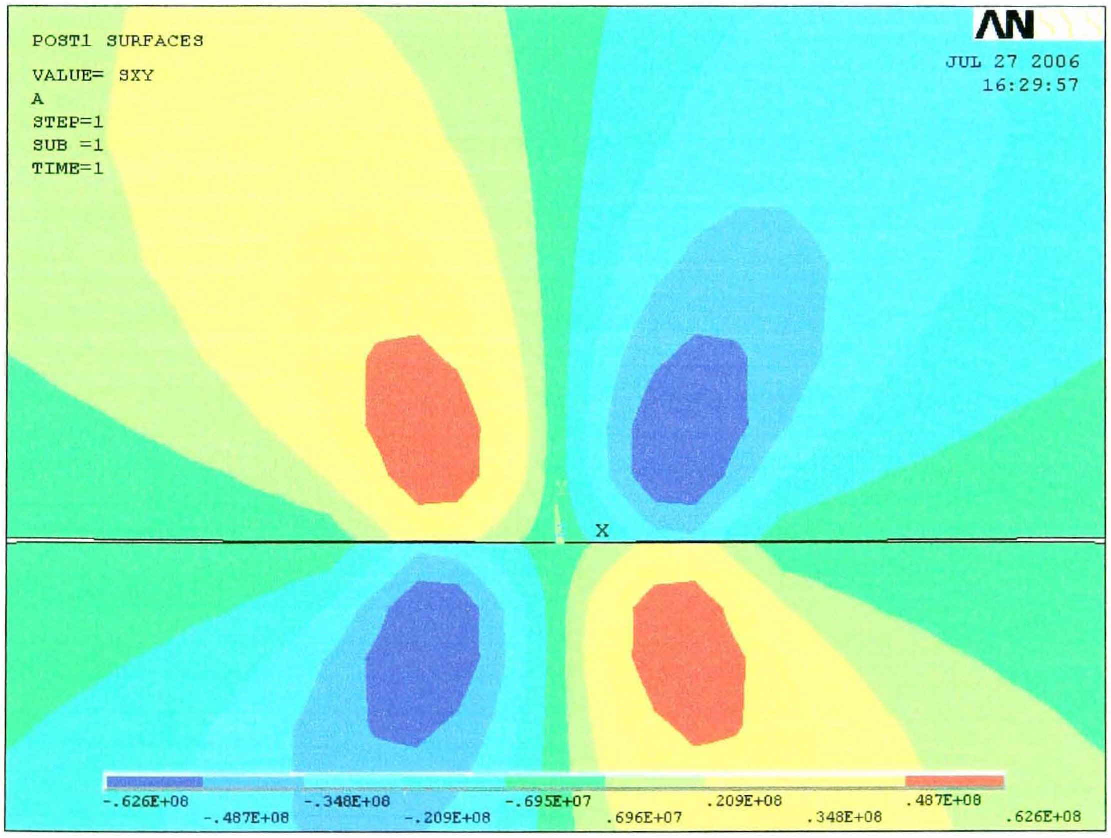

(b) Shear stress

Figure 4.8 Contour results of ANSYS stress analysis (Rolling with sliding)

4.2.5 Magnetic Conditions

To create a magnetic field, two types of permanent magnets with magnetic field densities of 1.1T and 0.4T were used. The properties of permanent magnets used and their initial magnetic curves are shown in Table 4.6 and Figure 4.9. On the other hand, the maximum magnetic flux density in real mechanical devices is roughly 2.0T as shown in Table 4.7. Therefore, the magnetic conditions used in this study are considered to be adequate.

ANSYS software was used to analyse magnetisation in the test specimens. Test specimens and permanent magnets were mounted as shown in Figure 4.10 and the same geometry and configuration are used for the finite element model shown in Figure 4.11. Results show that magnetisation created near the contact surface, shown in Table 4.8, was perpendicular and densities for the two types of permanent magnets are 0.08T and 0.02T. Therefore, magnetisation of specimen was considered to be in a weak domain wall displacement status, as the displacement was probably constrained by inclusions or dislocations. On the other hand, the magnetic force between the specimens was less than 2N and therefore that force was neglected.

The angles between the plane in which rolling takes place and the magnetic field was set as θ=0°, 45°, and 90°. Figure 4.12 illustrates the configurations used.

Table 4.6 Properties of magnets

Type of magnets	B_r [T]	BH_c [kA/m]
Rare earth magnets	1.1	987
Ferrite magnets	0.4	242

Table 4.7 Magnetic flux densities of objects

Objects	Magnetic flux densities [T]
Terrestrial magnetism	$5\text{x}10^{-5}$
Motors	0.1-1.0
Liner motors	1.5-2.0

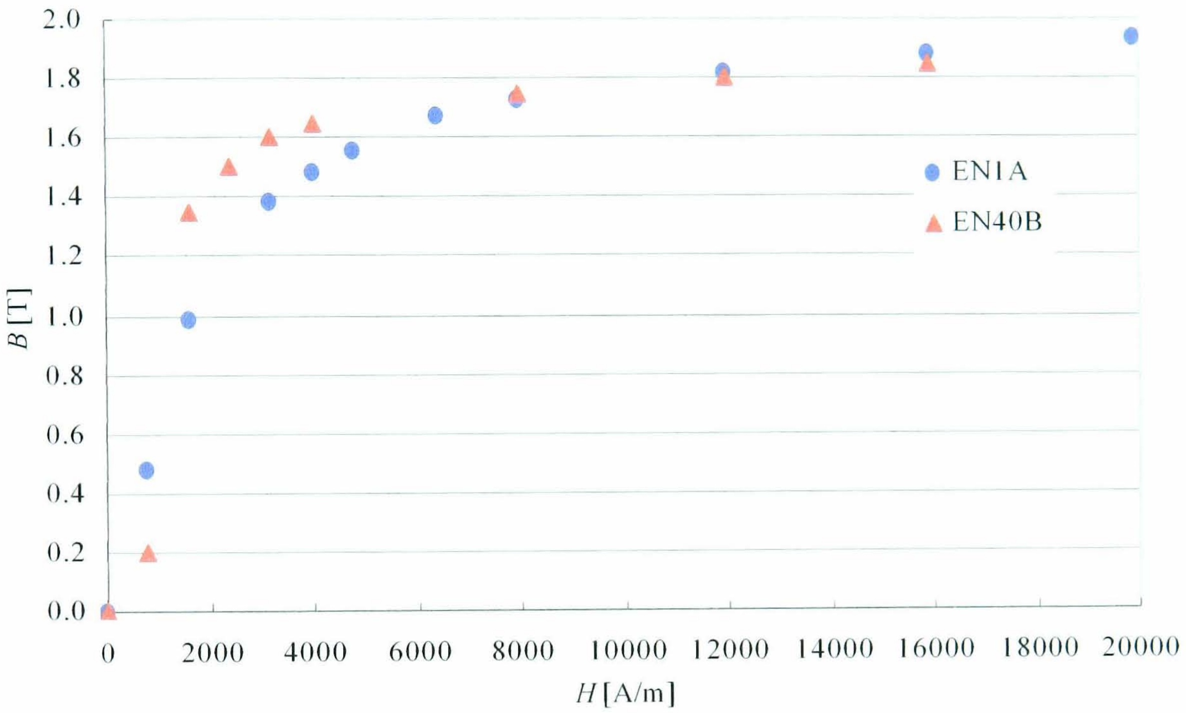

Figure 4.9 Magnetic properties of specimens

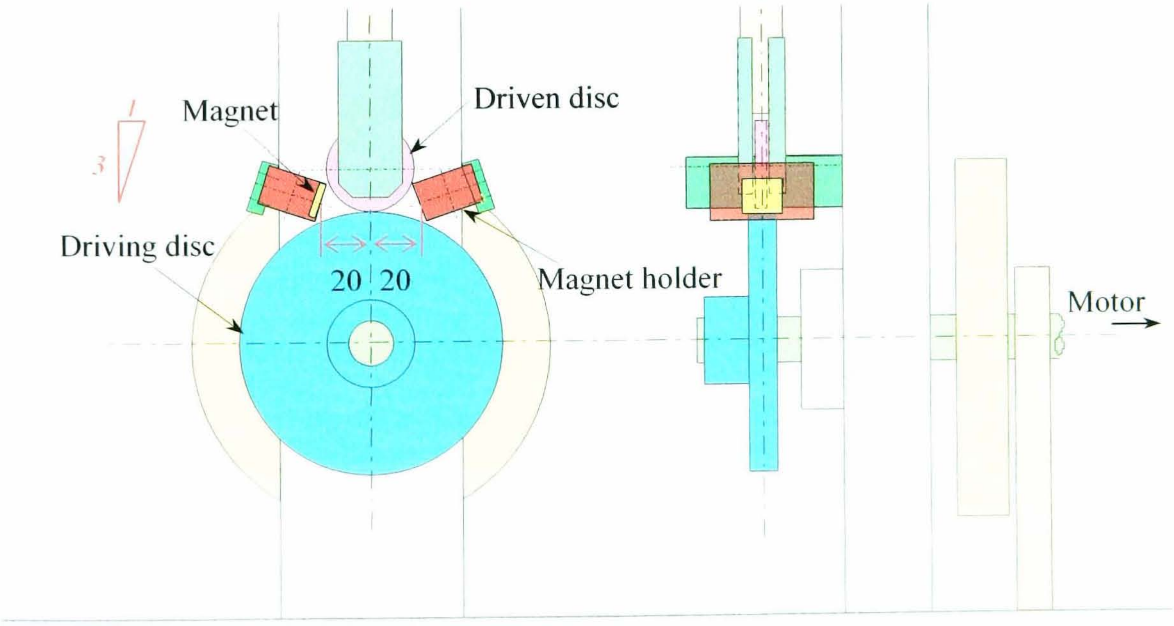

Figure 4.10 Position of permanent magnets

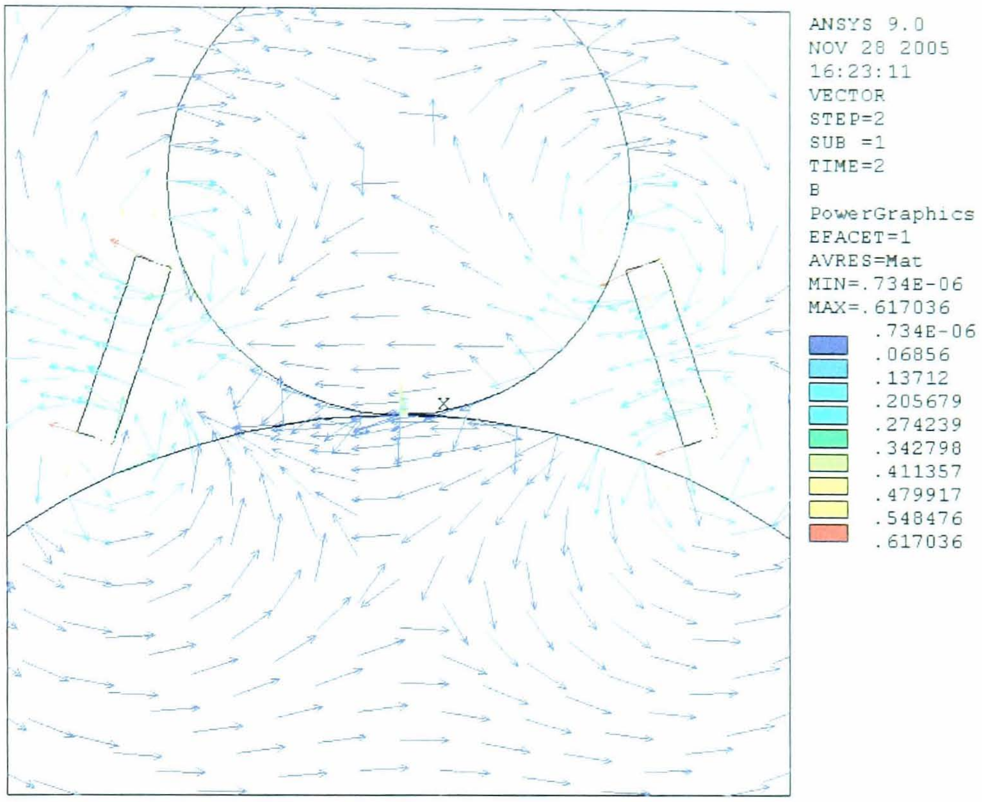

Figure 4.11 Magnetic fields around specimens

Table 4.8 Magnetic field analysis results

Type of magnets	B[T]	H[A/m]
Rare earth magnets	0.08	80
Ferrite magnets	0.02	25

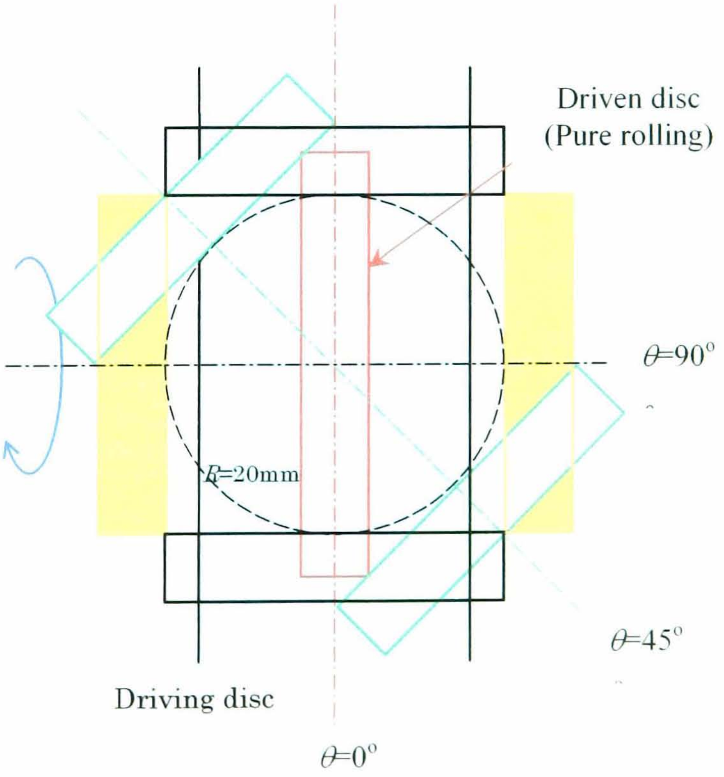

Figure 4.12 Angles between discs and magnets

4.2.6 Measured Parameters

All experiments were conducted in a laboratory air environment at the temperature of about 20°C. The load and speed were kept fixed during the duration of the test. To evaluate the effect of magnetic field, the following parameters were monitored;

(1) Weight loss of the driven disc.

(2) Surface roughness R_a.

(3) Appearance of disc surface and accumulation wear particles.

Prior to any test, the weight and surface roughness of the driven disc were measured and recorded. Surface roughness measurements were conducted and the initial inspection of the surface was carried out. The disc was then mounted into the test apparatus. Weight losses and surface roughness measurements were carried out after cleaning the disc.

The weight losses were measured by the difference in weight of the driven disc before and after the test. Wear particles generated during the test and stuck on the surface of the disc were carefully removed by ultrasonic cleaning.

The surface roughness measurements during this study were performed using a Rank Taylor Hobson instrument with a stepped motor. This technique relies on the physical contact of a stylus with the surface. In this technique, a sharp and very lightly loaded stylus is drawn at a constant speed over the surface. As the stylus travels it rises and falls to give vertical displacements in accordance with the profile of the reference surface. These displacements are then converted into an electrical signal, which is then amplified to give the surface profile.

The optical microscope used was OLYMPUS microscope producing two-dimensional images of the specimen surface. The magnification range for this system is between 20 and 1000.

The Scanning Electron Microscope (SEM) used for surface analysis was Cambridge S250. The SEM has five distinct systems, that is, the electron gun source, the condenser system, the scanning system, the detection facility and the display system. The image can be magnified in the range of 10 to 100, 000 times and provide a much greater depth of field comparing to an optical microscope.

(1) "The mechanical and physical properties of the British standard EN steels", Steel user service British iron and steel research association, (1964), Pergamon press.

(2) S.L. Al-Sabti, "Failure modes of polimethylmethacrylate resulting from rolling line contact", Ph.D Thesis, Brunel University, (2000).

Chapter 5 Experimental Results

5.1 Introduction

This chapter presents the effect of magnetic field in rolling contact experiments carried out under different condition of magnetic field density, rotational speed, direction of the magnetic field, material of test specimens and kinematics. It is divided into two main sections. The first deals with pure rolling fatigue experiments in horizontal magnetic field. Magnetic field effects are evaluated by weight loss, surface roughness and morphology of surface asperities.

The second section concerns the effect of introducing a tangential force into the contact. This is achieved by creating an angle between the two contacting discs which resulted in a slip.

5.2 Pure Rolling Tests

5.2.1 Pure Rolling of Steel Discs

Accumulated weight losses of the driven discs in pure rolling tests, shown in Figure 5.1, were proportional to the number of cycles when magnetic field was absent. Above $4x10^6$ cycles, total weight loss was over 1000 mg. On the other hand, weight loss in the magnetic field was lower for both magnetic field densities used. It increased in proportion to the number of cycles until around $2x10^6$ cycles, a similar trend as for the absence of magnetic fields. However, this trend reached plateau after that number of cycles. The trend was especially noticeable for the magnetic field of 1.1T. The amount of wear in the magnetic field was 287mg after $5.0x10^6$ cycles. From these results, it can be stated that the wear amount resulting from rolling contact fatigue was reduced due to the effect of horizontal magnetic field.

Surface roughness of the driven disc was also lower in the magnetic field. As shown in Figure 5.2, in the absence of the magnetic field, R_a value was raised from 0.1μm to approximately 0.5μm after $6x10^5$ cycles. After that, the value of R_a varied between about 0.4 and 0.6μm. In contrast, in the presence of the magnetic field, the roughness, after $6x10^5$ cycles, was only about 0.3 μm. After that, the R_a value was further decreased to about 0.1μm.

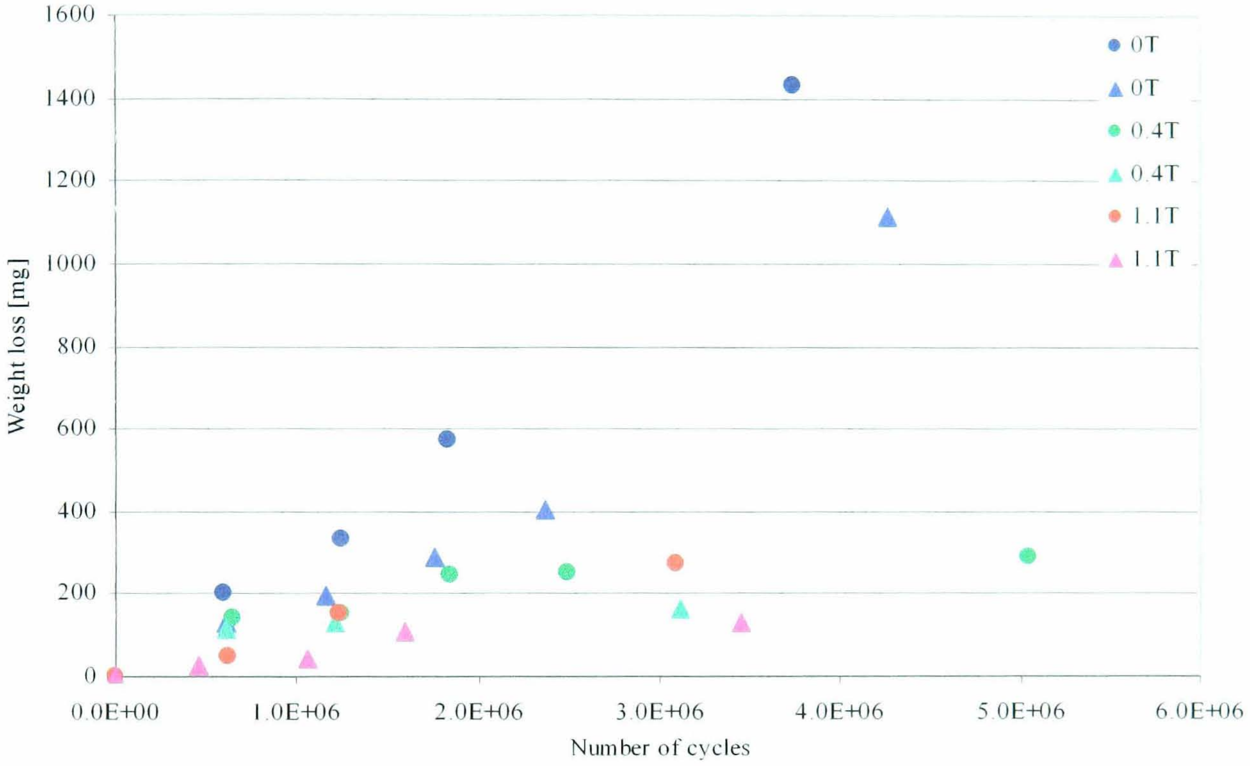

Figure 5.1 Accumulated weight losses of mild steel discs (Pure Rolling)

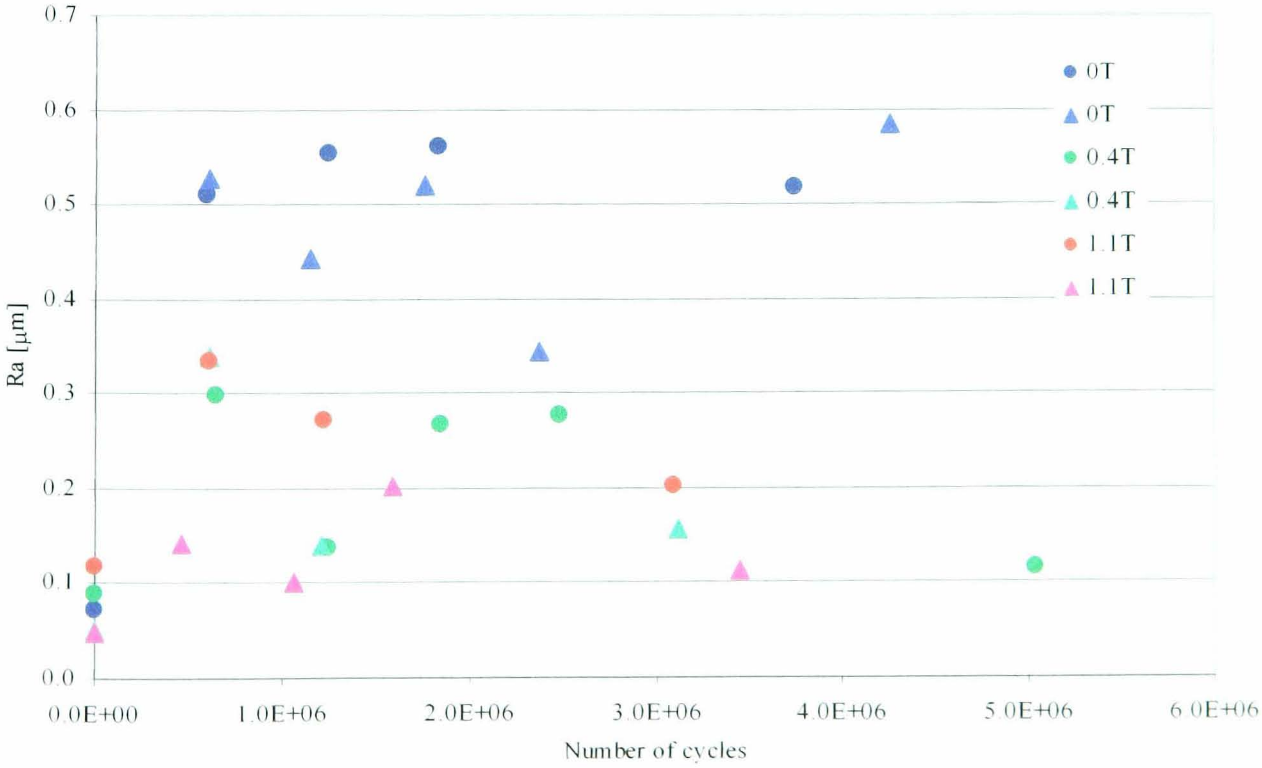

Figure 5.2 Surface roughness of mild steel discs (Pure Rolling)

Surface observations of mild steel discs under the optical microscope are shown in Figure 5.3. Without magnetic field and after 1×10^6 cycles, (see Figure 5.3 (a)), the outer layer was deformed plastically and stripe marks can be seen. The marks that lay perpendicular to the direction of rolling can be considered as the evidence of fatigue cracks in rolling friction. In contrast, under the horizontal magnetic field, a different pattern of the surface asperity was created. At the magnetic field density of 0.4T, a characteristic pattern, shown in Figures 5.3 (b) and (c), can be observed. It consists of a thin, plastically deformed outer layer and can be easily peeled off by cleaning (see Figure 5.3 (c) and (d)). The asperity under the layer was smoother than that without magnetic field. It agrees well with the results of surface roughness measurements. In addition, at 1.1T, a similar pattern to that at 0.4T was also observed on the surface as seen in Figures 5.3 (e) and (f). The difference between the two magnetic fields can be seen in surface asperity patterns created. The boundary between each particle on the surface was clearly defined at 0.4T and looks deeper than that at 1.1T.

Moreover, the effect of magnetic field on surface asperity was even clearer in SEM observations shown in Figure 5.4. The surface, after testing without magnetic field is shown in Figure 5.4 (a).

Figure 5.4 (b) shows an assembly of detached particles. The particles are flat and flake shaped. Therefore, under rolling condition, it is permissible to suppose that a crack was initiated at the subsurface region. In addition, the thickness of larger particles was estimated to be approximately 20-30μm. The thickness is about half of the depth of 63.2μm for the location of maximum shear strain-energy obtained from the Hertz's theory. Contrary to this, smoother surface and finer wear particles were observed due to the presence of the horizontal magnetic field as seen in Figure 5.4 (c) - (f). These particles, considered to origin from the surface, are shown in Figure 5.3 (c). The thickness of these particles is no more than 10μm.

Thus, it can be said that wear particles generated in rolling contact became finer due to the effect of the horizontal magnetic field. Therefore, when the thickness of wear particles is assumed to correspond to the location of a subsurface crack initiation point, it is apparent that the point was moved towards the surface. Also, the effect of the magnetic field presence was observed in particles' size.

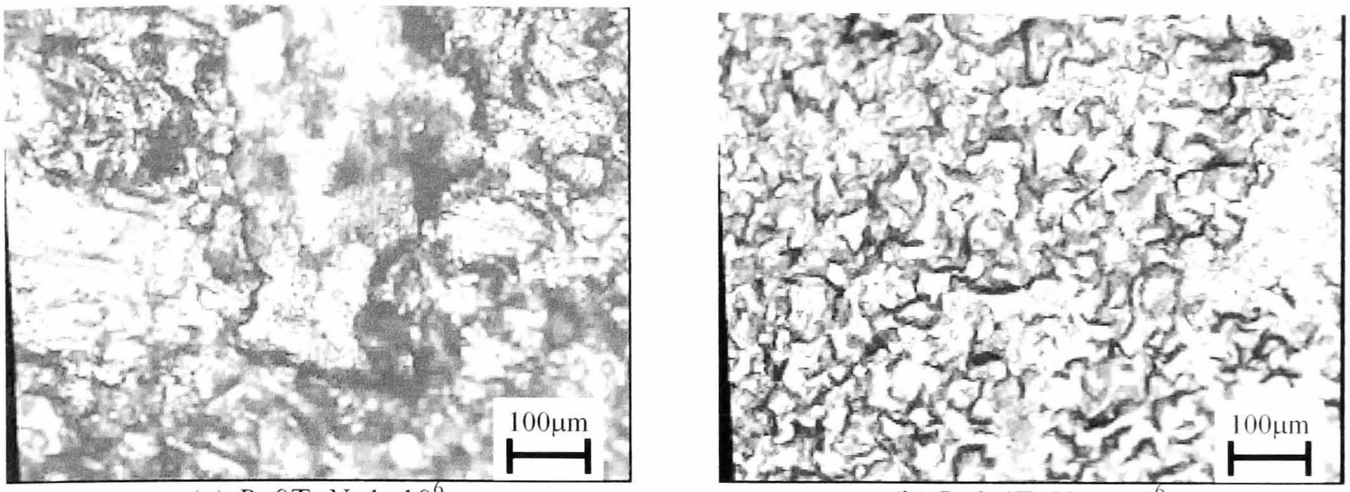

(a) B=0T, N=1x10^6 (b) B=0.4T, N=1x10^6

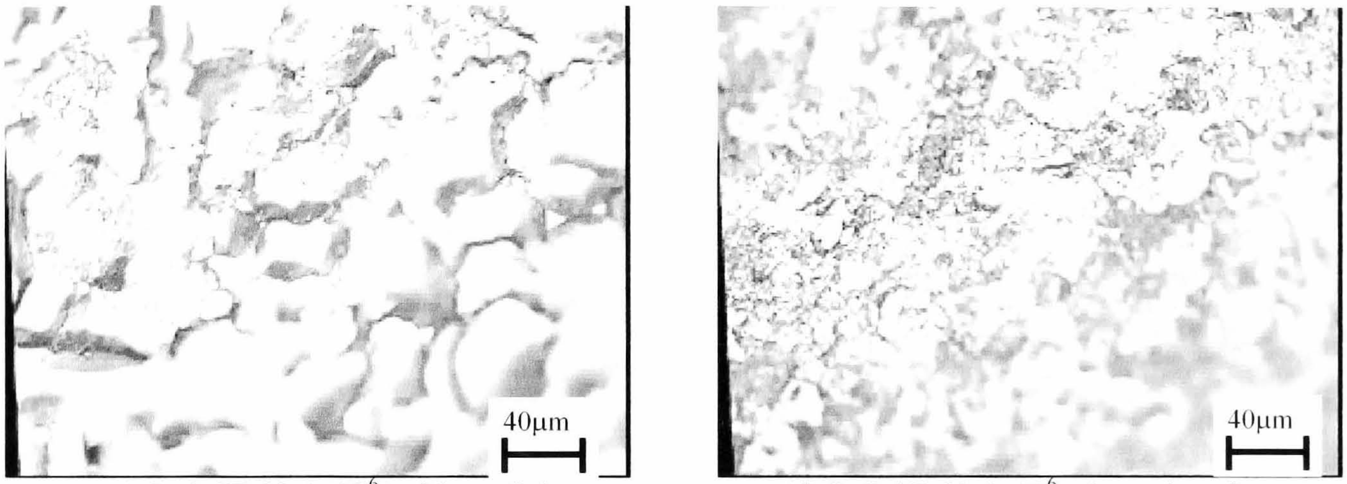

(c) B=0.4T, N=1x10^6, with particles (d) B=0.4T, N=1x10^6, cleaned surface

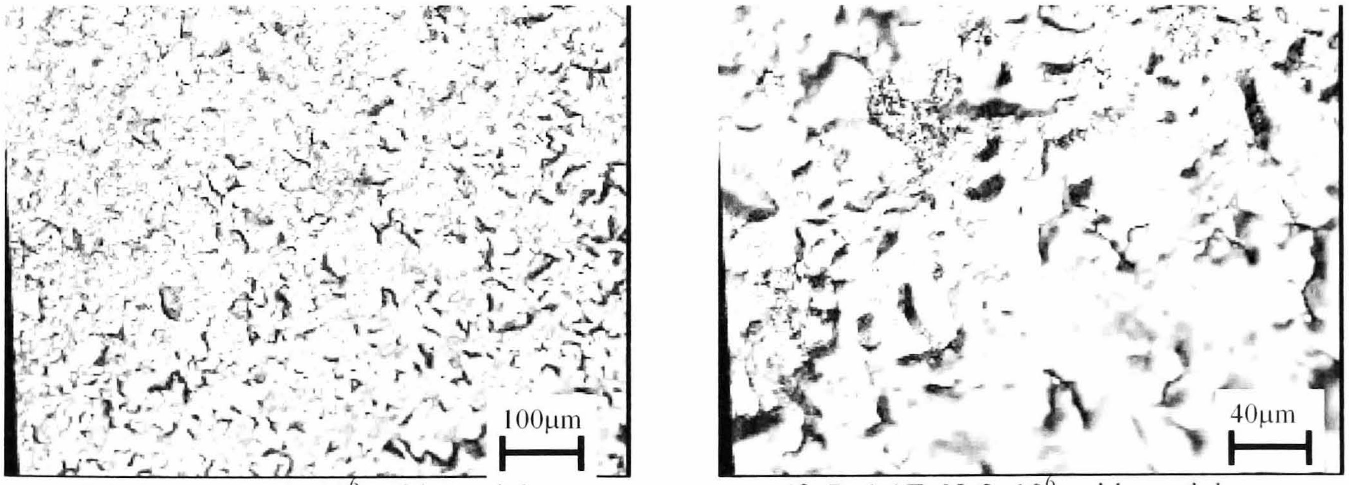

(e) B=1.1T, N=3x10^6, with particles (f) B=1.1T, N=3x10^6, with particles

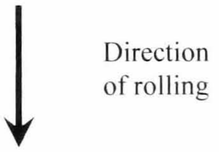

Figure 5.3 Surface observations of mild steel discs (Pure Rolling, Optical Microscope)

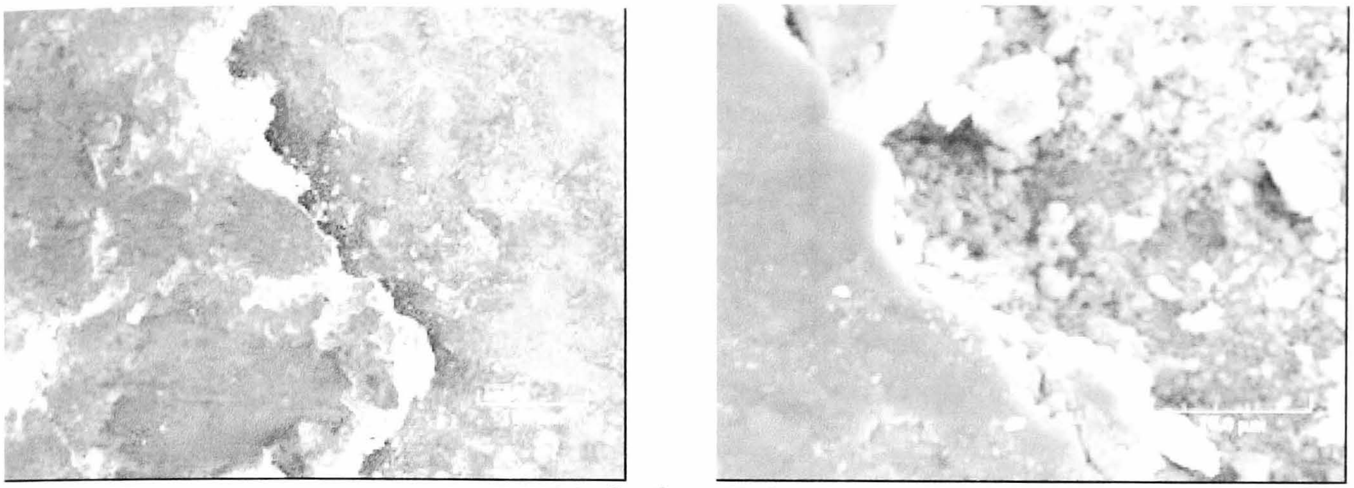

(a) Surface, B=0T

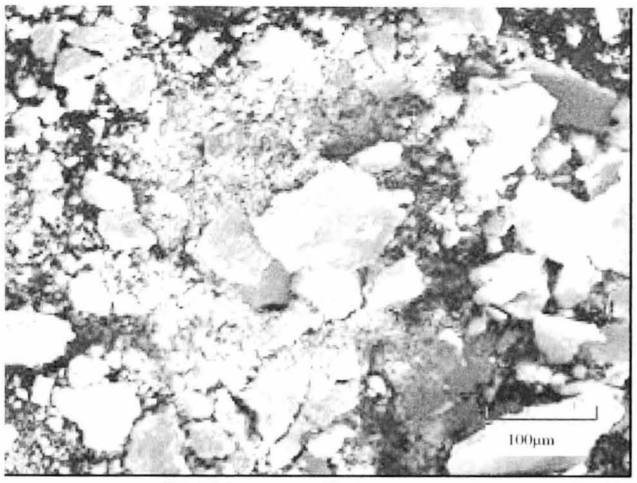

(b) Wear particles, B=0T

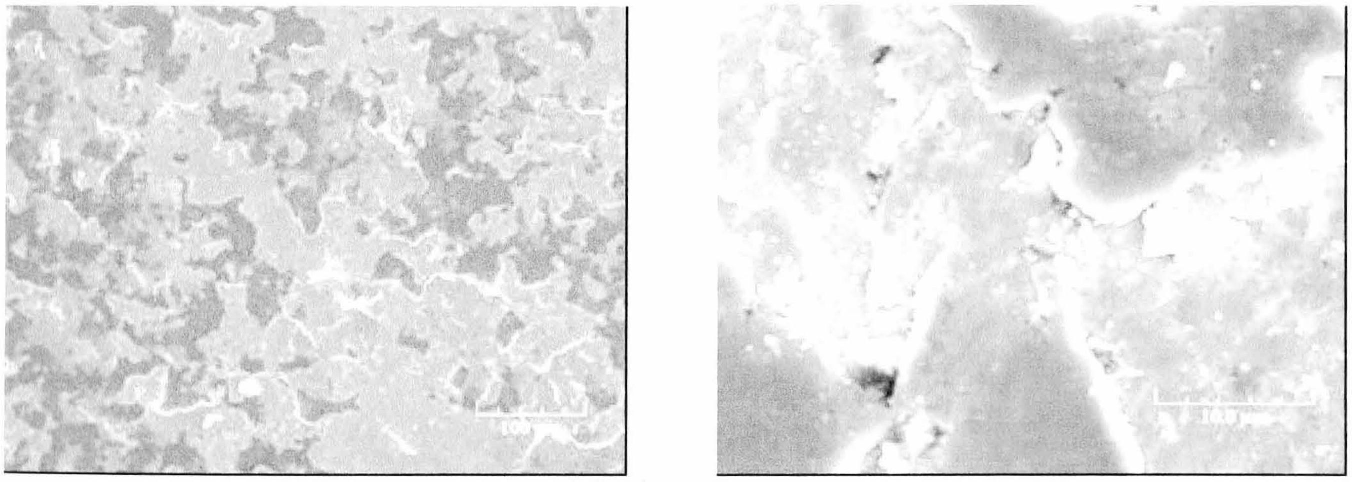

(c) Surface, B=0.4T

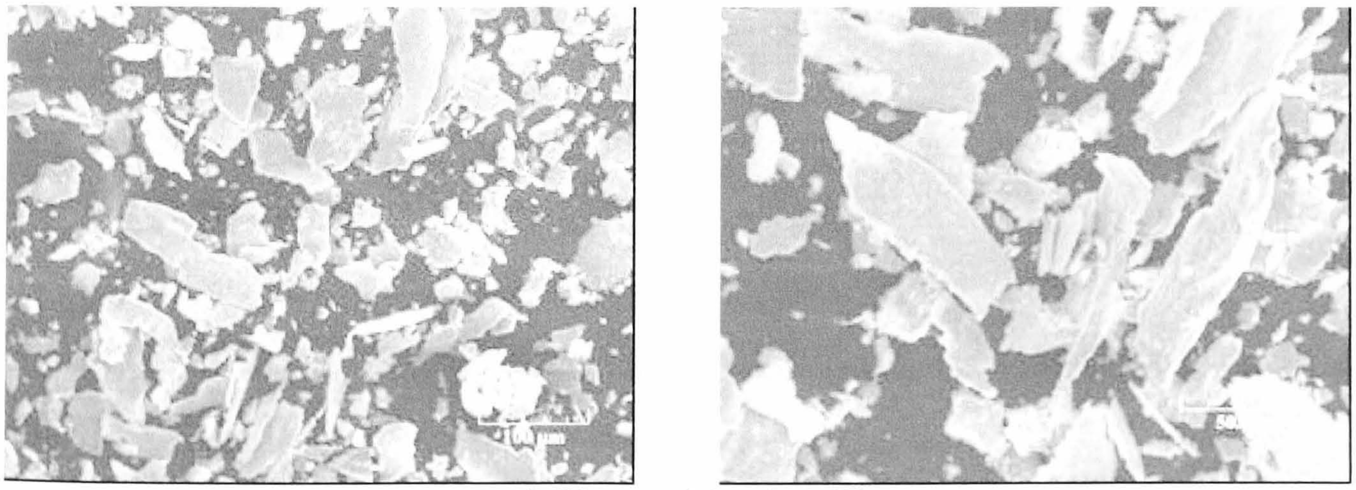

(d) Wear particles, B=0.4T

Figure 5.4 Surface and wear particles observations of mild steel discs (Pure Rolling, SEM)

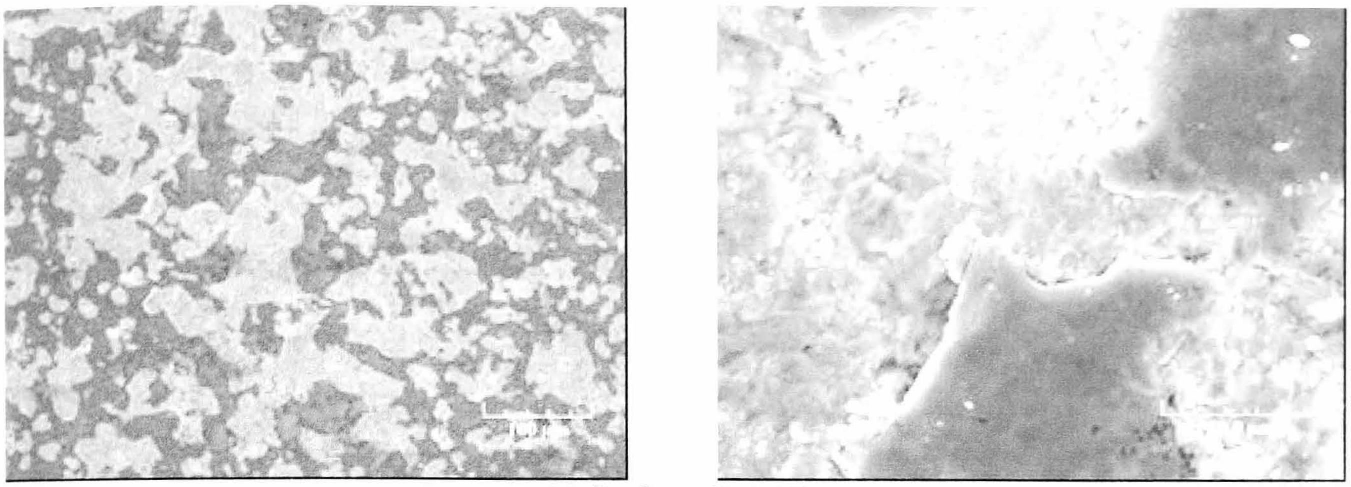

(e) Surface, B=1.1T

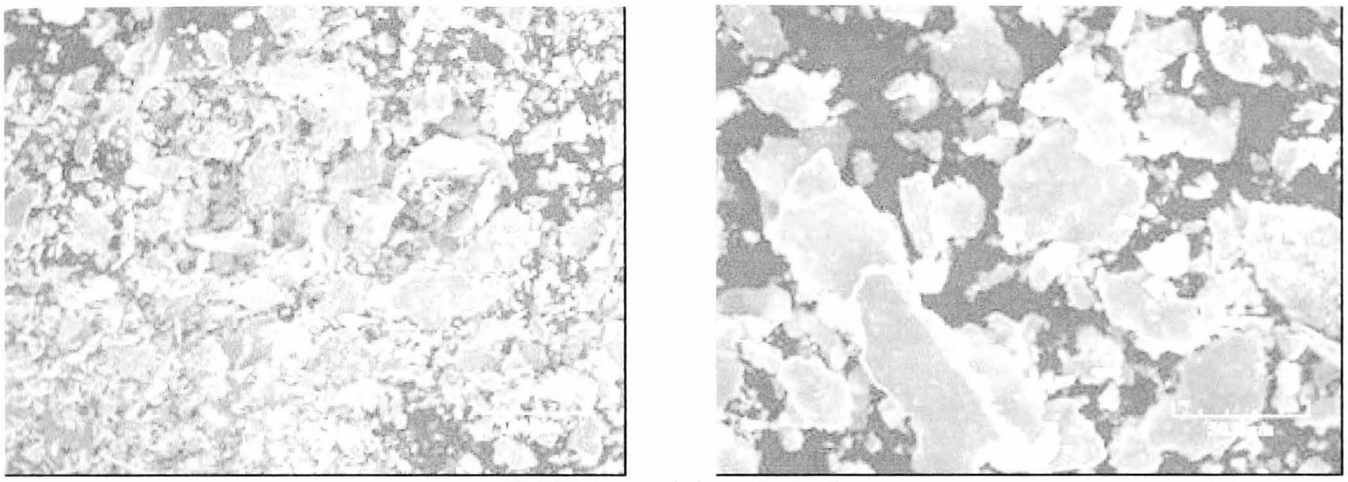

(f) Wear particles, B=1.1T

Figure 5.4 Surface and wear particles observations of mild steel discs (Pure Rolling, SEM)
(Continued)

5.2.2 Pure Rolling at Different Rotational Speeds

According to Muju$^{(1)}$, dislocation velocity in ferromagnetic substances is increased under the magnetic field and it affects characteristic of the adhesive wear.

To estimate this effect in rolling contact, two different rotational speeds: 450rpm and 180rpm were used. Weight losses at different rotational speeds are shown in Figure 5.5. In the absence of the magnetic field, the pattern of weight losses was almost the same for both speeds. In the presence of the magnetic field, weight losses were decreased at 180rpm. However, the decrease was lower than that at 450rpm and the total amount of wear was nearly the same as that for the without magnetic field condition.

Changes in surface roughness at different rotational speeds, shown in Figure 5.6, had a similar trend to that of weight losses. At without magnetic field, the R_a value was around 0.5μm and there was not so much difference between to the two rotational speeds. The values of R_a in the magnetic field, were between 0.10 to 0.34μm for both 0.4 and 1.1T and 450rpm. The results at 180rpm, however, were slightly higher on the whole although the range of the values was similar.

From these results, it can be concluded that the effect of magnetic field is less pronounced at the rotational speed of 180 rpm comparing to that at 450rpm.

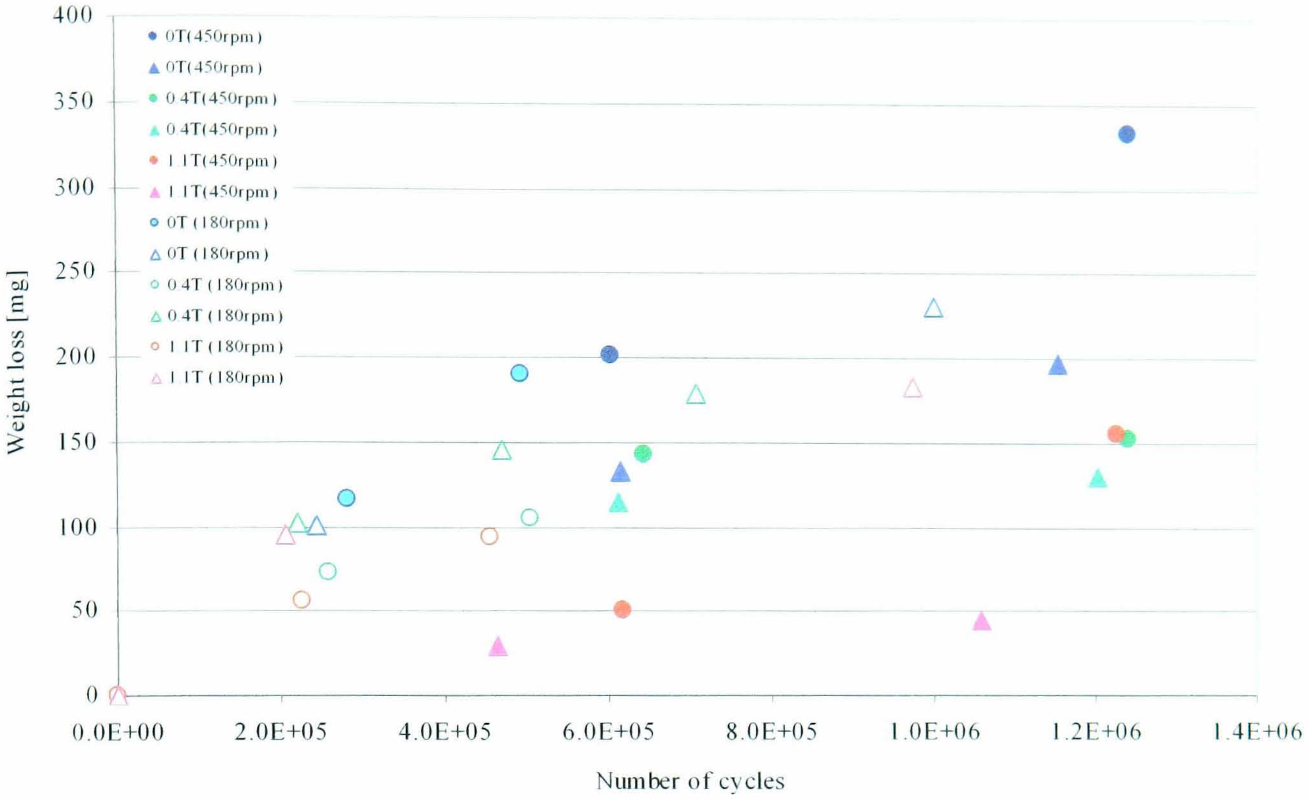

Figure 5.5 Accumulated weight losses of mild steel discs (Pure Rolling)

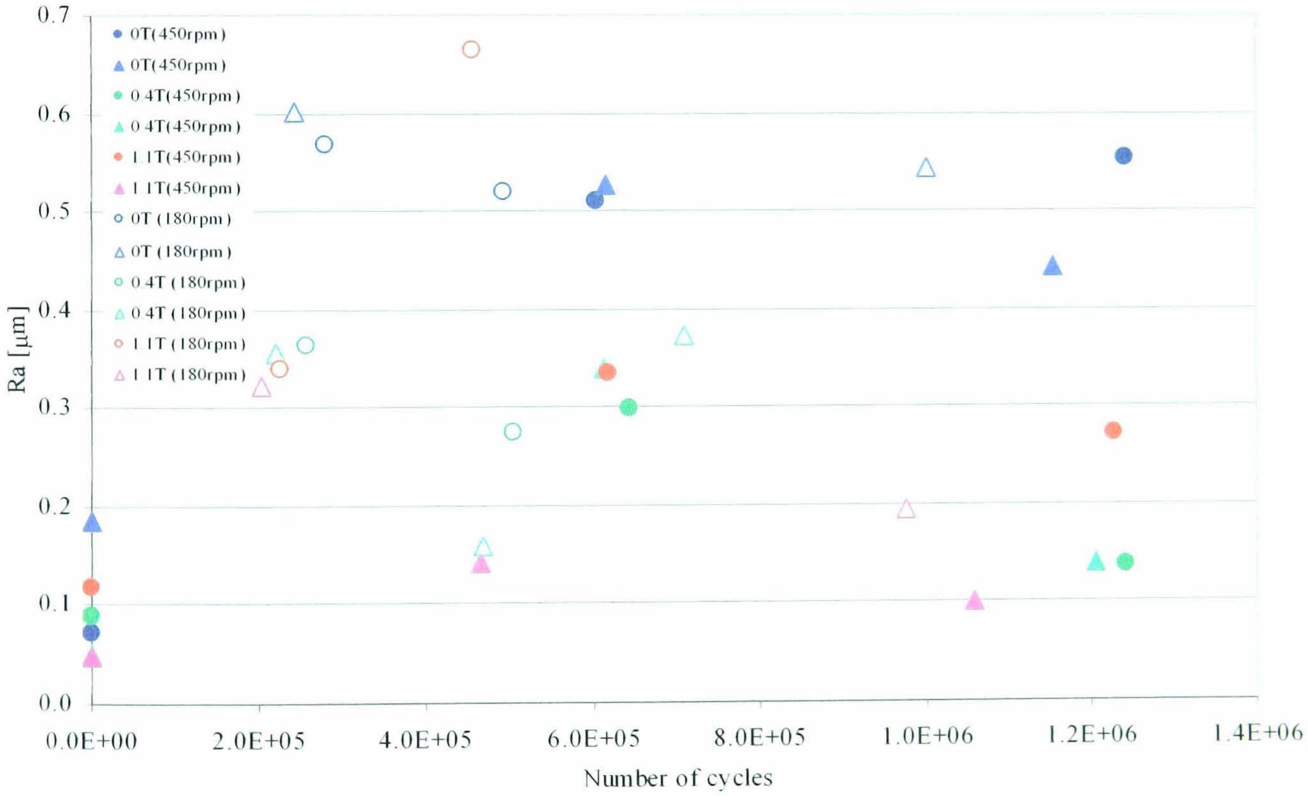

Figure 5.6 Surface roughness of mild steel discs (Pure Rolling)

5.2.3 Effect of Magnetic Field Orientation

The differences in weight losses for different angles, θ, are shown in Figure 5.7. With the magnetic field, wear decreased at all angles θ used. By varying the angle from $\theta=0^\circ$ to 45° and 90°, weight losses were increased. At the angle of $\theta=90^\circ$, weight losses came near to those obtained for the absence of the magnetic field. Moreover, surface roughness at $\theta=90^\circ$ was also similar to that recorded for the absence of the magnetic field (see Figure 5.8). Lower weight losses were obtained at $\theta=0^\circ$ and 45°, and the value of R_a was less than 0.3μm. At $\theta=90^\circ$ and the absence of the magnetic field, the value of R_a was greater than 0.34μm.

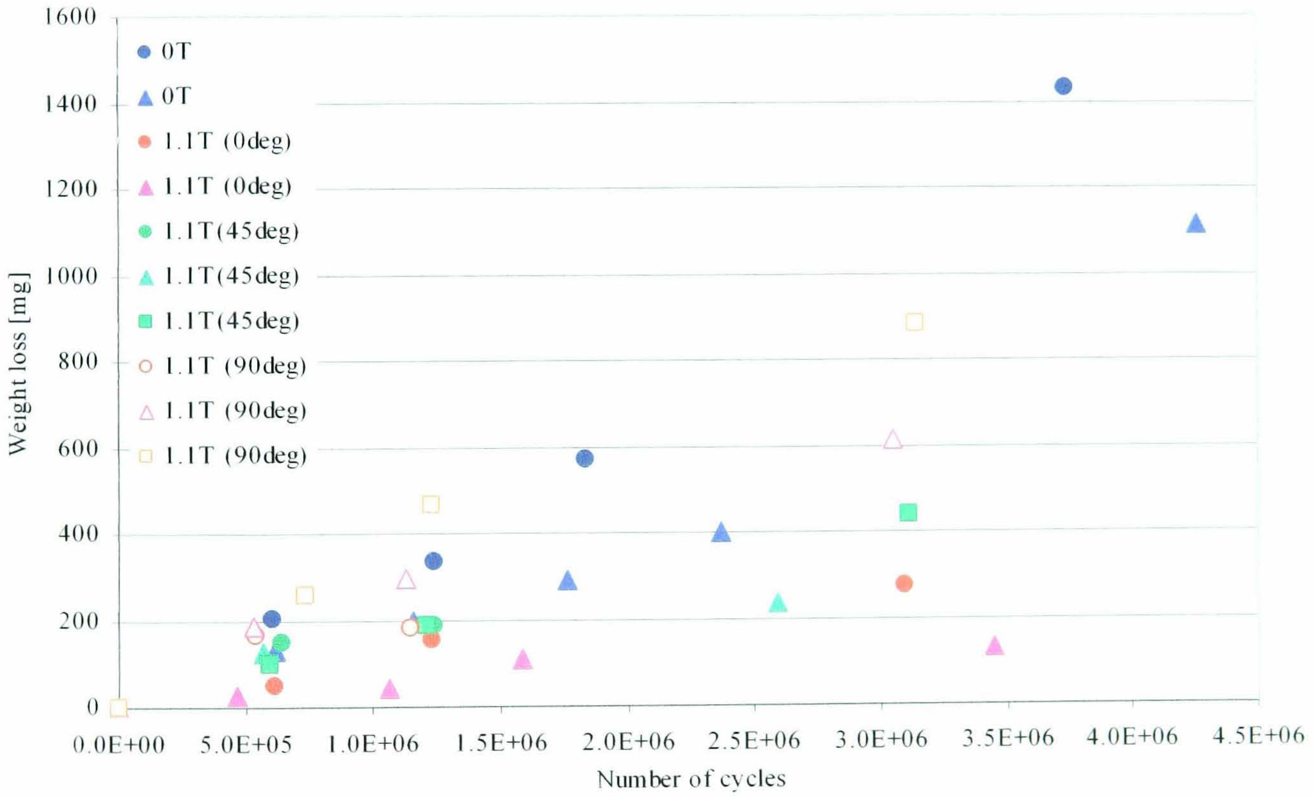

Figure 5.7 Accumulated weight losses of mild steel discs in different angles of θ (Pure Rolling)

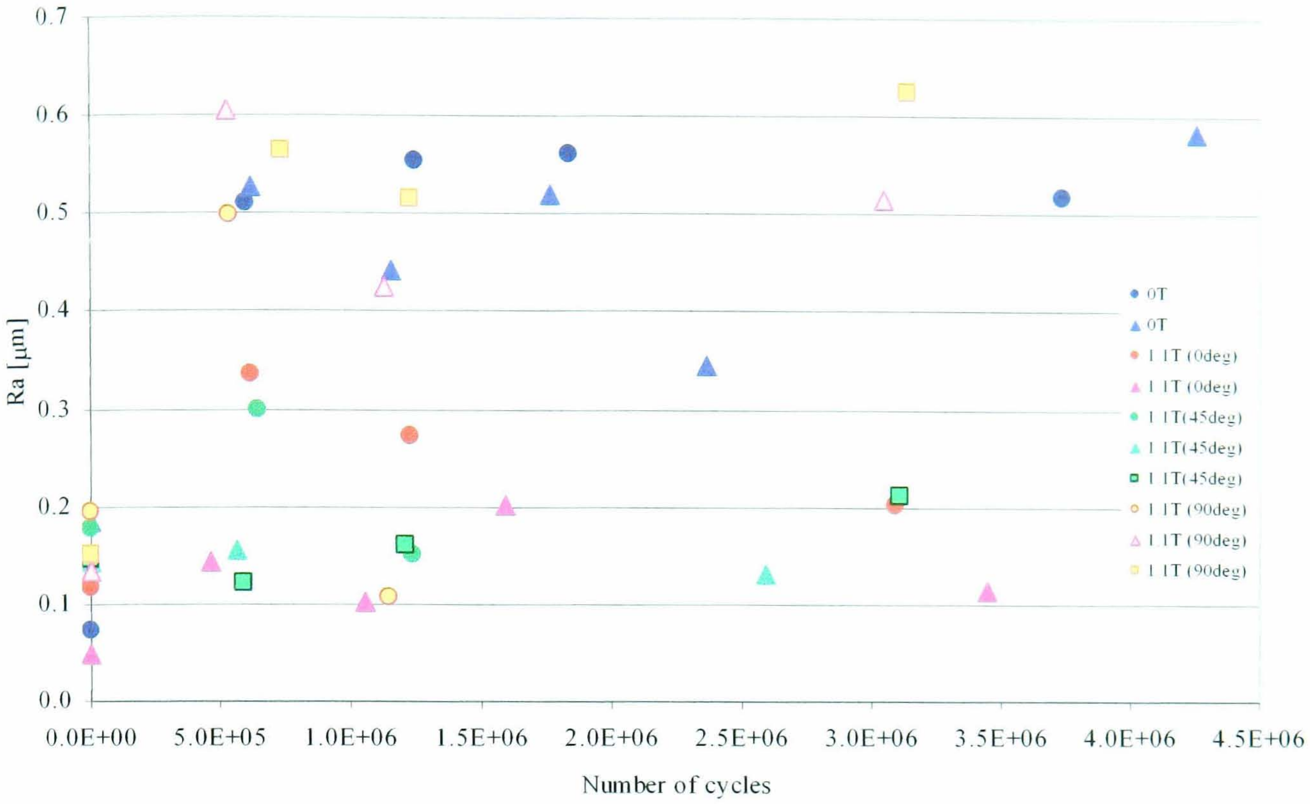

Figure 5.8 Surface roughness of mild steel discs at different angles of θ (Pure Rolling)

The effect of magnetic field orientation was also observed in the surface appearances. From optical microscope observations, shown in Figure 5.9, the asperities can be classified into two groups by the wear amounts and R_a values. First one is for θ=0° and θ=45°, and the second one is for B=0T and θ=90°. At θ=45°, characteristic pattern, similar to that at θ=0°, was observed on the surface. In contrast, at θ=90°, and in the absence of the magnetic field (see Figure 5.9(a)), deformed outer layer and stripe marks under the layer can be seen.

These characteristic features of the surface were also seen in SEM observations shown in Figure 5.10. On the other hand, effect of the magnetic field on wear particles was observed clearly. At the lower R_a values obtained at θ=0° and θ=45°, finer wear particles were observed. However, at θ=90°, in spite of similar R_a value and wear amount observed for without magnetic field, the shape of wear particles was completely different. The main difference, more or less the same for all of them, was the thickness of particles. The thickness of particles around 10µm, produced at θ=90° and the magnetic field presence, is not the same for particles generated in the absence of the magnetic field.

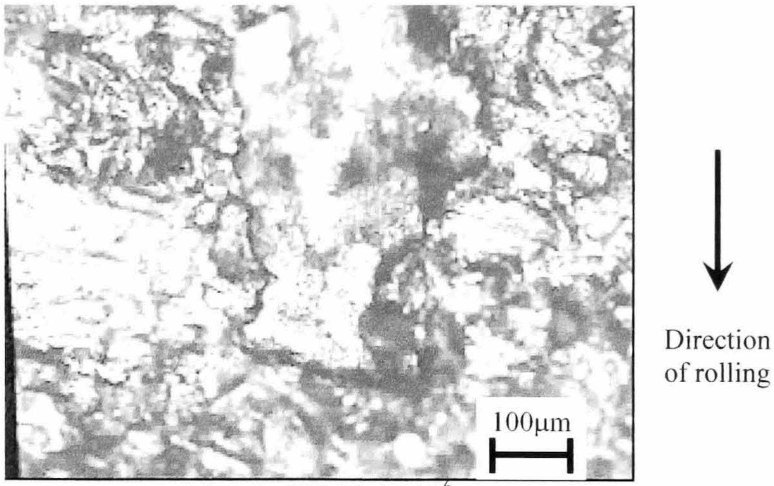

(a) B=0T, N=1x10^6

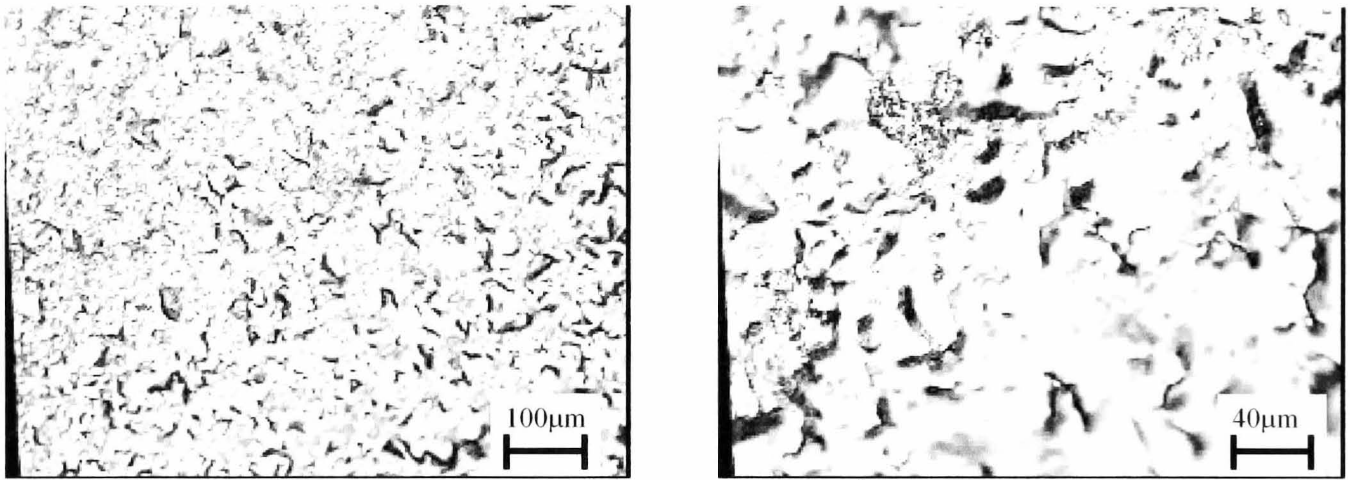

(b) B=1.1T, θ=0° N=3x10^6

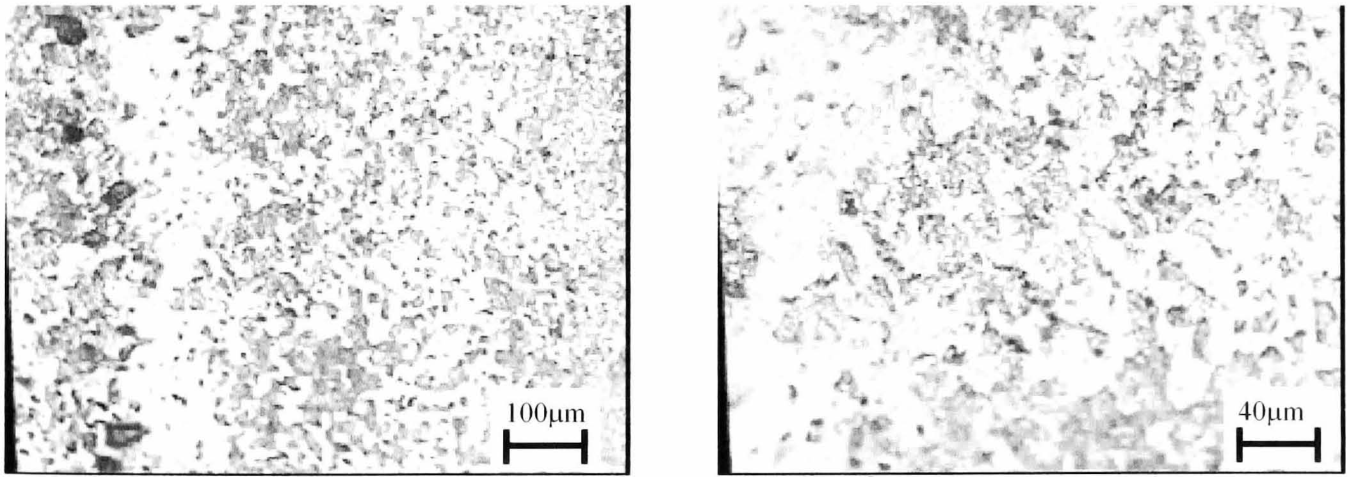

(c) B=1.1T, θ=45° N=1x10^6

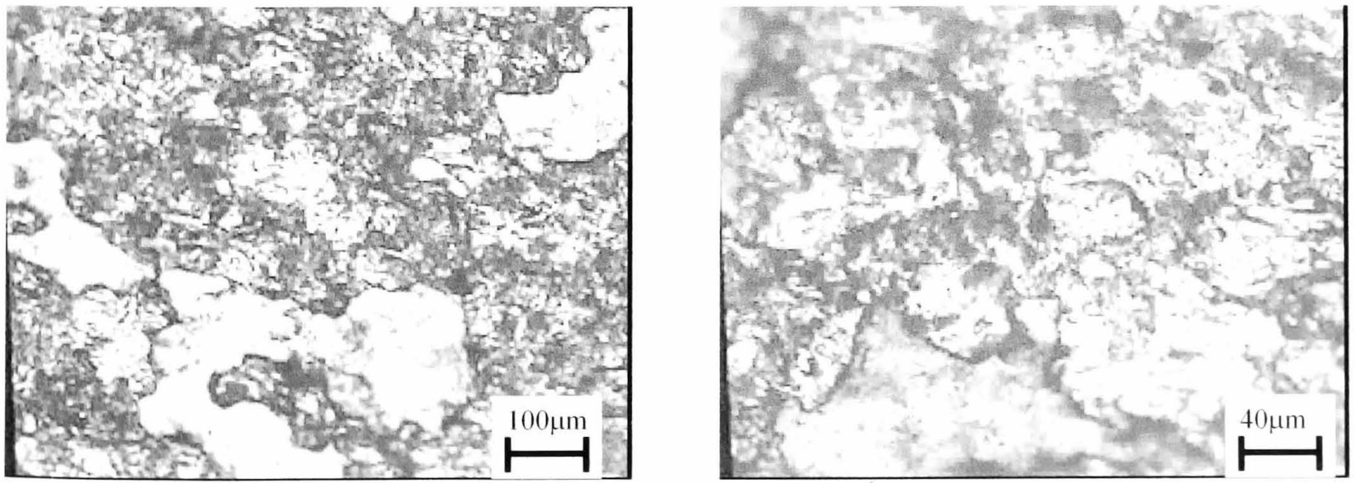

(d) B=1.1T, θ=90° N=1x10^6

Figure 5.9 Difference in θ on surface of mild steel discs (Pure Rolling, Optical Microscope)

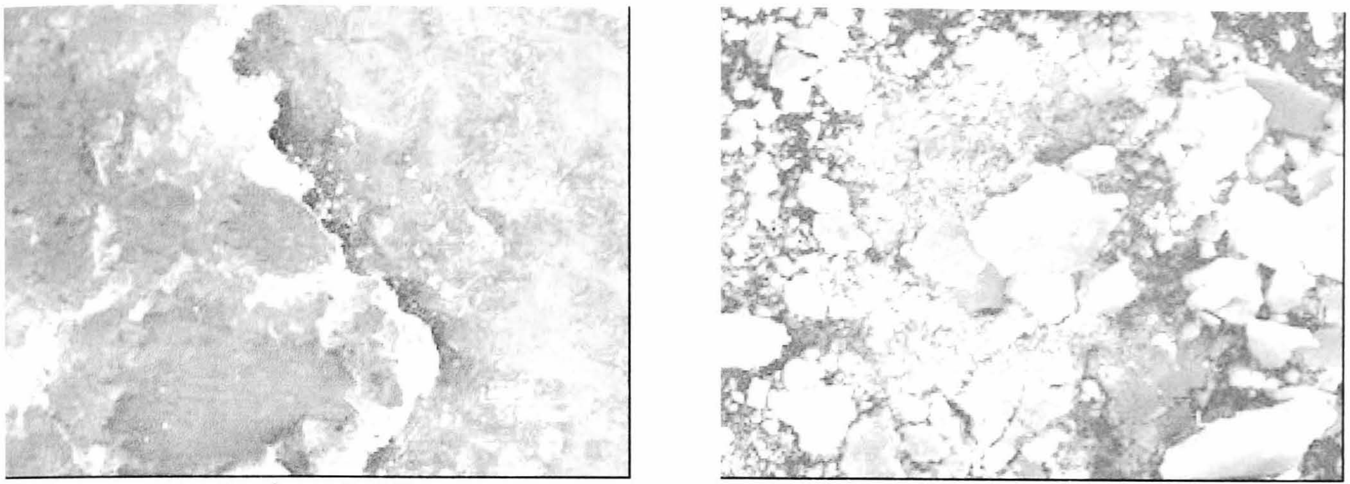

(a) Surface, B=0T

(b) Wear particles, B=0T

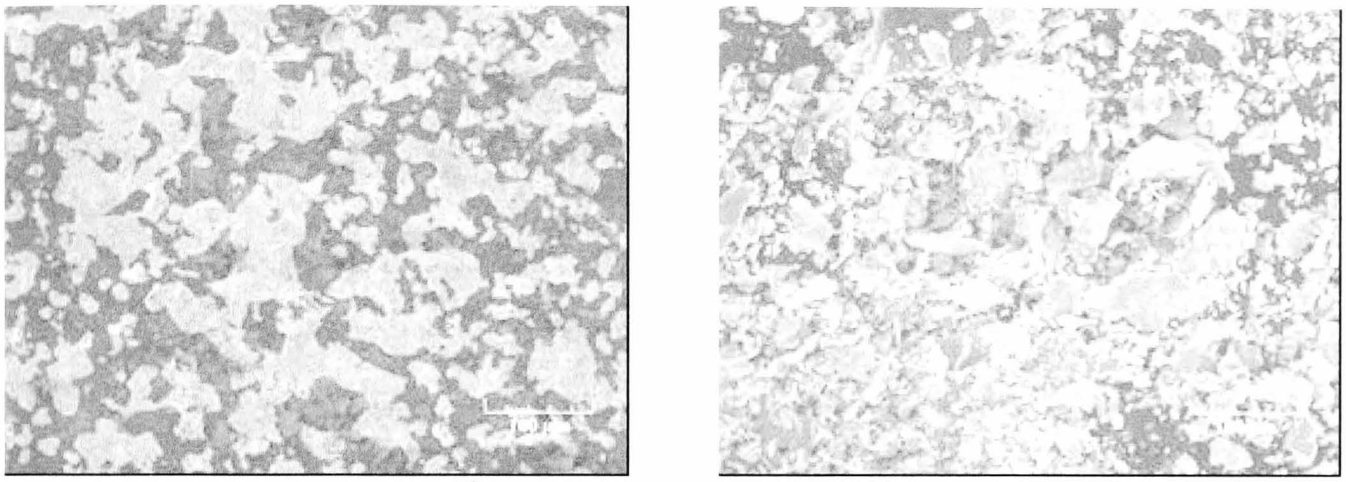

(c) Surface, B=1.1T, θ=0°

(d) Wear particles, B=1.1T, θ=0°

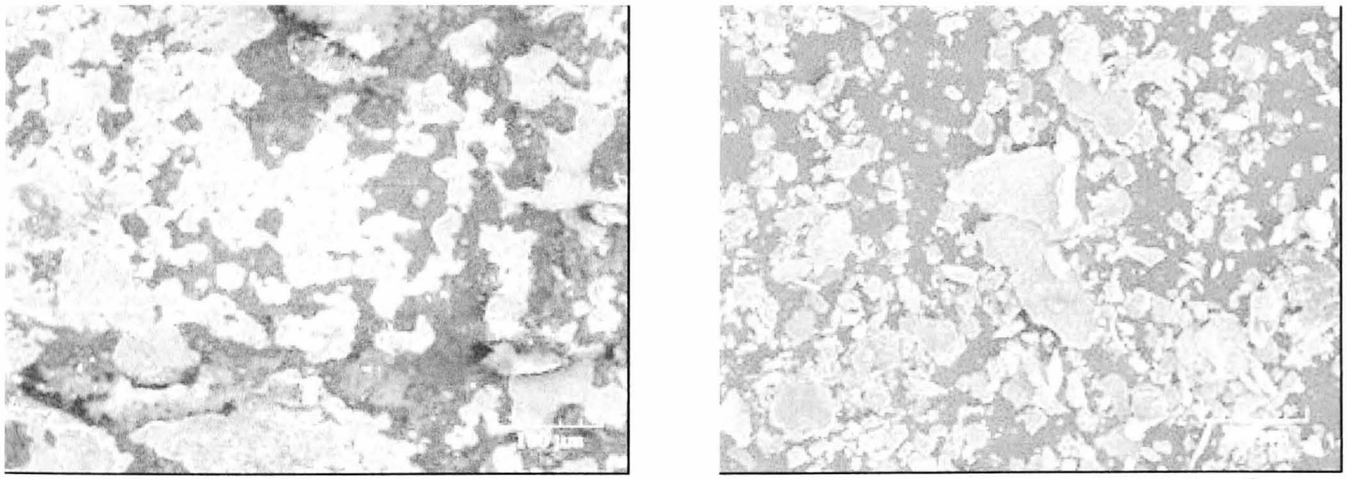

(e) Surface, B=1.1T, θ=45°

(f) Wear particles, B=1.1T, θ=45°

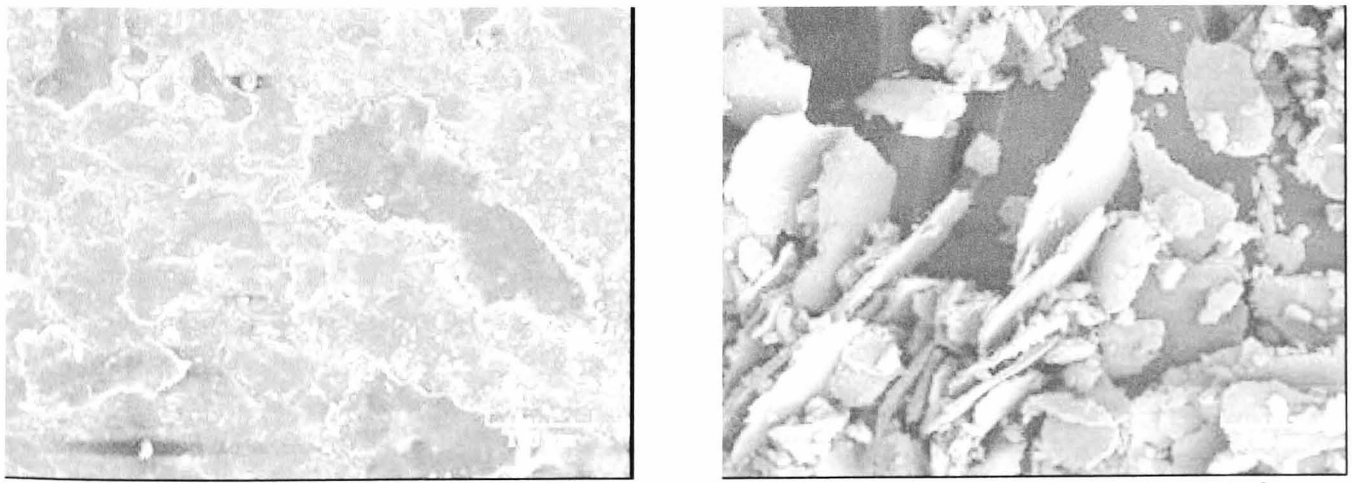

(g) Surface, B=1.1T, θ=90°

(h) Wear particles, B=1.1T, θ=90°

Figure 5.10 Difference in θ on Wear particles of mild steel discs (Pure Rolling, SEM)

5.2.4 Effect on a Non-Magnetic Material

To evaluate the effect for a non-magnetic material, driven disc was made of aluminium. Dimensions of the driven disc were the same as that for the steel disc. For the driving disc, the same EN40B steel was used. Due to the change in material, the load on the contact was also altered to P=50N. As a result, width of the contact area, a, and the maximum contact pressure, p_0, obtained from the Hertz's theory equations (2.2)-(2.5), changed to 71.2μm and 111.82MPa respectively.

From the results of weight losses and surface roughness, shown in Figure 5.11 and 5.12, the difference in performance between with and without magnetic field is negligible. In addition, there is also no difference in surface and wear particles appearance (see Figure 5.13). Therefore, it can be concluded that the effect of the magnetic field on a non-magnetic material in rolling contact is negligible.

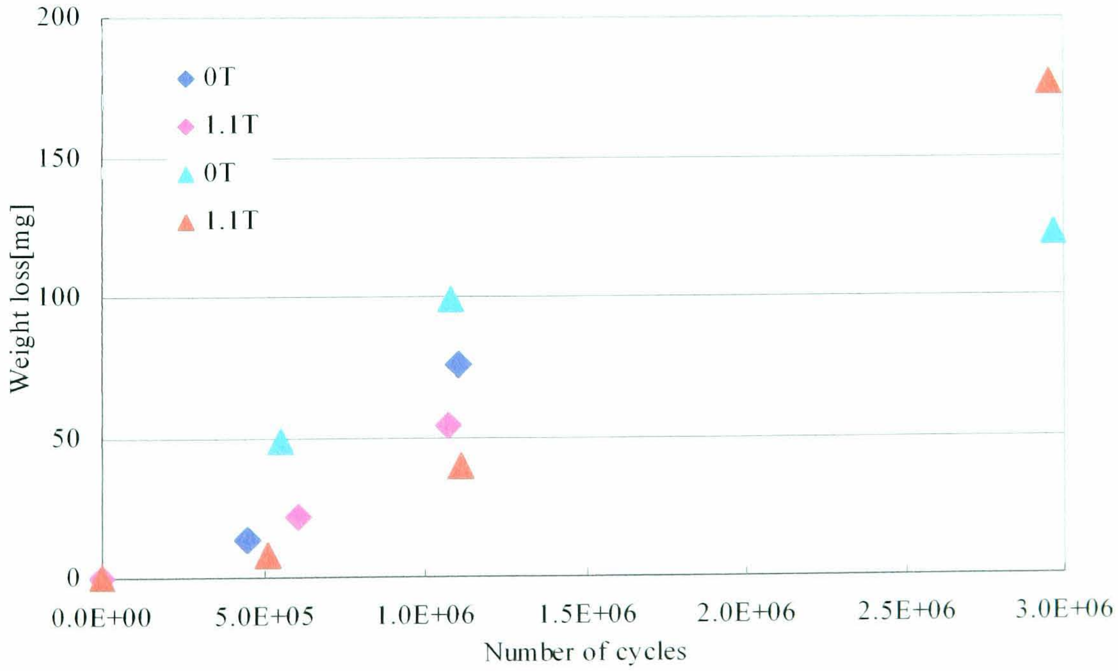

Figure 5.11 Accumulated weight losses of Al discs (Pure Rolling)

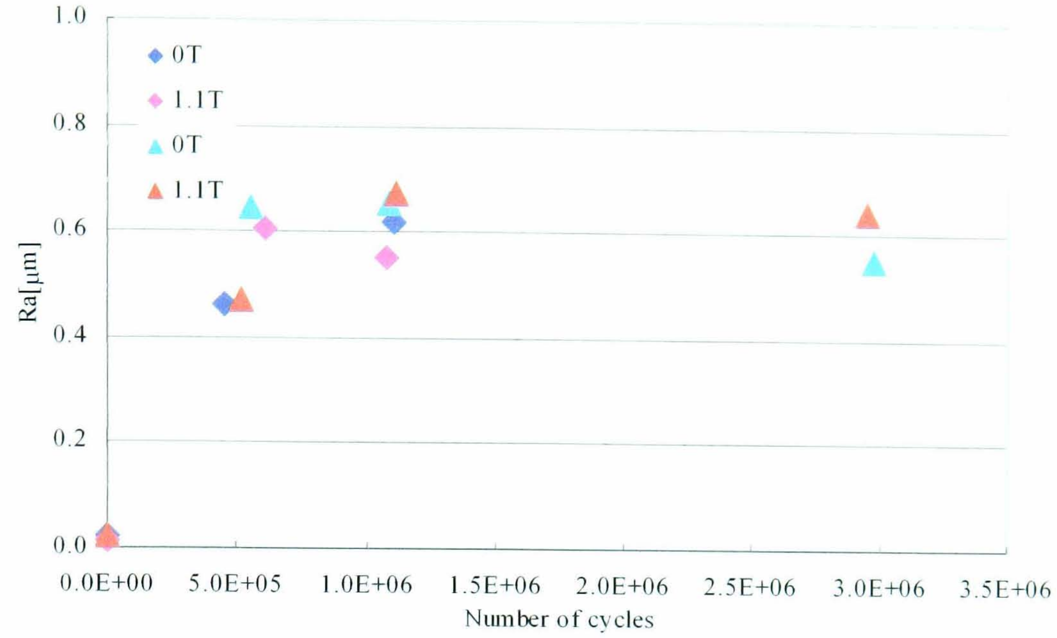

Figure 5.12 Surface roughness of Al discs (Pure Rolling)

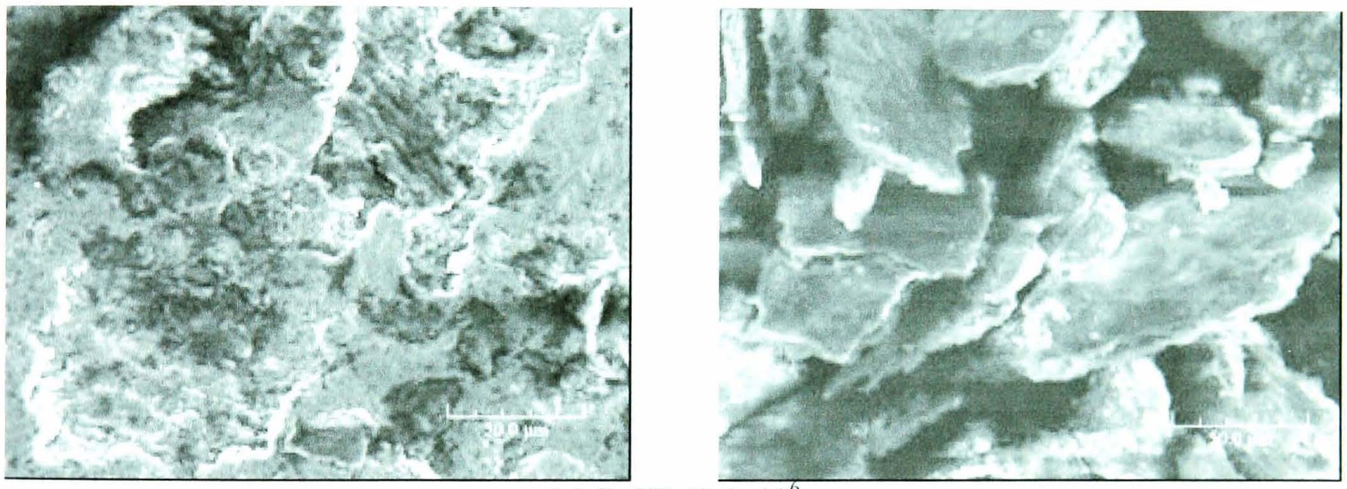

(a) B=0T, N=3x10^6

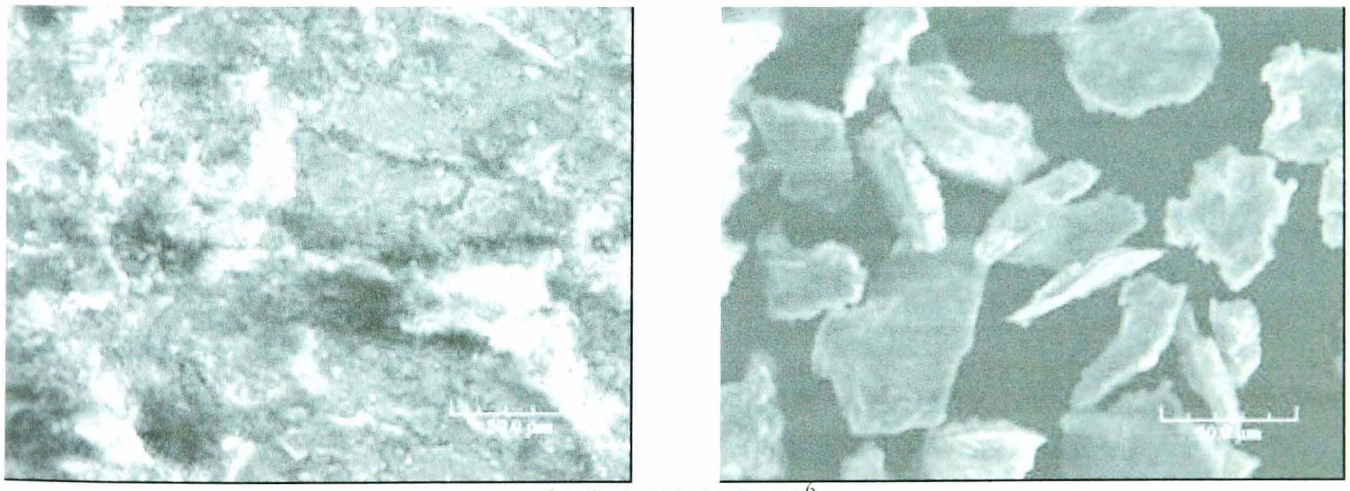

(b) B=1.1T, N=3x10^6

Figure 5.13 Surface and wear particles observations of Al discs (Pure Rolling, SEM)

5.3 Rolling with Sliding Tests

5.3.1 Rolling with Sliding of Steel Discs

As shown in Figure 5.14, weight losses of discs in tests with 10% sliding and without the presence of a magnetic field were increasing proportionally with the number of cycles; the same trend as that observed for pure rolling tests. With the horizontal magnetic field present, although wear amounts were reduced, weight losses generated under rolling with sliding were higher than those recorded without the presence of a magnetic field. This trend was especially noticeable at *B*=1.1T.

Figure 5.15 shows comparison of wear rates obtained at pure rolling and rolling with sliding. The wear rate ratio of rolling with sliding to pure rolling after 1x10^6 cycles was 3.7 at *B*=0T, 7.6 at *B*=0.4T and 17.1 at *B*=1.1T. The results justify saying that wear under magnetic field is increased due to the introduction of slip into the rolling contact.

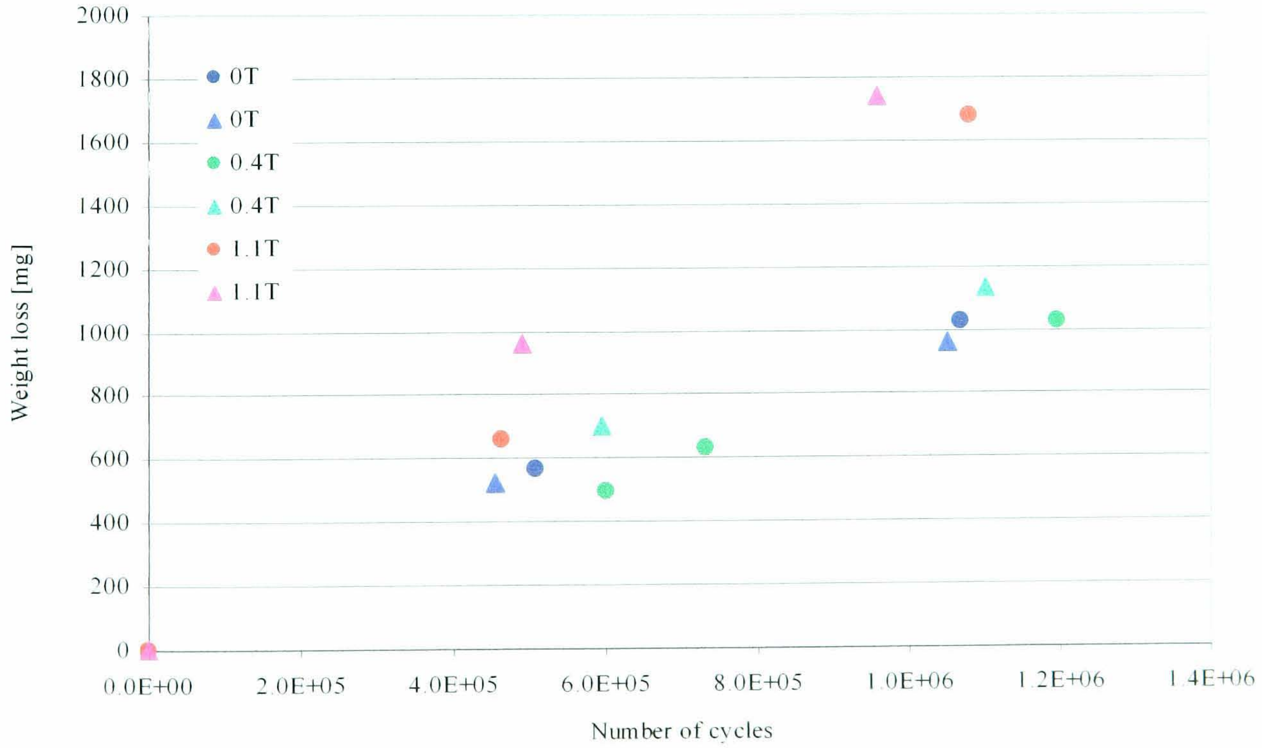

Figure 5.14 Accumulated weight losses of mild steel discs (10% Slide)

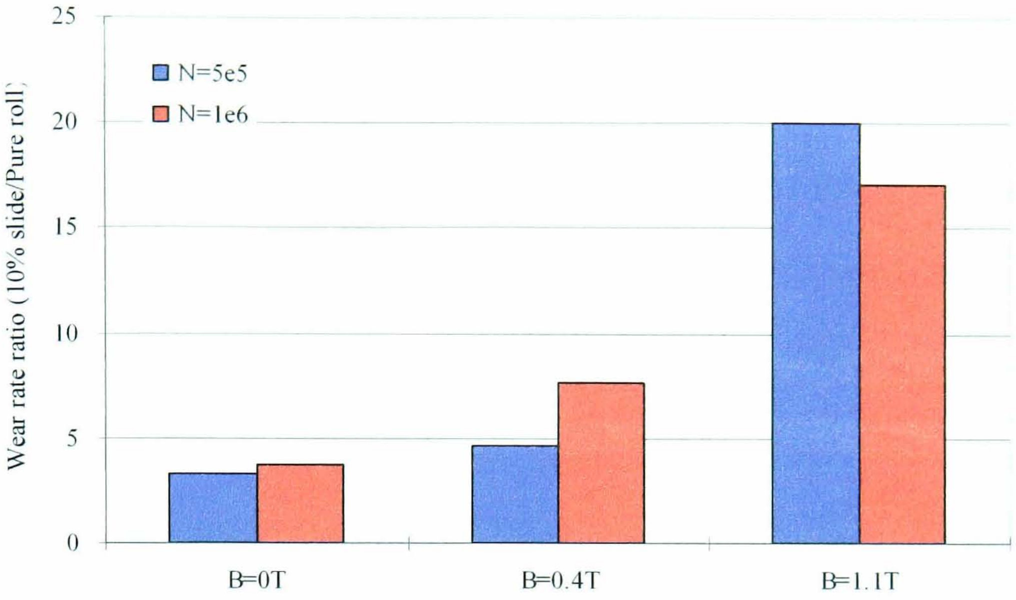

Figure 5.15 Weight rate ratios between pure rolling and 10% slide rolling

Surface roughness, R_a for rolling with sliding, shown in Figure 5.16, tended to be lower under the magnetic field; the same trend as for pure rolling. However, the differences in R_a values among magnetic conditions used were smaller than that for pure rolling. Specifically, comparing to pure rolling, R_a for without magnetic field condition was around 0.5μm and below 0.3μm for the magnetic field presence. Values of R_a for rolling with sliding were in the range of 0.47-0.59 μm for without magnetic field whereas for the magnetic field of 0.4T and 1.1T, R_a values were in the range of 0.34-0.38μm and 0.26-0.42μm respectively.

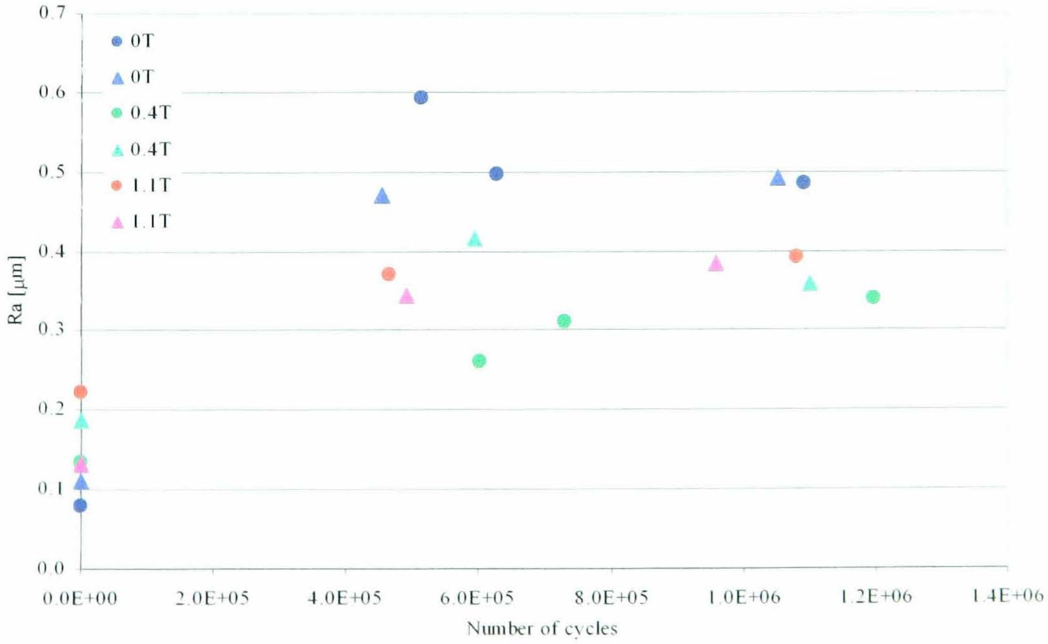

Figure 5.16 Surface roughness of mild steel discs (10% Slide)

Observations under the optical microscope, shown in Figure 5.17, reveal that surface asperities of the driven discs under rolling with sliding conditions are deformed plastically and have stripe marks when there is no magnetic field. Even under the horizontal magnetic field, a similar pattern of surface asperities was observed. The characteristic pattern due to plastically deformed surface layer and observed at pure rolling with the magnetic field does not appear at all magnetic densities used in rolling with sliding. From, The characteristic features of surface asperities revealed by SEM observations can be seen in Figure 5.18.

The effect of magnetic field is clearly observed in the morphology of wear particles. The particles at rolling with sliding without the magnetic field are finer than those generated for pure rolling. For that reason, as seen in Figure 5.4 (b) and Figure 5.18 (b), wear particles under the magnetic field are finer than that produced when the magnetic field is not present. Therefore, it can be said that wear particles become finer due to the effect of a magnetic field and it is common to both pure rolling and rolling with sliding.

B=0T, N=1x10^6

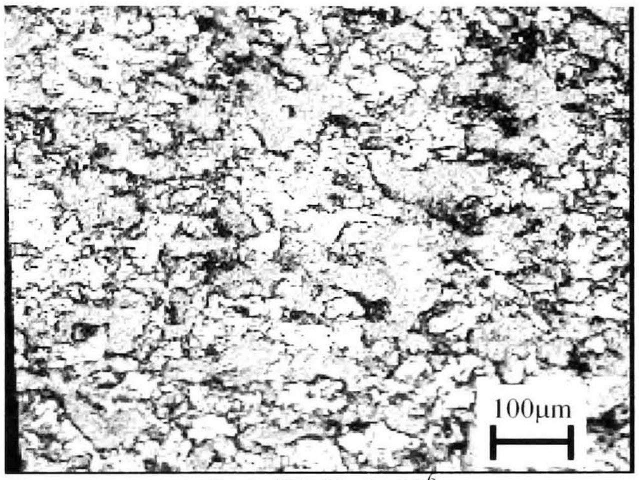

B=0.4T, N=1x10^6

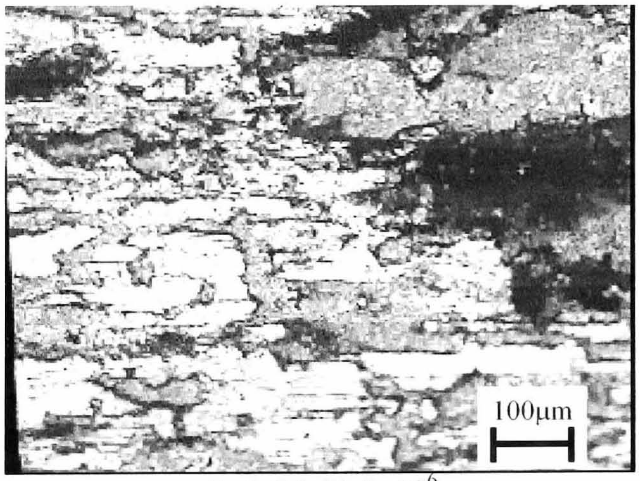

B=1.1T, N=1x10^6

Figure 5.17 Surface observations of mild steel discs (10% Slide, Optical Microscope)

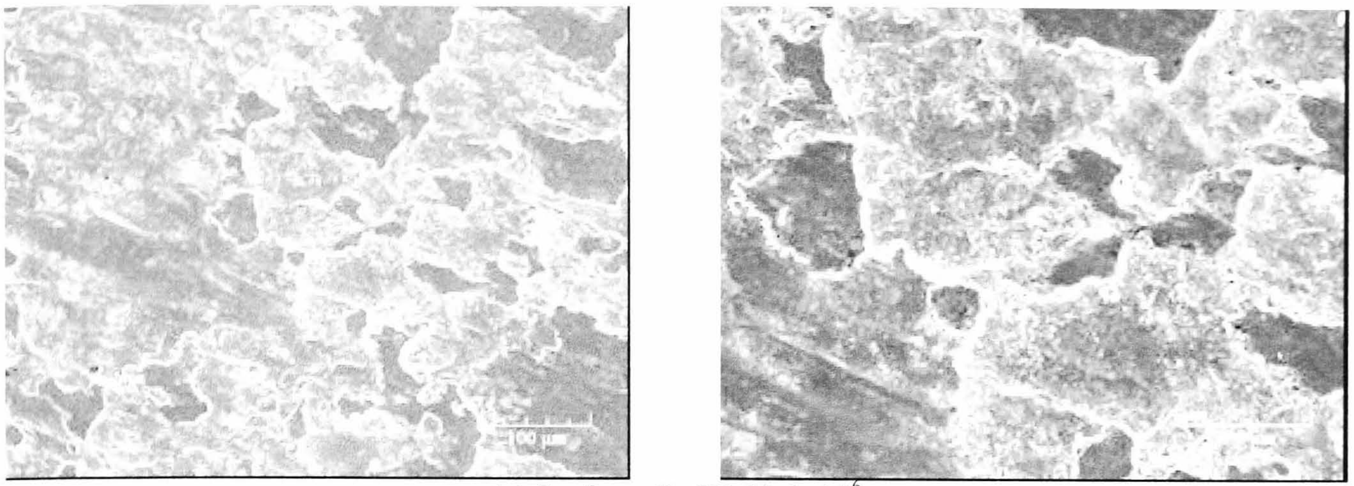

(a) Surface, B=0T, N=1x10^6

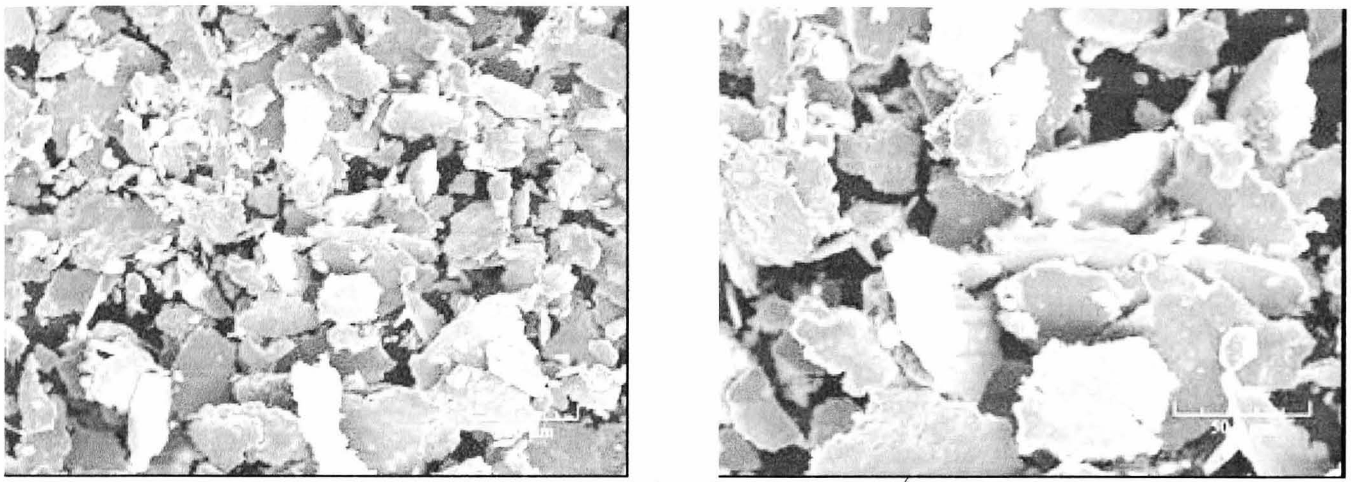

(b) Wear particles, B=0T, N=1x10^6

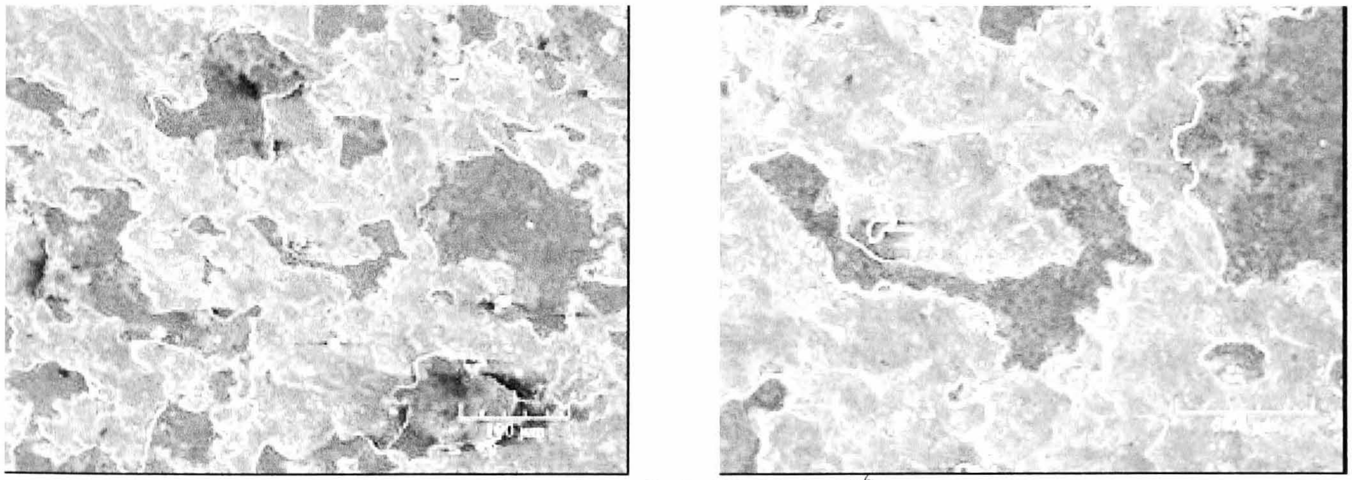

(c) Surface, B=0.4T, N=1x10^6

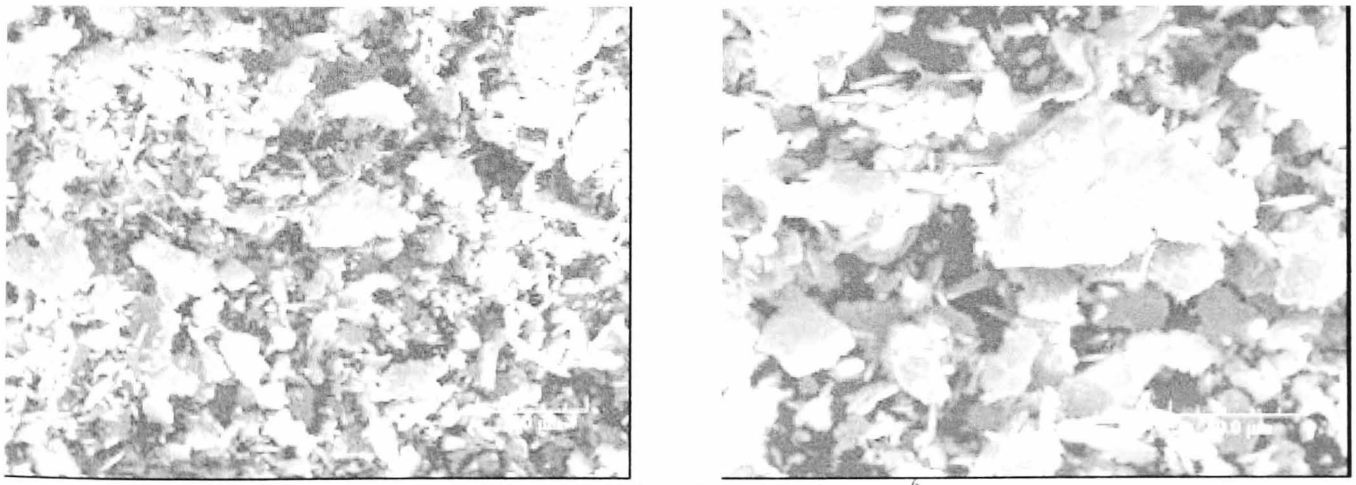

(d) Wear particles, B=0.4T, N=1x10^6

Figure 5.18 Surface and wear particles observations of mild steel discs (10% Slide, SEM)

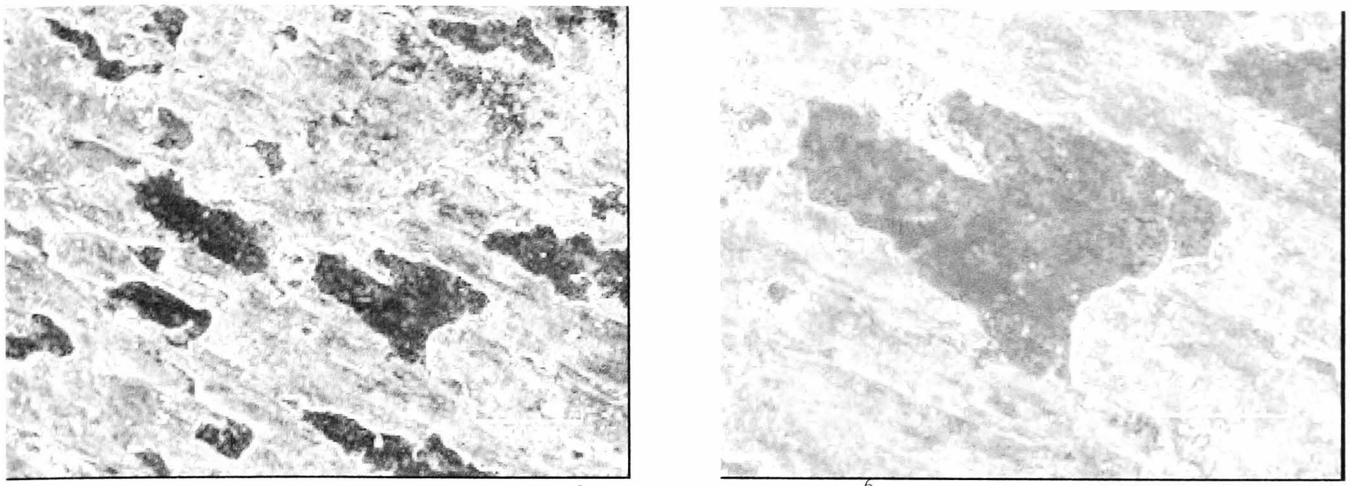

(e) Surface, B=1.1T, N=1x10^6

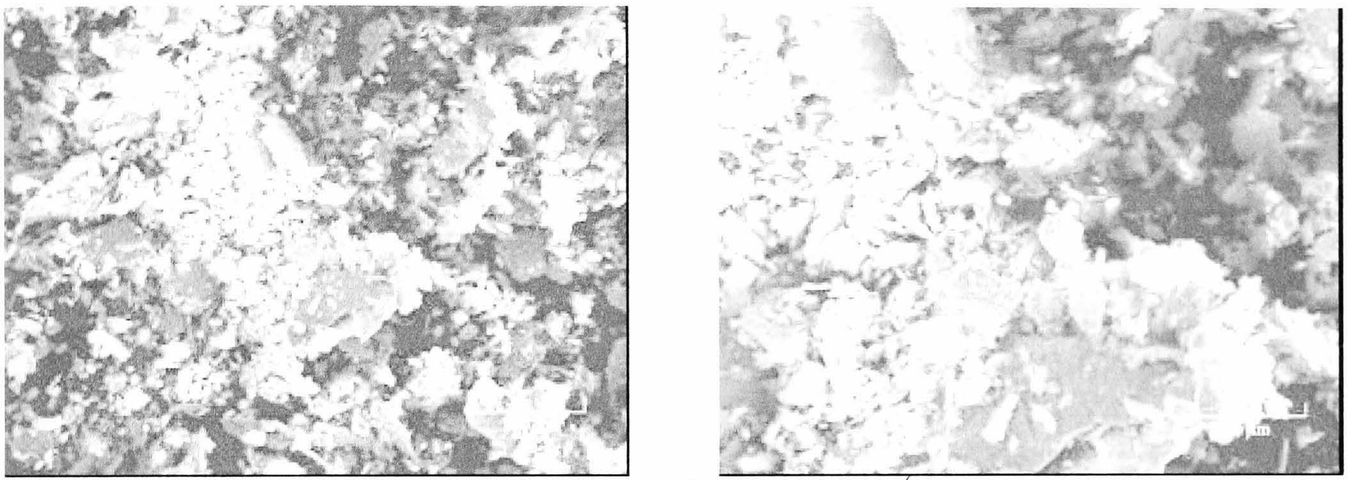

(f) Wear particles, B=1.1T, N=1x10^6

Figure 5.18 Surface and wear particles observations of mild steel discs (10% Slide, SEM) (Continued)

5.3.2 Effect of Magnetic Field Orientation

Wear amounts for different angles θ are shown in Figure 5.19. At θ=0° and 90°, weight losses were increased comparing to that for the absence of magnetic field. However, at θ=45°, the wear amounts were decreased and the overall trend was lower than that for without the magnetic field.

Nevertheless, as seen in Figure 5.20, surface roughness R_a values in the magnetic field are not corresponding to the wear amount. The values for magnetic conditions used were lower than that for without magnetic field. For each angle θ, the differences between them are small and vary around R_a=0.4μm.

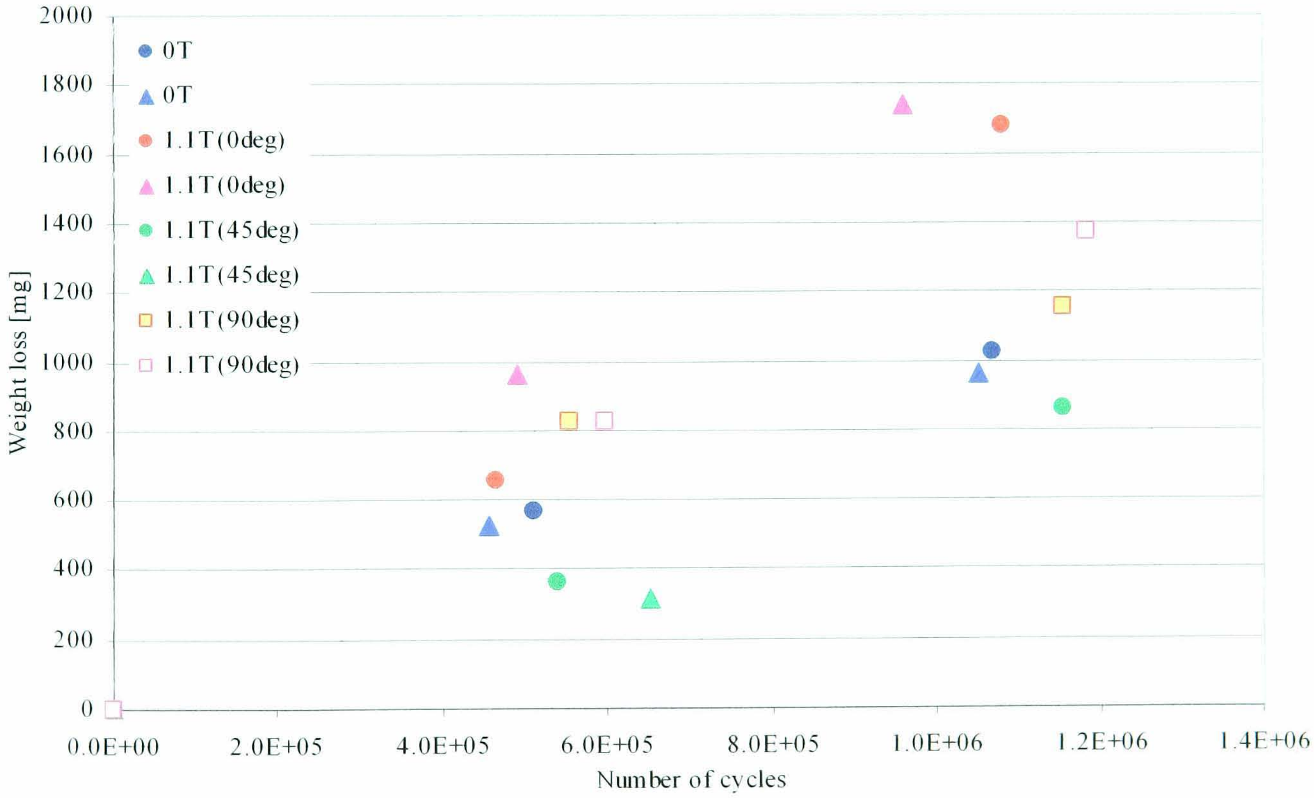

Figure 5.19 Accumulated weight losses of mild steel discs for different angles of θ (10% slide)

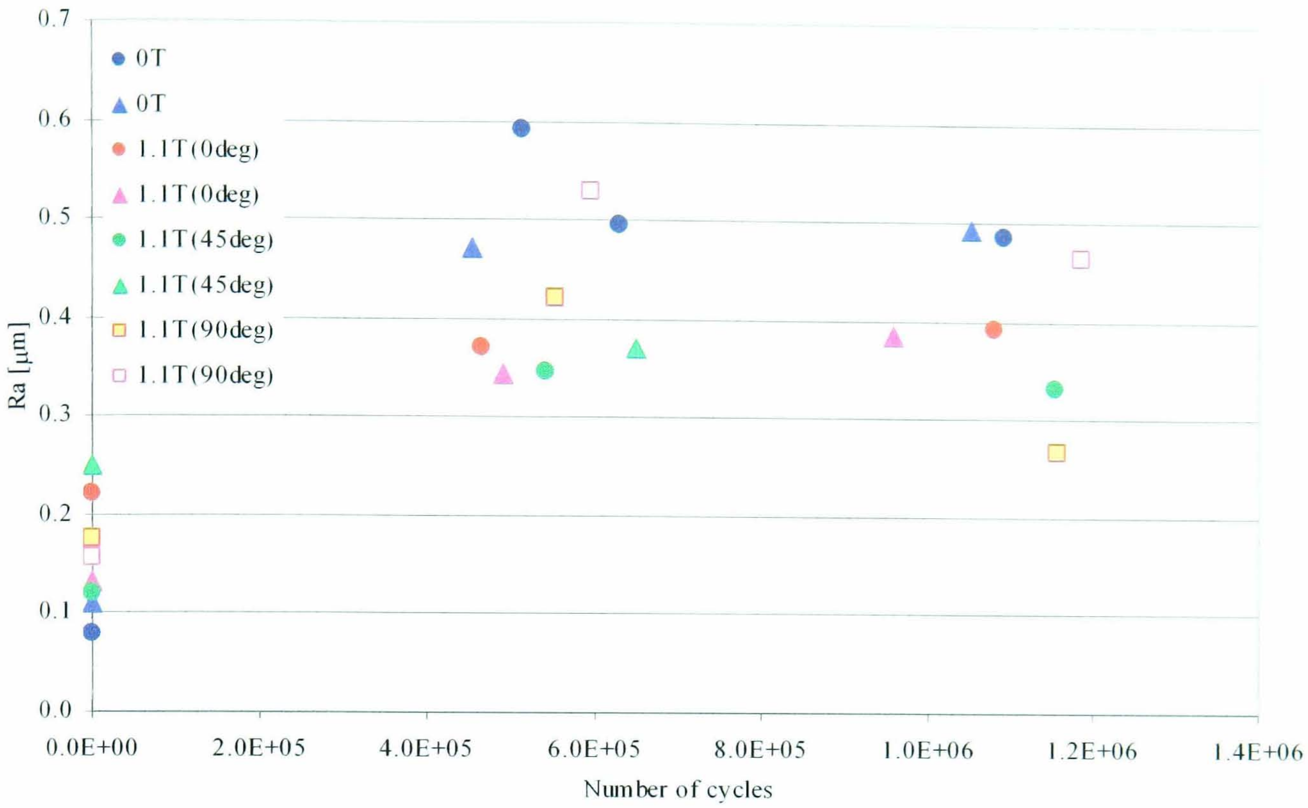

Figure 5.20 Surface roughness of mild steel discs for different angles of θ (10% Slide)

Surface observations under the optical microscope for different angles θ are shown in Figure 5.21. Plastically deformed top layers and stripe marks can be seen for all test conditions used and there is not much difference between them. Even SEM observations hardly reveal any differences in the surface appearance. The differences in wear particle appearances, produced at different magnetic field angles θ, are shown in Figure 5.22. At angles θ=0° and θ=45°, finer wear particles were observed. However, at the angle θ=90°, thin but larger flake shaped particles were observed. Even if compared to wear particles produced without the magnetic field their sizes are still larger. This trend is similar to the results obtained for pure rolling at different angles θ.

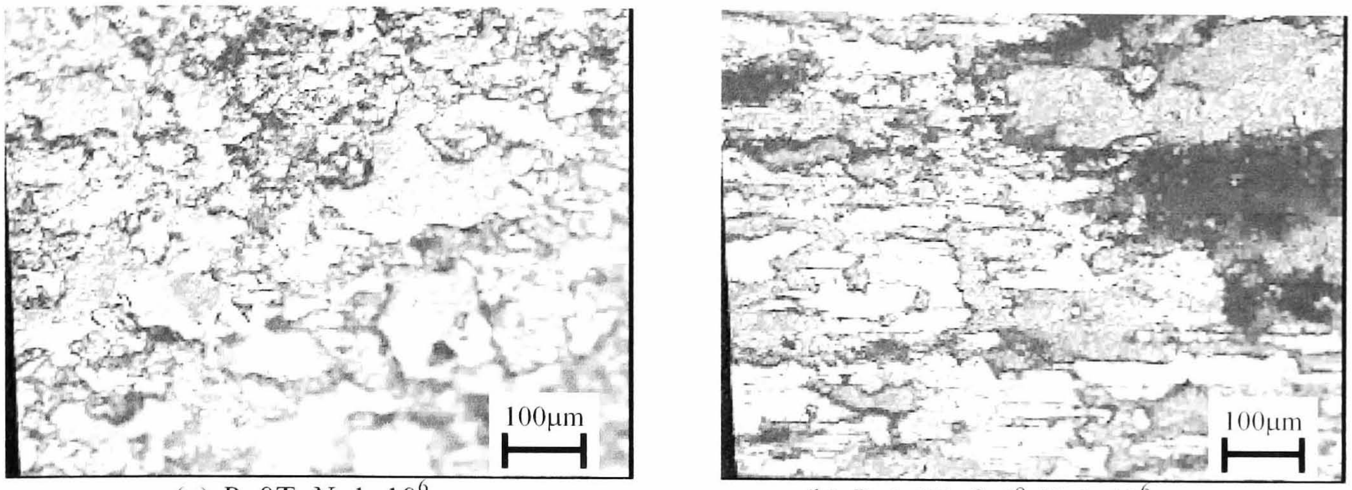

(a) B=0T, N=1x10^6 (b) B=1.1T, θ=0° N=1x10^6

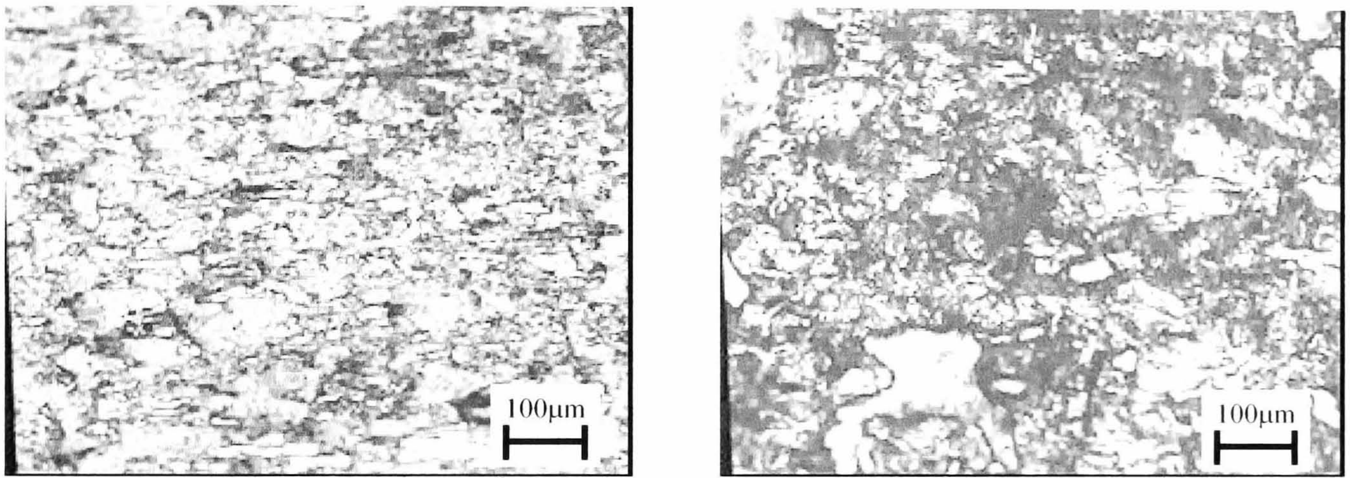

(c) B=1.1T, θ=45° N=1x10^6 (d) B=1.1T, θ=90° N=1x10^6

Figure 5.21 Surface observations of mild steel discs for different angles of θ (10% slide; Optical Microscope).

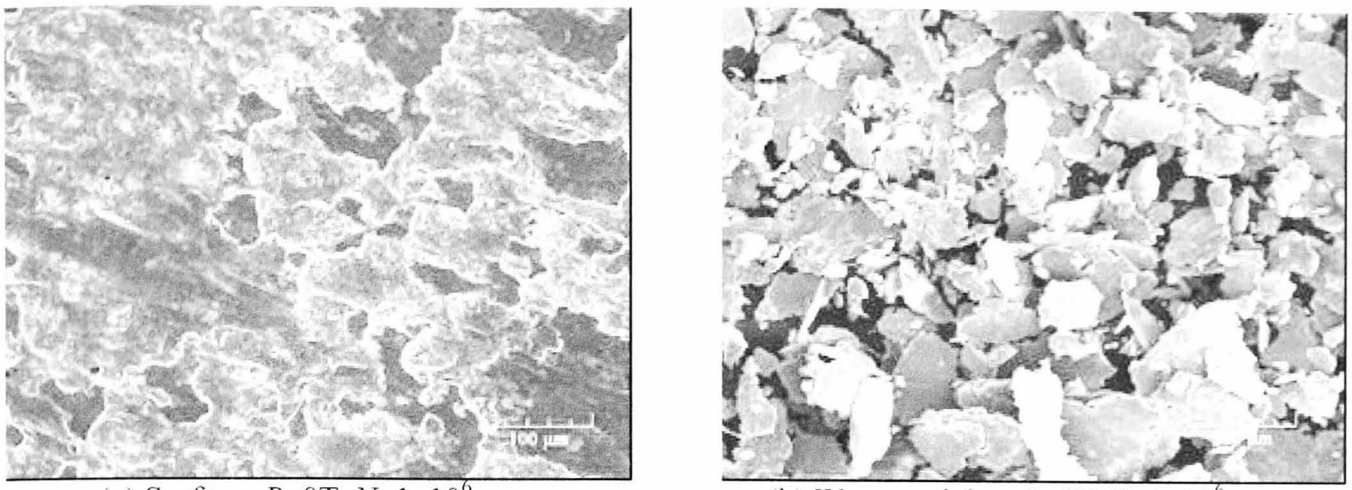
(a) Surface, B=0T, N=1x10^6 (b) Wear particles, B=0T, N=1x10^6

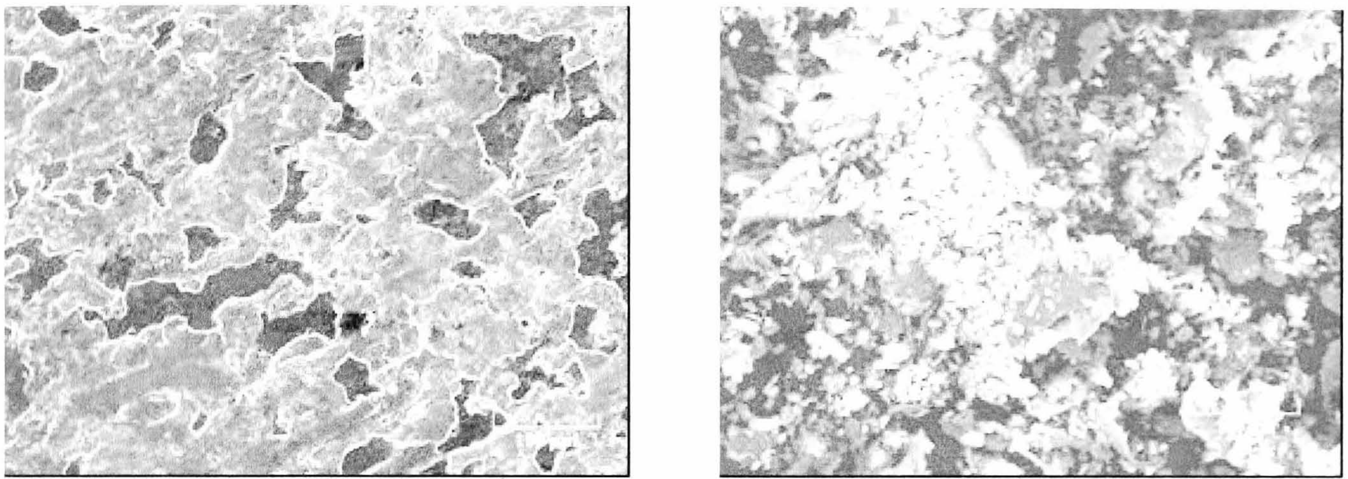
(c) Surface, B=1.1T, θ=0°, N=1x10^6 (d) Wear particles, Surface, B=1.1T, θ=0°, N=1x10^6

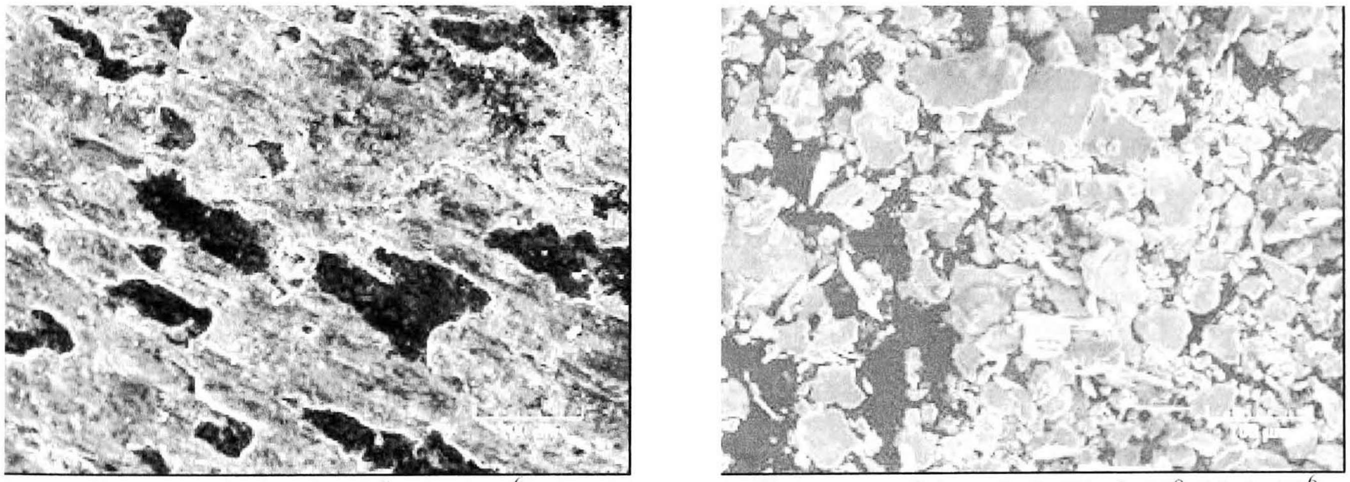
(e) Surface, B=1.1T, θ=45°, N=1x10^6 (f) Wear particles, B=1.1T, θ=45°, N=1x10^6

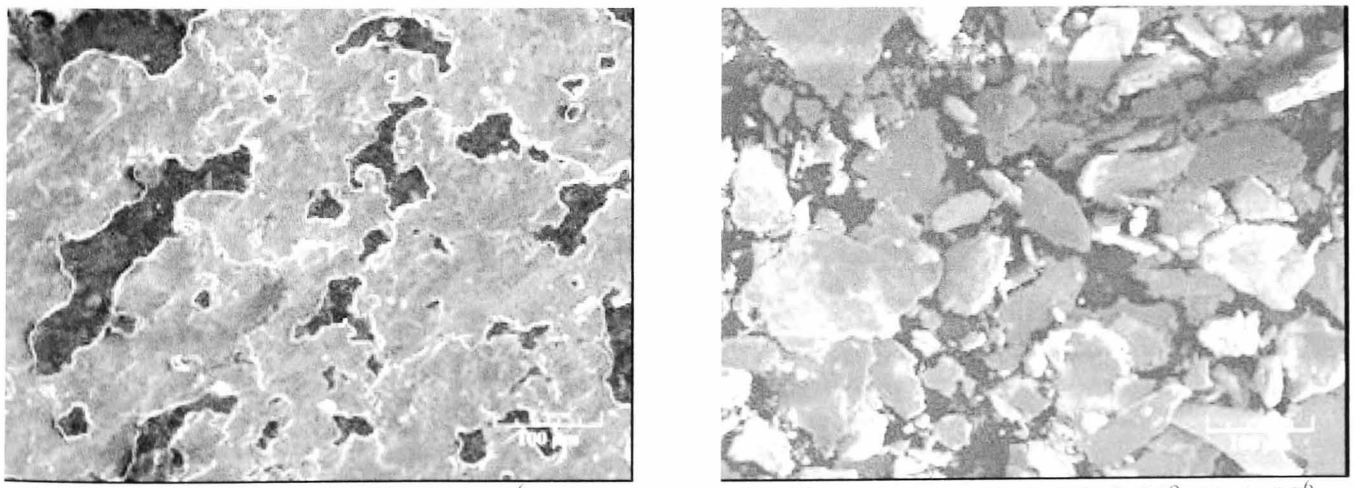
(g) Surface, B=1.1T, θ=90°, N=1x10^6 (h) Wear particles, B=1.1T, θ=90°, N=1x10^6

Figure 5.22 SEM observations of mild steel discs for different angles of θ (10% slide)

5.3.3 Effect of Magnetic Field on Sliding Wear

Results of rolling and rolling with sliding tests, confirm that the characteristics of pure rolling fatigue and rolling with sliding wear were changed due to the effects of the magnetic field. However, the wear amounts resulting from magnetic field effects were completely different. For instance, wear amount was decreased under pure rolling and increased under rolling with sliding. Therefore, tests in the magnetic field under pure sliding were conducted in order to evaluate the effect.

Testing was carried out in the same test apparatus and the same specimens were used. To make the specimen slide without rolling, the driven disc was immobilised. Two magnetic field densities, B=0.4T and 1.1T, and three magnetic field angles, θ=0°, 45°, and 90° were utilised. Other test conditions that is the load on the contact and rotational speed of the driving disc were the same as for the rolling test. All measurements were taken after 60 minutes of testing. The sliding distance corresponding to that test duration was 4200m. To evaluate the effect of magnetic field, measurements of weight loss of the driven disc and inspections of the disc surface and morphology of wear particles were carried out.

Figure 5.23 shows that the magnetic field presence and magnetic field density cause the increase in wear. Similar trend was observed for rolling with sliding.

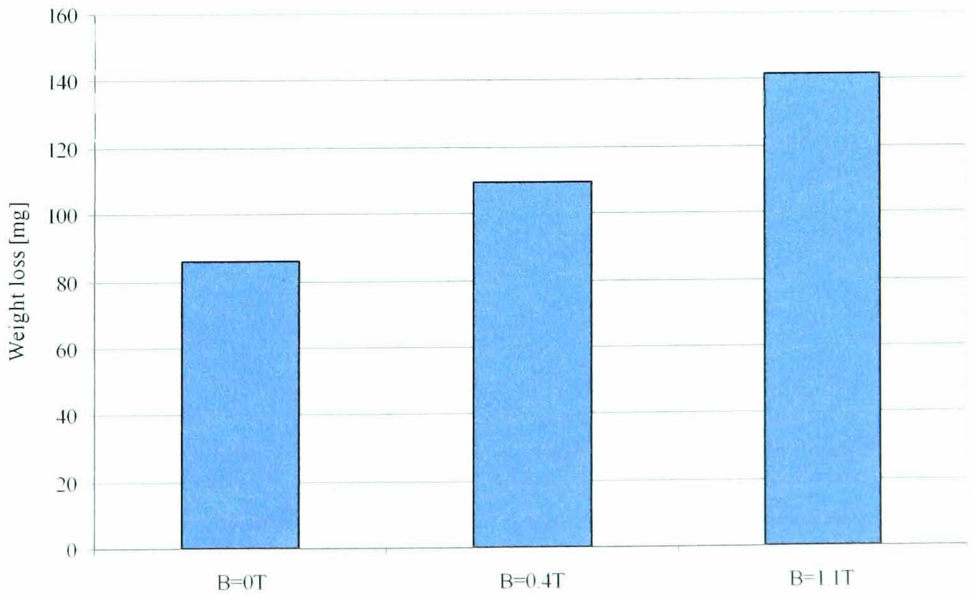

Figure 5.23 Weight losses recorded during sliding tests

Surface asperities of the driven disc had traces of plastic deformation as evidenced by the SEM images shown in Figure 5.24. Pure sliding under the horizontal magnetic field with density of B=0.4T produced more extensive deformations comparing to rolling with sliding. Also, finer wear particles were observed under pure sliding with the magnetic field present.

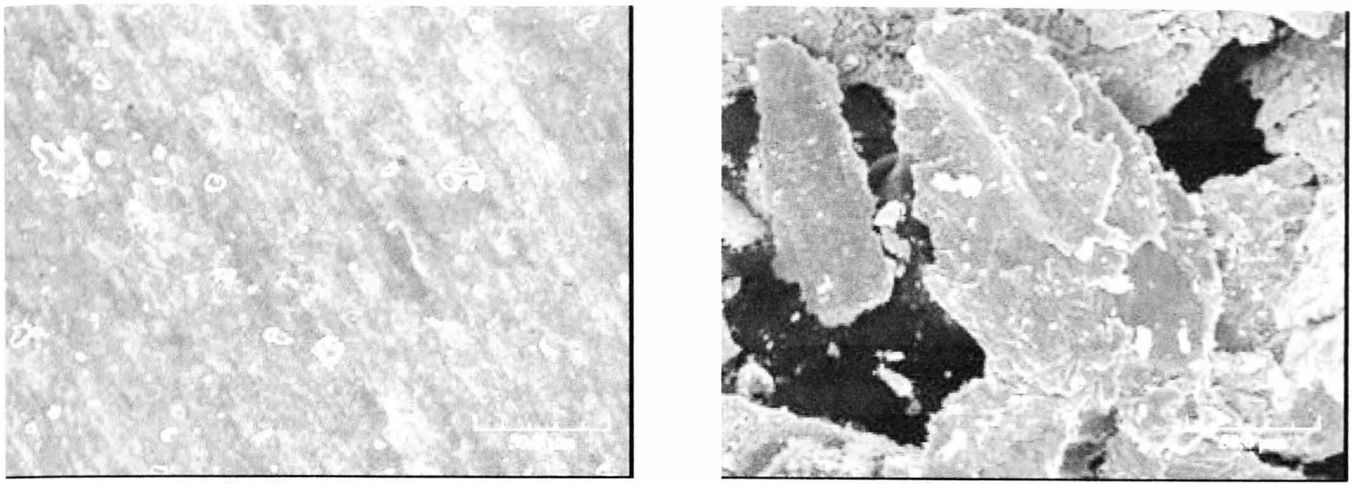

(a) Surface, B=0T (b) Wear particles, B=0T

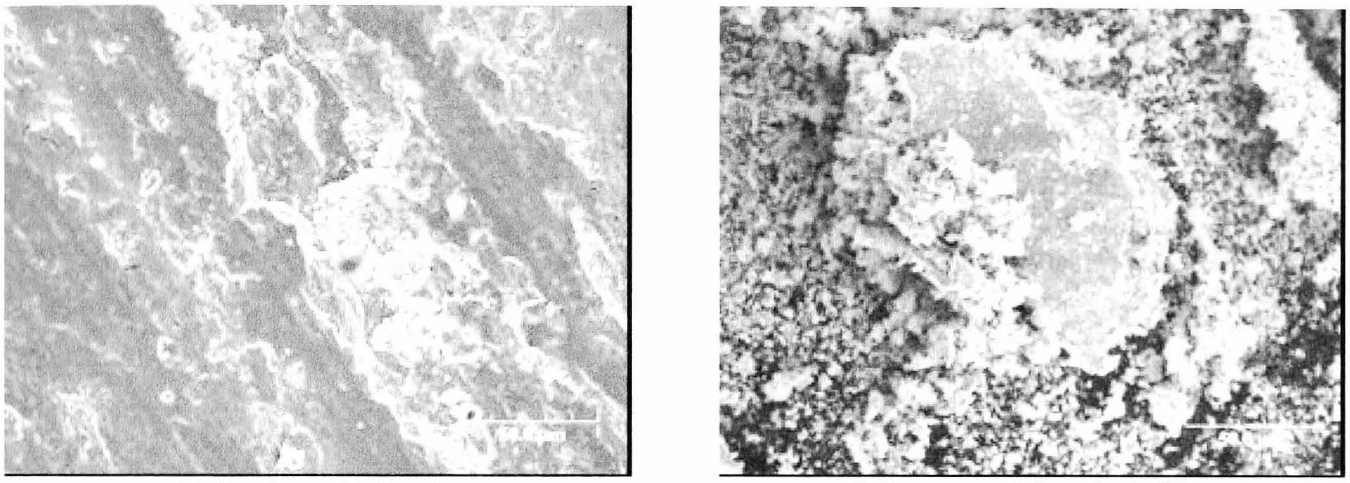

(c) Surface, B=0.4T (d) Wear particles, B=0.4T

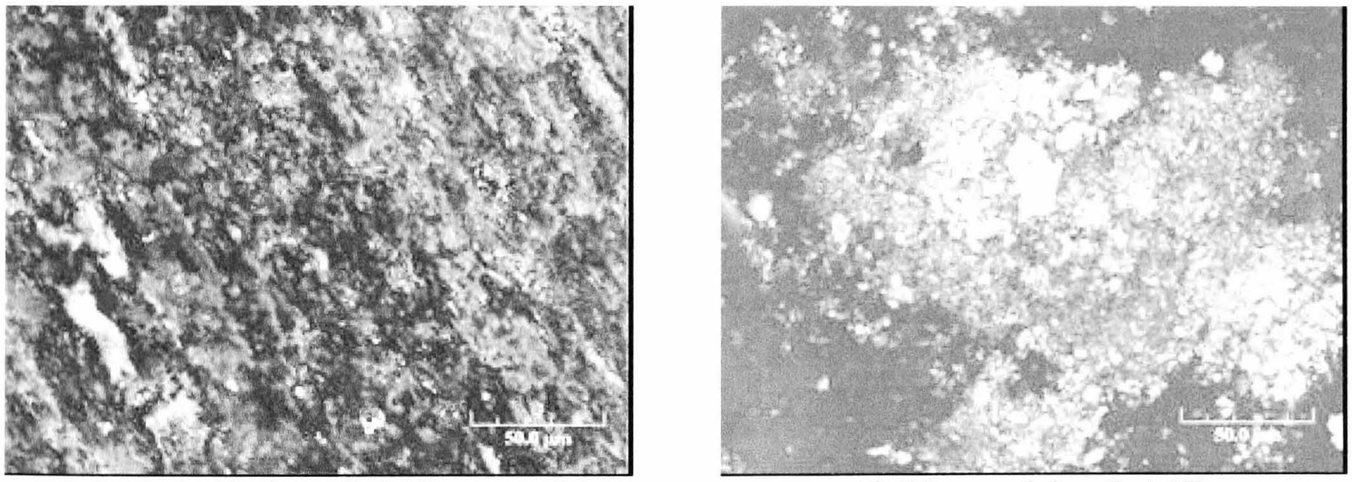

(e) Surface, B=1.1T (f) Wear particles, B=1.1T

Figure 5.24 Surface observations of mild steel discs in sliding tests (SEM)

In rolling with sliding tests, wear amount was varied due to the magnetic field direction and it was lowest at θ=45°. Figure 5.25 shows the results. Wear amounts were highest at angles θ=0° and 90°. Lowest wear amount was observed at θ=45° and it was smaller than that obtained for the absence of magnetic field.

Surface and wear particle observations revealed remarkable differences in the size of wear particles. As shown in Figure 5.26, largest particles were produced at B=0T and θ=90° when magnetic field density B=1.1T. Smallest particles were generated when θ=0° and θ=45° at B=1.1T.

Results obtained from rolling with sliding and pure sliding tests, allow the statement that characteristics of wear under these contact conditions are influenced by the direction of the magnetic field. At angles θ=0° and 90°, wear amount of the driven disc was increased but decreased at the angle θ=45°. However, finer wear particles were observed at θ=0° and 45°.

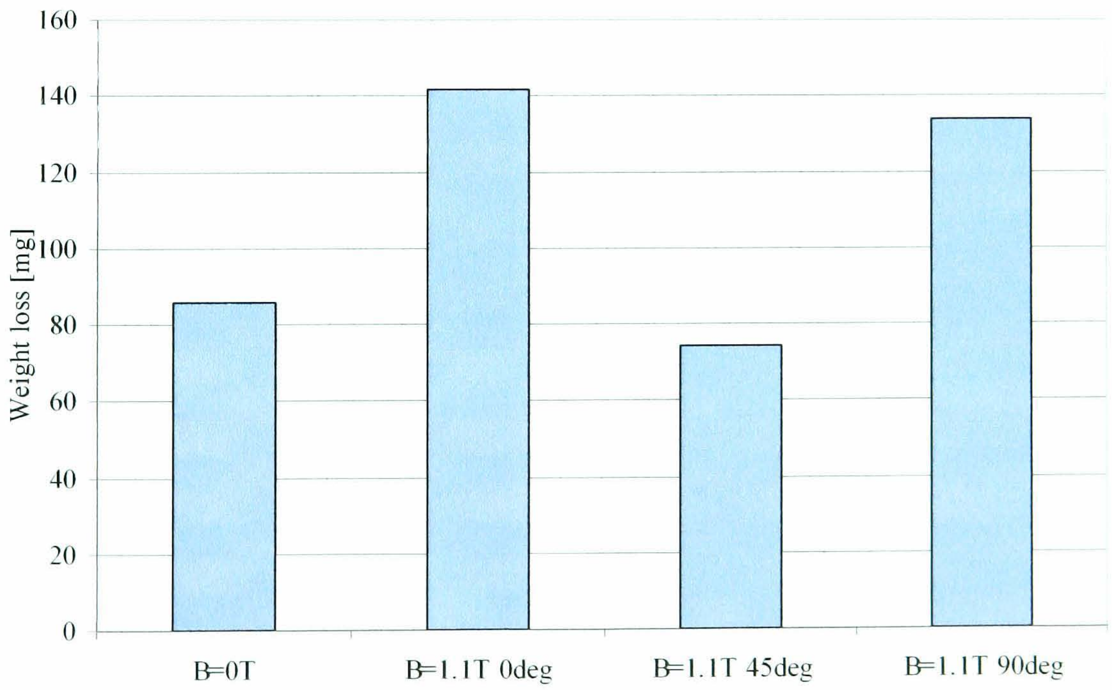

Figure 5.25 Weight losses of mild steel discs at different angles of θ (Sliding).

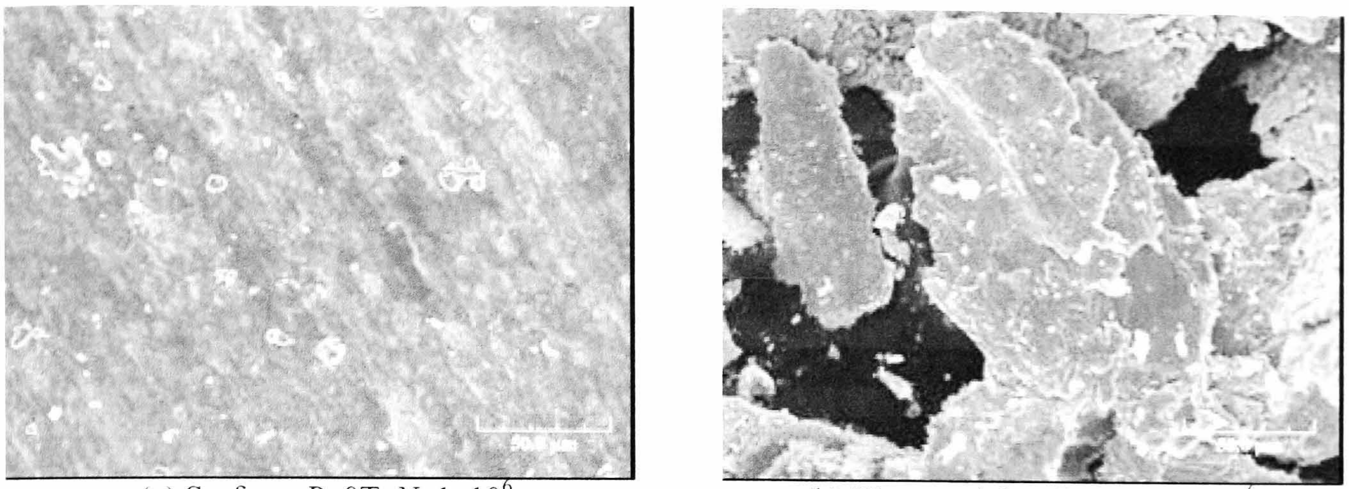

(a) Surface, B=0T, N=1x10^6 (b) Wear particles, B=0T, N=1x10^6

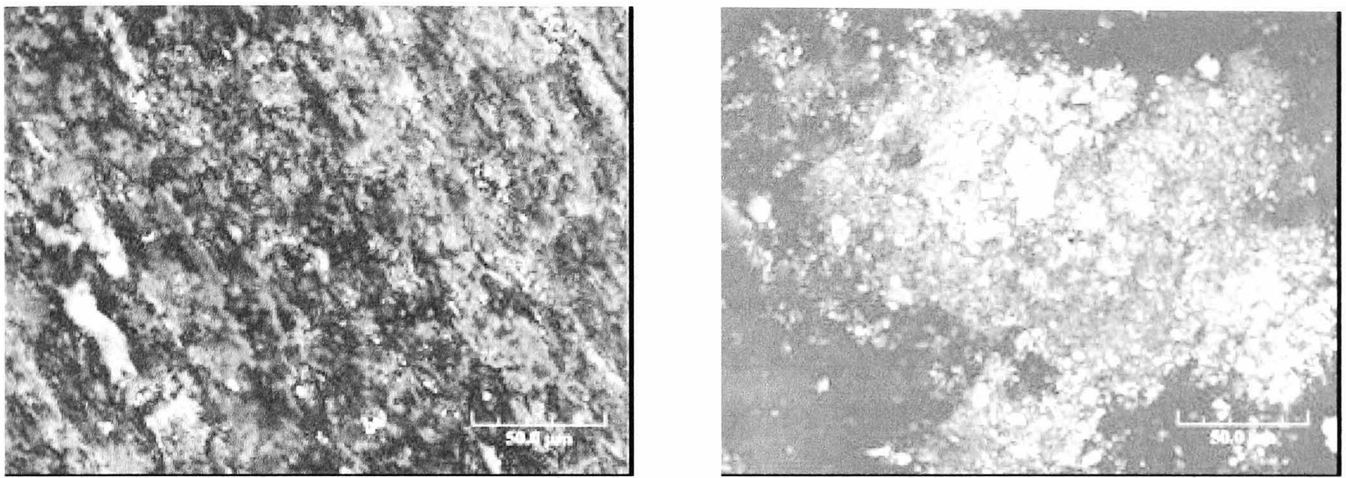

(c) Surface, B=1.1T, θ=0°, N=1x10^6 (d) Wear particles, Surface, B=1.1T, θ=0°, N=1x10^6

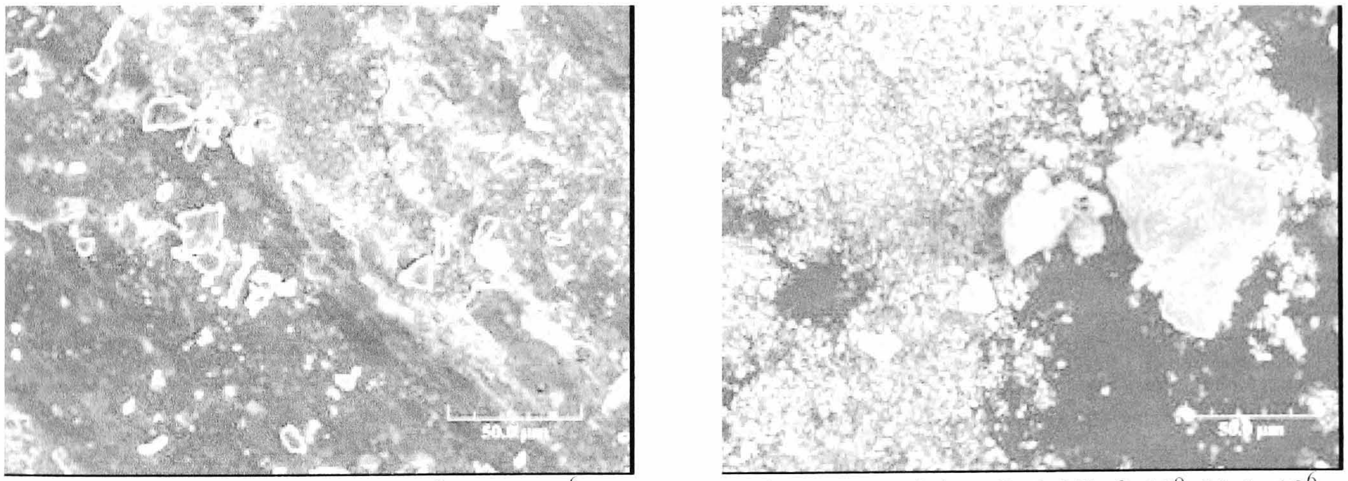

(e) Surface, B=1.1T, θ=45°, N=1x10^6 (f) Wear particles, B=1.1T, θ=45°, N=1x10^6

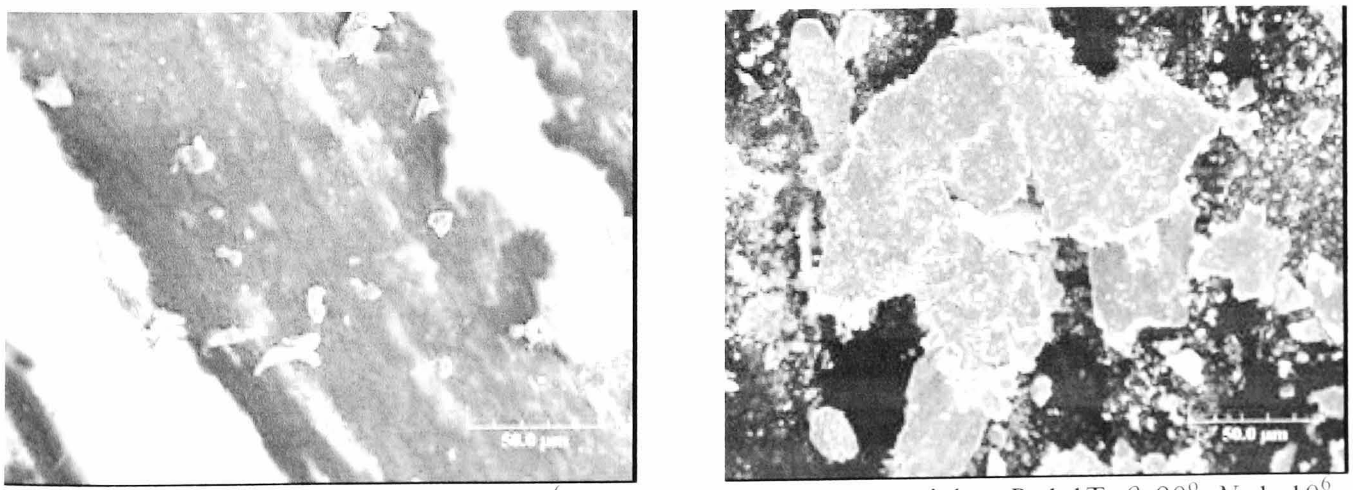

(g) Surface, B=1.1T, θ=90°, N=1x10^6 (h) Wear particles, B=1.1T, θ=90°, N=1x10^6

Figure 5.26 Surface observations of mild steel discs at different angles of θ (Sliding).

Chapter 6 Discussion

6.1 Introduction

This chapter presents likely reasons why a magnetic field affects rolling contact. It is organised into five main sections. First a summary of experimental results and their common trends is presented. The second section contains discussion of the results. The third section presents analysis of the contact conditions without magnetic field using ANSYS. The fourth section describes rolling contact characteristics under the magnetic field. And finally the fifth section suggests the mechanisms of magnetic field effect on a rolling contact utilizing magnetisation and crack initiation model involving dislocation behaviour.

6.2 Experimentally Observed Effects of the Magnetic Field

As a summary of results based on various effects of the magnetic field experimentally observed:

1) Wear

   Wear amount of the discs was decreased in pure rolling contact. However, the wear amount was increased in rolling with sliding contact.

2) Surface asperity

   Surface roughness R_a of the discs was reduced and thinner wear particles were observed. Thickness of wear particle produced in the presence of magnetic field was approximately 5μm while in the absence of magnetic field it was approximately 20μm.

3) Changes due to the rotational speed and direction of magnetic field

   Effect of magnetic field was less pronounced at lower rotating speeds and was varied for 0°, 45°, and 90° magnetic field directions.

6.3 Contact Conditions without Magnetic Field

As mentioned in Chapter 2, the mechanisms of crack initiation at rolling contact are mainly classified as surface crack and subsurface crack. From the thin, plate shaped particles observed during testing, shown in Figure 5.4, the cracks are supposed to be initiated at subsurface. Furthermore, it is accepted that softer materials, such as EN1A free cutting steel, have tendency to generate subsurface cracks (1). Thus, the cracks created during the tests can be assumed to be initiated from the subsurface region and stress status near the surface is considered in connection with subsurface crack initiation mechanism.

To analyse the stress status, the models shown in Figure 4.3 and 4.7 were utilised. The contact load on the driven disc P was set to 150N and the tangential load Q, applied to the driving disc was varied from 0N to 75N. Therefore, the value of μ, defined by Q/P, corresponds to 0 and 0.5.

Contact stress distribution at the centre of the discs and μ=0.3 is shown in Figure 6.1. The maximum contact pressure p_0 for all of the tangential load conditions was 265MPa and it corresponds to $1.09\sigma_y$ for EN1A steel. Comparing the value to the shakedown theory, yield at a rolling contact occurs when p_0=$1.79\sigma_y$, while the maximum contact pressure in the experiments is only 61% of that value. This means that the maximum contact pressure is not sufficiently high to cause yielding. Distributions of von Mises' stress τ_R for different tangential load conditions are presented in Figure 6.2. It can be seen that the region of the maximum value of τ_R is moved, gradually, to the surface by applying tangential load. Figure 6.3 shows ratio of the maximum shear strain-energy and the maximum contact pressure τ_R/p_0 as a function of depth. At the condition of μ=0, the maximum value of the ratio τ_R/p_0 varies from 0.334 to 0.344 and is located at the depth of 40-80μm. According to the Hertz's theory, the maximum value of τ_R/p_0 is 0.322 at the depth of 63.2μm. Also, the value of the ratio near the surface was increased by applying tangential load. Specifically, at the condition of μ=0.5, the ratio of τ_R/p_0 at the surface and at the depth of 40μm was 0.457 and 0.396 respectively. Therefore, it is considered that the crack initiation point is moved towards the surface due to the tangential load. This can be especially true for an unlubricated contact such as that used in this study.

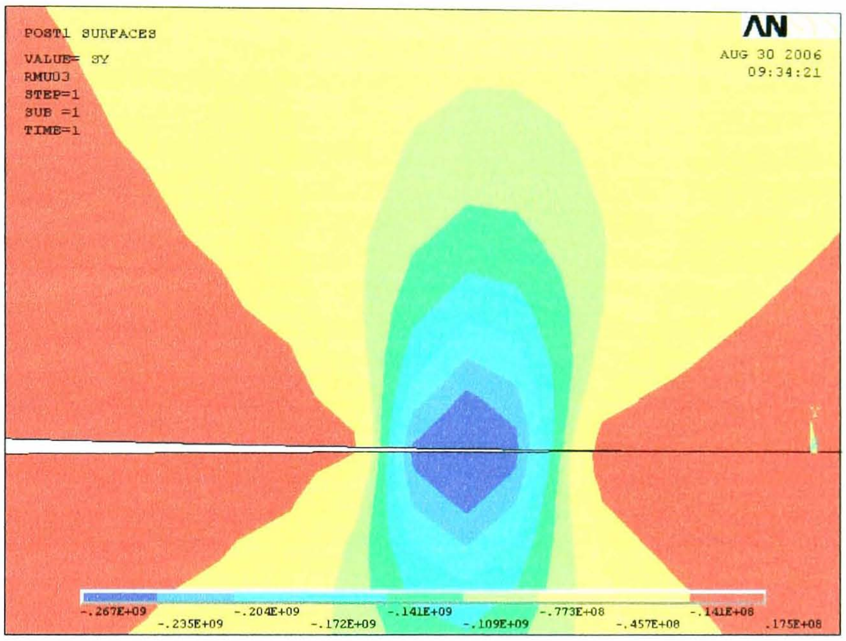

Figure 6.1 Contact stress distributions of the discs (Pure Rolling, P=150N, μ=Q/P=0.3)

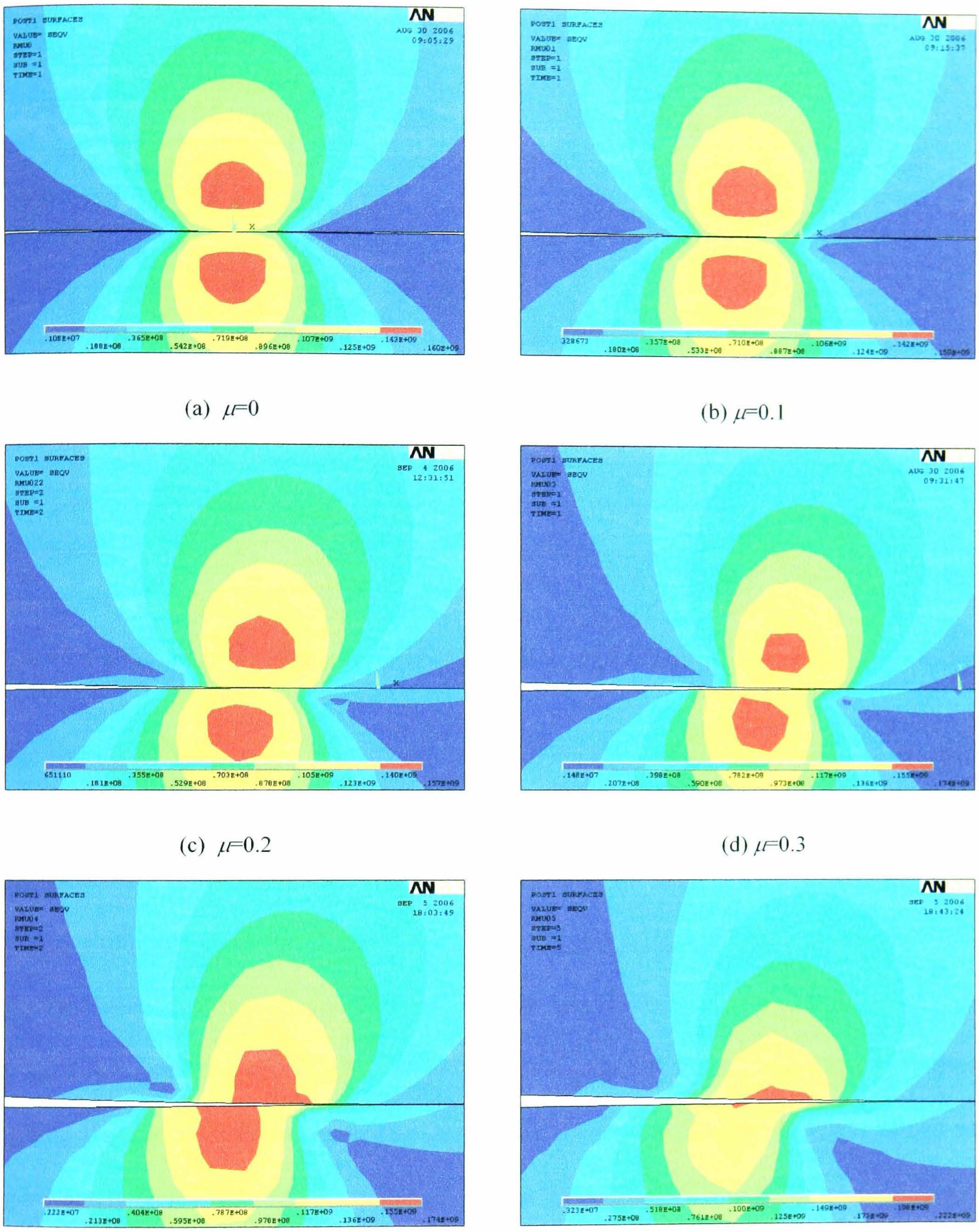

(a) μ=0

(b) μ=0.1

(c) μ=0.2

(d) μ=0.3

(e) μ=0.4

(f) μ=0.5

Figure 6.2 Von Mises' stress distributions in the discs (Pure Rolling)

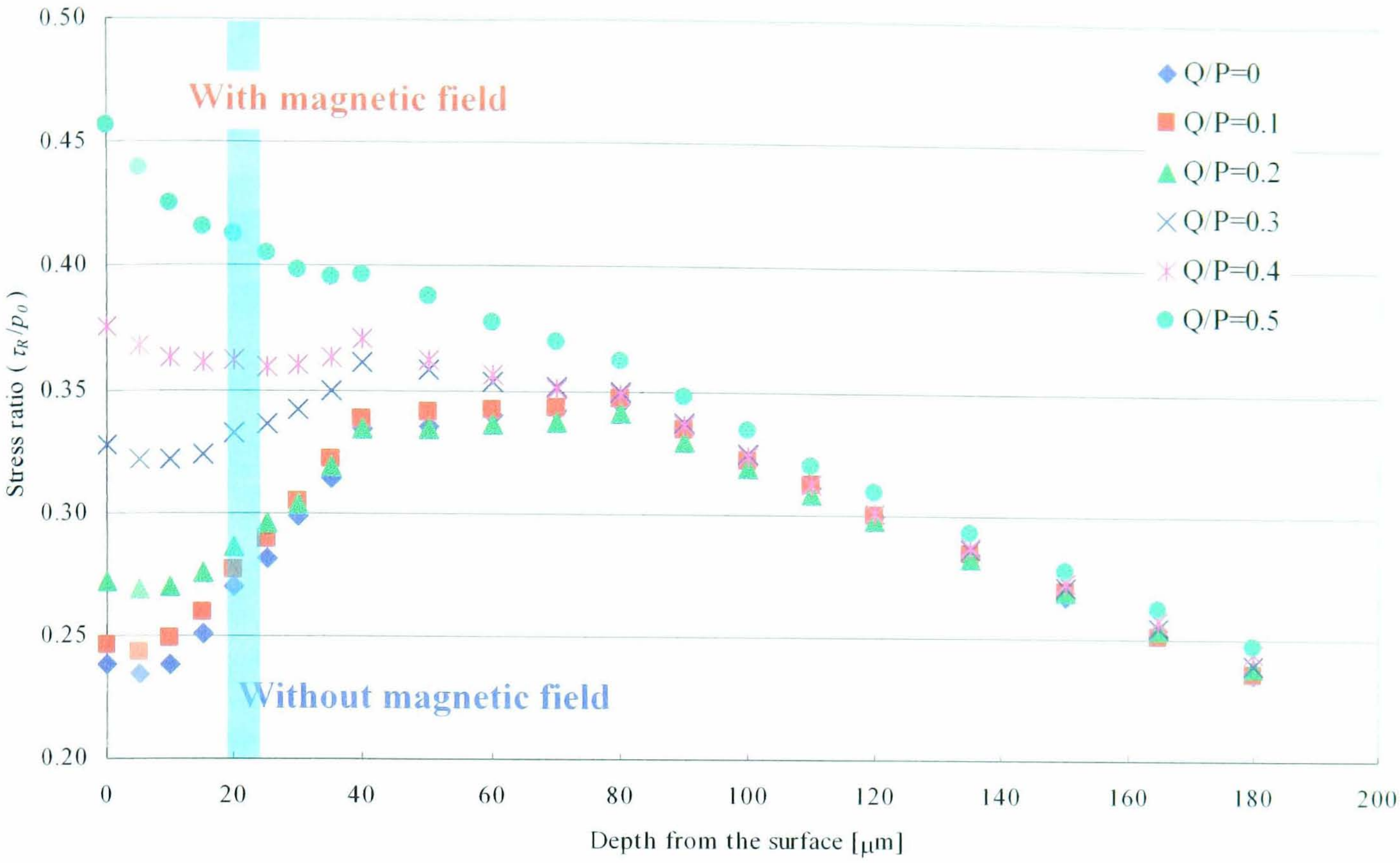

Figure 6.3 Stress distributions of τ_R/p_0 at subsurface and crack initiation points (Pure Rolling)

On the other hand, for crack initiation and dislocation movement, according to several dislocation models described in Section 2.4, dislocation pileup and energy accumulation are both needed for crack initiation. Therefore, when dislocations are piled up, crack could be initiated. From this viewpoint, Chin (3) explained that at a Hertzian contact, dislocations move from the region of strong shear stress gradient towards the region of weak gradient as shown in Figure 6.4. Applying this mechanism to the contact condition used in this study, gradient of τ_R along the depth measured from the surface within the contact region and obtained from Figure 6.3 is shown in Figure 6.5 (a)-(f). It can be seen from the diagrams that there are discontinuous points at the depths of about 20μm, 40μm, and 80μm for all conditions. Comparing this to the experimental results, at the depth of 20μm a possible crack initiation point was observed during testing and corresponds to a discontinuous point at this depth. It can be suggested, therefore, that dislocations could be piled up at that point. Thus, if crack initiation is ruled by dislocation, which, in turn, is controlled the gradient of τ_R, it could be possible that the crack initiates at the depth of 20μm. However, to initiate the crack, fixed shear strain-energy satisfying plastic deformation criterion, $k=\sigma_Y/\sqrt{3}=0.529p_0$, is needed but the value obtained from the analysis was insufficient even if $\mu=0.5$.

Such differences were also observed in other studies. According to Miyoshi (2), rolling contact fatigue occurred even if the amplitude of the maximum contact pressure was below the yield point. As possible reasons, he proposed effects of plastic deformation due to surface asperity or edge of a disc or residual stress creation within the specimens.

In order to justify crack initiation at the depth of 20μm the argument that maximum contact pressure is increased due to the surface roughness or plastic deformation at the edge of the disc would have to be accepted.

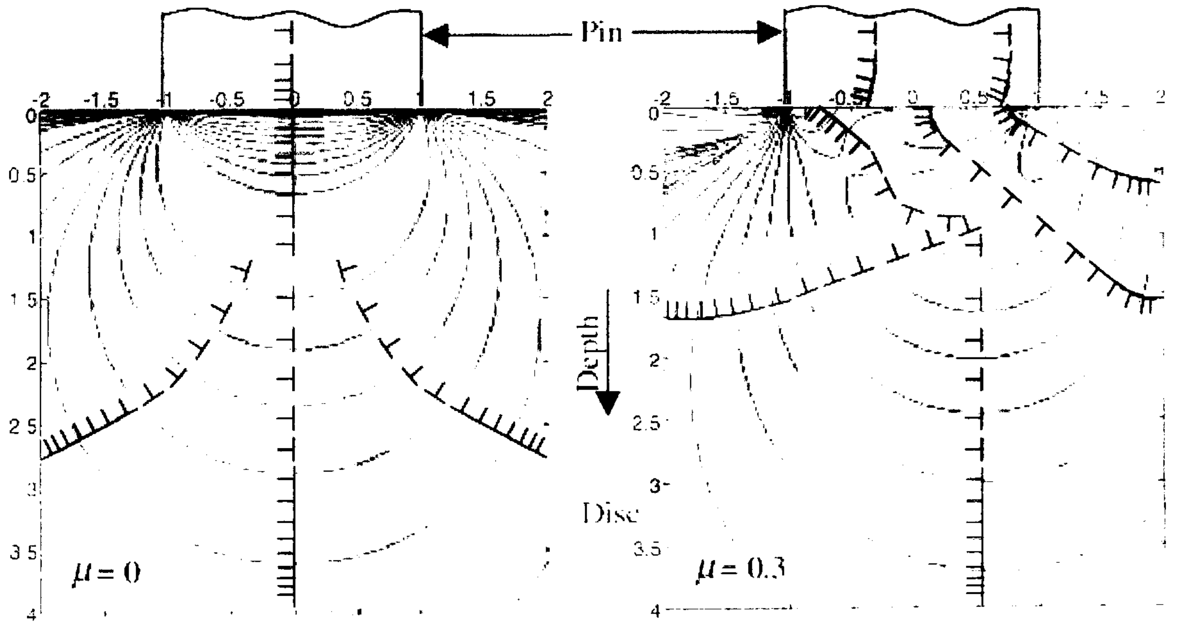

Figure 6.4 Distribution of shear stress and pileup of dislocations near the contact surface (3)

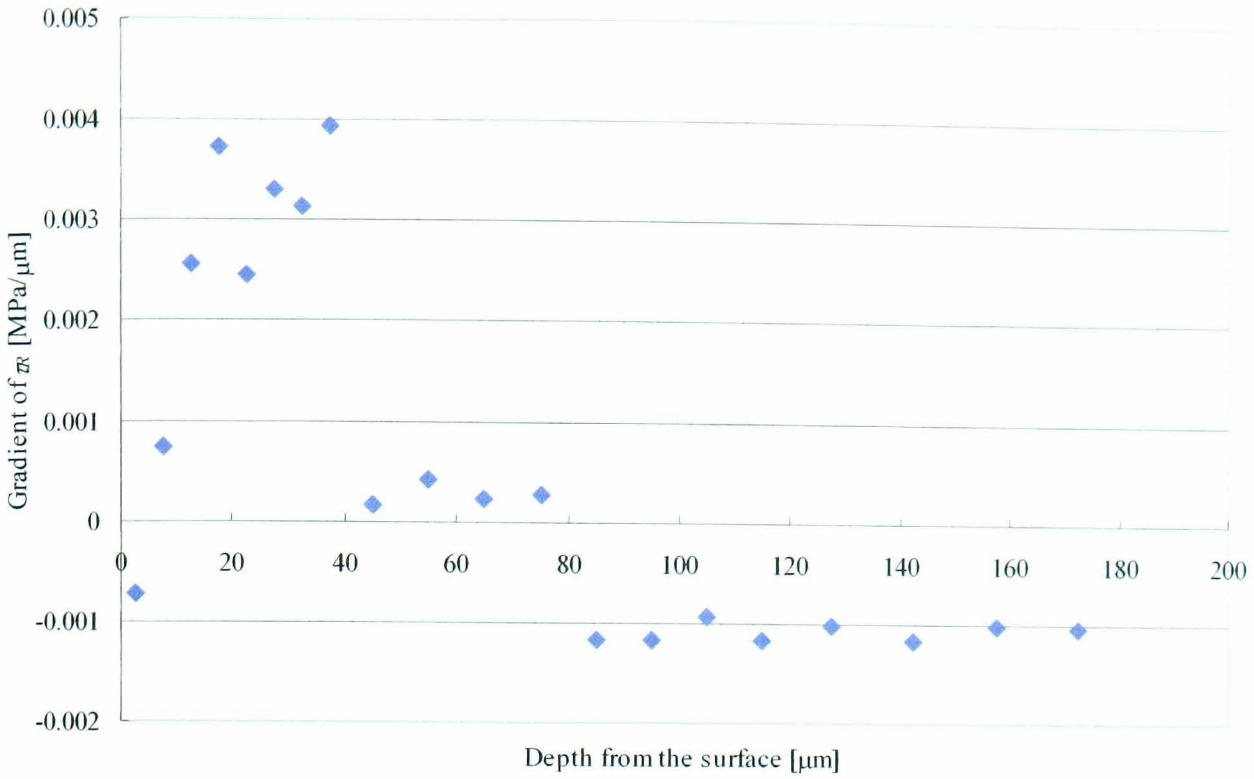

(a) *Q*/*P*=0

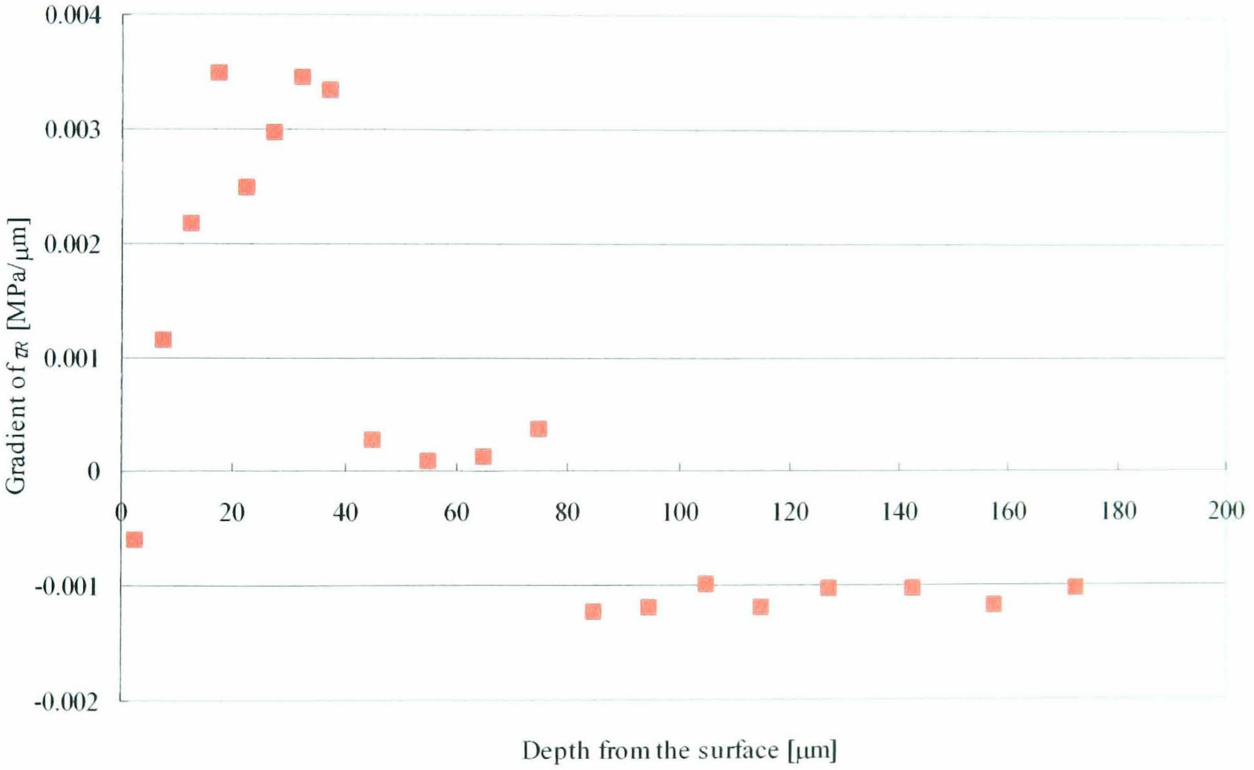

(b) *Q*/*P*=0.1

Figure 6.5 Von Mises' stress gradients at contact region (Pure Rolling)

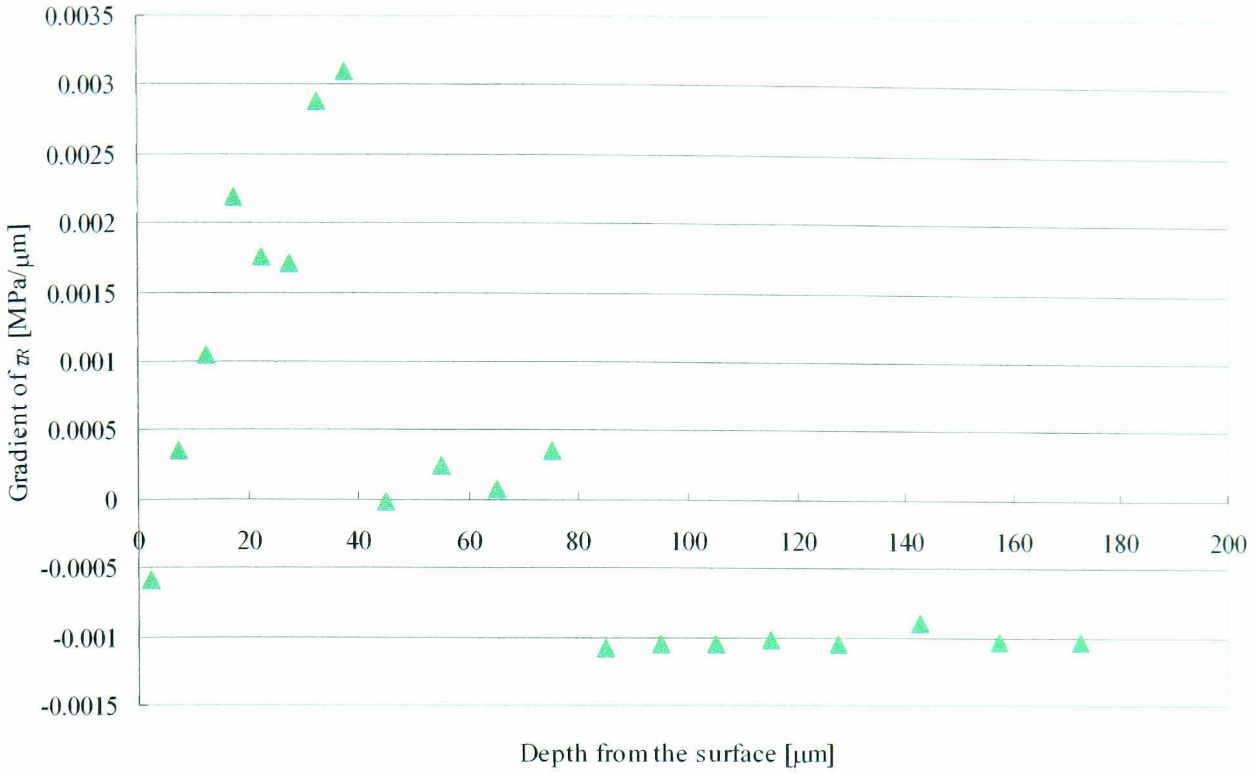

(c) *Q*/*P*=0.2

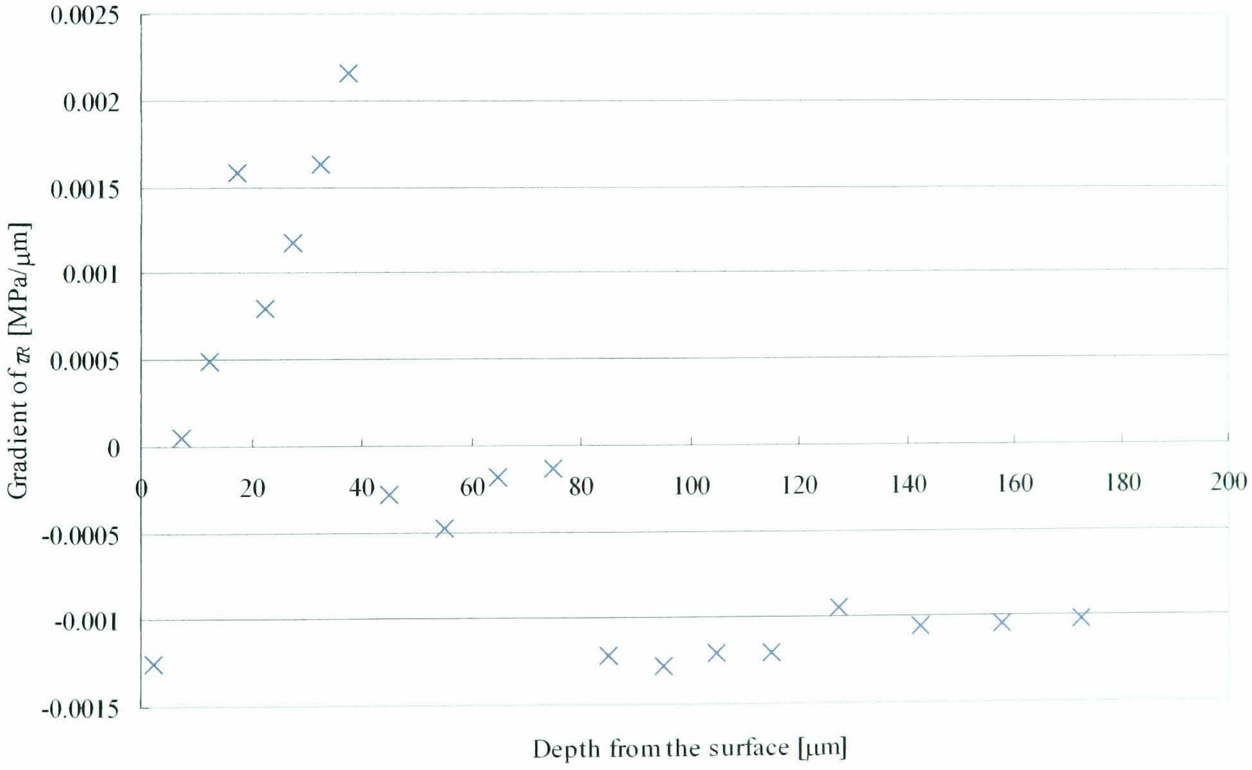

(d) *Q*/*P*=0.3

Figure 6.5 Von Mises' stress gradients at contact region (Pure Rolling)
(Continued)

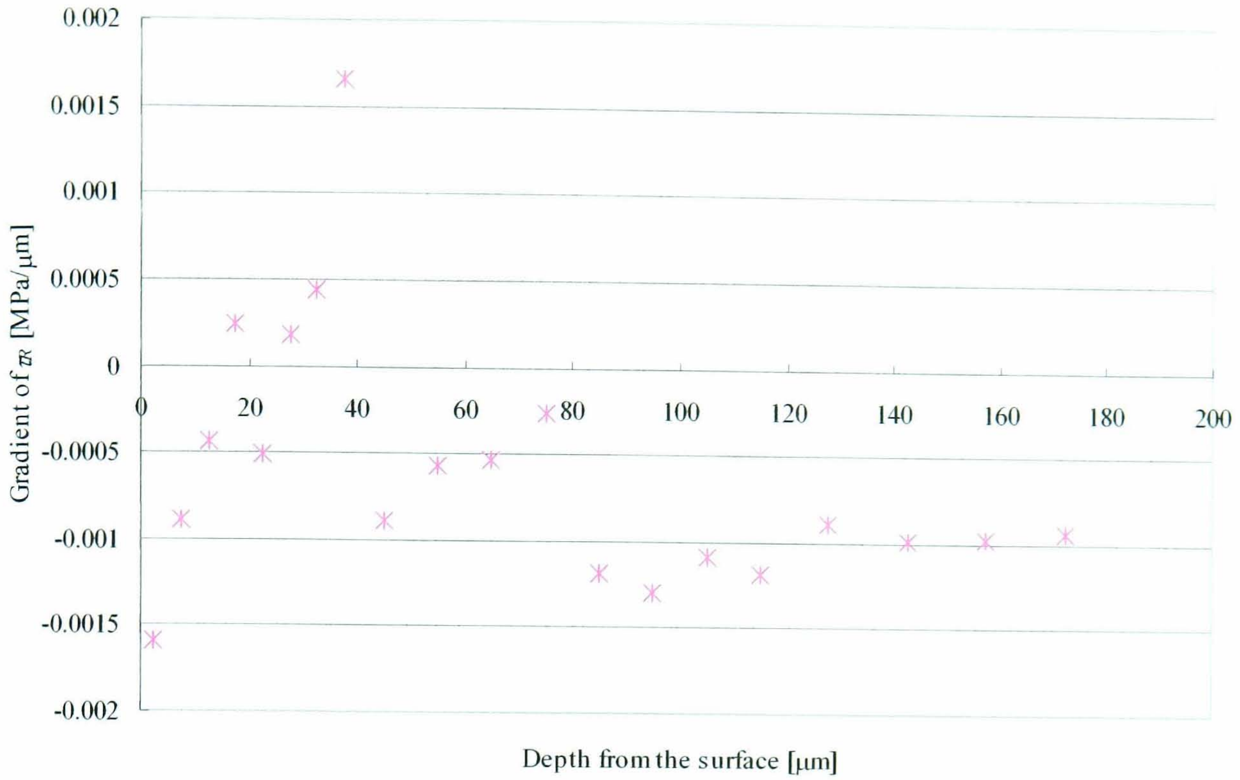

(e) *Q*/*P*=0.4

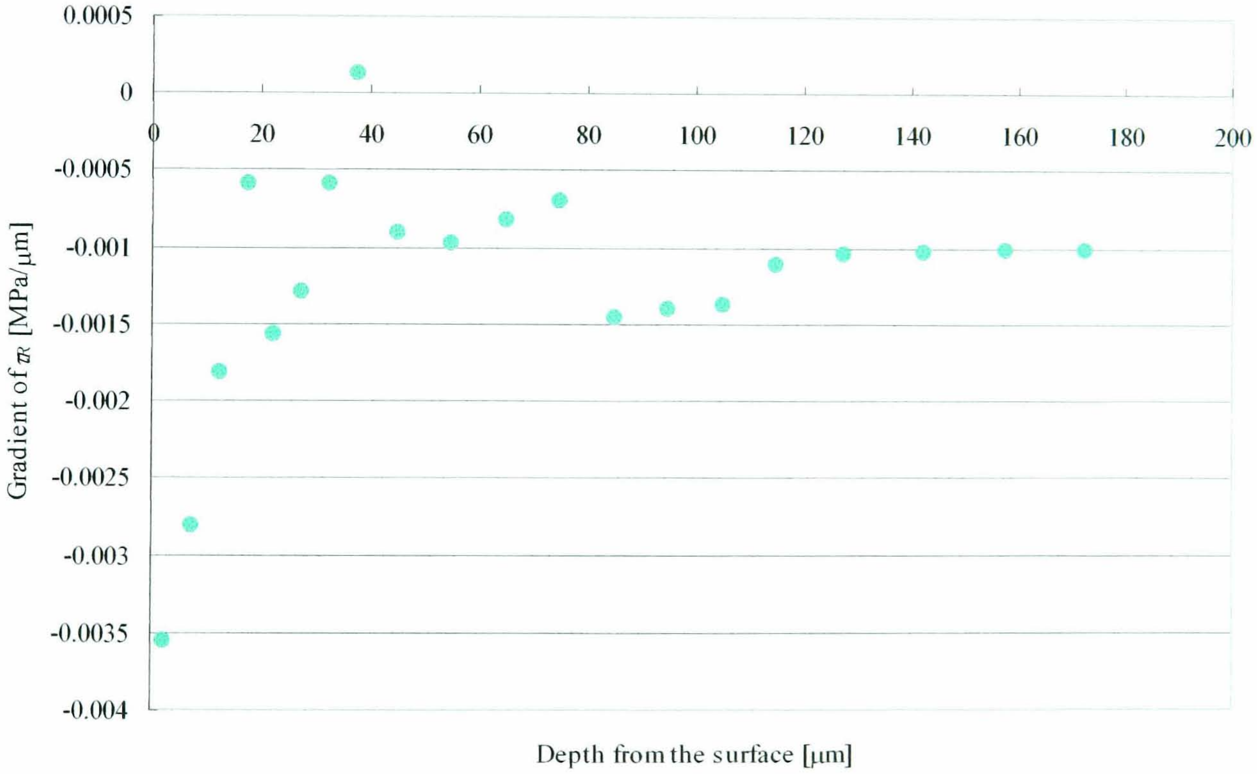

(f) *Q*/*P*=0.5

Figure 6.5 Von Mises' stress gradients at contact region (Pure Rolling)
(Continued)

For the analysis of rolling with sliding contact condition, the same load on the contact as that for the pure rolling was applied. Contact stress distribution at the centre of the disc and μ=0.3 is shown in Figure 6.6. The maximum contact pressure p_0 was 282MPa and it corresponds to $1.16\sigma_Y$, which was 6% higher than that for the pure rolling due to the narrower contact area. However, this value is still insufficient to cause yielding. Therefore, effects such as residual stresses are supposed to be involved.

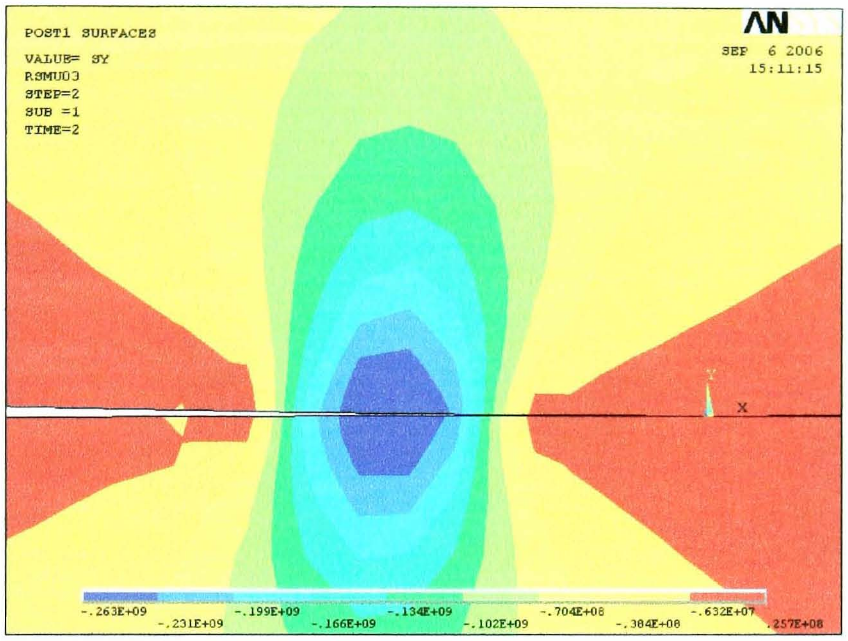

Figure 6.6 Contact pressure distributions of the discs (10% Slide, P=150N, μ=Q/P=0.3)

At the pure rolling condition, crack initiation point is considered to be moved towards the surface by a tangential load. As shown in Figure 6.7, this tendency is quite noticeable when the driven disc was turned about its vertical axis. Comparing the distribution of von Mises' stress obtained for the pure rolling and rolling with sliding, the tendency was clearly observed above μ=0.3. Therefore, it can be suggested that the crack initiation point was moved towards the surface due to the contact condition and this is also confirmed by wear particles morphology shown in Figure 5.4(b) and Figure 5.18(b).

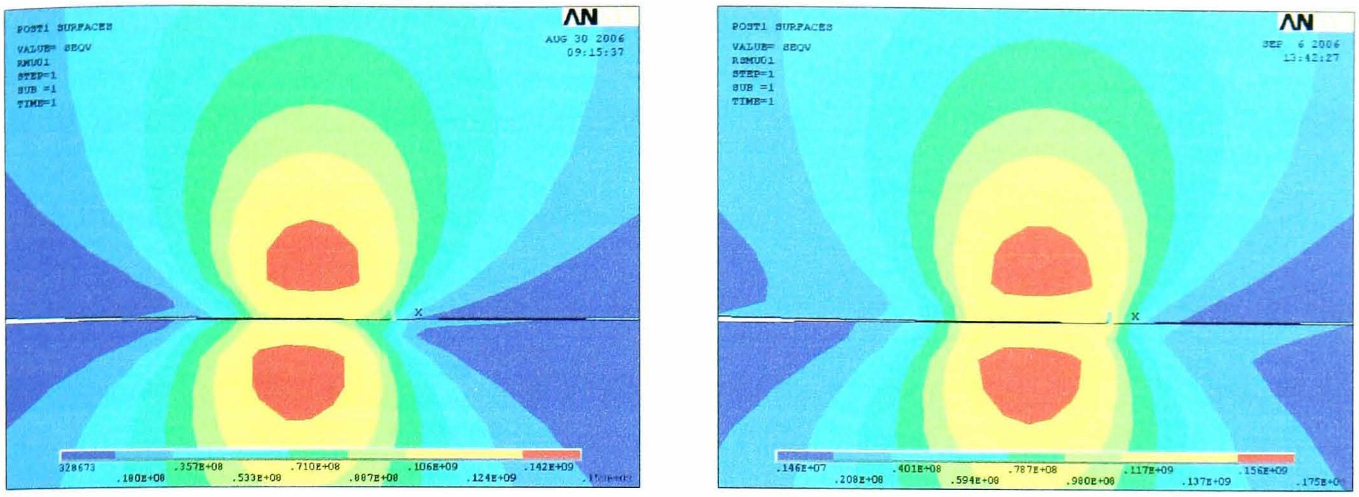

(a) μ=0.1

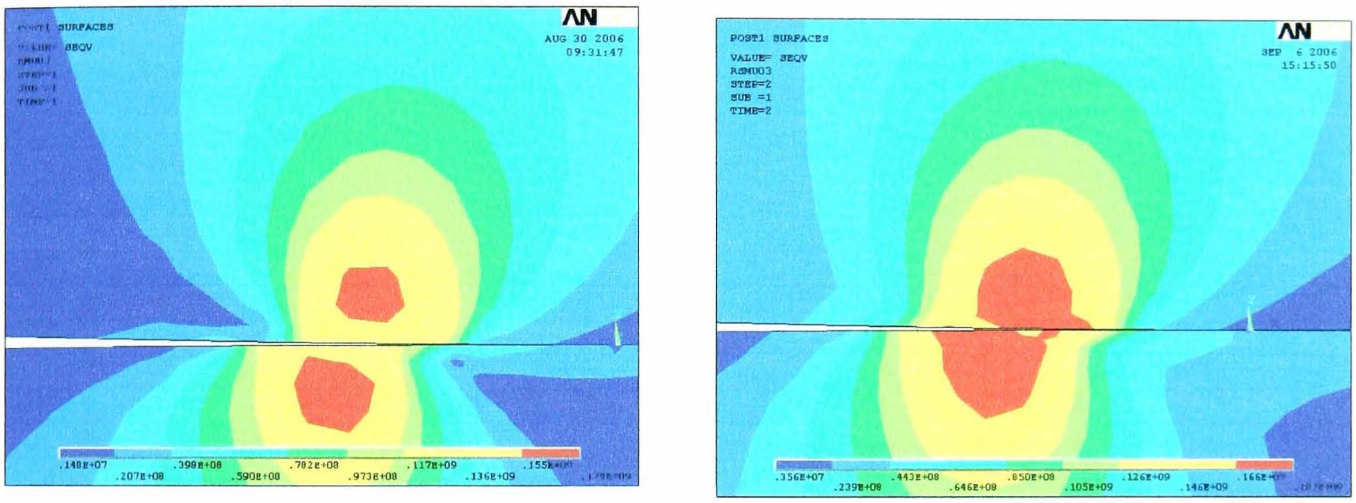

(b) μ=0.3

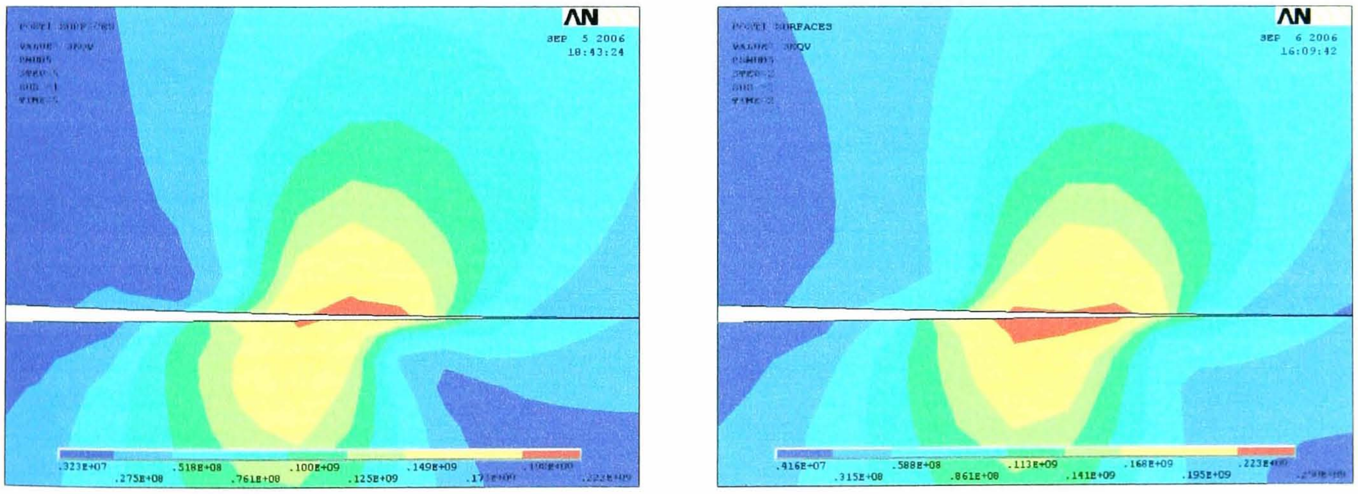

(c) μ=0.5

Pure Rolling

10% Slide

Figure 6.7 Comparison of von Mises' stress distributions in contact conditions

Furthermore, as shown in Figure 6.8, using distribution of τ_R, the ratio of τ_R/p_0 reached 0.50 above μ=0.4. The plastic deformation criterion, $k=\sigma_Y/\sqrt{3}=0.529p_0$, suggests a possibility of crack initiation right below the contact surface.

For these reasons, it is considered that there was some tangential loading during the experiments and that was sufficient to move the maximum strain-energy point towards the contact surface.

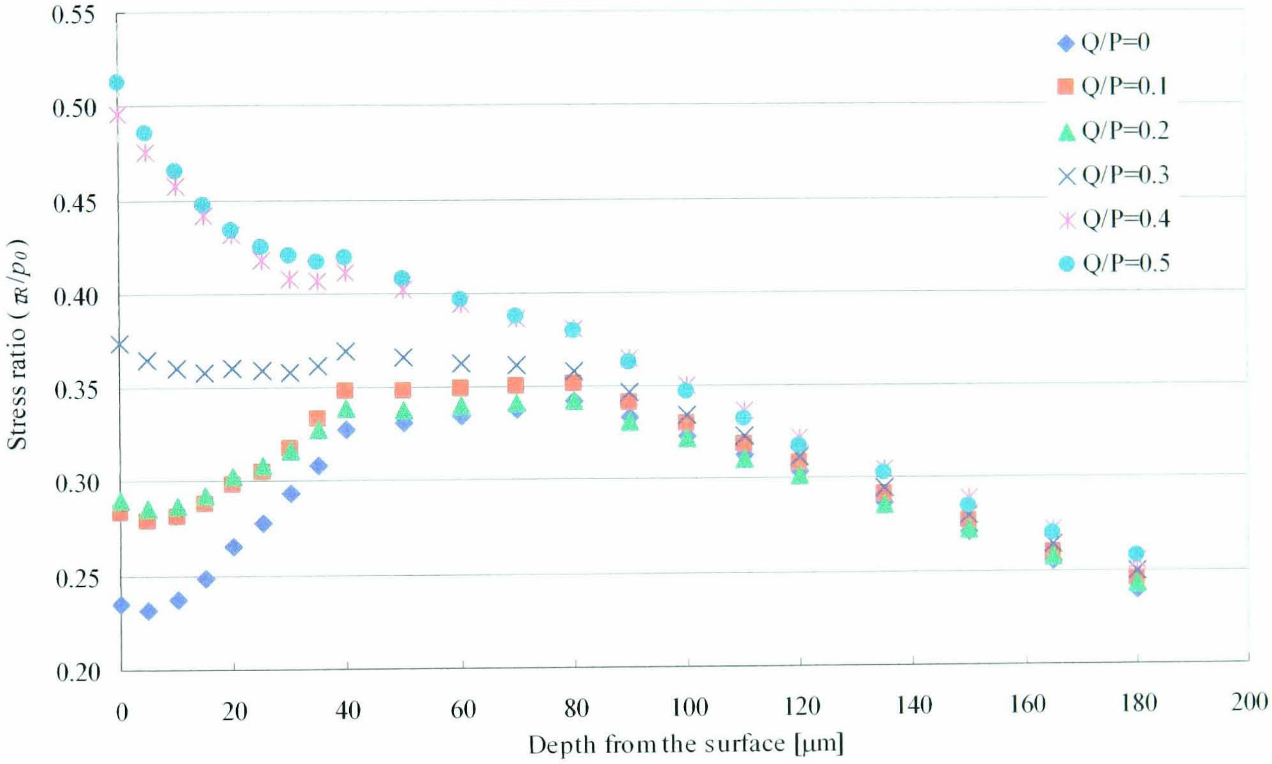

Figure 6.8 Stress distributions of τ_R/p_0 at subsurface and crack initiation points (10% Slide)

6.4 Rolling Contact Characteristics under the Magnetic Field

Due to effects of the magnetic field, thinner wear particles were observed under all test conditions used. The thicknesses produced under with and without magnetic field were approximately 5μm and 20μm respectively. In connection with finer wear particles generated in the presence of the magnetic field, Hiratsuka and Sasada (4) pointed out severe-mild wear transition in sliding wear with a magnetic field applied. They argued that strongly oxidised wear particles, trapped on rubbing surface due to a magnetic force, protected rubbing surface and produced mild wear by remaining on the surface.

The wear particles observed in this study are flat and thinner than those produced by the severe-mild wear transition where crushing action is involved. Their shape and size seem to be directly linked to the movement of the crack initiation location towards the contact interface resulting from the presence of the magnetic field. If finer particles were spread over the surface due to crashing, the evidence of that would have been seen through the particle's shape. However, there was no evidence of that in SEM observations. The same conclusion can be drawn from surface observations with the help of the optical microscope. Therefore, it is justified to say that wear particles were generated due to subsurface cracks located at the depth of about 5μm as schematically shown in Figure 6.9.

Wear amount trends were different for the two rolling contact conditions used. However, by considering the thicknesses of wear particles together with the total wear amount, the tendencies for different contact conditions can be clarified.

The total wear amount can be calculated by multiplication the number of wear particles and the size of the particle. To put it simply, it is assumed that wear particles in this study are generated with a fixed thickness due to the presence of the magnetic field and the size of the particles is depended on their thickness. Hence, the wear amount is determined by multiplication of the number of wear particles and the thickness of a wear particle.

For instance, as shown in Figure 6.8, the crack initiation location is considered to correspond to the thickness of a particle, that is 20μm in the absence of the magnetic field and 5μm in the presence of the magnetic field. Differences in crack initiation location result in differences in the particles' volume and the number of cycles required to detach the particle. When a wear particle is detached from the surface, a crack initiated at the shallower location would be shorter than that initiated at the deeper location. Thus, by evaluating the number of cycles required to detach one layer, the effect of magnetic field can be explained. Equation (6.1) is used to calculate the number of cycles required.

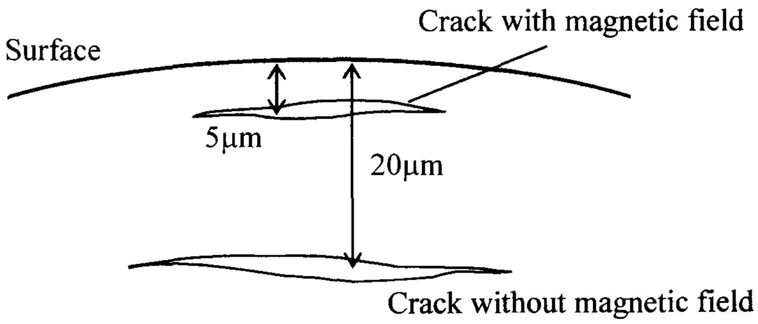

Figure 6.9 Differences in crack initiation points at subsurface with and without magnetic field

$$n = \frac{N\rho\pi dat}{W} \qquad (6.1)$$

where:
n - Number of cycles to detach one layer
W- Wear amount [mg]
N- Number of cycles to wear W
ρ - specific gravity of the disc (=7.85 [mg/mm^3])
t - Thickness of wear particle
(20[μm] at without magnetic field and 5[μm] with magnetic field)
d - Diameter of the disc (=50 [mm])
a - Thickness of the disc (=4 [mm])

By applying Equation (6.1) and utilising measured, accumulated weight losses shown in Figure 5.1 and Figure 5.14, the number of cycles n under different contact and magnetic conditions can be estimated. Figure 6.10 shows that applying magnetic field resulted in reduced n, and the trend was the same for the two different kinematic contact conditions used.

For the pure rolling without magnetic field $n = 3.8\text{x}10^5$ and for the magnetic fields n is equal to $1.2\text{x}10^5$ at B=0.4T and $1.5\text{x}10^5$ at 1.1T. For rolling with sliding, n values were further reduced to $2.5\text{x}10^4$ at B=0.4T and $1.5\text{x}10^4$ at 1.1T. In the absence of the magnetic field and the same kinematic contact conditions, n is equal to $8.7\text{x}10^4$. Therefore, it can be concluded that the wear particles were detached easier due to the effect of the magnetic field under both kinematic contact conditions used.

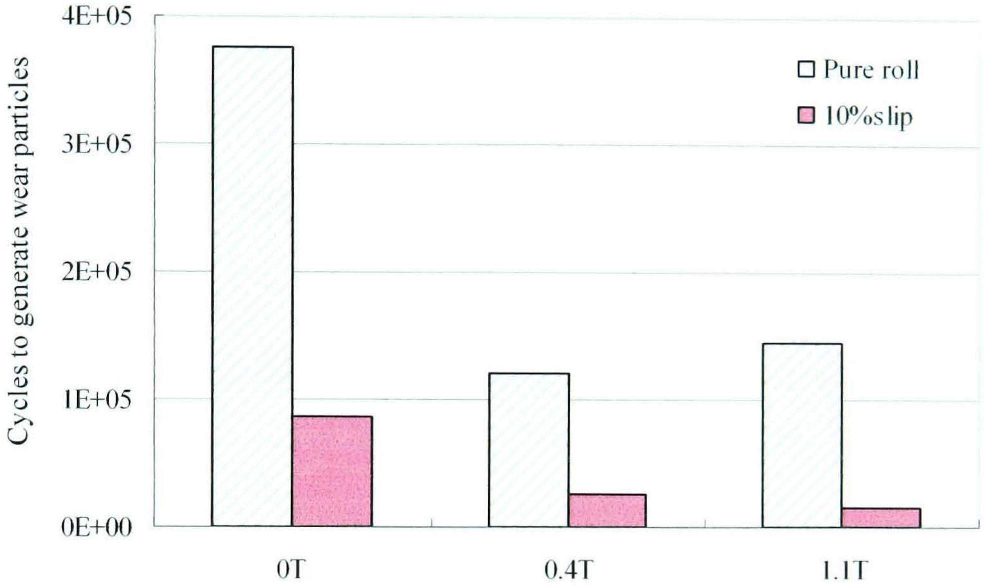

Figure 6.10 Cycles to generate wear particles with and without magnetic field

As a result, it is concluded that the number of cycles required to generate wear particles is shortened by the magnetic field effect and the tendency is the same for the two different contact conditions. Therefore, it is suggested that the differences in observed weight losses are due to the size of the particles. At pure rolling and the presence of the magnetic field wear particles were much smaller than that produced in the absence of the magnetic field so that the weight losses were reduced even though the number of cycles required to generate the particles was decreased. On the other hand, during the rolling with sliding, the particles were not so small when compared to the particles produced in the absence of magnetic field and, therefore, the wear amount increased. The number of cycles to generate wear particles, shown in Figure 6.10, includes complete process leading to the detachment of wear particles, that is, to initiate the crack, to propagate it to a critical length and to detach the particle. The differences for each of the process stages are not reflected in the calculations.

However, considering the depth of around 5μm, at which supposedly by crack initiation took place, the maximum shear strain-energy τ_R at that depth was even less than that in the absence of magnetic field and corresponds to the minimum value of τ_R at μ=0.3 in Figure 6.3. These results mean that the crack initiates after a low number of cycles and a low maximum shear strain-energy is required due to the effect of the magnetic field. Therefore, the following can be assumed:

(1) Increase in the load conditions resulting in alternation of energy status due to magnetisation

(2) Decrease in the strength of a specimen producing alternation of material properties due to magnetisation

In the next section, the mechanisms of magnetic effect are elaborated taking into account:

(1) Magnetisation of the specimen and its energy status.

(2) Connection between the contact stress and the magnetisation status.

(3) Relation of various test conditions to the magnetic field effects.

6.5 Mechanisms of Magnetic Field Effect in Rolling Contact

6.5.1 Magnetisation of the Specimen and its Energy Status

(1) Magnetic status without magnetic field

As described in Section 3.2, magnetic domains have a tendency to be divided into many thin domains to minimize the total energy when no external magnetic field exists. The total energy per area is expressed as (5):

$$e = e_m + e_{ex} + e_a \qquad (6.2)$$

where:
e - Total energy
e_m- Magnetostatic energy
e_{ex}- Exchange energy
e_a- Anisotropy energy

These energies are expressed as functions of the thickness of domains by Equations (6.3) and (6.4).

$$e_m = \frac{2I_s^2 d}{\pi^2 \mu_0} \sum_{n=1}^{\infty} \frac{1}{n^2 d} \int_0^d \sin n\left(\frac{\pi}{d}\right) x dx \qquad (6.3)$$

$$e_{ex} + e_a = \frac{l}{d}\left(\frac{JS^2\pi^2}{a^2 N} + KNa\right) \qquad (6.4)$$

where:
I_s - Saturation magnetisation
d - Thickness of domain
μ_0- Permeability of vacuum (=4πx10^7)
l - Thickness of the crystal
J - Exchange integral
S - Total spins quantum number
a - Lattice constant
N- Number of atoms in a domain wall
K- Anisotropy constant

To understand the magnetic status of the driven disc, distribution of magnetic domain walls is estimated by applying the above equations. For the estimation, the case of 180° domain walls are considered as a typical model, schematically shown in Figure 6.11, is considered to represent the driven disc at l=4x10^{-3}m of thickness. Saturation magnetisation I_s is applied as 1.93T for EN1A steel and other constants are applied with values of Fe, J=2.16x10^{-21}, S=1, N=150 and K=4.2x10^4. The thickness of the domain is obtained by substituting these values into Equations (6.3) and (6.4) is 3.98x10^{-6}m. Thus, it can be conjectured that domain walls in the driven disc nearby the contact region exist at intervals of several microns when no magnetic field is applied.

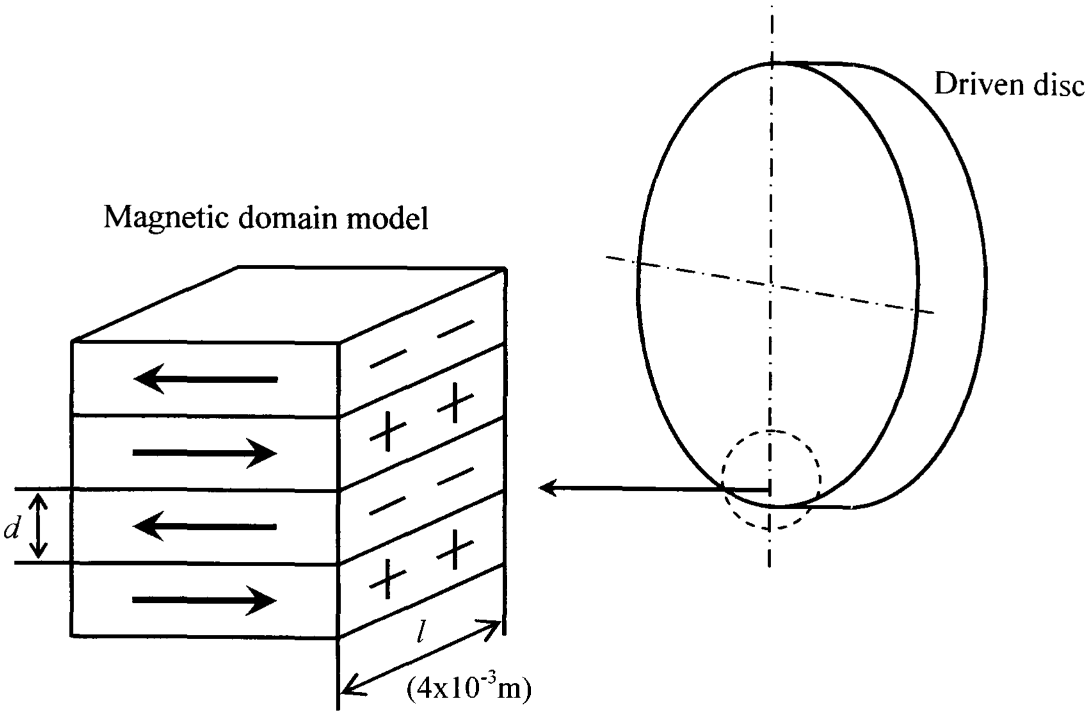

Figure 6.11 180° magnetic domain wall model in the specimen

(2) Magnetic status under magnetic field

According to ANSYS analysis, obtained magnetic densities nearby the contact surface for the two types of permanent magnets used are 0.08T and 0.02T. Therefore, magnetisation of specimen is considered to be in a weak domain wall displacement status, because inclusions or dislocations probably restricted the displacement. Therefore, rotation magnetisation and magnetostriction can be ignored under this condition.

Table 6.1 Magnetic fields analysis results

Type of magnets	B_r [T]	B[T]	H[A/m]
Rare earth magnets	1.1	0.08	80
Ferrite magnets	0.4	0.02	25

Due to magnetisation, domain walls require energy to displace in order to expand magnetic domains therefore turn to the magnetic field for energy, which is given by Equation (3.4). The value obtained for rare earth magnets by substituting I_s =1.93T for EN1A steel and H=80A/m is:

$$\Delta U_m = 2I_s H \cos\theta = 2\text{x}1.93[\text{T}]\ \text{x}80[\text{A/m}] = 309.2[\text{J/m}^3]$$

where:

ΔU_m- Energy for magnetisation
I_s - Saturation magnetisation
H- Magnetic field
θ - Angle between the magnetic field direction and the easy direction (assumed to be at θ=0°).

Knowing that domain walls are pinned by dislocations, it can be guessed that domain walls move with dislocations and the energy for magnetisation stored up at domain walls is also varied with them. Therefore, it can be considered that the dislocation movement determines movement of domain walls. It can also be estimated after Makar (6) that characteristic of magnetisation of steel is influenced by the amount of carbon and stress. In consequence, it is necessary to know the behaviour of dislocations in the vicinity of the contact region.

6.5.2 Connection between the Contact Stress and the Magnetisation Status

Assuming that crack initiates at the depth of 5μm under the magnetic field, as described in Section 6.3, it can be supposed that dislocations have a tendency to pileup to the surface due to lower τ_{max} gradient nearby the surface. However, to initiate the crack, energy accumulation to cause plastic deformation is needed. Considering the crack initiation model in the rolling contact under the magnetic field, dislocations nearby the contact region are supposed to be in domain wall, which are given energy due to magnetisation. Therefore, when dislocations are piled up at the depth of around 5μm, it is likely that crack would be initiated there due to magnetisation.

To examine the feasibility of crack initiation model with the magnetic field, energy status at the subsurface region has to be estimated. Mean distance between dislocations is approximately 1-10μm at dislocation density of 10^{-10}-10^{-12} and domain wall is about 100-200b (where b is lattice constant, b=2.8x10^{-10}m for Fe) and it corresponds to 0.03-0.04μm. Schematic model for the relation between dislocations and domain walls in position is shown in Figure 6.12.

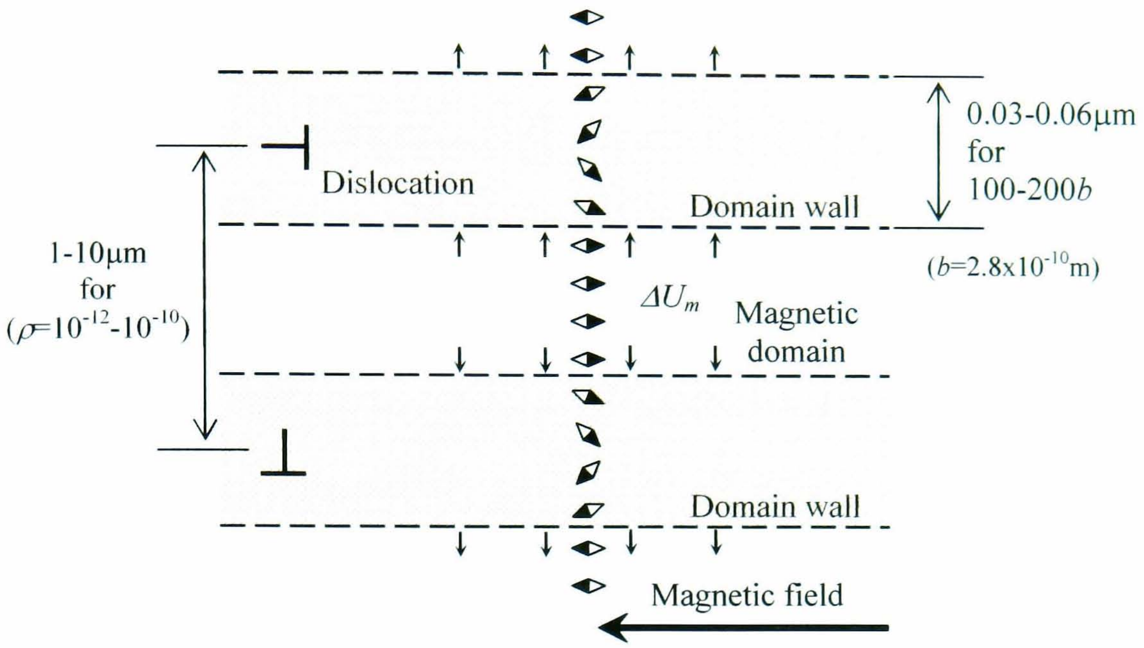

Figure 6.12 Relation between dislocations and domain walls in position

As described in previous section, due to the magnetic field, energy for magnetisation is accumulated in domain walls under the test conditions used and it is estimated to be about 300J/m^3. Thus, assuming that a 1mm x 4mm area of domain wall lies at the depth of 5μm in the subsurface, the energy is estimated to be:

$$300\ [\mathrm{J/m^3}] \times 1 \times 10^{-3}\ [\mathrm{m}] \times 4 \times 10^{-3}\ [\mathrm{m}] \times 0.03\text{-}0.06 \times 10^{-6}\ [\mathrm{m}] = 3.6\text{-}7.2\times10^{-11}\ [\mathrm{J}]$$

On the other hand, thermally activated process is considered as a factor to help dislocation movement. As described in Section 2.4, thermally activated process represents activation energy due to thermal vibration of the lattice and supplied as external work to make a motion of a dislocation. The value is about 4x10^{-21}J in room temperature and 1.8x10^{-20}J even if T=1300K (7). Comparing the process to the energy accumulation in domain wall due to magnetisation, the value of the activation energy could be sufficient to activate dislocation motion, even if a very small quantity is provided.

In addition to the effect of magnetic field on the behaviour of dislocations, stress relaxation effect according to Jones (8) is the reason for dislocation velocity enhancement effect.

6.5.3 Magnetic Field Effects under Various Test Conditions

(1) Effect of rotational speed

Test results obtained at two different rotational speeds indicate that the effects of magnetic field at the lower speed were weaker than that at higher rotational speed. The effect of sliding velocity on adhesive wear was explained by Muju (9) who argued that under the magnetic field influence, the time to saturation of dislocation density will be shortened in regions of plastic deformation as shown in Figure 6.13. It can be assumed that a similar phenomenon is taking place also in rolling contact. However, surface roughness measurements indicate that the value of R_a in the presence of the magnetic field and lower rotational speed was closer to that obtained in the absence of the magnetic field and higher rotational speed rather than to that obtained for the absence of the magnetic field. Therefore, it can be suggested that the crack initiation mechanism for both rotational speeds is the same even though wear amount is different.

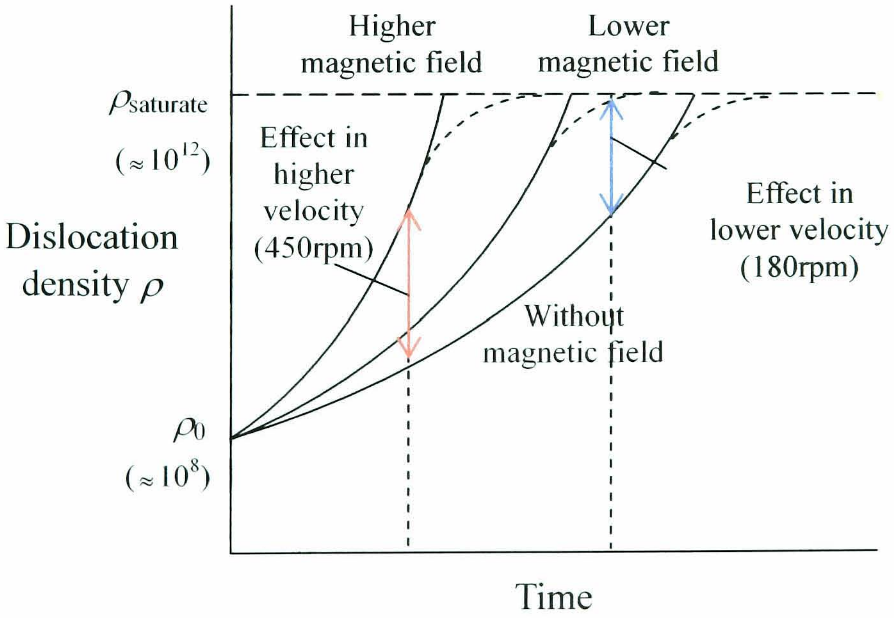

Figure 6.13 Trend in dislocation densities under magnetic and without magnetic conditions (9)

(2) Effect of slip

The effect of magnetic field on rolling with slip is the same as for the pure rolling judging by the shape of wear particles and the number of cycles required to generate wear particles. Experimental results allow to say that the effect of magnetic field on wear amounts at different rolling contact conditions can be interpreted, as argued in Section 6.4, by the product of the thickness of the particle and the number of cycles required to generate the wear particle. The reason for the differences in the particle sizes observed under the contact conditions used is mainly considered in terms of the stress status. As shown in Figure 6.14, the value of τ_R/p_0 near the surface under rolling with sliding condition is higher than that for the pure rolling when a tangential load is applied and this fact suggests the reason. Similar mechanism is also considered to apply for pure sliding as evidenced by the experimental results. This is supported, for instance, by Chin and Zaidi (10) observations that cracks in the subsurface region were generated in sliding contact.

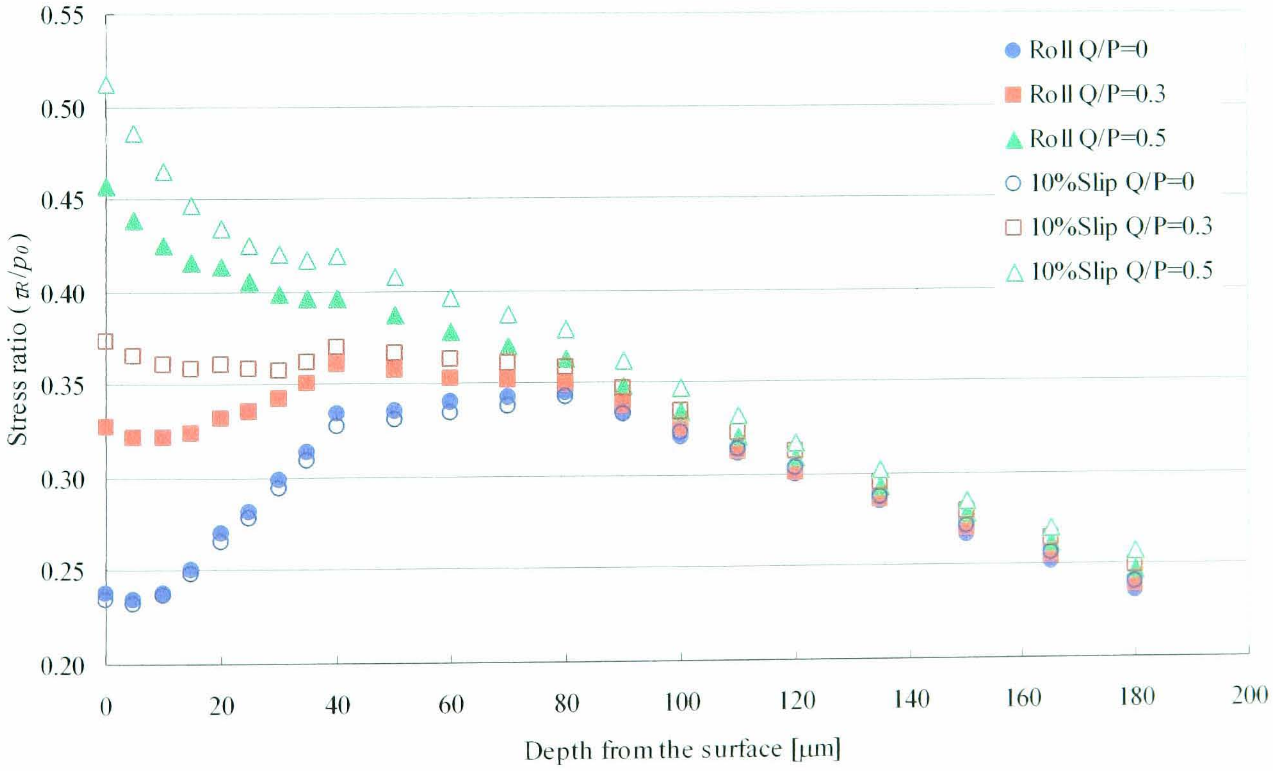

Figure 6.14 Comparison of τ_R/p_0 in different contact conditions

(3) Effect of magnetic field orientation

It is apparent from the tests carried out at different magnetic field orientations and different contact conditions, that the magnetic field angle of θ=90° produced different effects compared to those obtained at θ=0° and 45°. Therefore, demagnetising field effect is considered. As described in Section 3.4, demagnetising field is a magnetic field inside of ferromagnetic body, which is opposite to magnetisation. Therefore, demagnetising field acts as resistance for magnetisation. Demagnetising factor N determines the amplitude of demagnetising field and the shape of specimen decides the value. For instance, a disc shape, as shown in Figure 6.15, has demagnetising factor N=1 for the thickness direction and 0 (5). Introducing this factor into experimental results, it is proposed that at the magnetic field orientation angle θ=90° magnetisation of the driven disc is considerably weakened and, therefore, different results were observed.

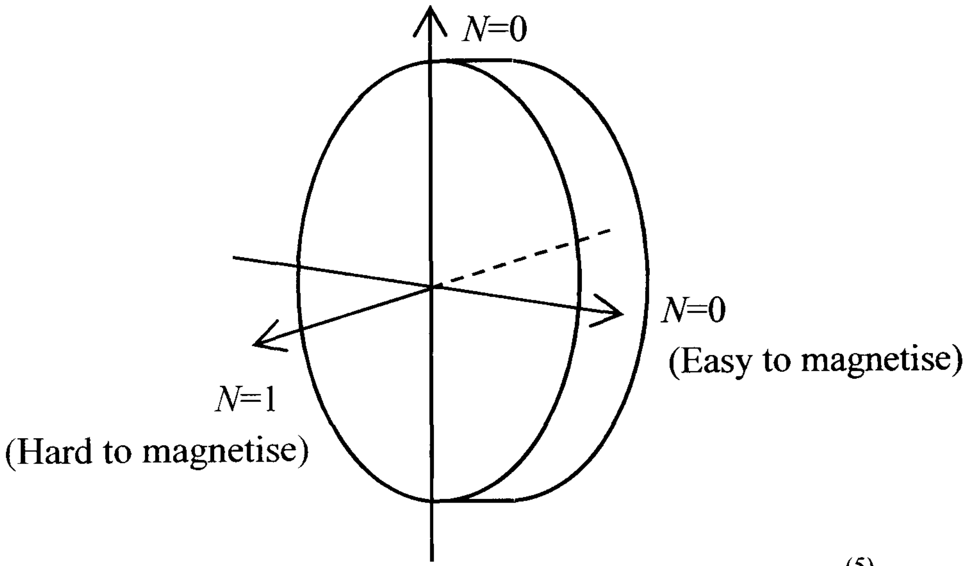

Figure 6.15 Demagnetising factors for a disc shape (5)

(1) T. Suzuki, "Evaluation and life prediction of pitting for carburised steel", Toyota Central R&D Labs Technical R&D review Vol. 34,(1999), pp. 25-34

(2) H. Miyoshi, Journal of Japanese Society of Tribologists, Vol. 20, (1975), pp.843-851.

(3) K.J. Chin, H. Zaidi and T. Mathia, "Oxide film formation in magnetized sliding steel/steel contact—analysis of the contact stress field and film failure mode", Wear, Vol. 259, (2005), pp. 477-481.

(4) K. Hiratsuka, T. Sasada, "Wear of metals in a magnetic field", Wear, Vol. 160, (1993), pp. 119-123.

(5) S. Chikazumi, "Physics of magnetism", John Wiley & Sons, Inc. (1964)

(6) J.M. Makar and B.K. Tanner, "The in situ measurement of the effect of plastic deformation on the magnetic properties of steel: Part I – Hysteresis loops and magnetostriction", Journal of Magnetism and Magnetic Materials, Vol. 184, (1998), pp. 193-208.

(7) O. Izumi, "Atomism for material strength", The Japan Institute of Metals, (1985).

(8) J. J. Jonas, "The back stress in high temperature deformation", Acta Metal., Vol. 17, (1969), pp. 397-405.

(9) M.K. Muju and A. Ghosh, "A model of adhesive wear in the presence of a magnetic field", Wear, Vol. 41, (1977), pp.103-116.

(10) K.J. Chin, H. Zaidi, M.T. Nguyen and P.O. Renault, "Tribological behaviour and surface analysis of magnetized sliding contact XC 48 steel/XC 48 steel", Wear, Vol. 250, (2001), pp. 470-476.

Chapter 7 Conclusions and Future Work

7.1 Conclusions

An experimental investigation using the two-disc machine has been carried out to evaluate the effect of horizontal magnetic field on rolling contact of steel discs operating under different contact conditions and to elucidate a possible mechanism for crack initiation under the influence of magnetic field. In order to suggest the subsurface crack initiation model at a Hertzian contact with magnetic field, magnetisation of ferromagnetic substance and its connection to energy status was also investigated.

A. Observed effects of magnetic fields on rolling contact performance

(1) Subsurface crack initiation points

Wear particles produced in a series of experiments under horizontal magnetic field had a thickness of about 5μm. It can be therefore postulated that the subsurface crack initiation point was moved toward surface due to magnetic field presence. The difference is also reflected in surface roughness.

(2) Wear particles generation cycles

Number of cycles required to generate wear particles are decreased due to the magnetic field influence on crack initiation location. This tendency was more pronounced under rolling with sliding condition.

(3) Wear amount

Wear amount of the discs was determined by the factors mentioned above. In this study, it was decreased in pure rolling contact and increased under rolling with sliding conditions.

(4) Effect of rotational speed

The effects of magnetic field at the lower rotational speed were weaker than that at higher rotational speed.

(5) Effect of the magnetic field orientation

Wear amounts and the state of surface roughness were both affected by different magnetic field orientations. For that reason, the effect of demagnetising field depending on the specimen's shape is considered. At magnetic field orientation angle, θ=90°, demagnetising field acted as resistance for magnetisation and the overall effects were weakened.

B. Subsurface crack initiation model in magnetic field

Subsurface crack initiation model, accounting for the presence of magnetic field, is proposed utilizing (1) magnetisation status of the specimen and (2) dislocation status at the contact region.

(1) Magnetisation status of the specimen

Magnetisation status of the specimen nearby the contact region, obtained from FE analysis, suggests that domain wall displacement is restricted by inclusions such as dislocations. Therefore, it can be supposed that the domain walls within contact region migrate with dislocations movement.

(2) Dislocation status within the contact region

Assuming that dislocation movement is determined by the gradient of shear stress, dislocation pileup could occur close to the surface and might coincide with the shift in crack initiation point due to the magnetic field presence. Therefore, the increase in magnetic domain walls is due to magnetisation and the move towards the contact surface with dislocations piled up by the shear stress gradient. In addition, the value of the magnetisation energy accumulated at the domain walls is large enough to compare to the energy due to thermally activated process and it is possible to consider that the magnetisation energy helps the dislocation pileup. As a result, cracks are initiated at the depth of about 5μm from the surface even if von Mises' shear strain-energy criterion at this location is not fulfilled on its own to cause crack initiation.

7.2 Recommendations for Further Work

The effect of horizontal magnetic field on rolling contact was investigated experimentally and the crack initiation model in the magnetic field suggested. However, to understand and to explain the effect further, the following is recommended.

(1) Magnetic conditions

The magnetisation status created in the experiments affected wear but domain wall movement was restricted by inclusions. A stronger magnetic field could be used so that domain walls are freed from inclusions and rotation magnetisation status is created.

(2) Stress conditions

From the investigation, crack initiation points are considered to vary from about 20μm to 5μm due to the magnetic field effect. However, the crack initiation point without magnetic field is different from the point suggested by von Mises' shear strain-energy criterion. Therefore, although the crack initiation model in the magnetic field suggests a link between the magnetic field energy status and the stress field energy status and explains the tendency of the experimental results produced in this study. This link is not fully explained and elaborated.

To elaborate the mechanisms in detail, the following should be considered.

(1) The cycle to initiate crack and crack propagation in magnetised specimen

(2) Dislocation movement and crack initiation model under stress field

(3) Domain wall movement model accounting for its energy status due to magnetisation

At the present time, there are several numerical techniques available to solve each of these problems, for example, molecular dynamic simulation for dislocation movement and micromagnetic model to describe magnetisation process inside a domain wall. To utilize these techniques, understanding of the mechanism governing magnetisation energy effect on dislocation movement is required.

Appendix A A History of Wear and Fatigue Tests in Magnetic Fields

Year	Authors	Title	Source	Contact	Material	Magnetic field	Load	Velocity	Results
1977	M.K. Muju A. Ghosh	A model of adhesive wear in the presence of a magnetic field - I	Wear 41 (1977) 103-116	Tool wear Pin / Cylinder	HSS / MS MS / Brass (Job / Tool) Brass / MS Ni / Brass (Pin / Cylinder)	DC Electromagnet 125-400 [Oe] The tool (or pin) is magnetised.	78 - 157 [N]	10 - 140 [m/min]	(1) Wear in magnetic field HSS / MS: Decreased MS / Brass: Increased Brass / MS: Decreased Ni / Brass: increased (2) Yield stress of MS is lowered by magnetisation
1979	M.K. Muju A. Ghosh	A model for cross diffusion across a sliding contact in the presence of magnetic field	Wear 53 (1979) 35-42	Tool wear Pin / Cylinder	MS / Al HSS / Brass (Job / Tool) Fe / Brass Brass / MS (Pin / Cylinder)	DC Electromagnet 125-250 [Oe] The tool (or pin) is magnetised.	78 - 157 [N]	10 - 180 [m/min]	(1) Wear in magnetic field MS / Al: Increased HSS / Brass: Increased Fe / Brass: Increased Brass / MS: Varied by velocity Decreased at 10-70 [m/min] Increased at 70-100 [m/min]
1980	M.K. Muju A. Radhakrishna	Wear of non magnetic materials in the presence of a magnetic field	Wear 58 (1980) 49-58	Pin / Cylinder	Brass / MS SUS / MS (Pin / Cylinder)	DC Electromagnet 125-250 [Oe] The tool (or pin) is magnetised.	98 [N]	10 - 150 [m/min]	(1) Wear in magnetic field Brass / MS: Varied by velocity SS / MS: Varied by velocity (2) Wear in magnetic field was determined by hardness ratio and rubbing velocity.
1980	M.K. Muju A. Ghosh	Effect of a magnetic field on the diffusive wear of cutting tools	Wear 58 (1980) 137-145						

Year	Authors	Title	Source	Contact	Material	Magnetic field	Load	Velocity	Results
1986	K. Hiratsuka T. Sasada S. Norose	The magnetic effect on the wear of metals	Wear 110(1986) 251-261	Pin / Disc	Ni / Ni Fe / Fe (Pin / Disc)	DC Electromagnet 4400 [Oe](Horizontal) 3700 [Oe](Vertical)	9.8 - 15.9 [N]	5-500 [mm/s]	(1) Severe-mild wear transfer with magnetic field in air (2) Severe wear but lowered μ and wear in N_2 and Ar gas atmosphere with magnetic field. Large sphere particles were observed at the conditions.
1987	Y. Yamamoto S.Gondo	Effect of a magnetic field on boundary lubrication	Tribology International, 20 (1987) 342-346						
1993	I.K. Bhat M.K. Muju P.K. Mazumdar	Possible effects of magnetic fields in fatigue	Int J Fatigue 15 No.3 (1993) 193-197	Fatigue (Stage 2)	MS	DC Electromagnet 0-7.5 [A]	175 [MPa]		Fatigue life was decreased due to the magnetic field.
1993	K. Hiratsuka T. Sasada	Wear of metals in a magnetic field	Wear 60 (1993) 119-123	Pin / Disc	Cu / Fe Zn / Fe (Pin / Disc)	DC Electromagnet 3700 [Oe](Vertical)	9.8 [N]	204 [mm/s]	(1) Wear in magnetic field Cu/Fe: Severe-mild transfer Zn/Fe: Wear was increased
1993	K. Kumagai, K. Suzuki O. Kamiya	Study on reduction in wear due to magnetization	Wear 162-164 (1993) 196-201	Pin / Rotor	Ni / Steel (Pin / Rotor)	DC Electromagnet 0.6-1.2 [mT] Vertical to the rubbing surface	1-3 [N]	5-30 [m/min]	(1) Wear was decreased due to the magnetic field (2) Smaller and sphere wear particles were observed. (3) Oxidation was increased due to magnetic field.

Year	Authors	Title	Source	Contact	Material	Magnetic field	Load	Velocity	Results
1995	D. Paulmier H. Zaidi R. Bedri E.K. Kadiri L.Pan Q. Jiang	Steel surface modifications in magnetised sliding contact	Surface and Coatings Technology 76-77(1995) 583-588	Pin / Disc	Steel / Steel	DC Electromagnet 0-45000 [A/m] (Vertical)	0-10 [N]	0-1.5 [m/s]	(1) μ was lower and stable under the magnetic fields (2) Wear and *Ra* were decreased due to the magnetic fields (3) Oxidation and Hv were increased due to the magnetic fields (4) These effects were remarkable at above $H=2x10^3$ A/m
1995	H. Zaidi L. Pan D. Paulmier F. Robert	Influence of a magnetic field on the wear and friction behaviour of a nickel/XC48 steel couple	Wear 181-183 (1995) 799-804	Pin / Disc	Ni / Steel (Pin / Disc)	DC Electromagnet 0-50000 [A/m] (Vertical)	0-10 [N]	0-1.5 [m/s]	(1) μ was lower and stable under the magnetic fields (2) Wear was decreased due to the magnetic fields (3) Hv was increased due to the magnetic fields (4) These effects were remarkable at above $H=2x10^3$ A/m

Year	Authors	Title	Source	Contact	Material	Magnetic field	Load	Velocity	Results
1996	M.El Mansori H. Zaidi E.K. Kardiri D. Paulmier	Surface modifications of a non- ferromagnetic copper/ferromagnetic steel XC48 couple in magnetized sliding contact	Surface and Coatings Technology 86-67(1996) 511-515	Pin / Disc	Cu / Steel (Pin / Disc)	DC Electromagnet 0-45000 [A/m]	0 - 10 [N]	0-5 [m/s]	(1) Wear was increased due to the magnetic fields (2) Oxidation and Hv were increased under the magnetic fields
1998	M.El Mansori M. Schmitt D. Paulmier	Role of transferred layers in friction and wear for magnetized dry frictional applications	Surface and Coatings Technology 108-109(1998) 479-483	Pin / Disc	Steel / Graphite (Pin / Disc)	DC Electromagnet 0-60000 [A/m]	5 [N]	1 [m/s]	(1) μ was lowered in air and increased in Ar & vacuum. (2) Wear was decreased in air and increased in Ar & Vacuum (3) Oxidation was increased in air. (4) Steel was transformed to graphite in Ar & vacuum.
1998	Y. Fahmy T. Hare R. Tooke H. Conrad	Effects of a pulsed magnetic treatment on the fatigue of low carbon steel	Scripta Materia 38 (1998) 1355-1358	Fatigue (tensile)	Plain carbon steel	Magnetic pulse 360 [Oe], 14 [Hz]	360, 422 [MPa]		Fatigue life was increased by pulsed magnetic treatment.
1999	M.El Mansori M. Schmitt D. Paulmier	Influence of magnetic field on surface modification and friction behaviour of sliding couple aluminium / XC48 steel	Surface and Coatings Technology 120-121(1999) 653-658	Pin / Disc	Aluminium alloy / 0.48% C steel (Pin / Disc)	DC Electromagnet 0-45000 [A/m] (Vertical)	3.4 [N]	0.67 [m/s]	(1) μ was lower and stable under the magnetic field. (2) Wear and Hv were increased due to the magnetic field. (3) Oxidation was promoted

Year	Authors	Title	Source	Contact	Material	Magnetic field	Load	Velocity	Results
1999	M. El Mansori D. Paulmier J. Ginsztler M.Horvath	Lubrication mechanisms of a sliding contact by simultaneous action of electric current and magnetic field	Wear 225-229 (1999) 1011-1016	Pin / Disc	Steel / Graphite (Pin / Disc)	DC Electromagnet 0-60000 [A/m] (Vertical) DC electric current 0-25 [A]	2 - 7 [N]	1 [m/s]	(1) Lower μ with the magnetic fields (2) Rough and disoriented surface at 3N but smooth and oriented surface at 7N under the magnetic fields
1999	M. El Mansori D. Paulmier	Effects of selective transfer on friction and wear of magnetised steel-graphite sliding couples	Applied Surface Science 144-145 (1999) 233-237	Pin / Disc	Steel / Graphite (Pin / Disc)	DC Electromagnet 0-60000 [A/m]	5 [N]	1 [m/s]	(1) Oxidation is promoted with the magnetic field (2) Hv is decreased
2000	K. Sato T.A. Stolarski Y.Iida	The effect of magnetic field on fretting wear	Wear 241 (2000) 99-108	Ball / Plate (Fretting)	Steel / Steel	Permanent magnet 0.01, 0.13 [T] (Vertical)	40 - 100 [N]	50 [Hz] 0.1 [μm]	(1) Wear is increased but μ is not changed under the magnetic field. (2) Abrasive wear is promoted by O_2 with magnetic field
2001	K.J. Chin H. Zaidi M.T. Nguyen P.O. Renault	Tribological behaviour and surface analysis of magnetized sliding contact XC48 steel / XC48 steel	Wear 250 (2001) 470-476	Pin / Disc	Steel / Steel	AC Electromagnet 50Hz, 0-8000 [A/m] (Vertical)	62.85 [N]	0.38 [m/s]	(1) μ was higher and stable under the magnetic field. (2) Wear was decreased (3) Oxidation and Hv were increased (4) Subsurface crack was observed with magnetic field

Year	Authors	Title	Source	Contact	Material	Magnetic field	Load	Velocity	Results
2001	H. Zaidi, K.J. Chin J. Frene	Analysis of surface and subsurface of sliding electrical contact steel / steel in magnetic field	Surface and Coatings Technology 148 (2001) 241-250	Pin / Disc	Steel / Steel	AC Electromagnet 50Hz, 0-8000 [A/m] (Vertical) DC electric current 0-10 [A]	62.85 [N]	0.38 [m/s]	(1) Higher μ but less wear with the magnetic field. (2) Higher μ and more wear with the magnetic field and electric current.
2003	M El Mansori F. Pierron D. paulmier	Reduction of tool wear in metal cutting using external electromotive sources	Surface and Coatings Technology 163-164 (2003) 472-477	Tool wear	Steel / Steel	DC Electromagnet 0-70000 [A/m]	Feed 0.1125 [mm/rev]	Speed 20-51 [m/min]	(1) Wear of tool was decreased with the magnetic field (2) Surface of the tool was modified to finer with magnetic field. (3) Temperature of the tool was increased with the magnetic field. (4) The trends were remarkable above:$3x10^3$ A/m
2003	O. Bataineh B. Klamecki B.G. Koepke	Effect of pulsed magnetic treatment on drill wear	Journal of Materials Processing Technology 134 (2003) 190-196	Drill wear	Steel / Steel	Magnetic pulse 360 [G], 10 [Hz] 100 [G], 100 [Hz]			(1) Wear of the drill was reduced by magnetic treatment (2) Thrust force was reduced (3) Temperature of the drill was increased.
2003	H.Y. Bi Z.J. Wang	Wear of medium carbon steel in the presence of Nd-Fe-B permanent magnetic field	Material Letters 57 (2003) 1752-1755	Ring / Block	Steel / Steel	Nd-Fe-B permanent magnet 45, 193 [mT]	30 [N]	200 [rpm]	(1) Wear and μ were reduced with the magnetic fields (2) Smoother surface and more oxidised particles were observed

Year	Authors	Title	Source	Contact	Material	Magnetic field	Load	Velocity	Results
2004	M El Mansori V. Iordache P. Seitier D. Paulmier	Improving surface wearing of tools by magnetization when cutting dry	Surface and Coatings Technology 188-189 (2004) 566-571	Tool wear	Steel / Steel	DC Electromagnet 0-30000 [A/m]	Feed 0.1 [mm/rev]	1 [m/min]	(1) μ and cutting ratio were decreased but shear strain and Hv were increased with the magnetic field. (2) Irregular shape of cutting chips were observed when applying the magnetic fields.
2005	K.J. Chin H. Zaidi T. Mathia	Oxide film formation in magnetized sliding steel / steel of the contact stress field and film failure mode	Wear 259 (2005) 477-481	Pin / Disc	Steel / Steel	DC Electromagnet 0-18000 [A/m]	60 - 240 [N]	0.38 [m/s]	(1) Oxide layer was formed on the rubbing surface with the magnetic fields. (2) Wear was decreased and stabilised with the magnetic fields.

Appendix B Drawings for the Test Apparatus Modifications

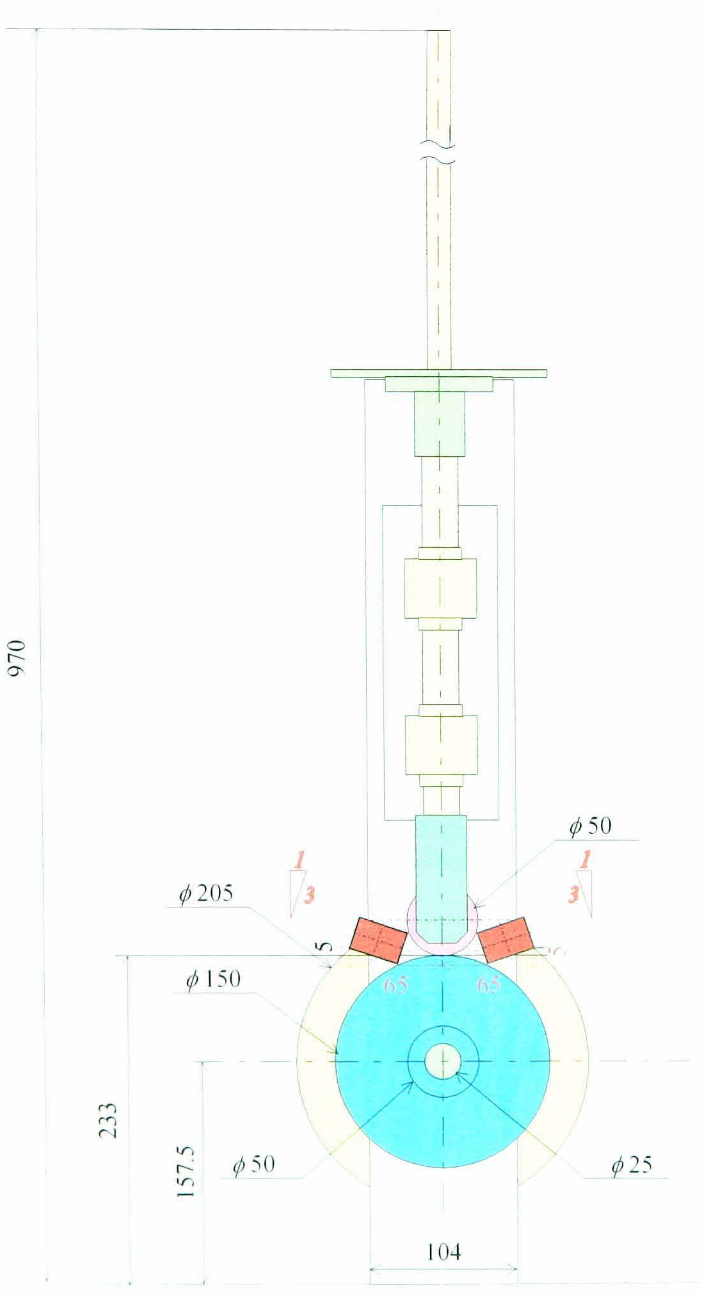

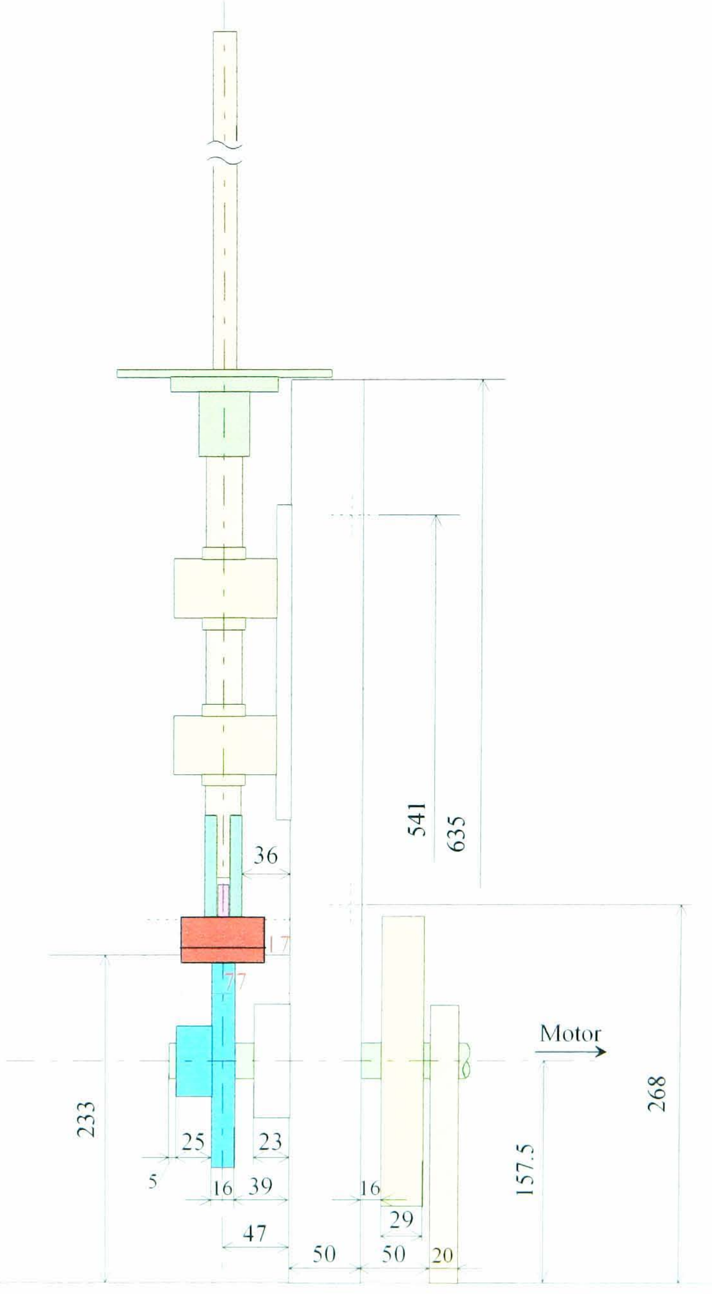

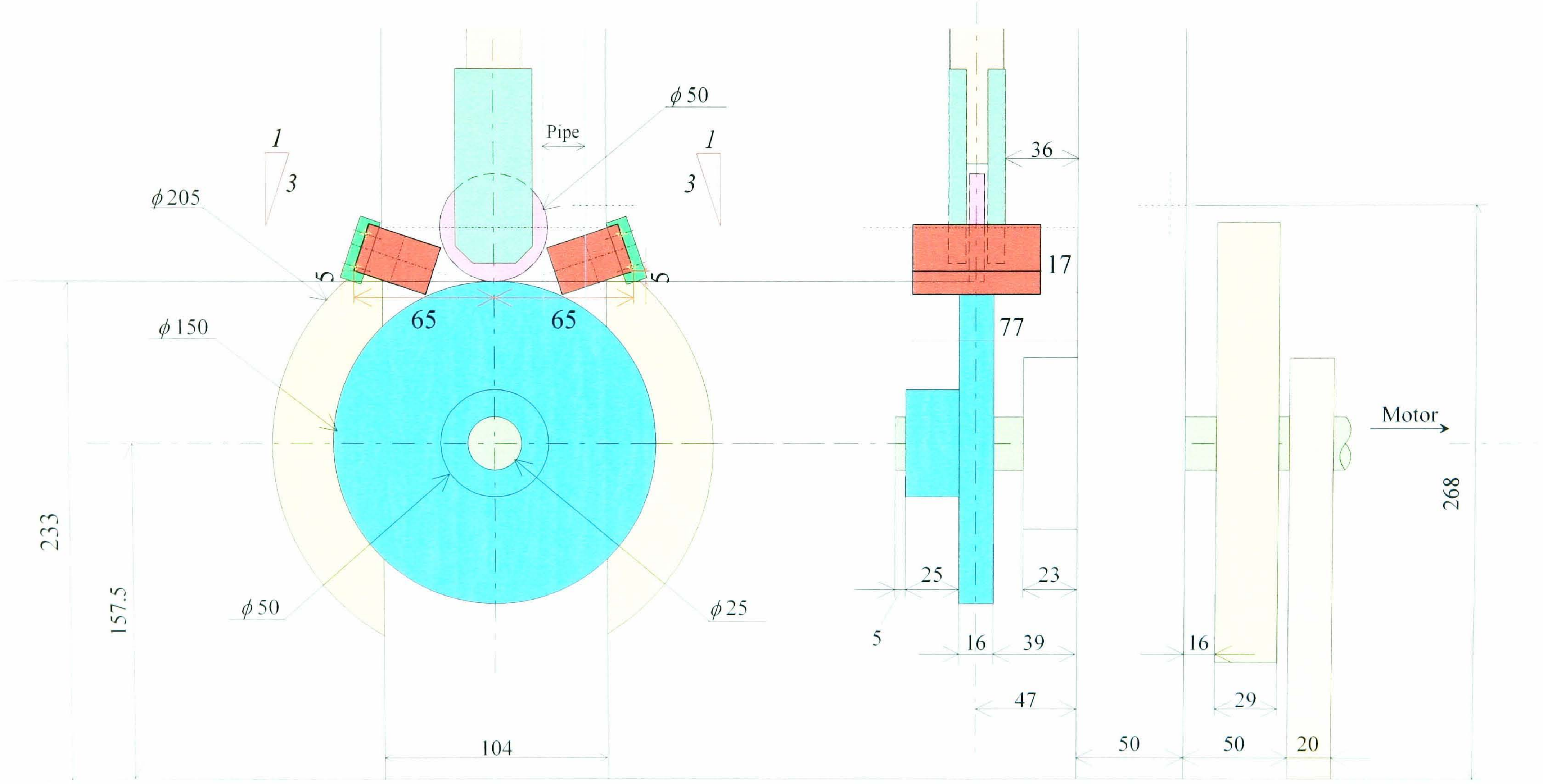

ϕ 50
Pipe
1
3
1
3
ϕ 205
5
5
65
65
ϕ 150
233
157.5
ϕ 50
ϕ 25
104
36
17
77
25
23
5
16
39
47
Motor
268
16
29
50
50
20

No.	Name	Material	Quantity
AB	Magnets & cartridges (blue)		2
C-1	Support (yellow)	Steel	1
C-2	Jacket (green)	Aluminium	1
C-3	Jacket (green)	Aluminium	1

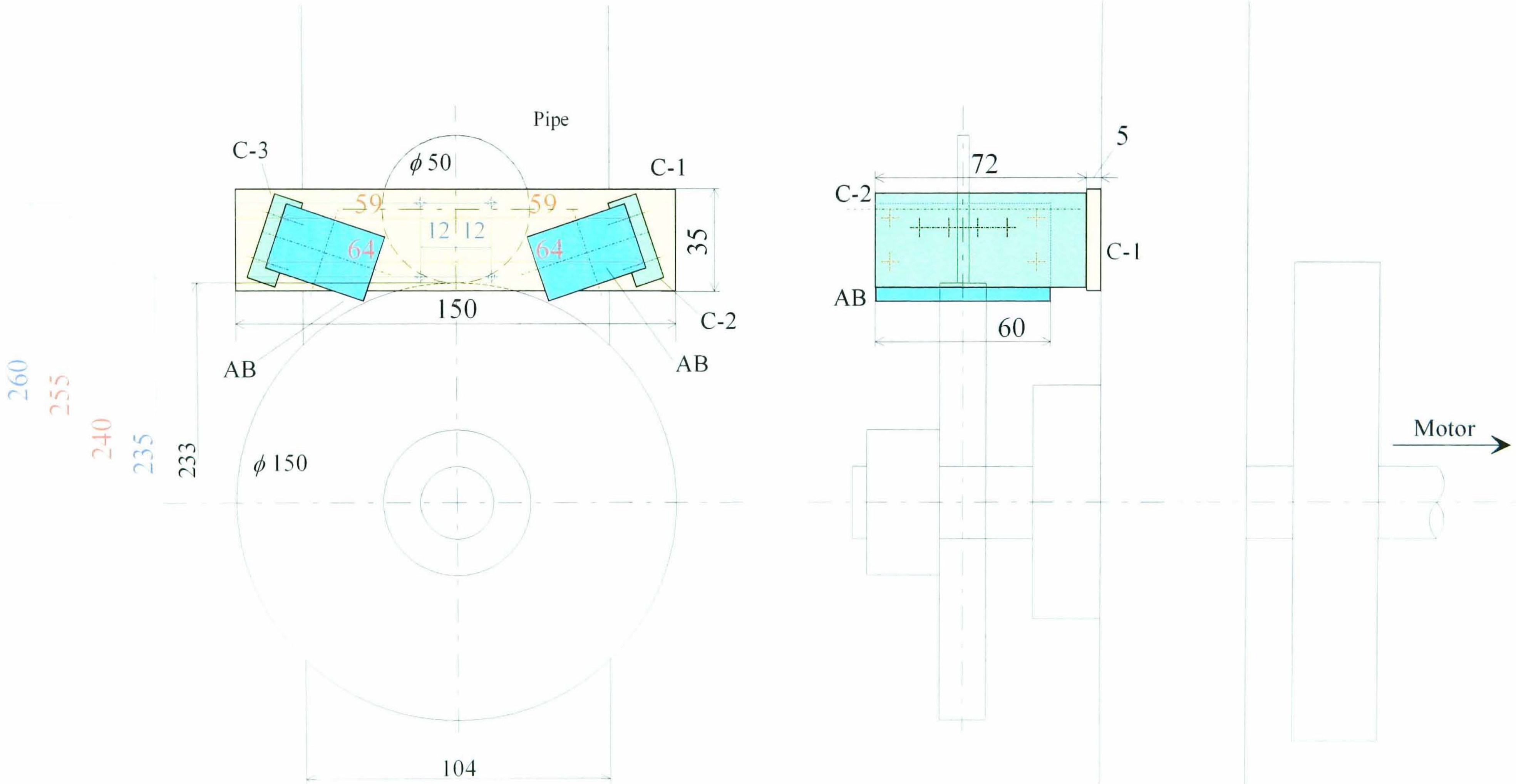

Attachments of magnets (1/3)

Maginification : 1/1

Material : Aluminium
(or another non-magnetic materials)

Drawn by Yusuke Iida (2899)

"A"

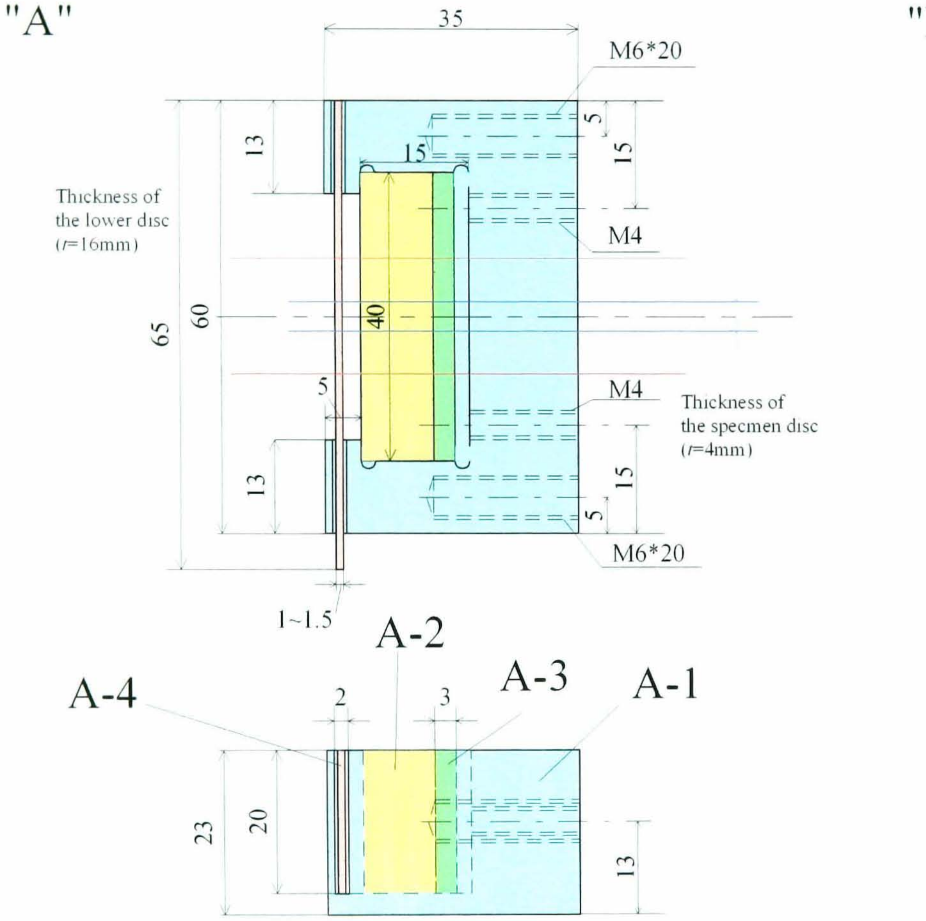

"B"

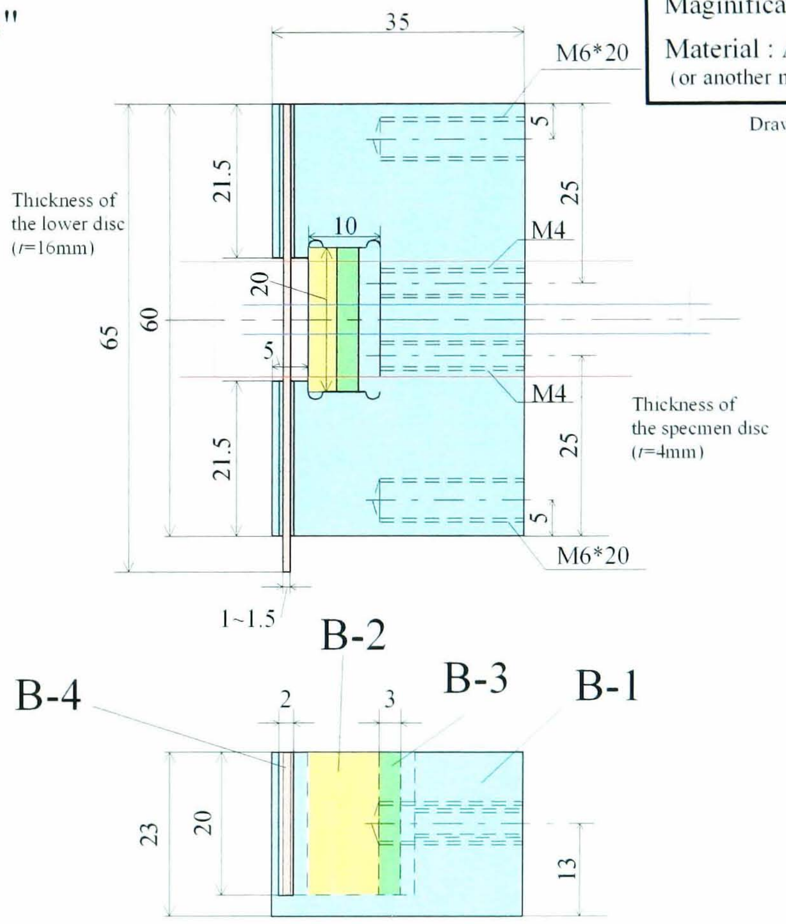

No.	Name	Material	Quantity
A-1	Cartridges (Blue)	Aluminium (non-magnetic materials)	2
A-2	Magnets (Yellow)	Ferrite (buy from a company)	2
A-3	Magnet holders (green)	Aluminium (non-magnetic materials)	2
A-4	Shields (Red)	Aluminium (non-magnetic materials)	2
A-5	B&N (M6*50)	Stainless steel (non-magnetic materials)	4
A-6	B&N (M4*30)	Stainless steel (non-magnetic materials)	4

No.	Name	Material	Quantity
B-1	Cartridges (Blue)	Aluminium (non-magnetic materials)	2
B-2	Magnets (Yellow)	NdFeB (buy from a company)	2
B-3	Magnet holders (Green)	Aluminium (non-magnetic materials)	2
B-4	Shields (Red)	Aluminium (non-magnetic materials)	2
B-5	B&N (M6*50)	Stainless steel (non-magnetic materials)	4
B-6	B&N (M4*30)	Stainless steel (non-magnetic materials)	4

Attachments of magnets (2/3)

Maginification : 1/1

Material : Aluminium

Drawn by Yusuke Iida (2899)

"A"

A-1

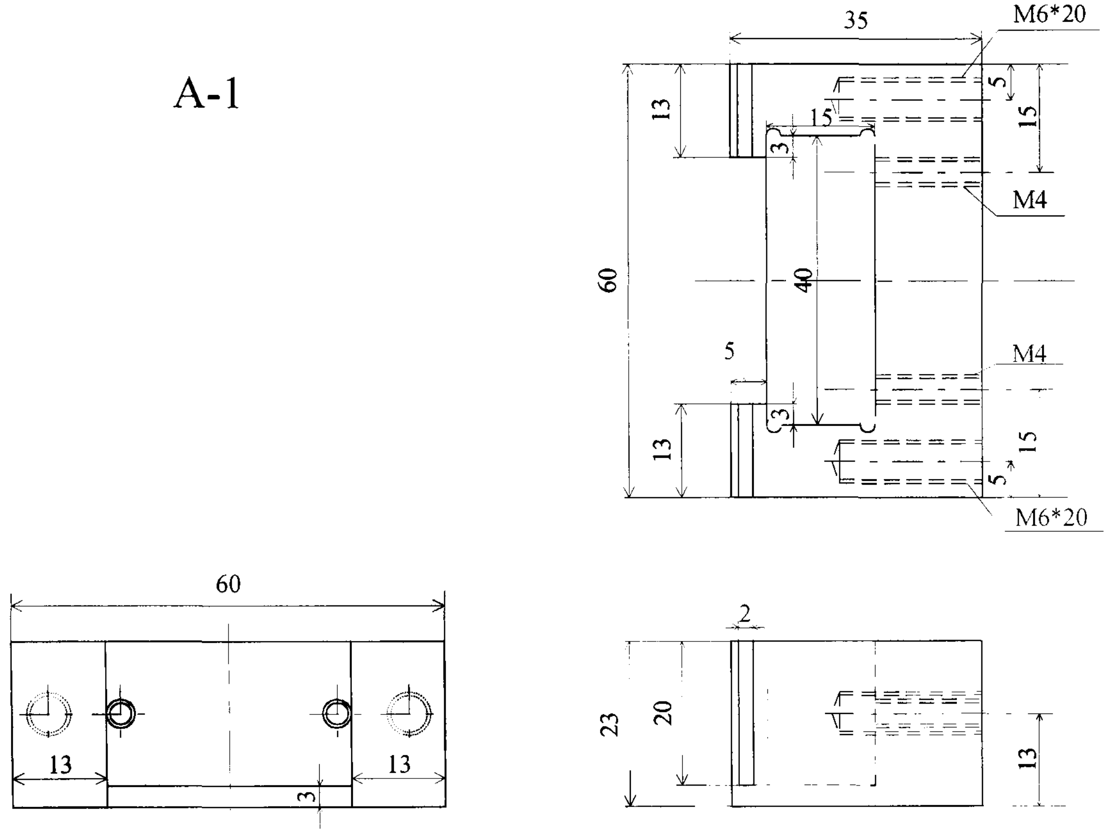

A-3

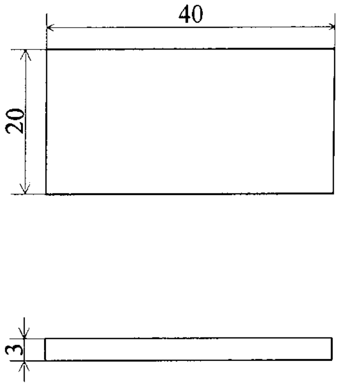

A-4

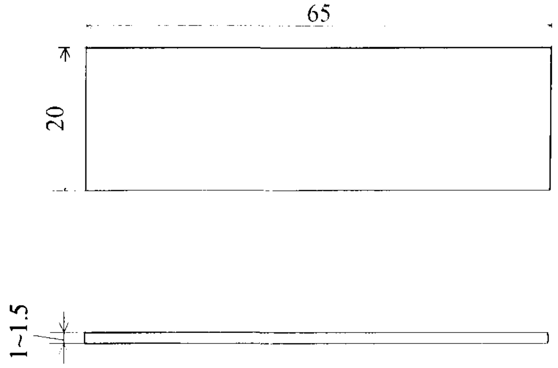

No.	Name	Material	Quantity
A-1	Cartridges	Aluminium	2
A-2	Magnets	Ferrite (buy from a company)	2
A-3	Magnet holders	Aluminium	2
A-4	Shields	Aluminium	2
A-5	B&N (M6*50)	Stainless steel	4
A-6	B&N (M4*30)	Stainless steel	4

Attachments of magnets (3/3)

Maginification : 1/1
Material : Aluminium

Drawn by Yusuke Iida (2899)

"B"

B-1

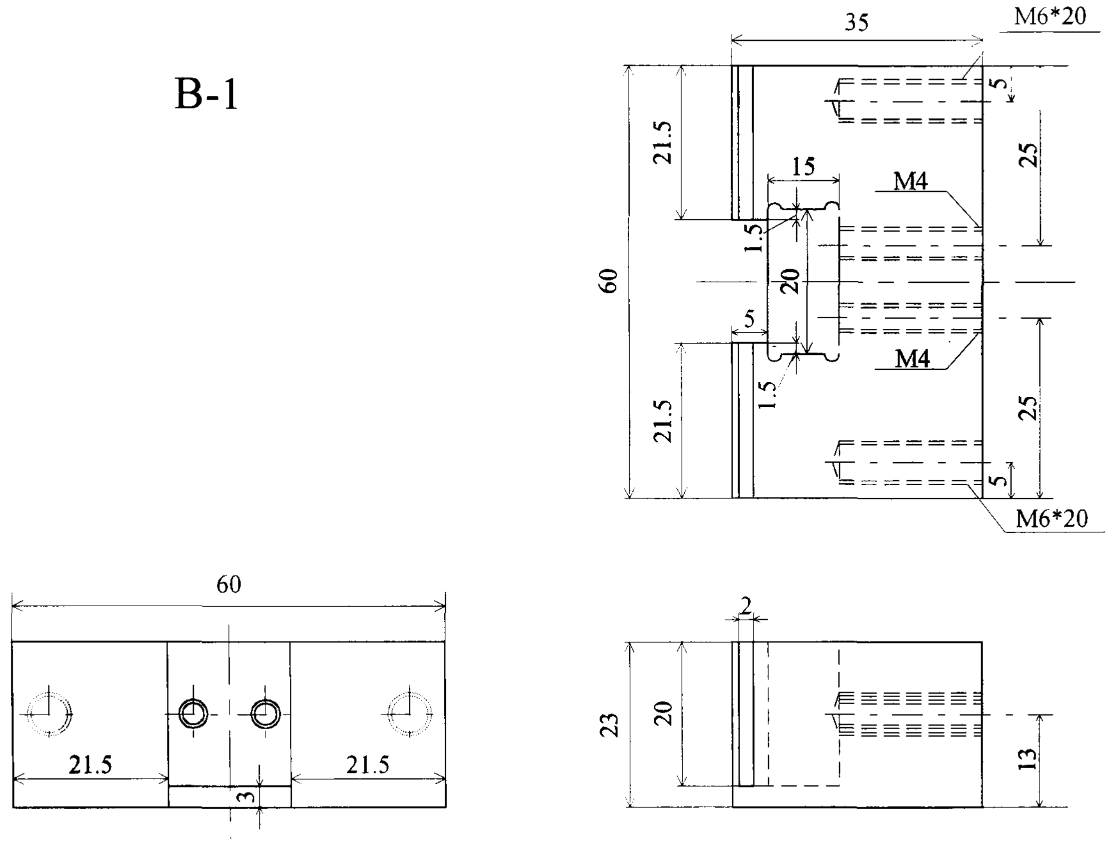

B-3

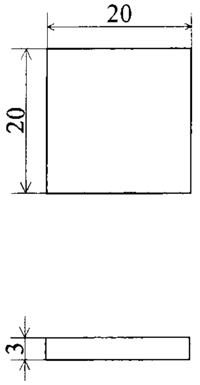

B-4

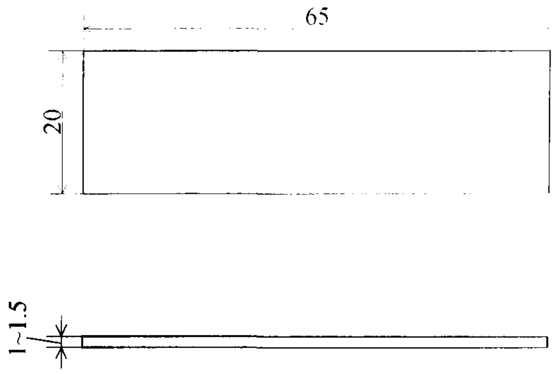

No.	Name	Material	Quantity
B-1	Cartridges	Aluminium	2
B-2	Magnets	NdFeb (buy from a company)	2
B-3	Magnet holders	Aluminium	2
B-4	Shields	Aluminium	2
B-5	B&N (M6*50)	Stainless steel	4
B-6	B&N (M4*30)	Stainless steel	4

Support and jackets

Maginification : 1/1

Drawn by Yusuke Iida (2899)

C-1

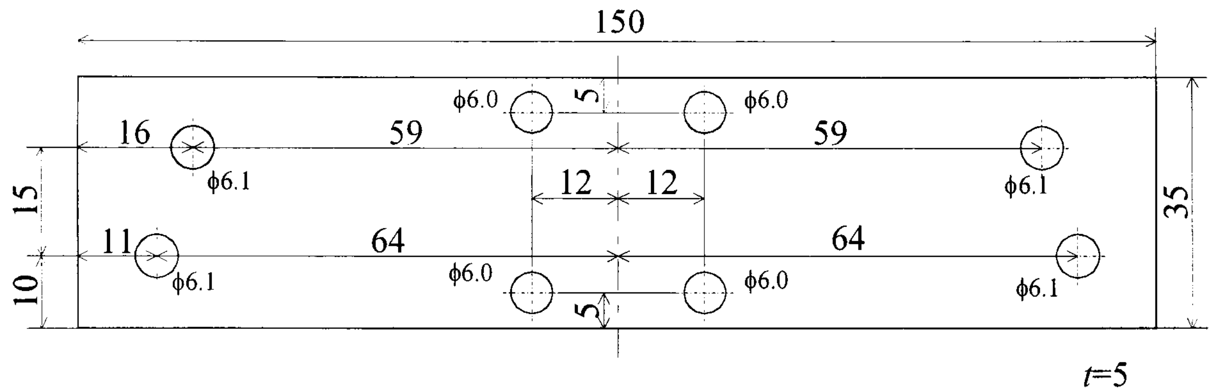

C-2

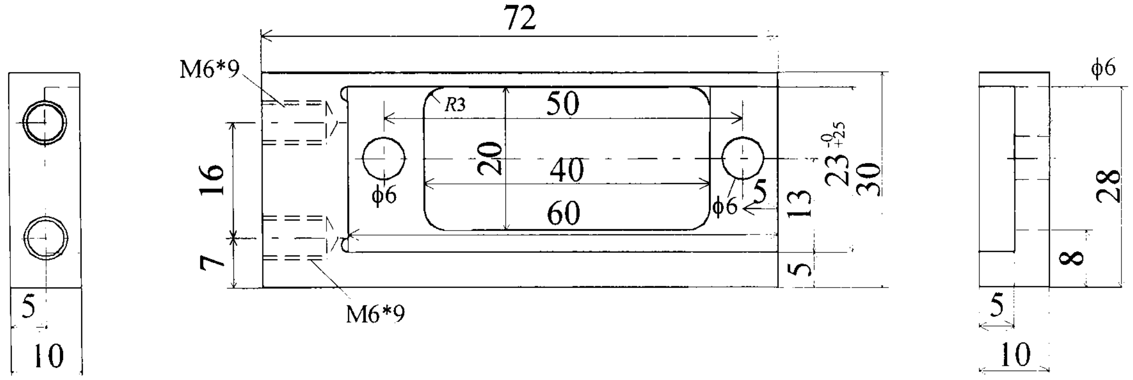

C-3

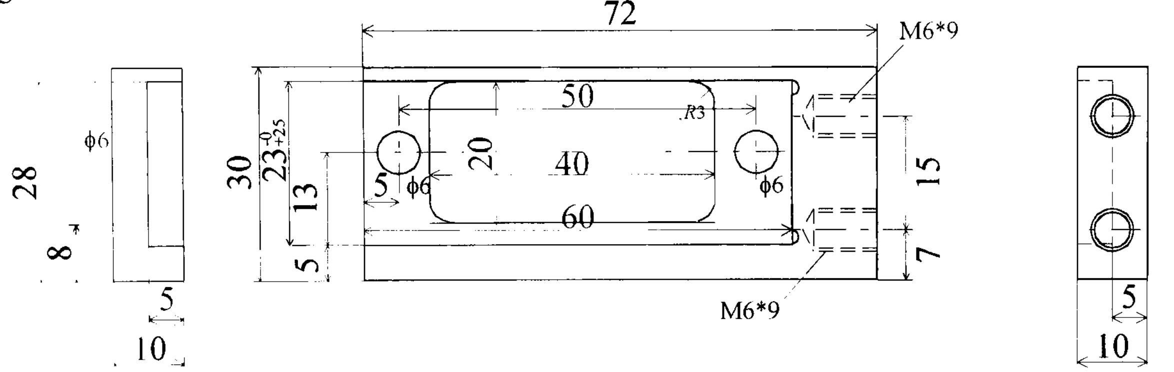

No.	Name	Material	Quantity
C-1	Support	Steel	1
C-2	Jacket	Aluminium	1
C-3	Jacket	Aluminium	1

Appendix C Surface Observations in SEM

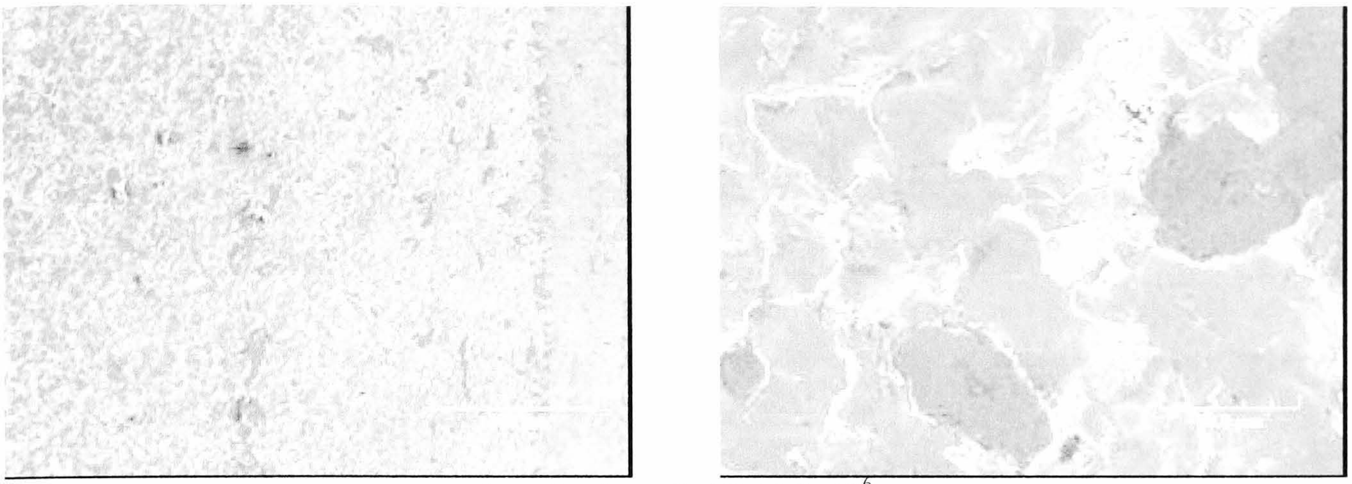

Pure Rolling, B=0T, N=3x10^6

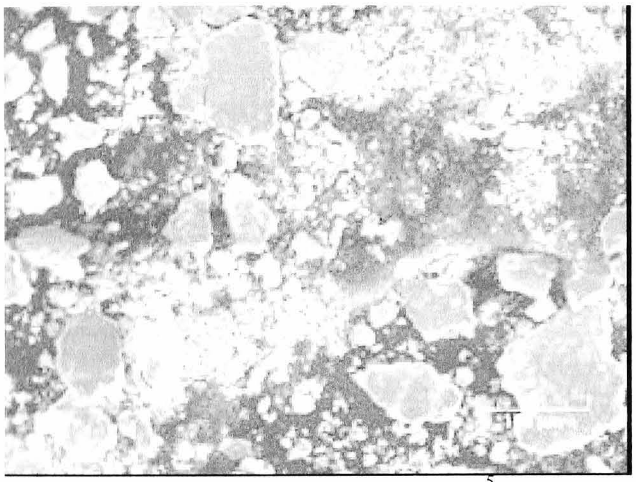

Pure Rolling, B=0T, N=5x10^5

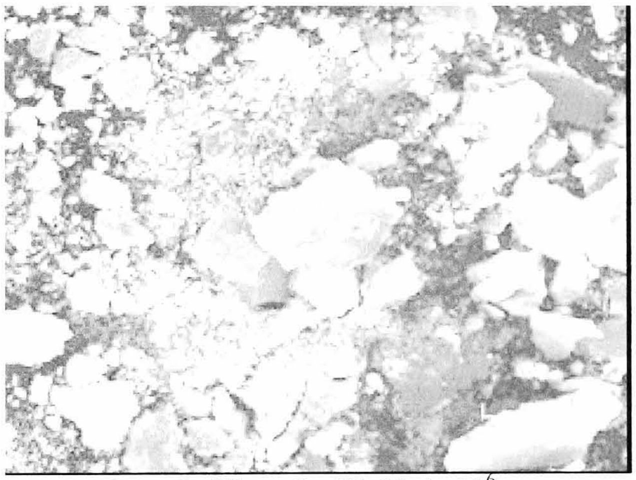

Pure Rolling, B=0T, N=1x10^6

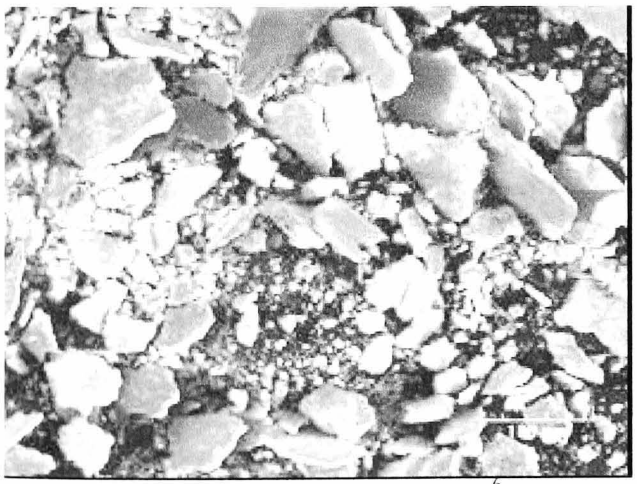

Pure Rolling, B=0T, N=3x10^6

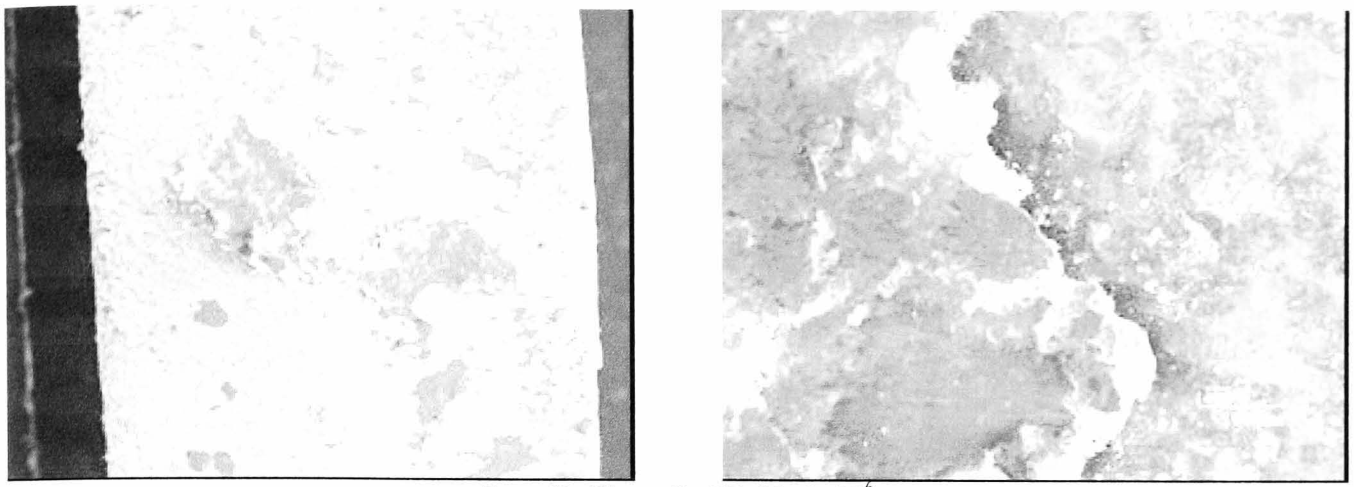

Pure Rolling, B=0T, N=4x10^6

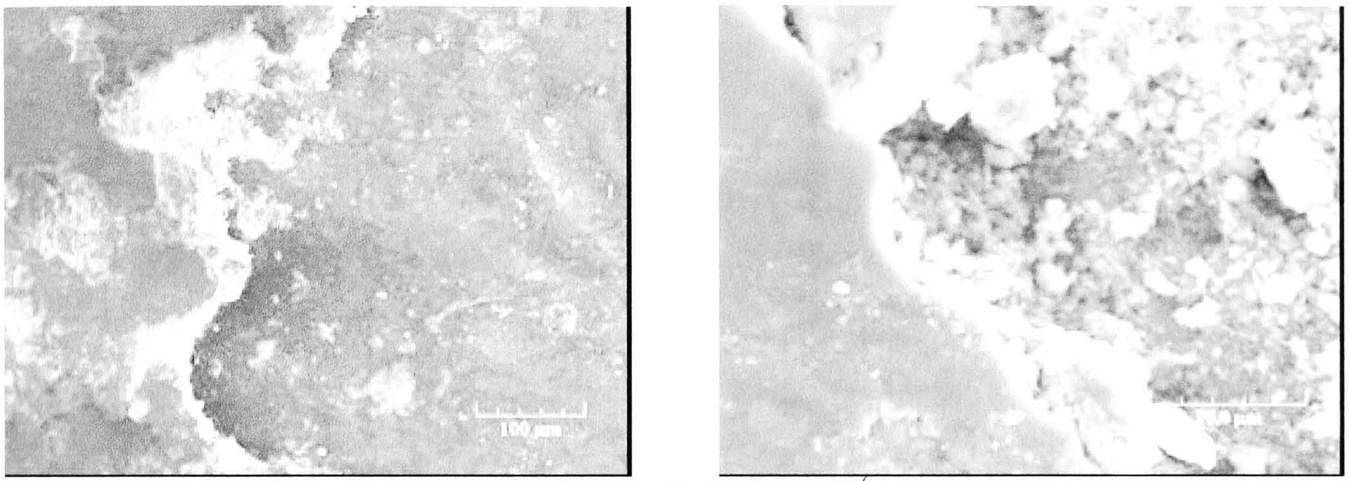

Pure Rolling, B=0T, N=4x10^6

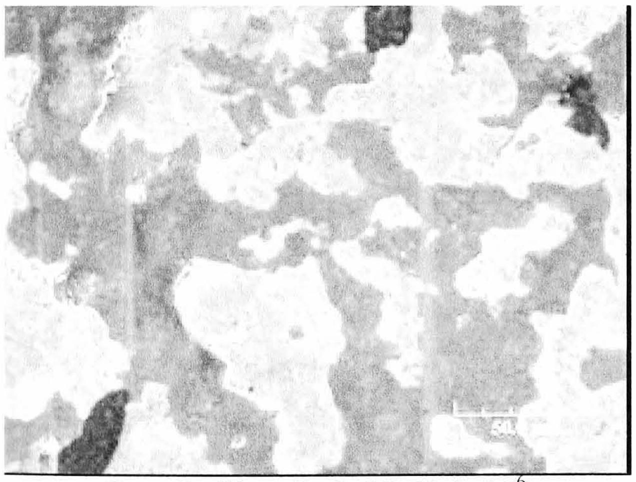

Pure Rolling, B=0.4T, N=1x10^6

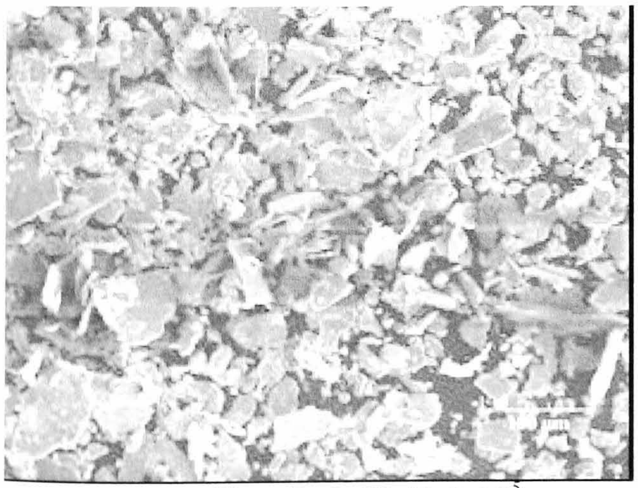

Pure Rolling, B=0.4T, N=5x10^5

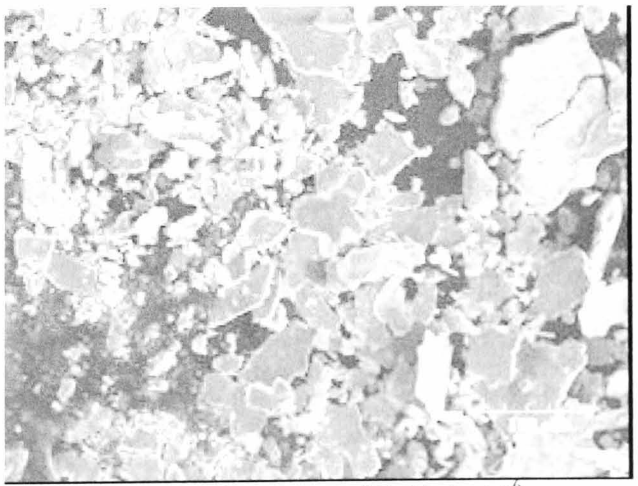

Pure Rolling, B=0.4T, N=1x10^6

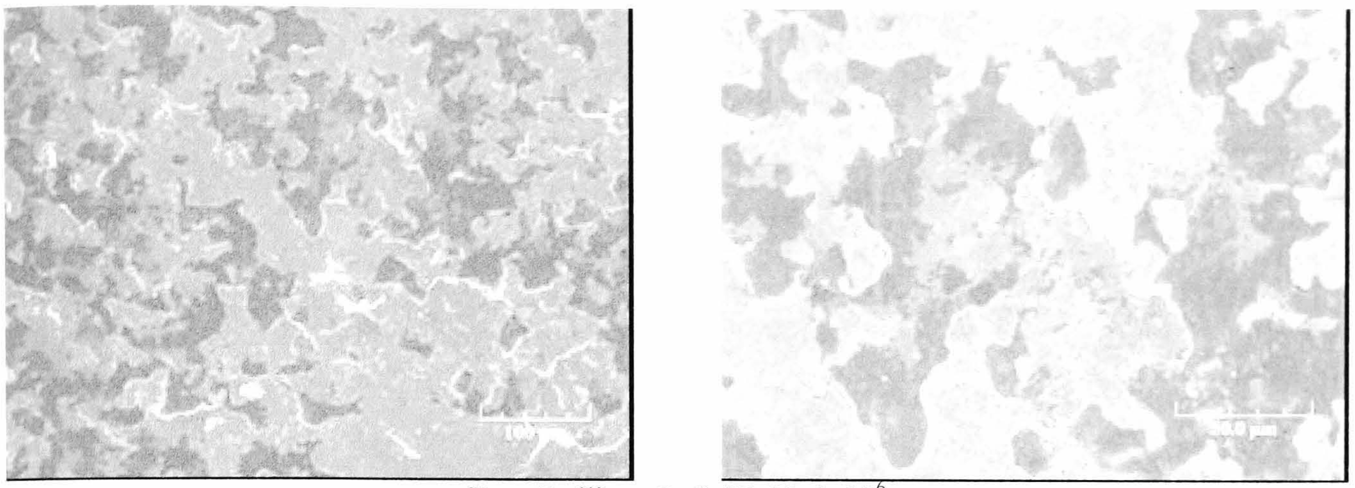

Pure Rolling, B=0.4T, N=5x10^6

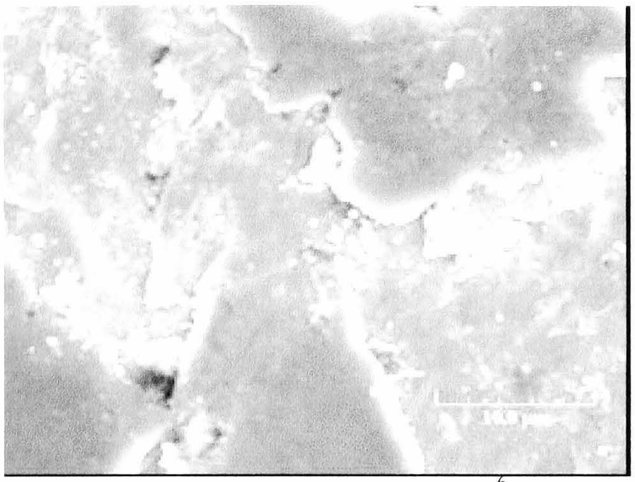

Pure Rolling, B=0.4T, N=5x10^6

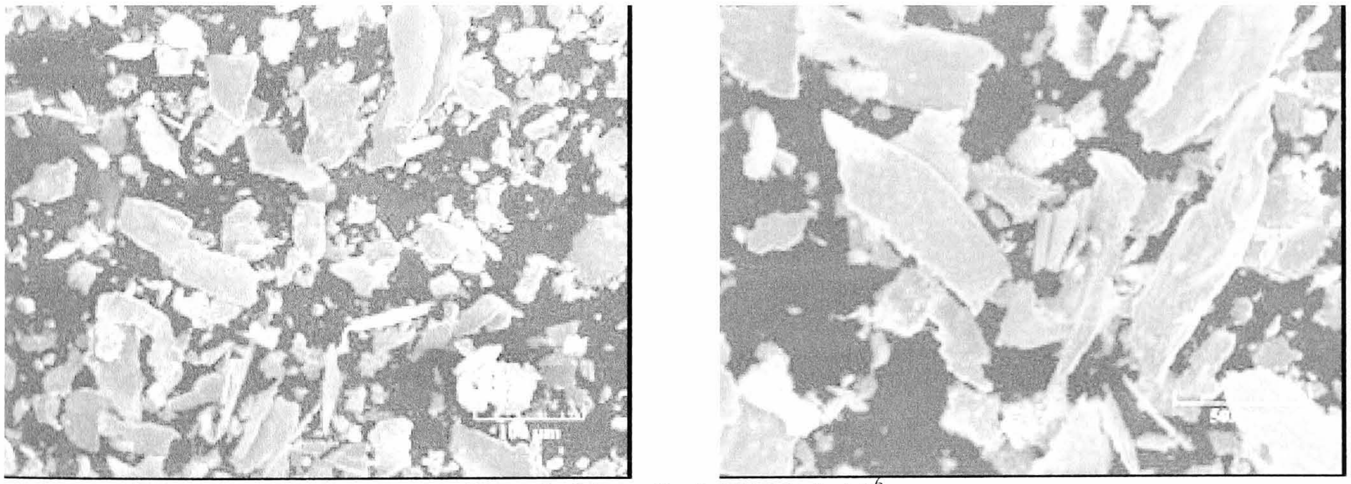

Pure Rolling, B=0.4T, N=5x10^6

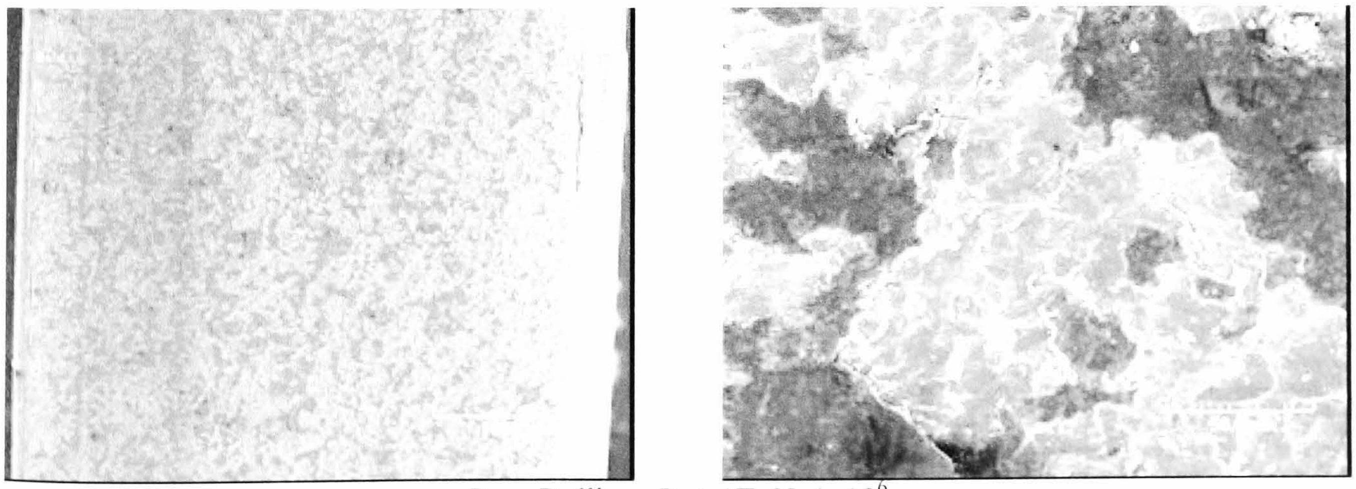

Pure Rolling, B=1.1T, N=1x10^6

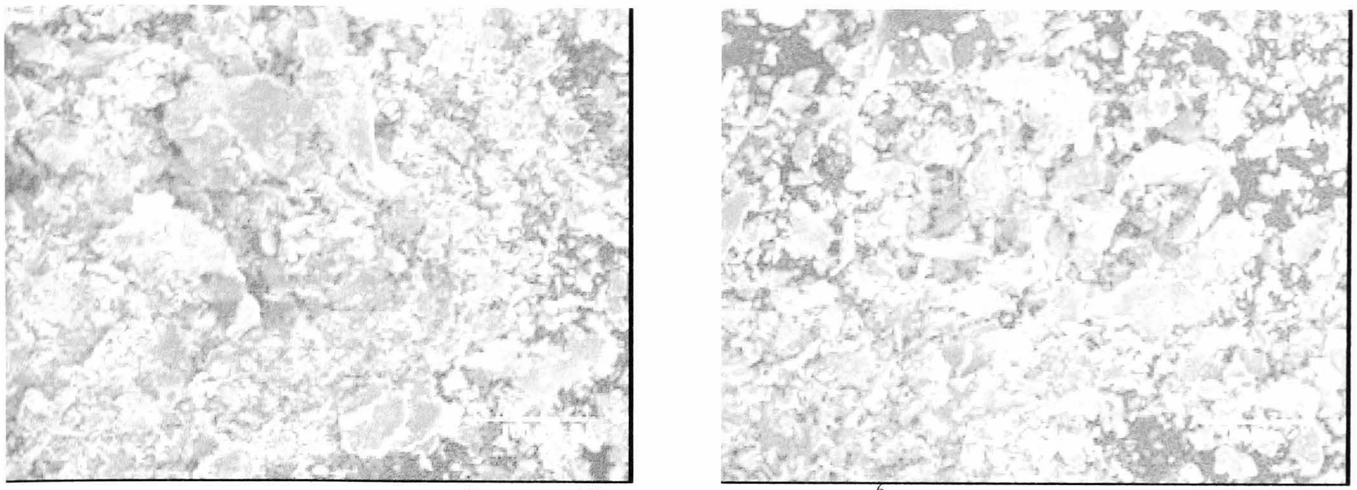

Pure Rolling, B=1.1T, N=1x10^6

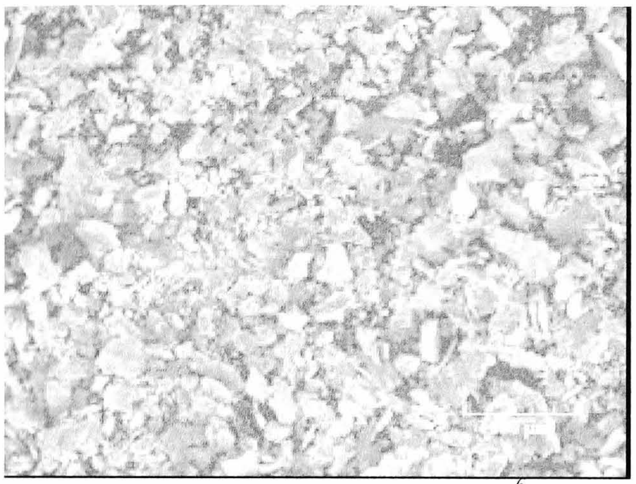

Pure Rolling, B=1.1T, N=1x10^6

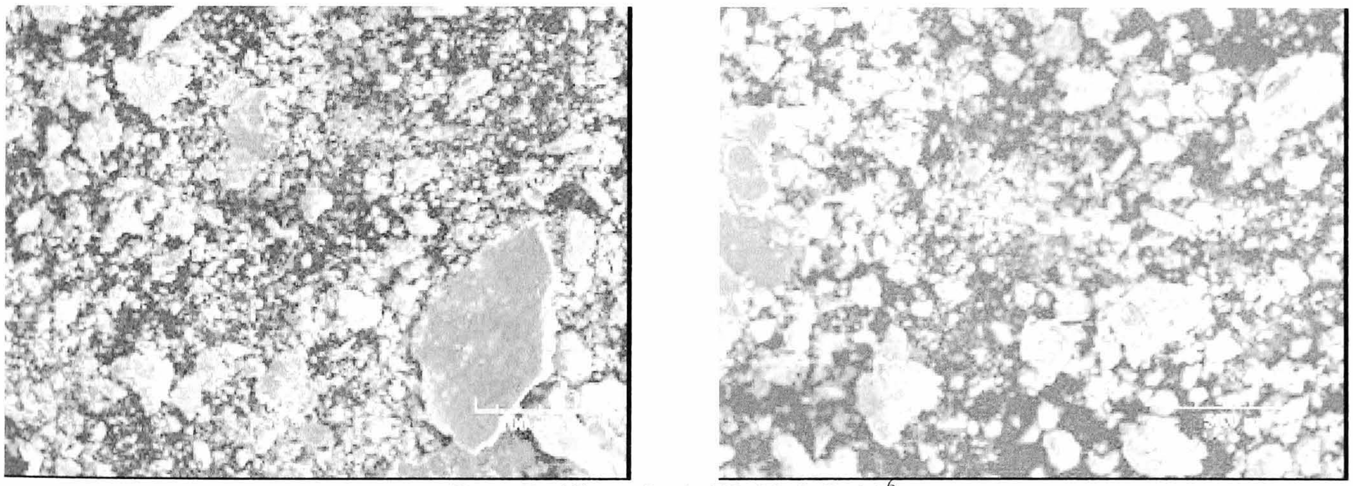

Pure Rolling, B=1.1T, N=3.5x10^6

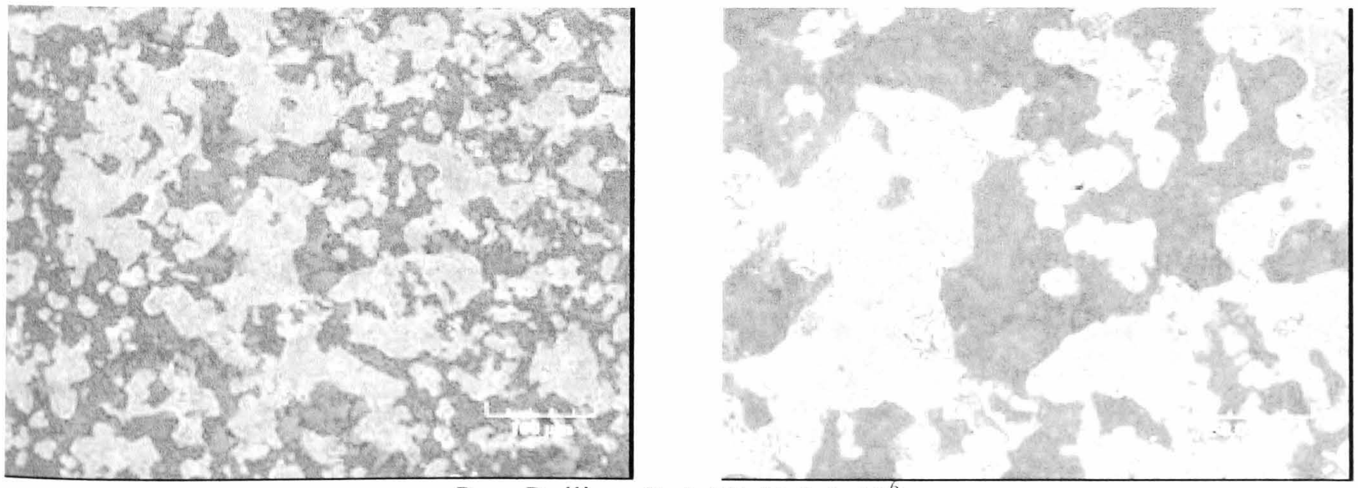

Pure Rolling, B=1.1T, N=3.5x10^6

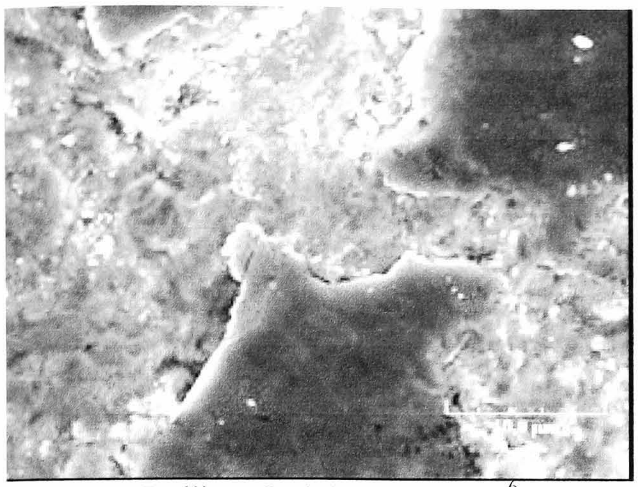

Pure Rolling, B=1.1T, N=3.5x10^6

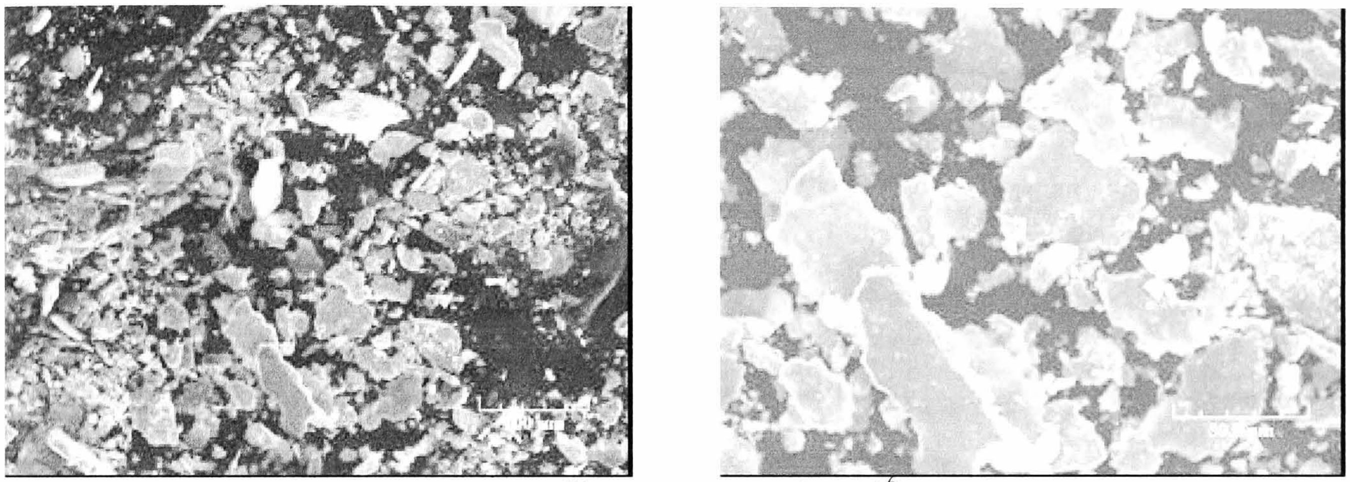

Pure Rolling, B=1.1T, N=3.5x10^6

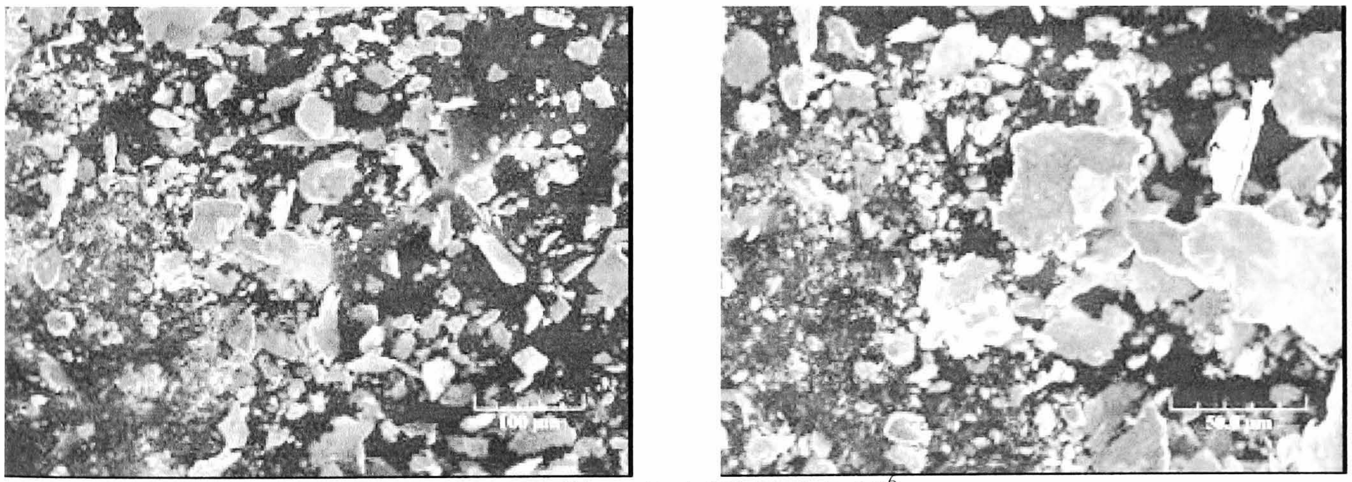

Pure Rolling, B=1.1T, N=3.5x10^6

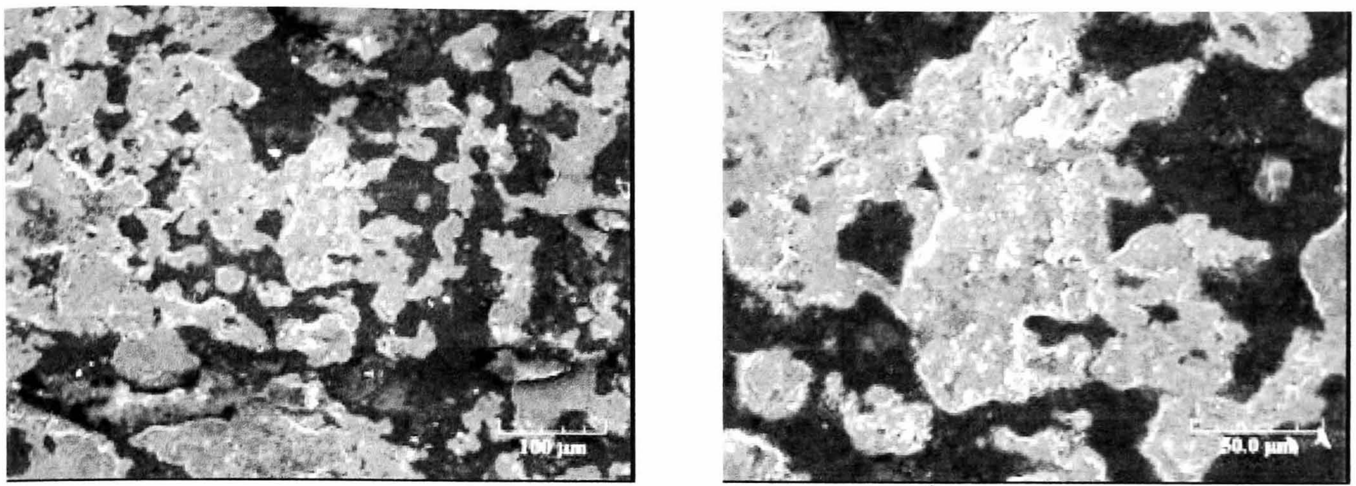

Pure Rolling, B=1.1T, θ=45°, N=1x10^{6}

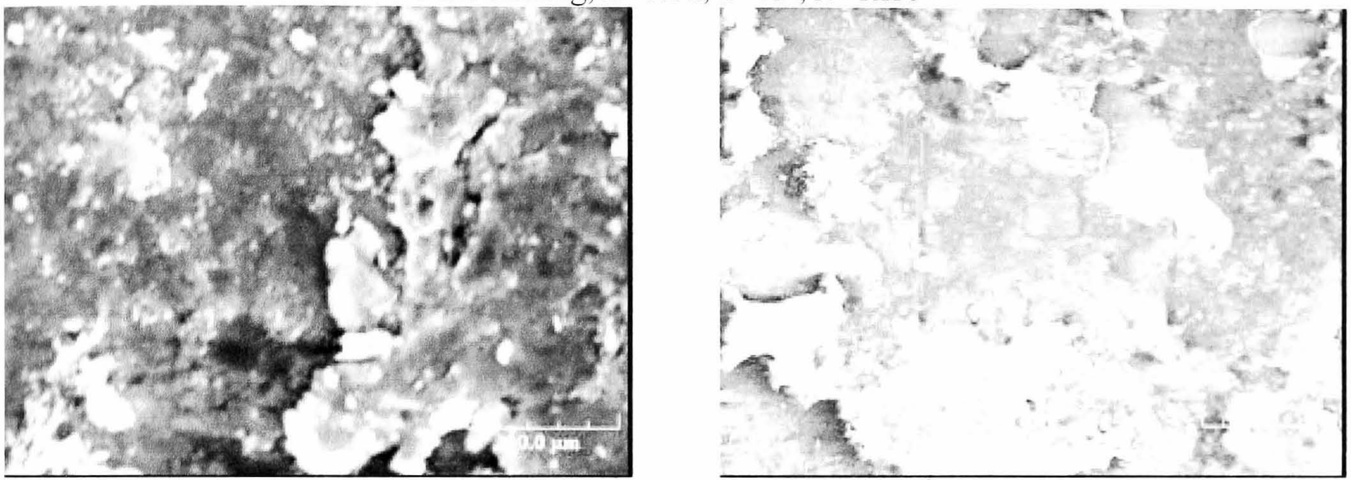

Pure Rolling, B=1.1T, θ=45°, N=1x10^{6}

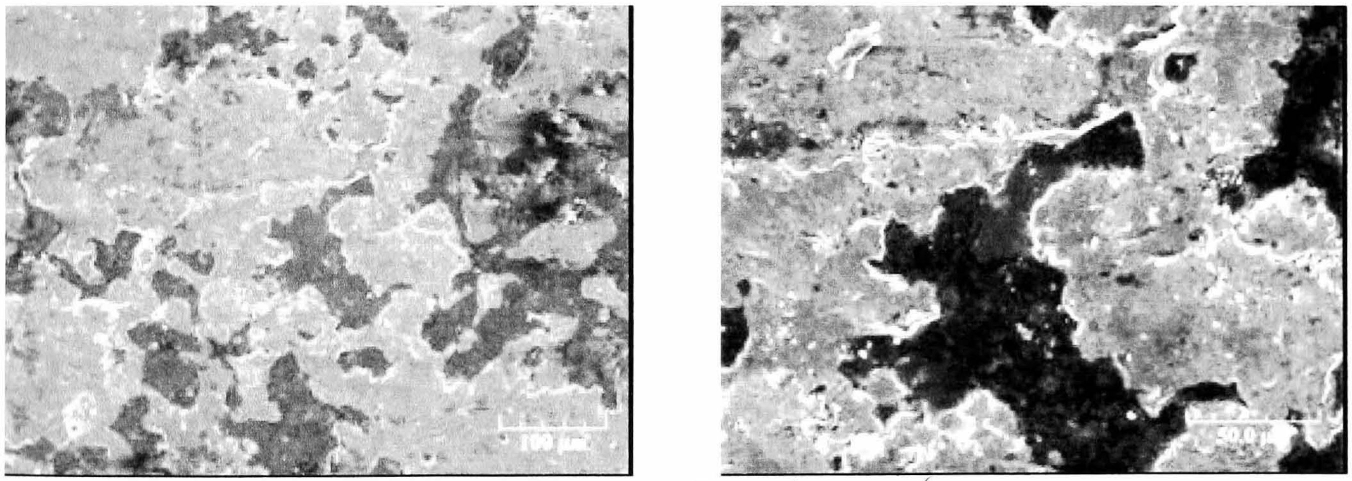

Pure Rolling, B=1.1T, θ=45°, N=1x10^{6}

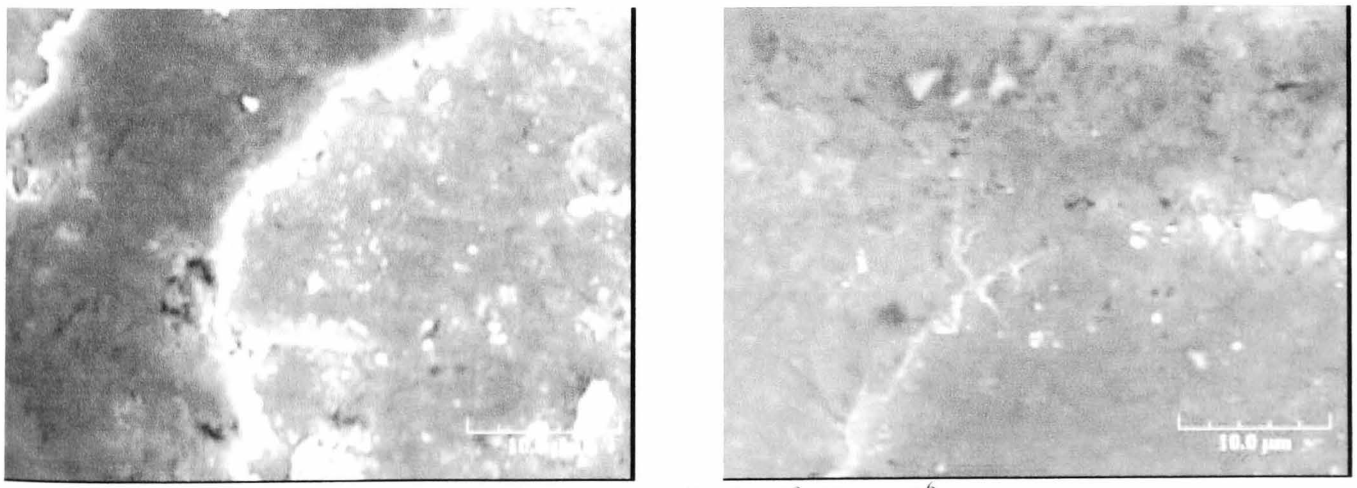

Pure Rolling, B=1.1T, θ=45°, N=1x10^{6}

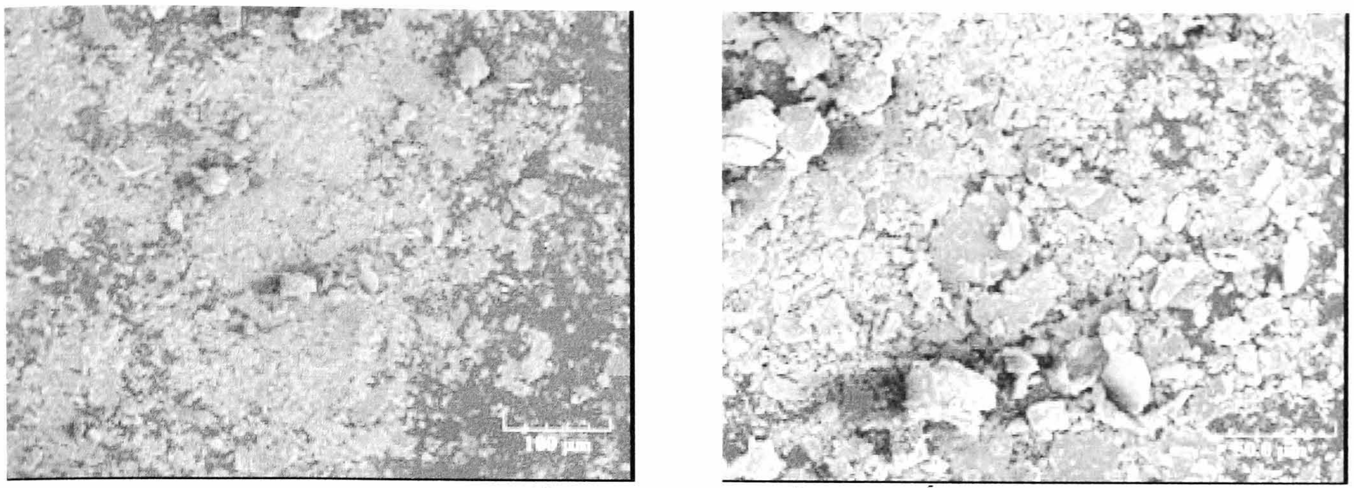

Pure Rolling, B=1.1T, θ=45°, N=5x10^5

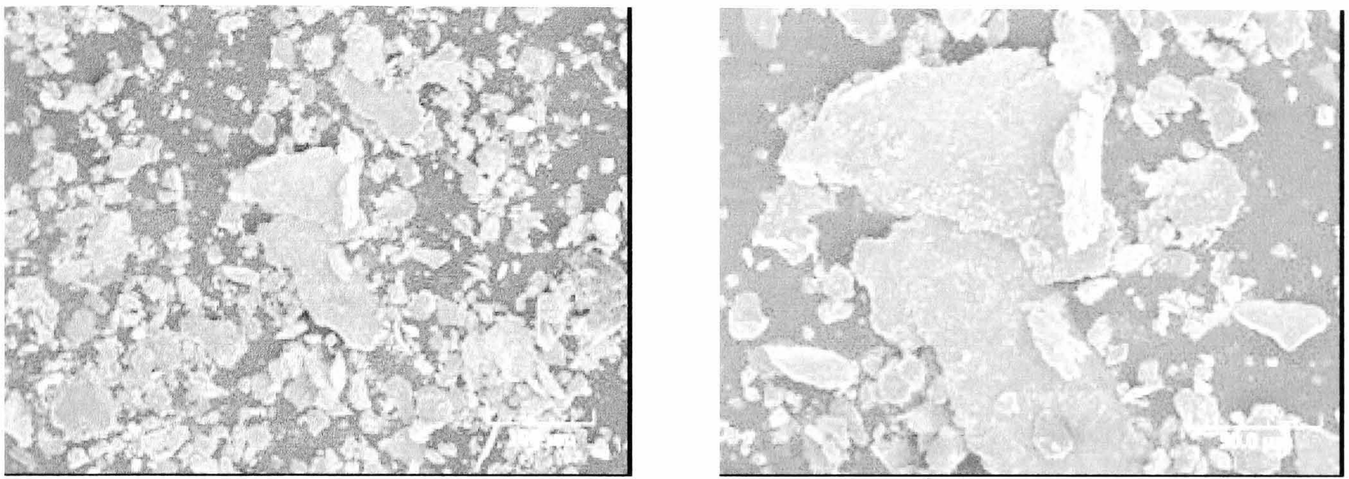

Pure Rolling, B=1.1T, θ=45°, N=1x10^6

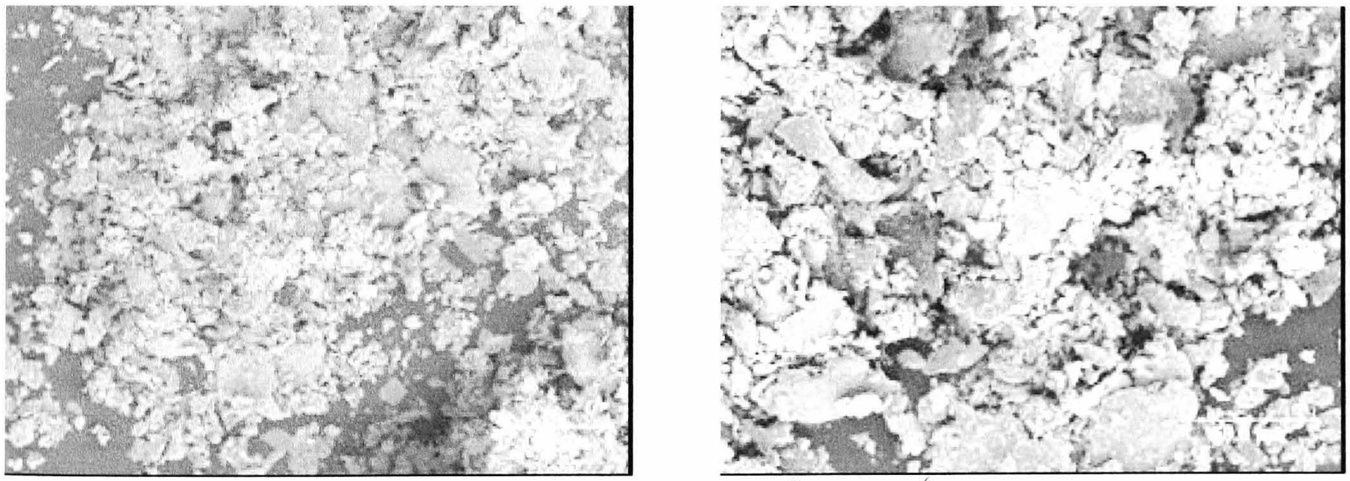

Pure Rolling, B=1.1T, θ=45°, N=3x10^6

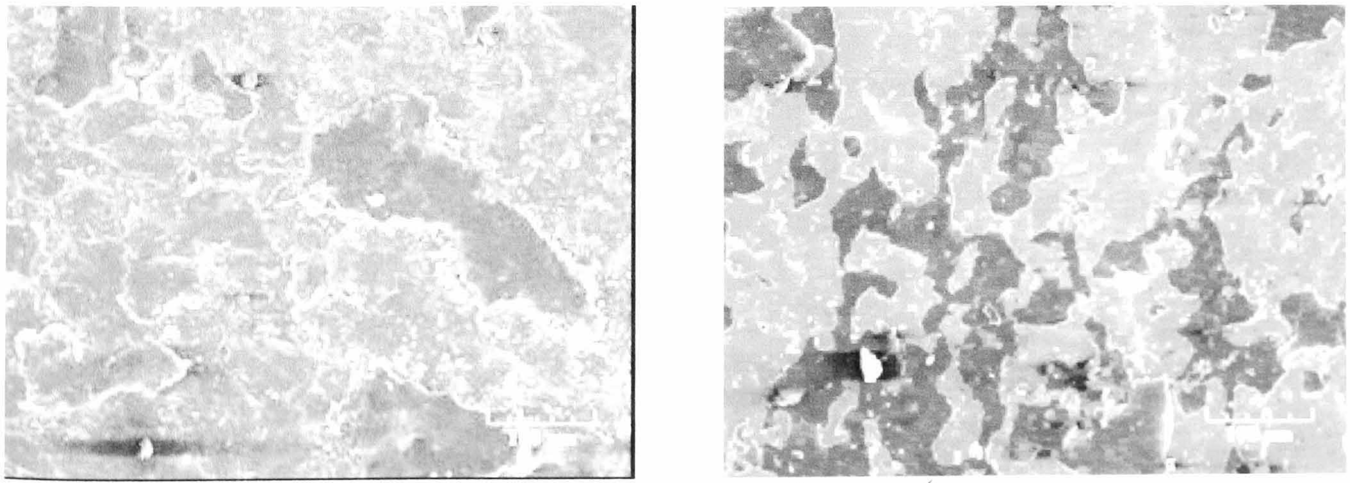

Pure Rolling, B=1.1T, θ=90°, N=1x10^6

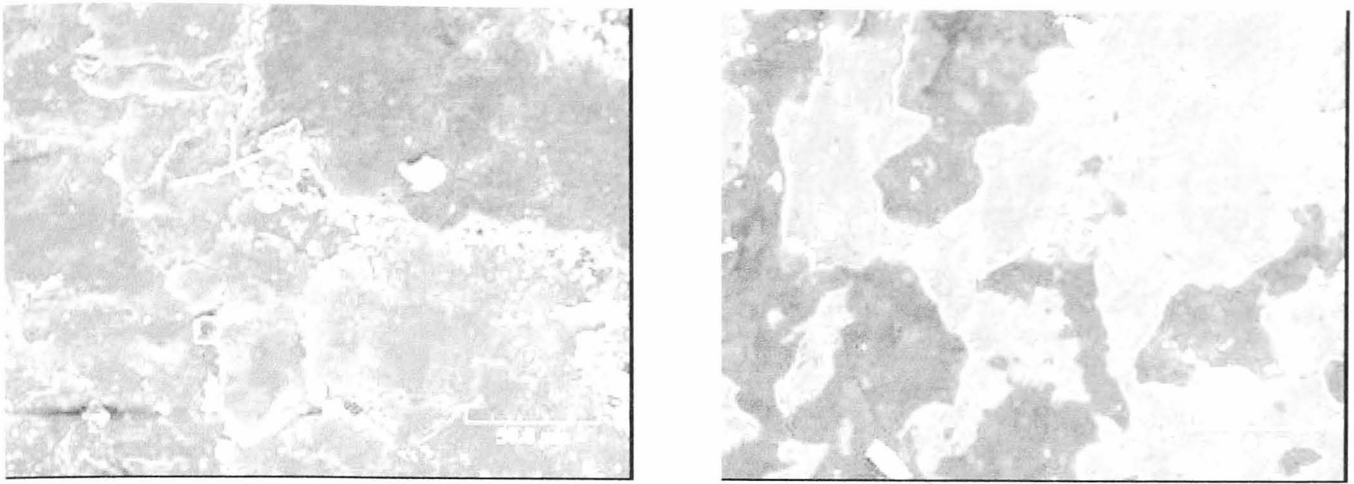

Pure Rolling, B=1.1T, θ=90°, N=1x10^6

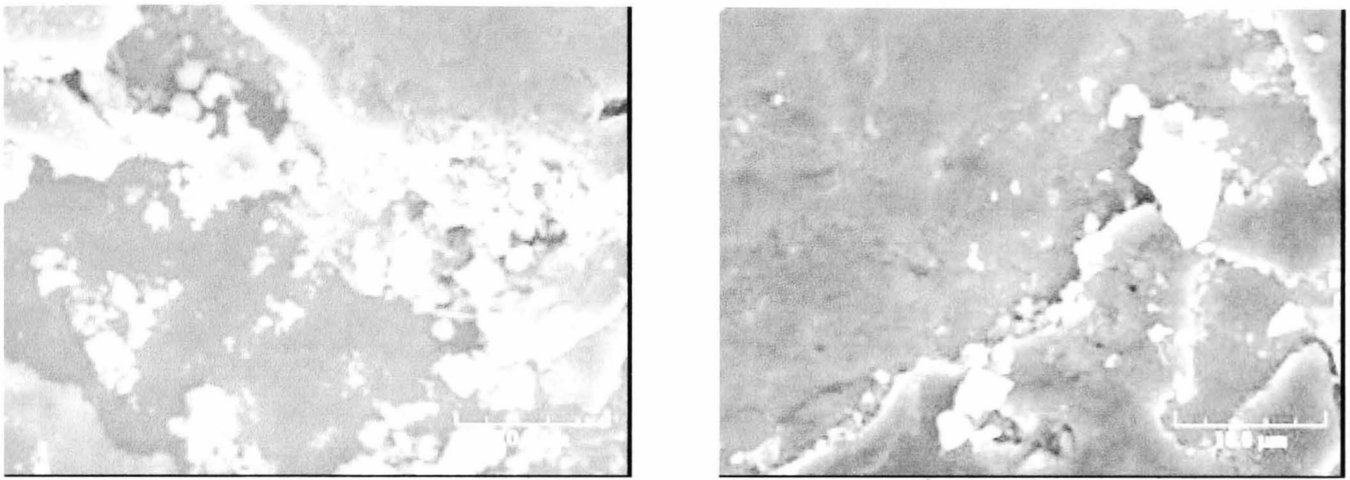

Pure Rolling, B=1.1T, θ=90°, N=1x10^6

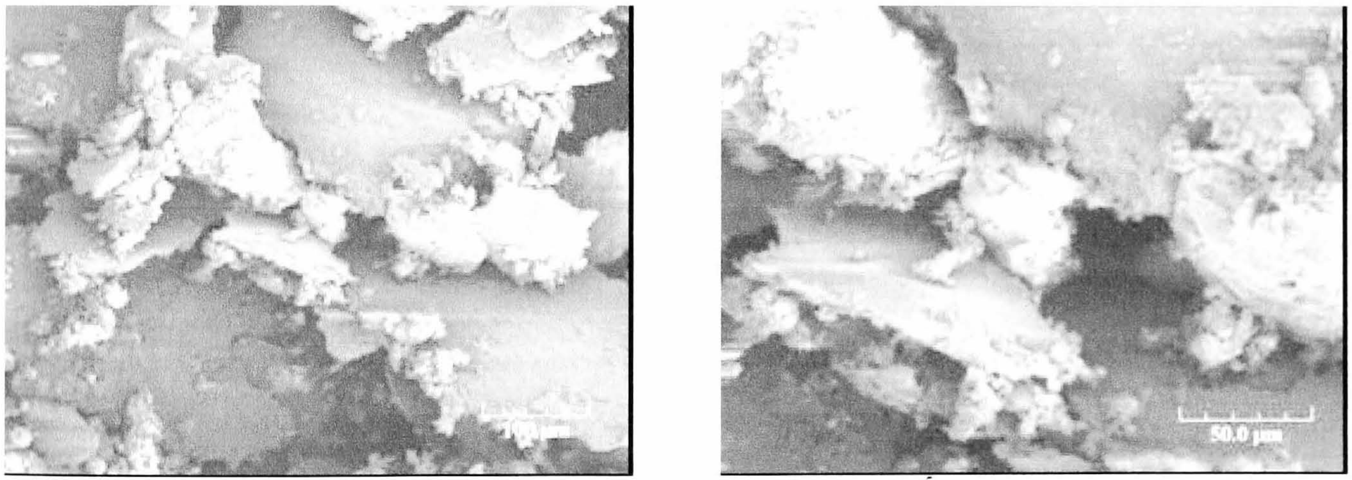

Pure Rolling, B=1.1T, θ=90°, N=5x10^5

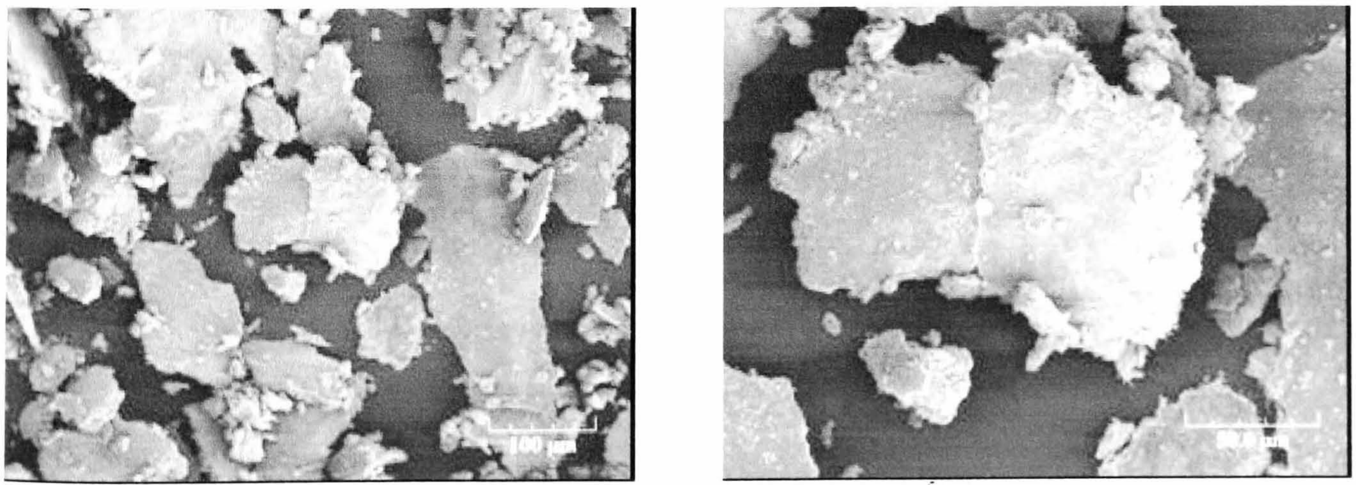

Pure Rolling, B=1.1T, θ=90°, N=5x10^5

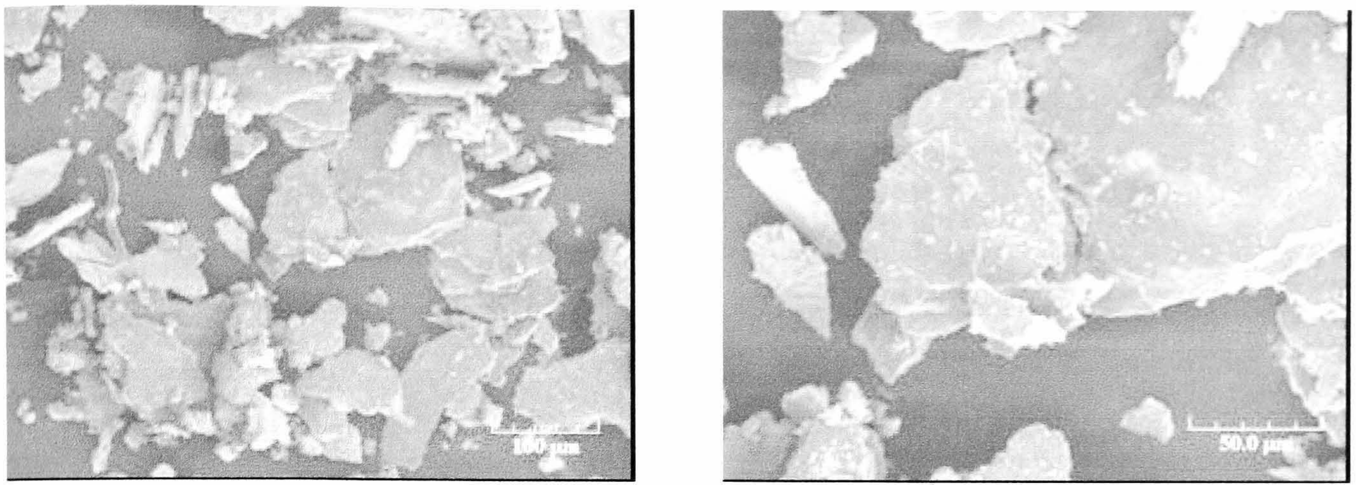

Pure Rolling, B=1.1T, θ=90°, N=1x10^6

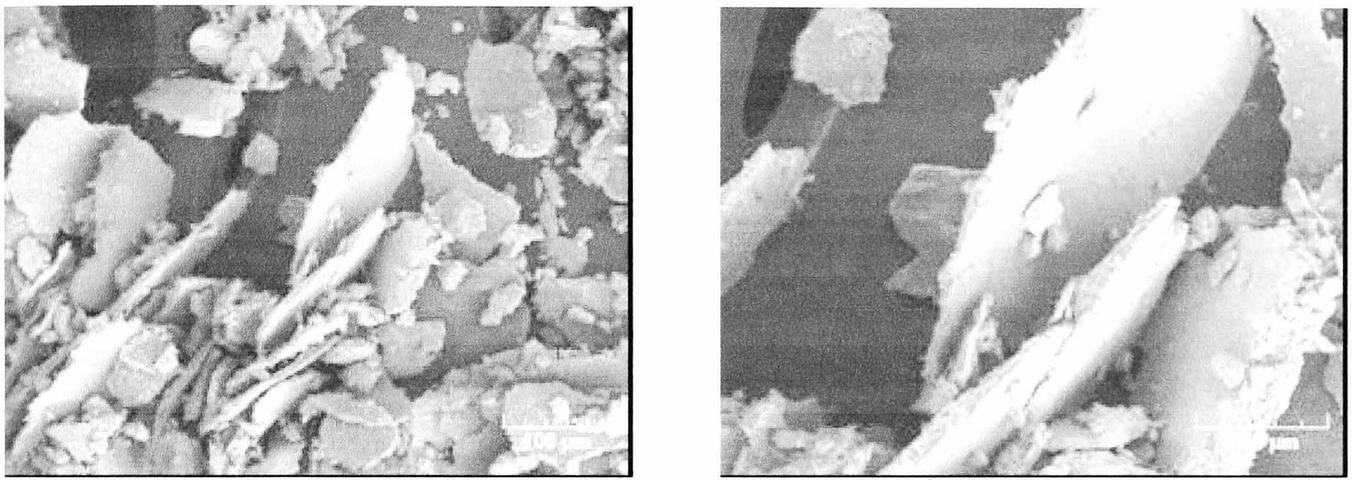

Pure Rolling, B=1.1T, θ=90°, N=1x10^6

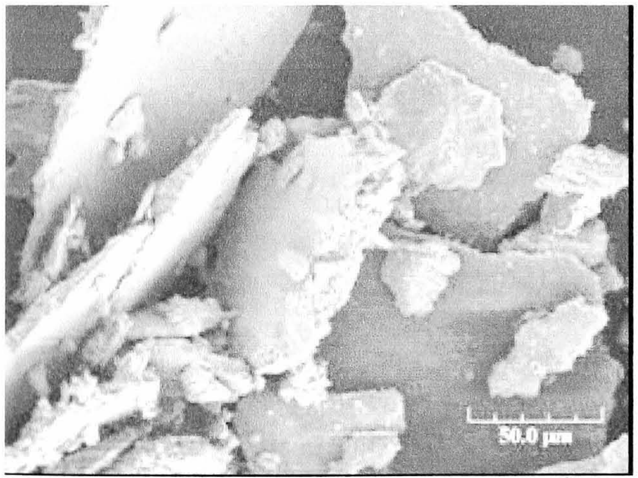

Pure Rolling, B=1.1T, θ=90°, N=1x10^6

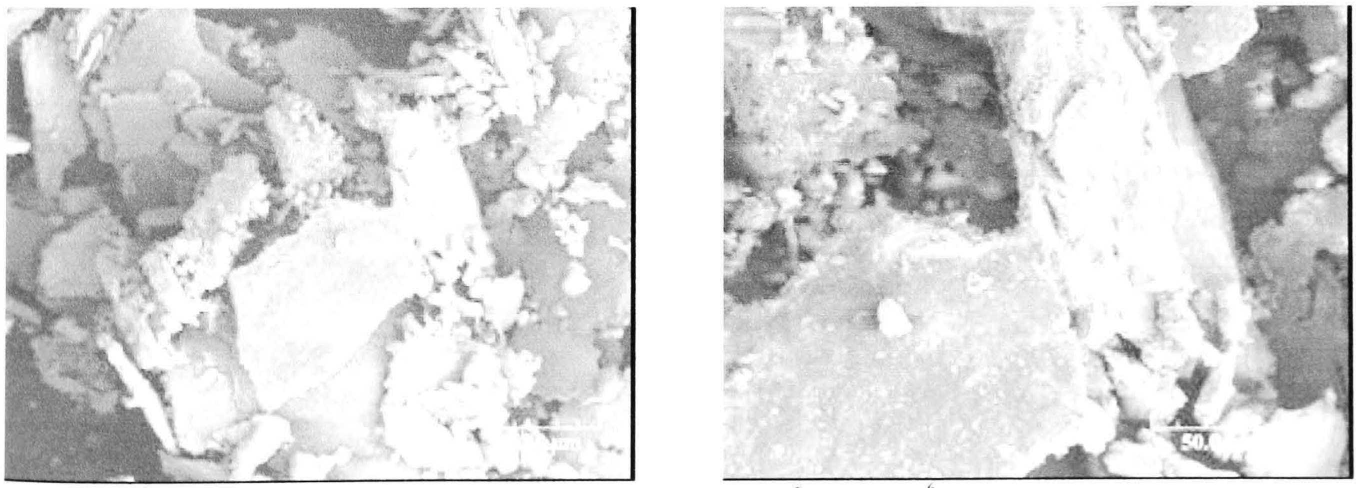

Pure Rolling, B=1.1T, θ=90°, N=3x10^6

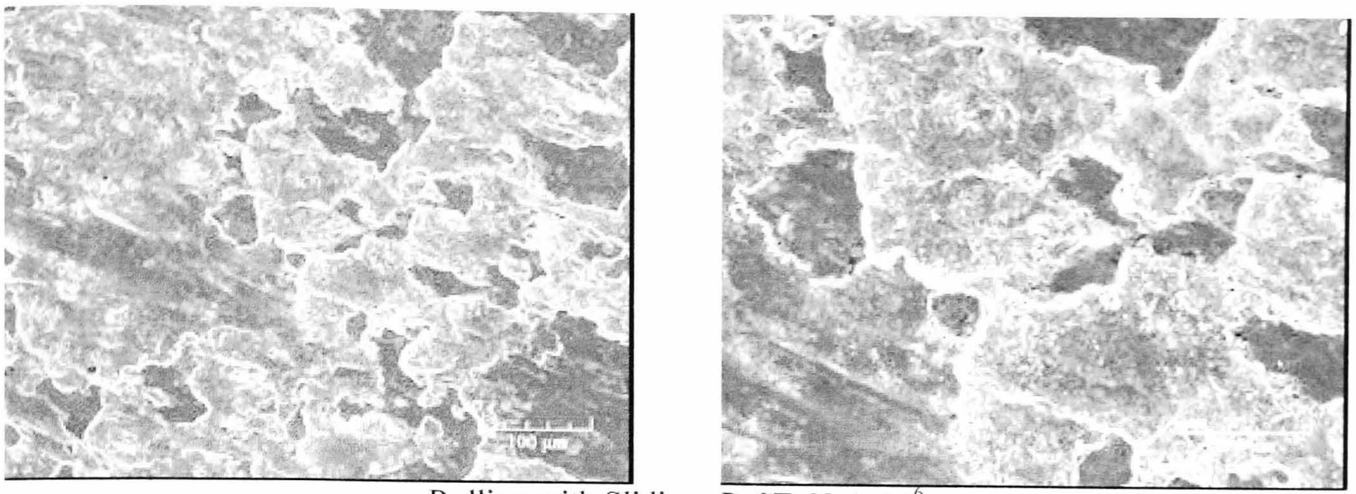

Rolling with Sliding, B=0T, N=1x10^6

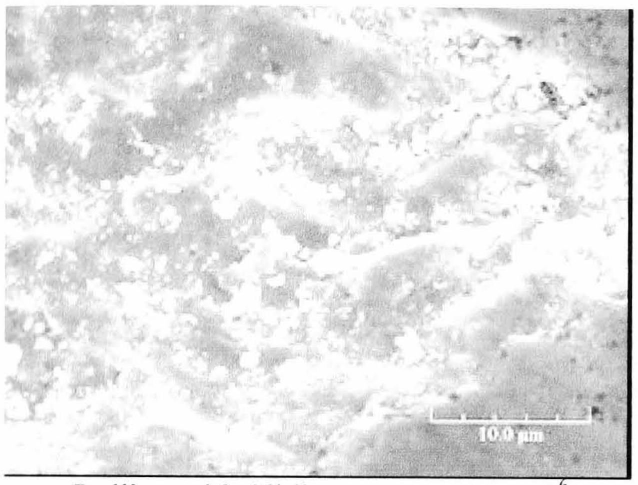

Rolling with Sliding, B=0T, N=1x10^6

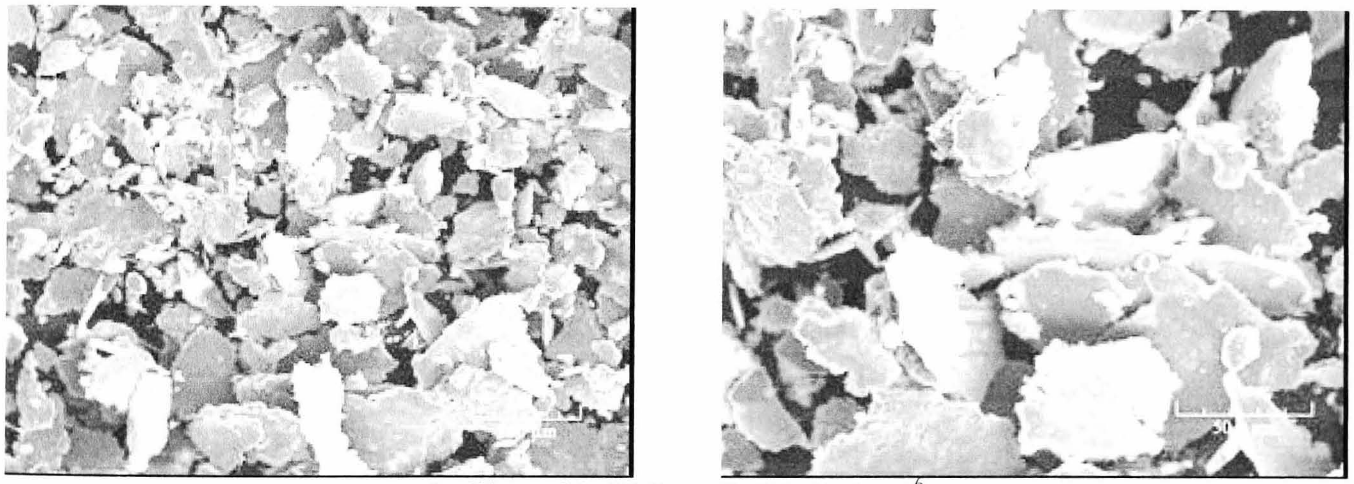

Rolling with Sliding, B=0T, N=1x10^6

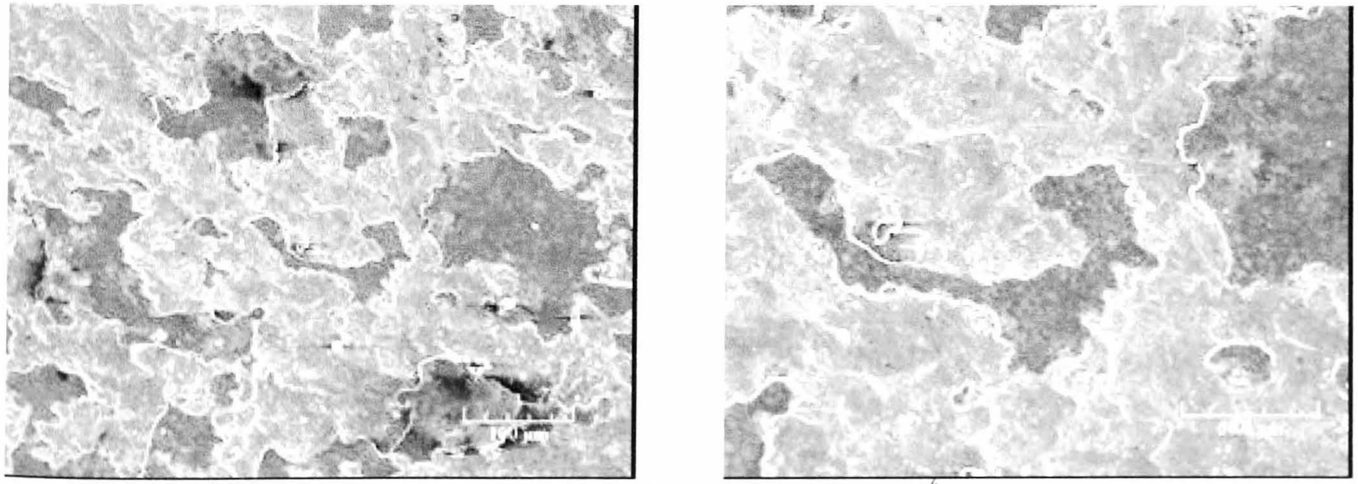

Rolling with Sliding, B=0.4T, N=1x10^6

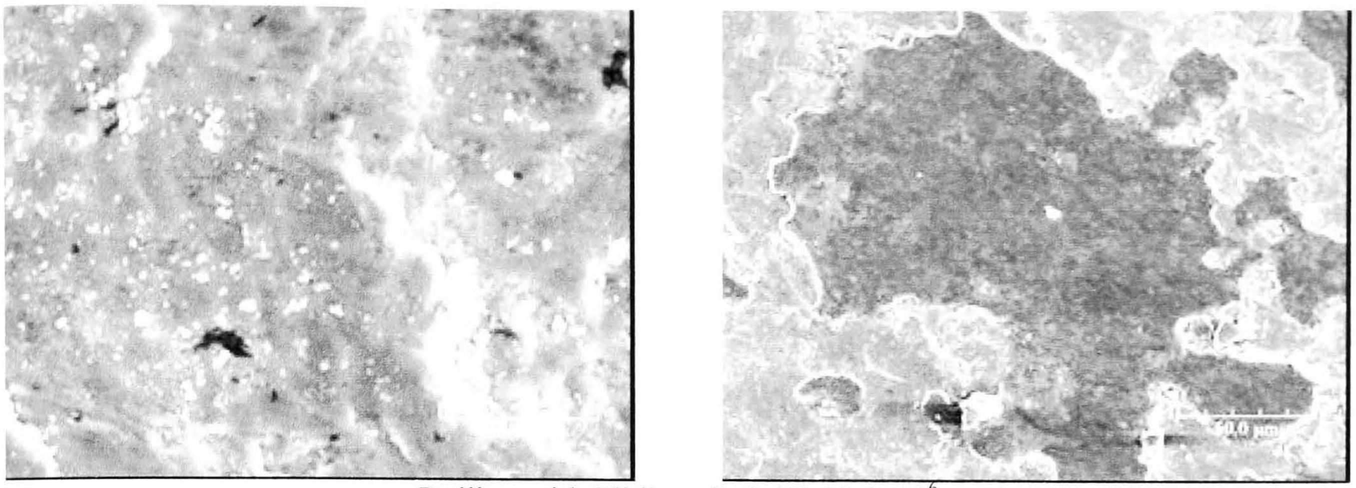

Rolling with Sliding, *B*=0.4T, *N*=$1\text{x}10^6$

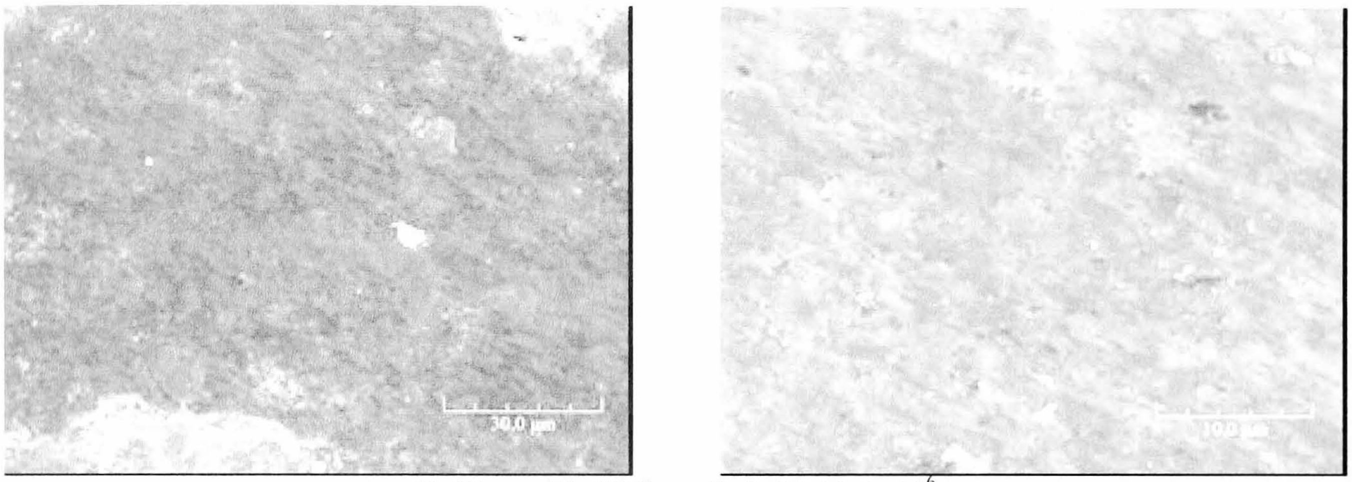

Rolling with Sliding, *B*=0.4T, *N*=$1\text{x}10^6$

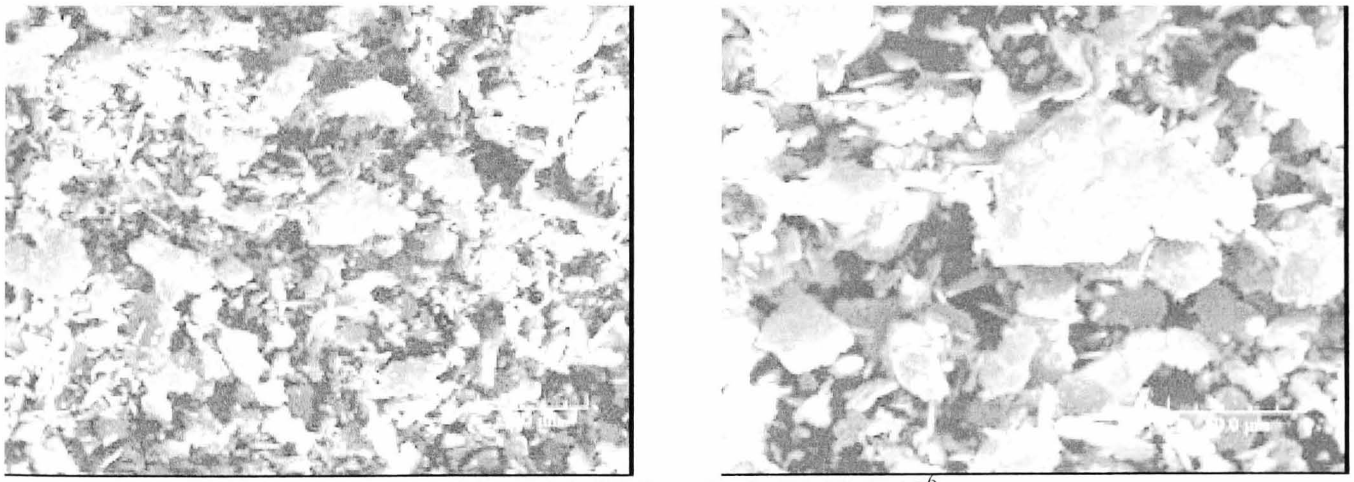

Rolling with Sliding, *B*=0.4T, *N*=$1\text{x}10^6$

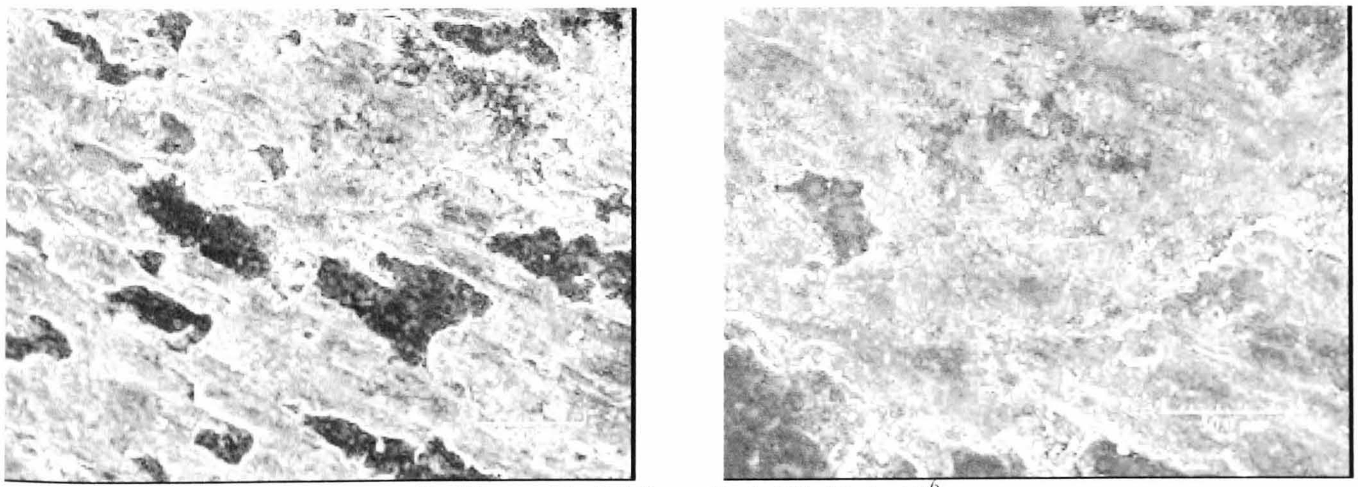

Rolling with Sliding, *B*=1.1T, *N*=$1\text{x}10^6$

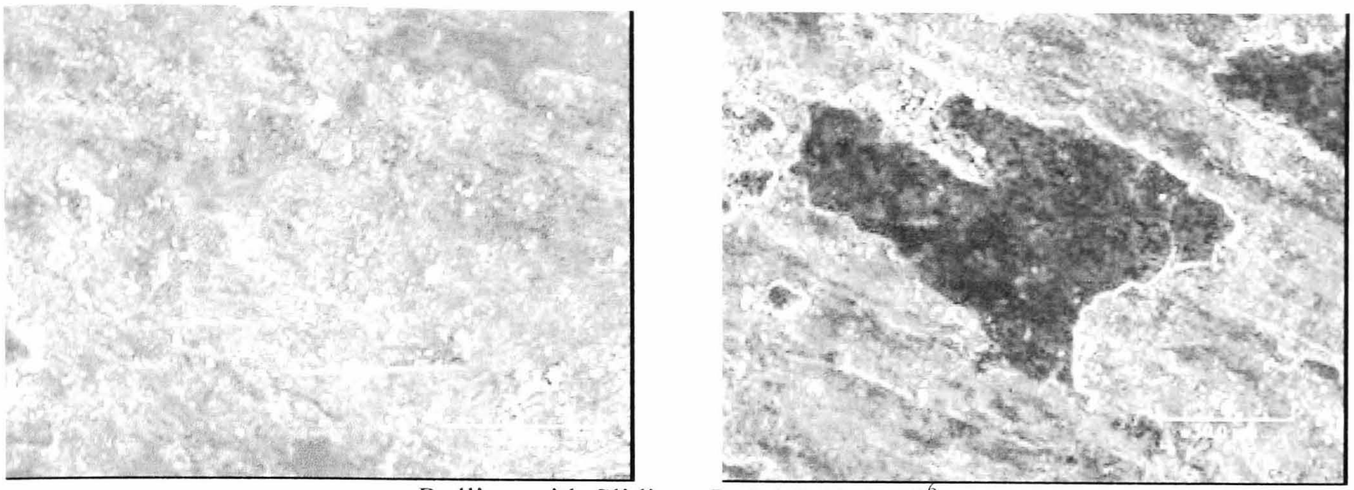

Rolling with Sliding, B=1.1T, N=1x10^6

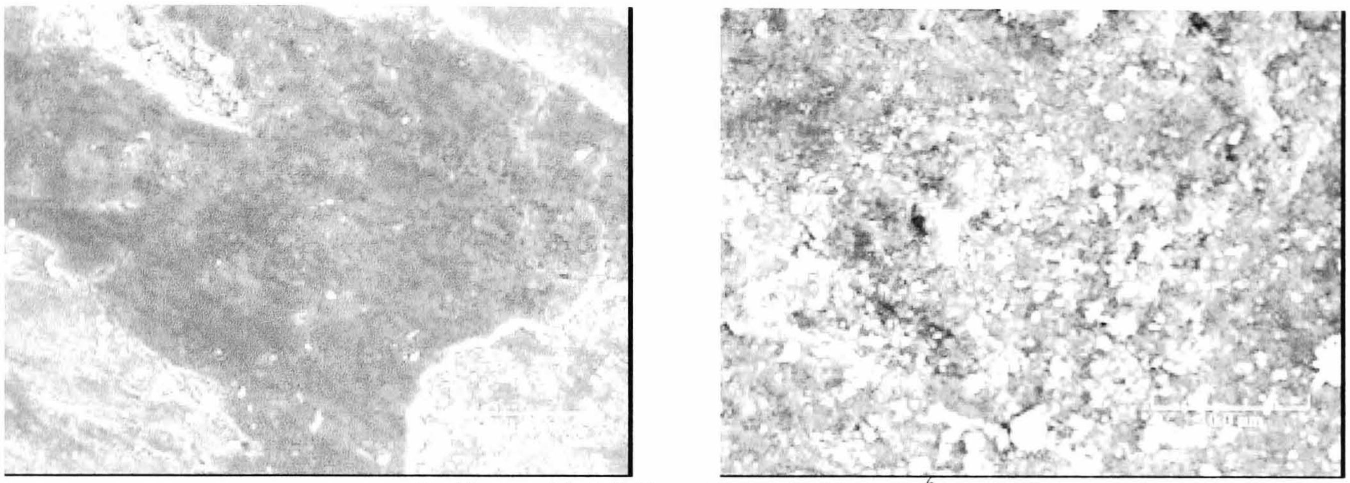

Rolling with Sliding, B=1.1T, N=1x10^6

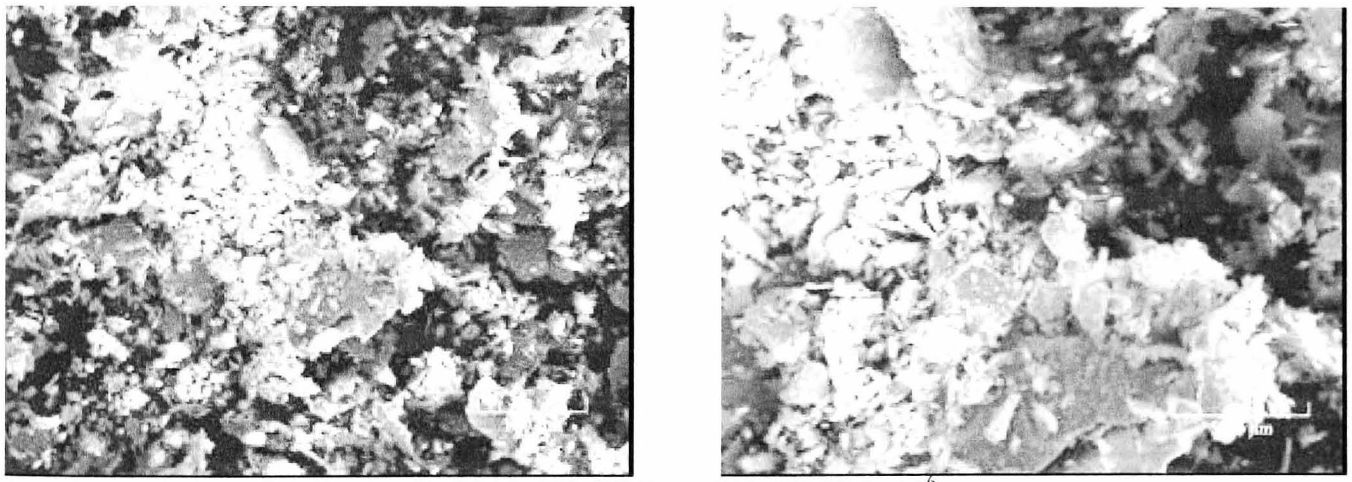

Rolling with Sliding, B=1.1T, N=1x10^6

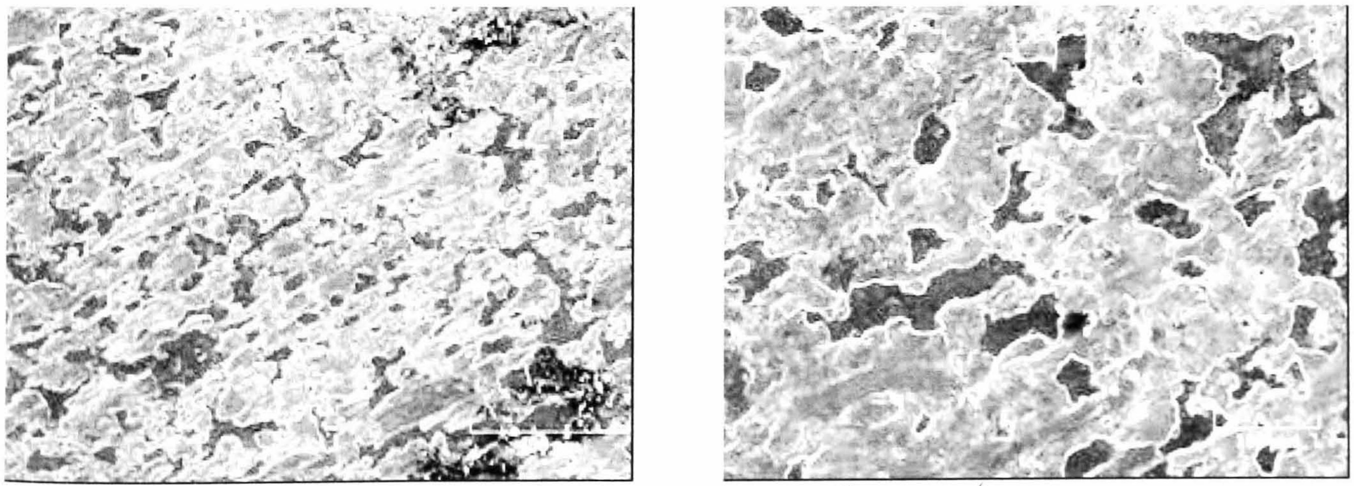

Rolling with Sliding, B=1.1T, θ=45°, N=1x10^6

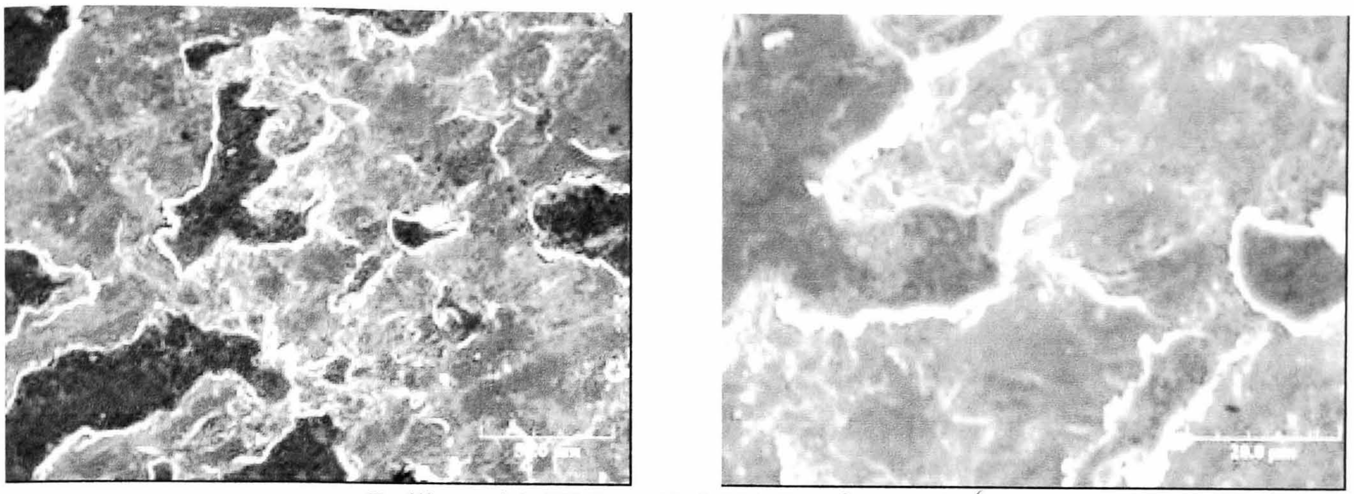

Rolling with Sliding, B=1.1T, θ=45°, N=1x10^6

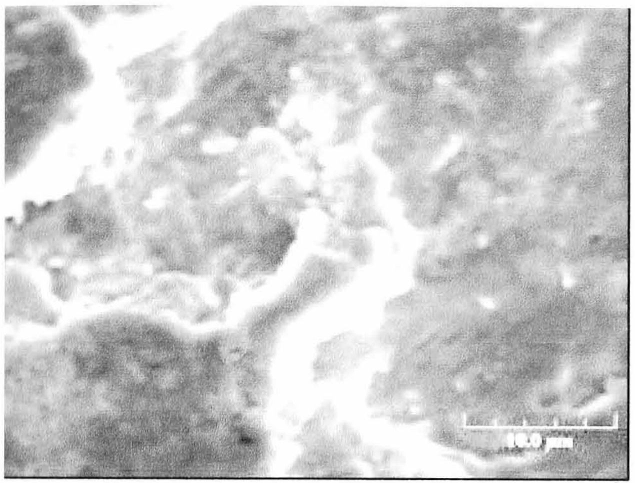

Rolling with Sliding, B=1.1T, θ=45°, N=1x10^6

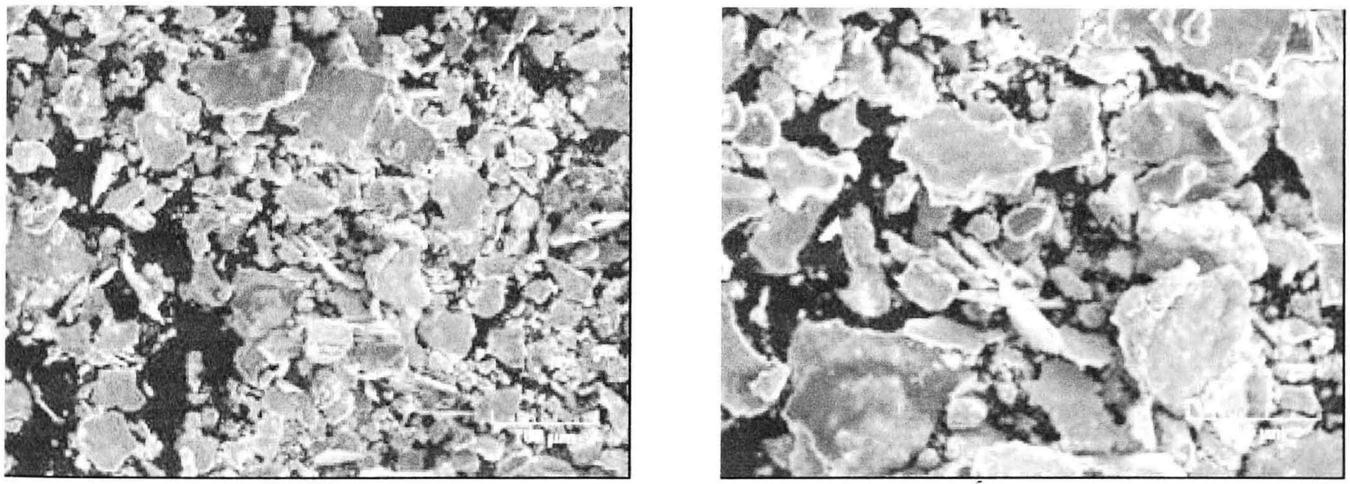

Rolling with Sliding, B=1.1T, θ=45°, N=5x10^5

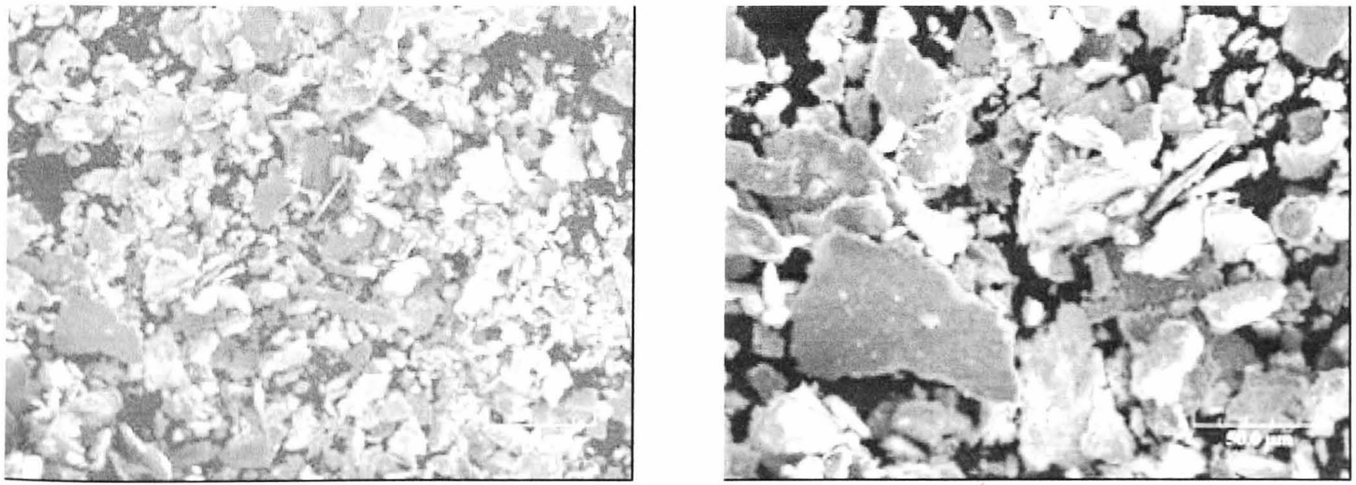

Rolling with Sliding, B=1.1T, θ=45°, N=1x10^6

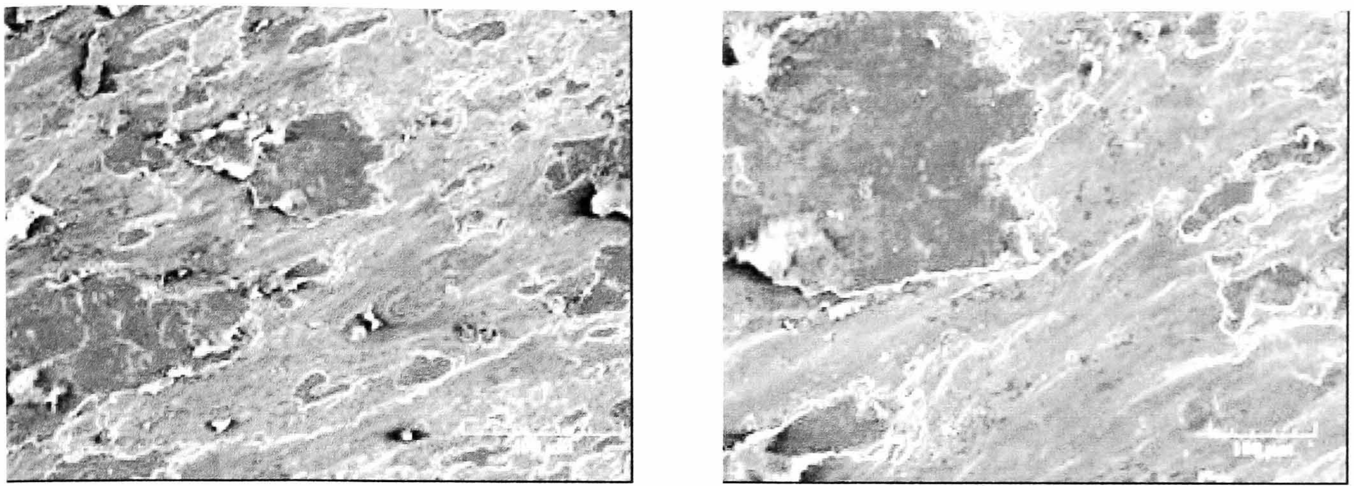

Rolling with Sliding, B=1.1T, θ=90°, N=1x10^{6}

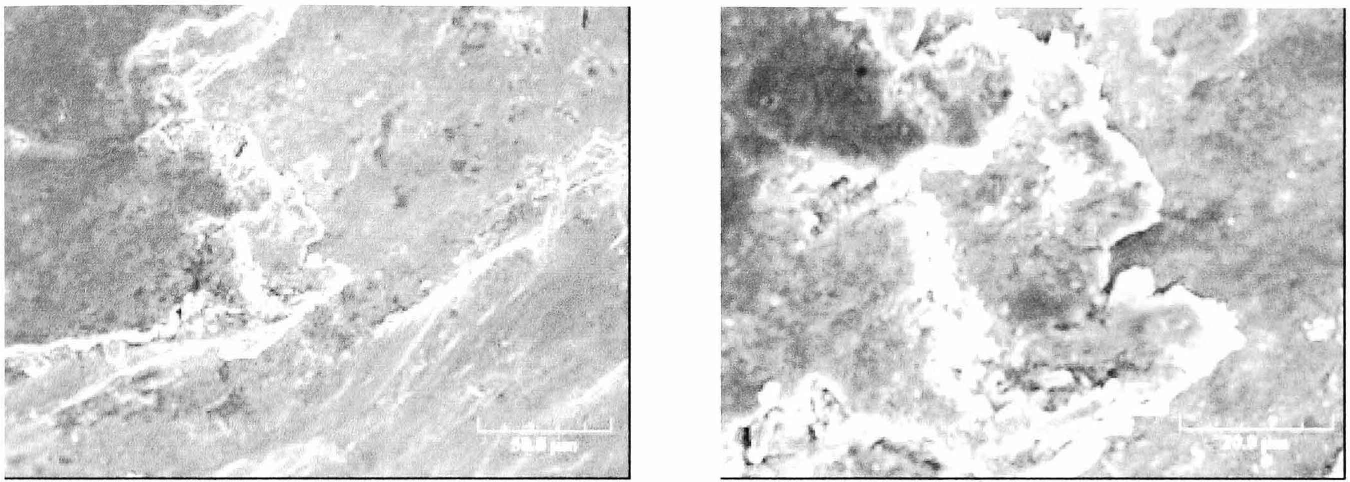

Rolling with Sliding, B=1.1T, θ=90°, N=1x10^{6}

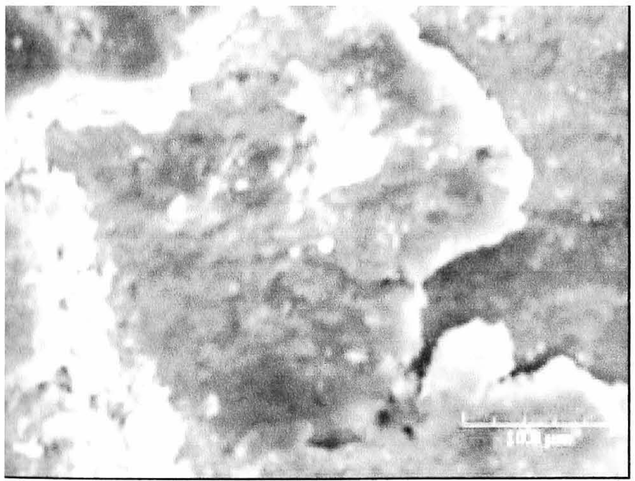

Rolling with Sliding, B=1.1T, θ=90°, N=1x10^{6}

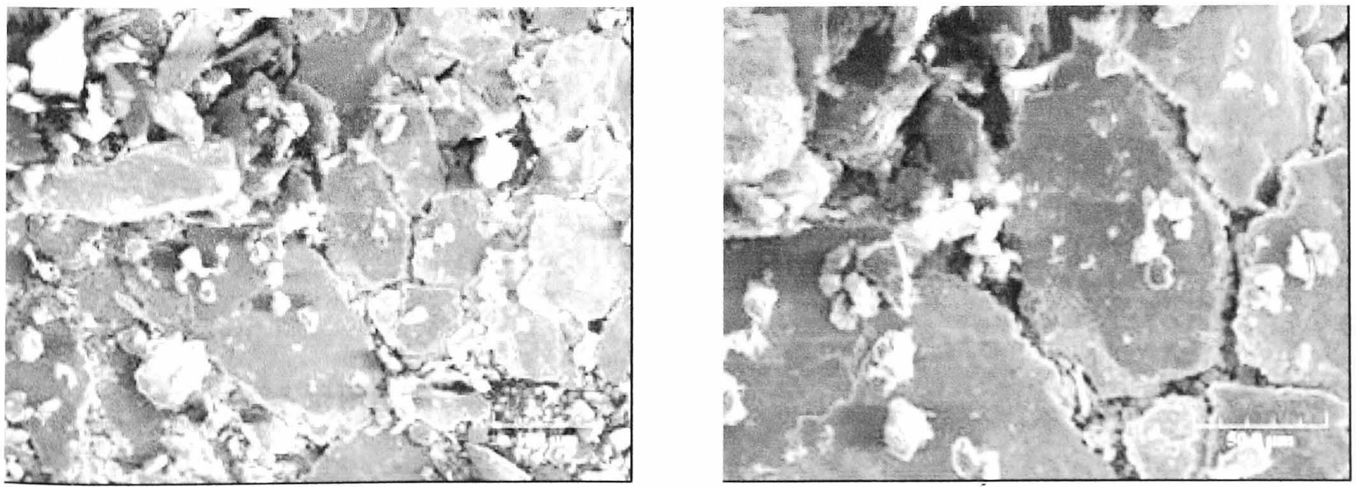

Rolling with Sliding, B=1.1T, θ=90°, N=5x10^{5}

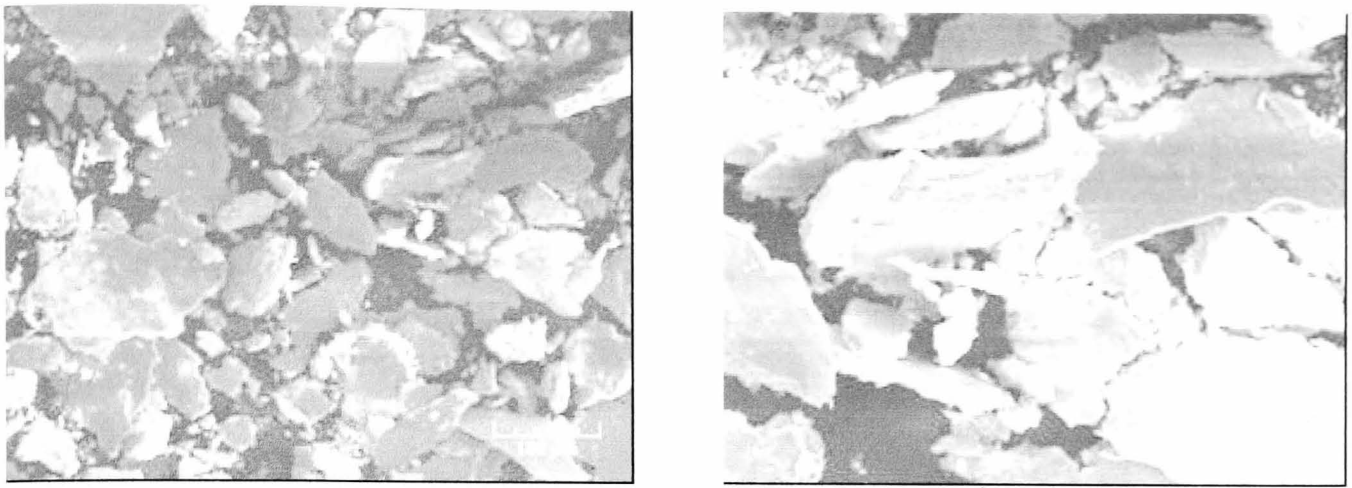

Rolling with Sliding, B=1.1T, θ=90^o, N=1x10^6

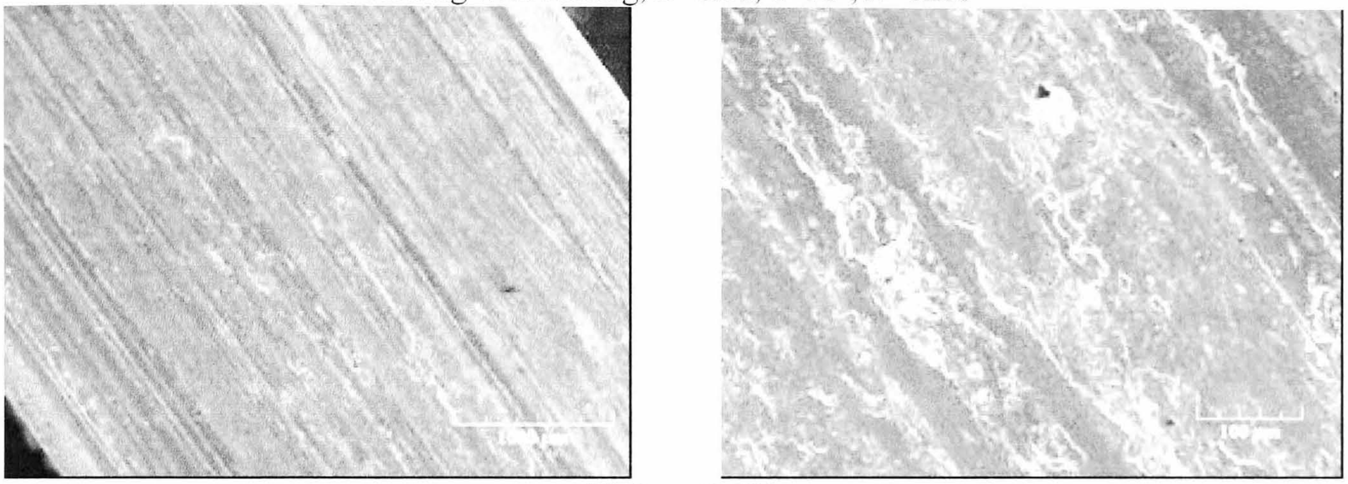

Sliding, B=0T

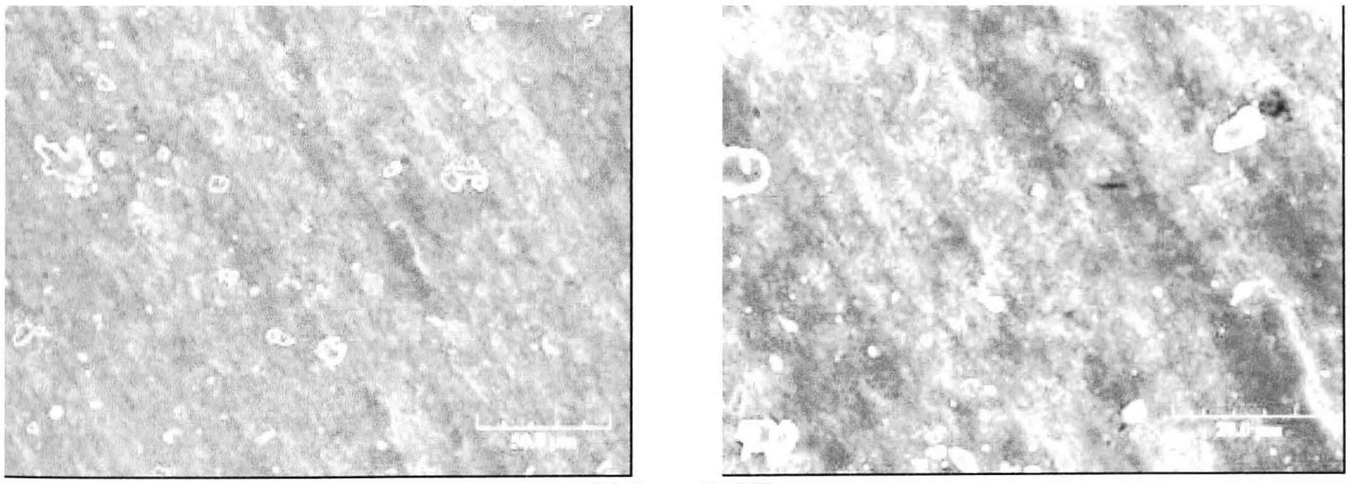

Sliding, B=0T

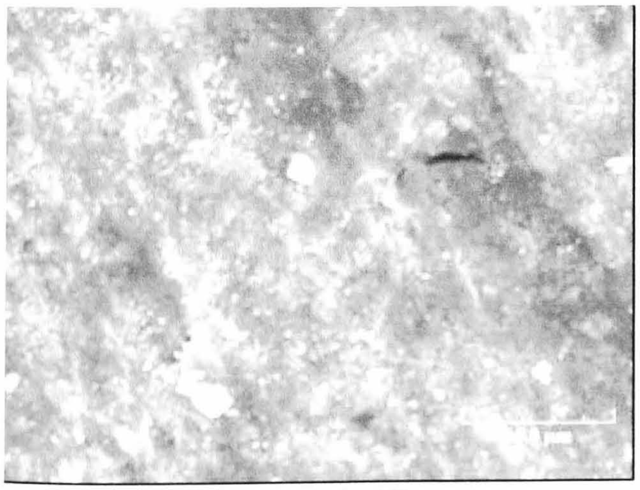

Sliding, B=0T

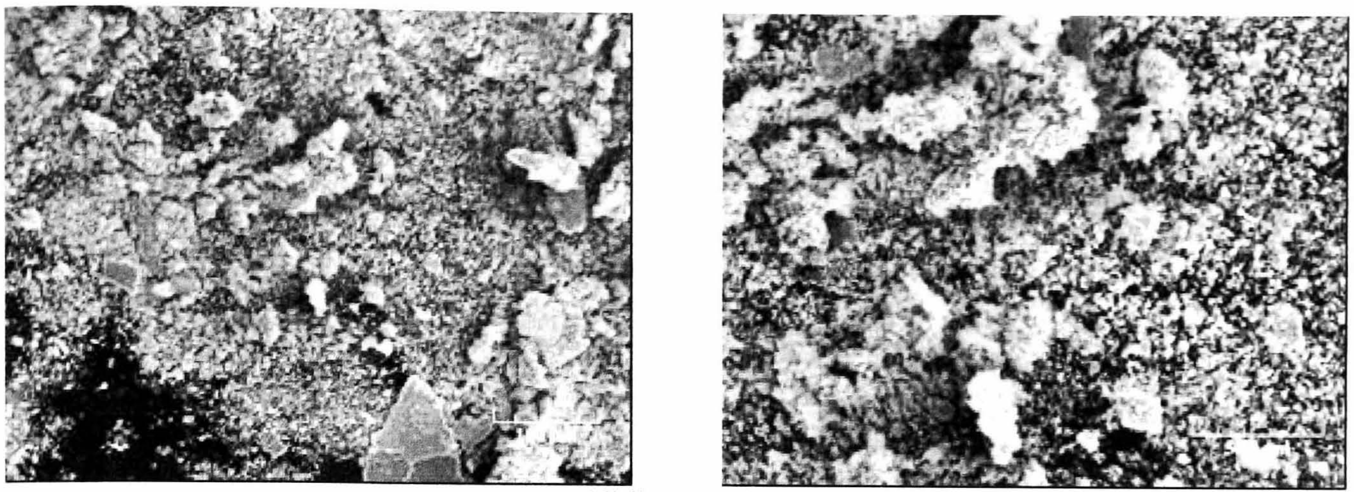

Sliding, B=0T

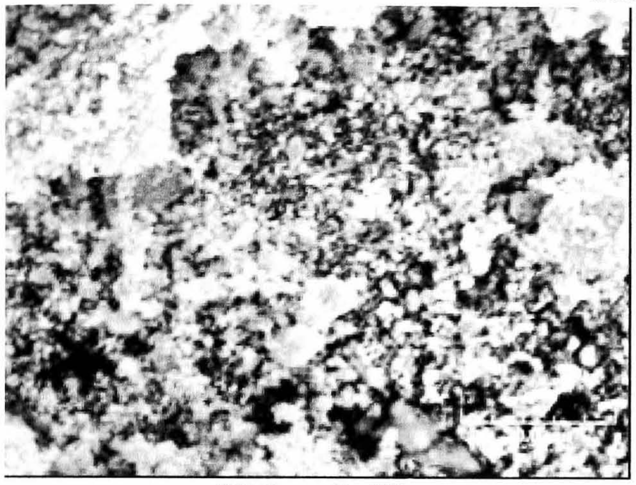

Sliding, B=0T

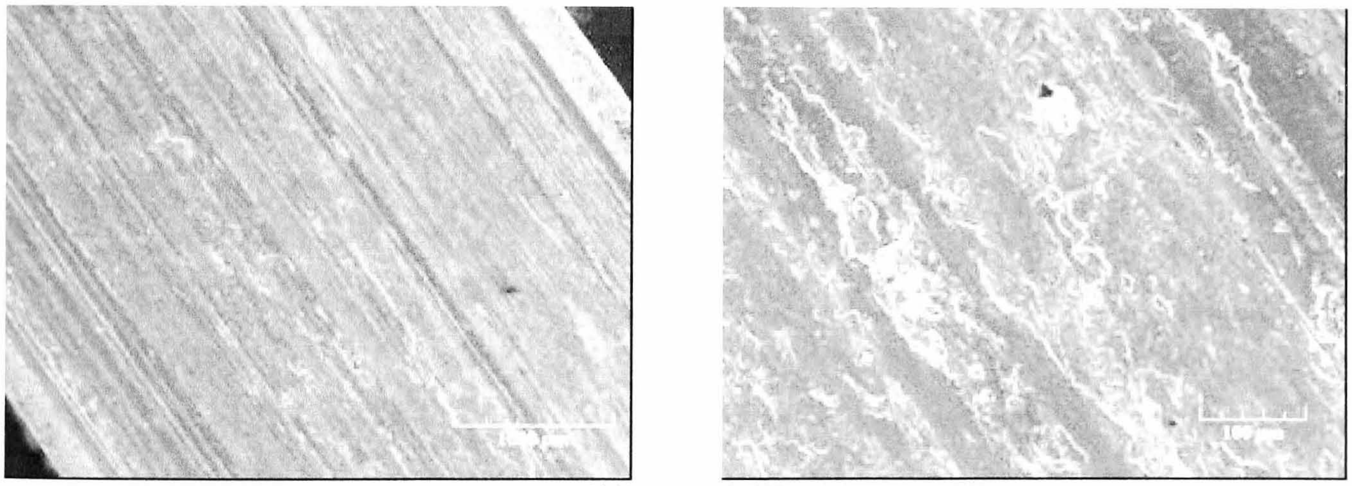

Sliding, B=0.4T

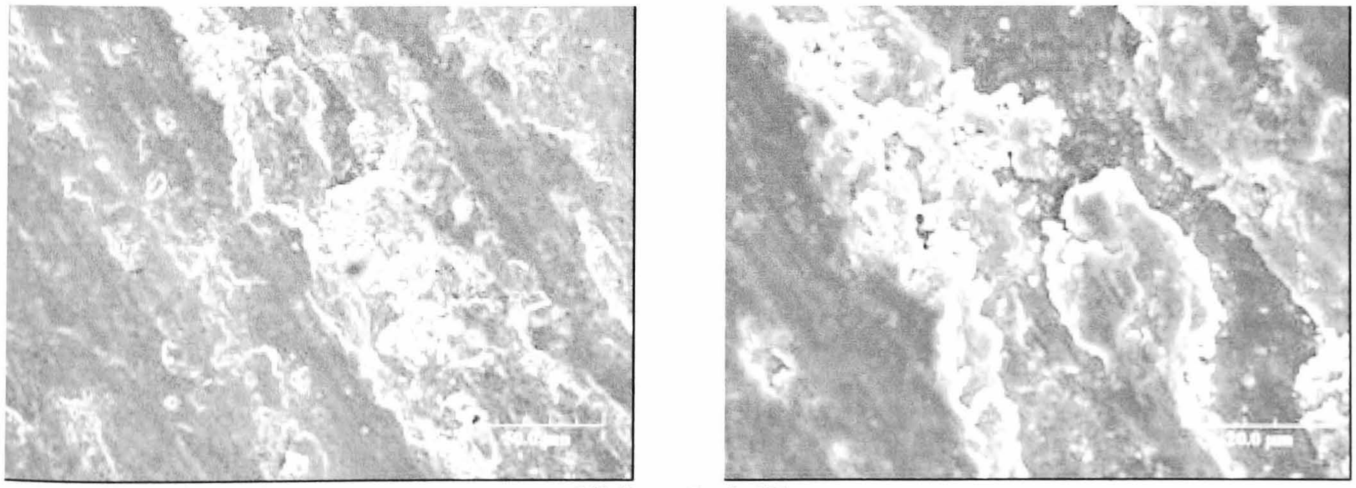

Sliding, B=0.4T

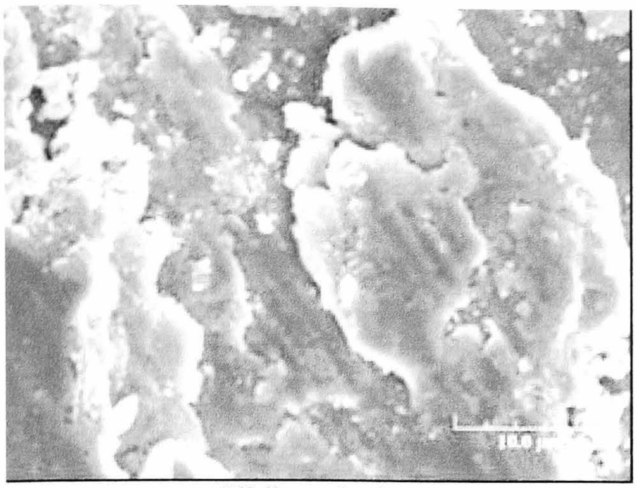

Sliding, B=0.4T

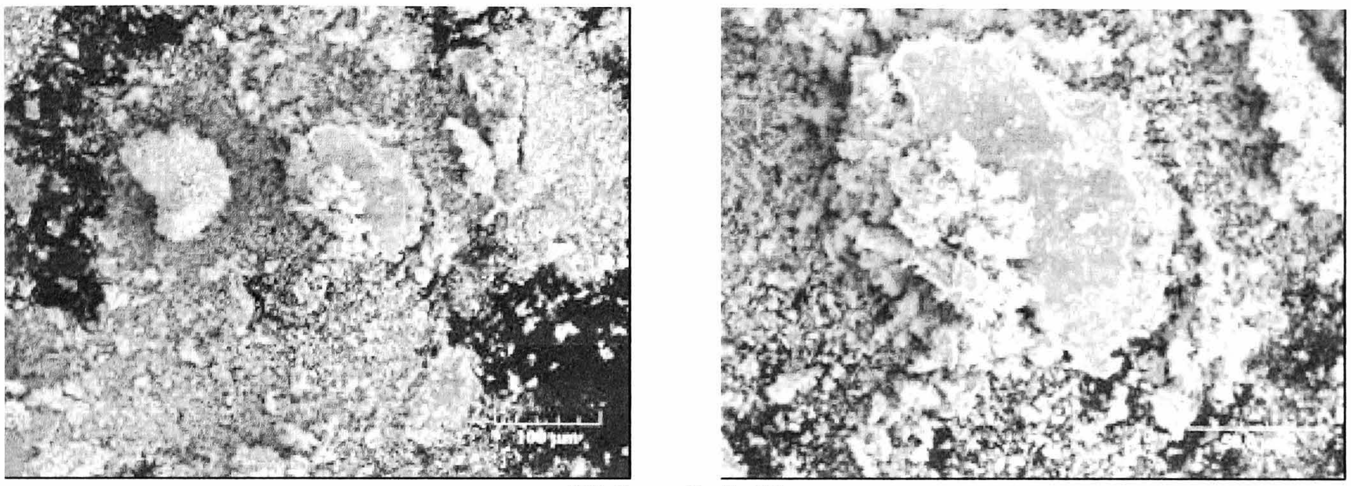

Sliding, B=0.4T

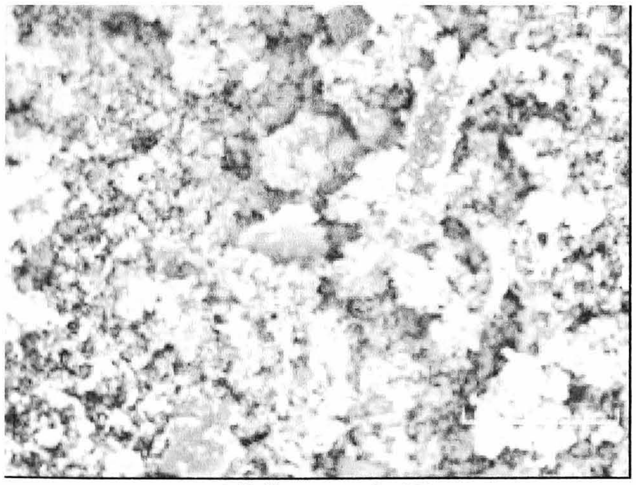

Sliding, B=0.4T

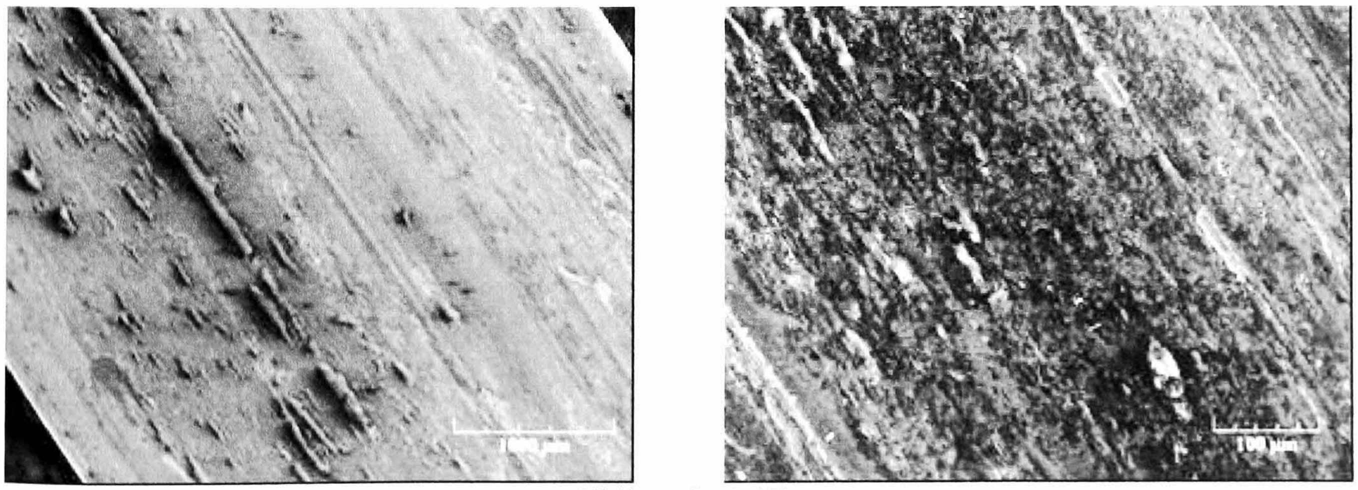

Sliding, B=1.1T

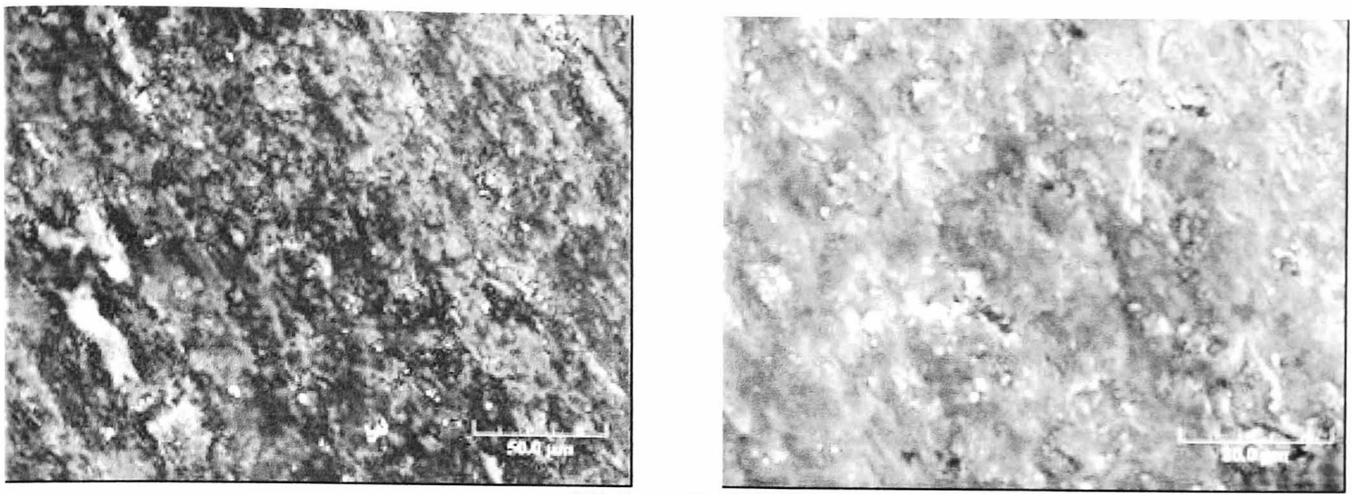

Sliding, B=1.1T

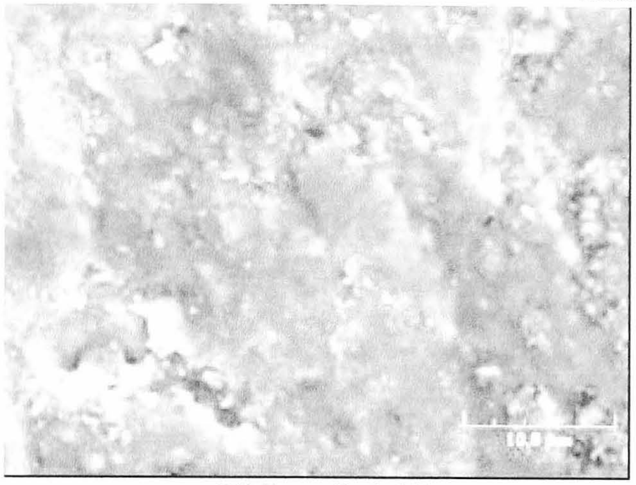

Sliding, B=1.1T

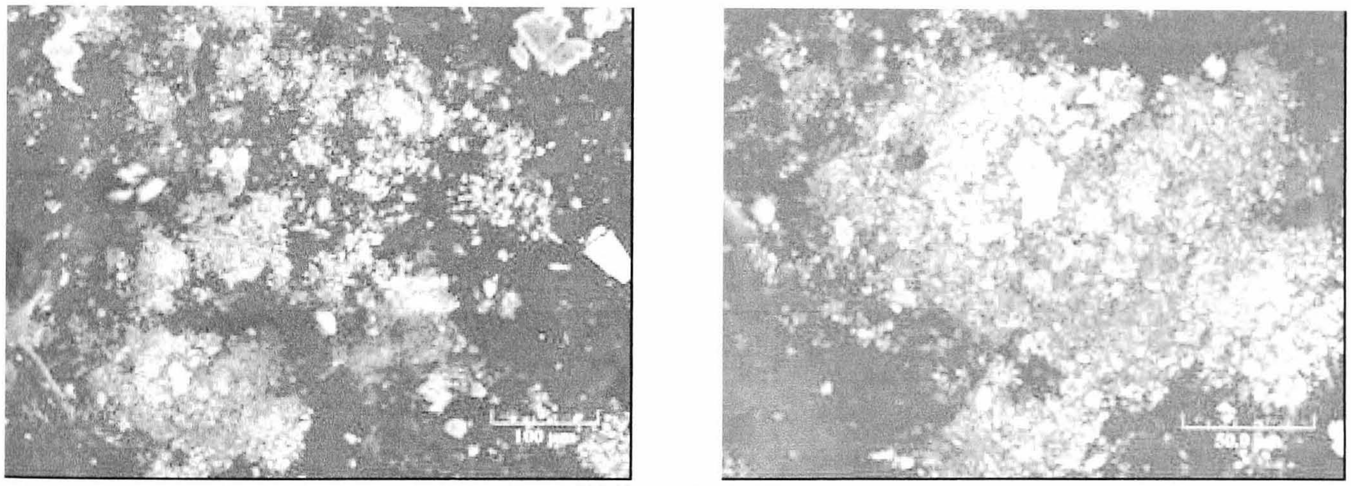

Sliding, B=1.1T

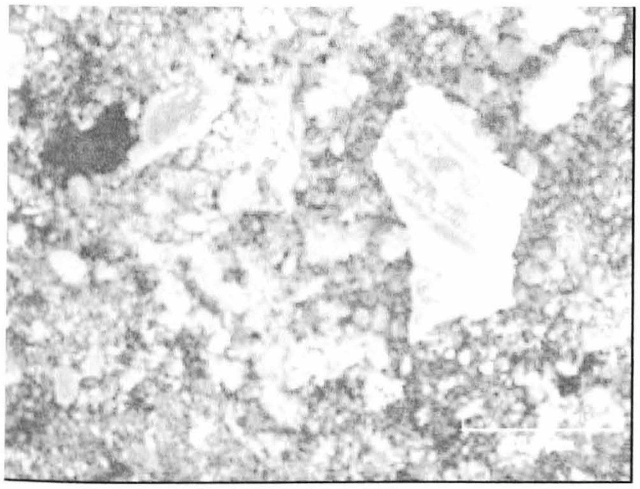

Sliding, B=1.1T

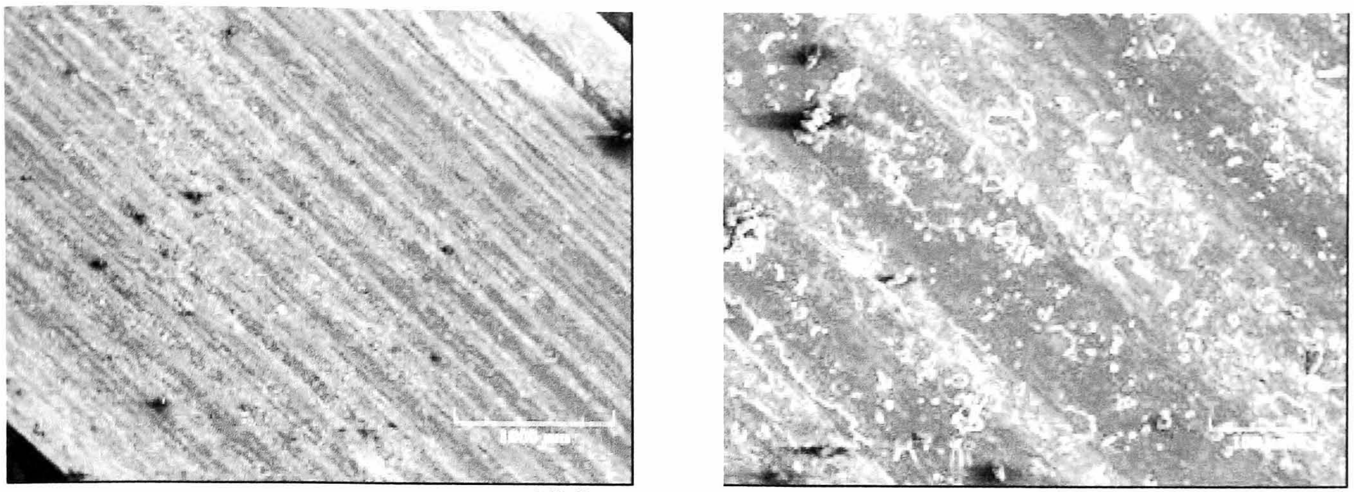

Sliding, *B*=1.1T 45deg

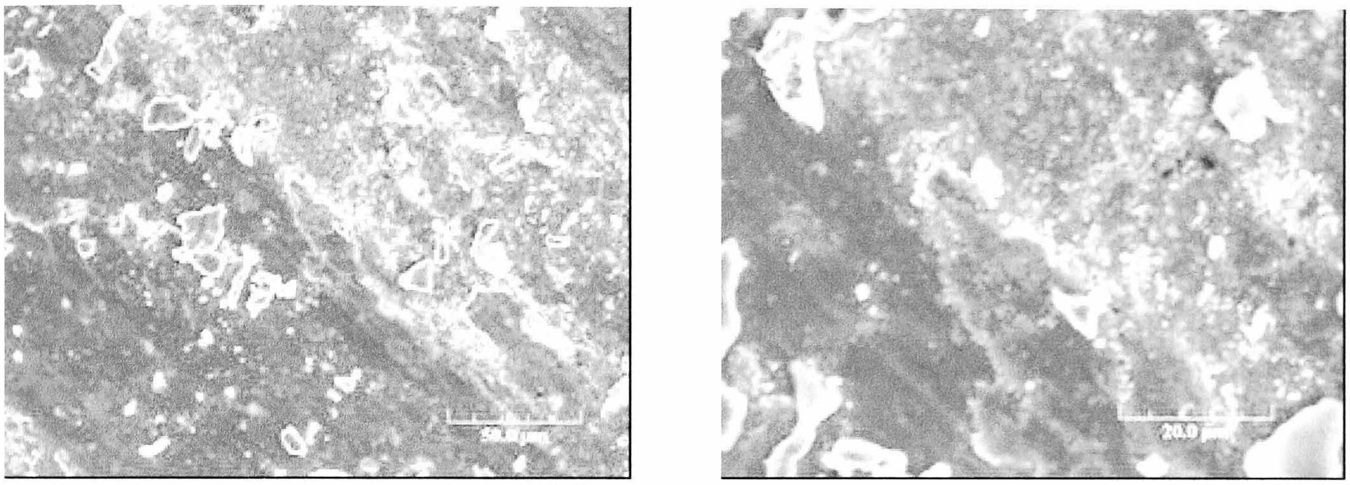

Sliding, *B*=1.1T 45deg

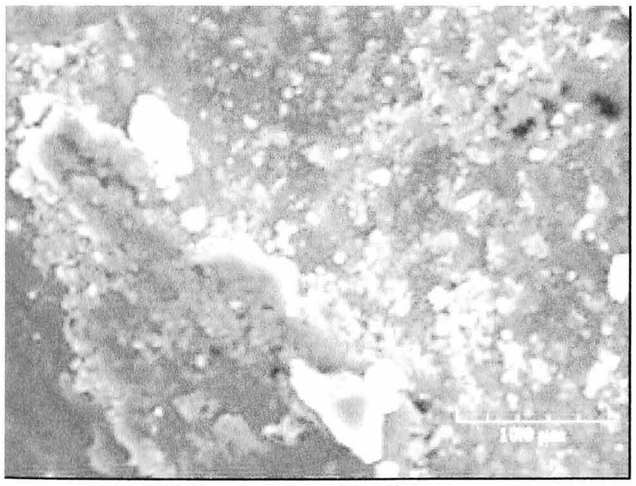

Sliding, *B*=1.1T 45deg

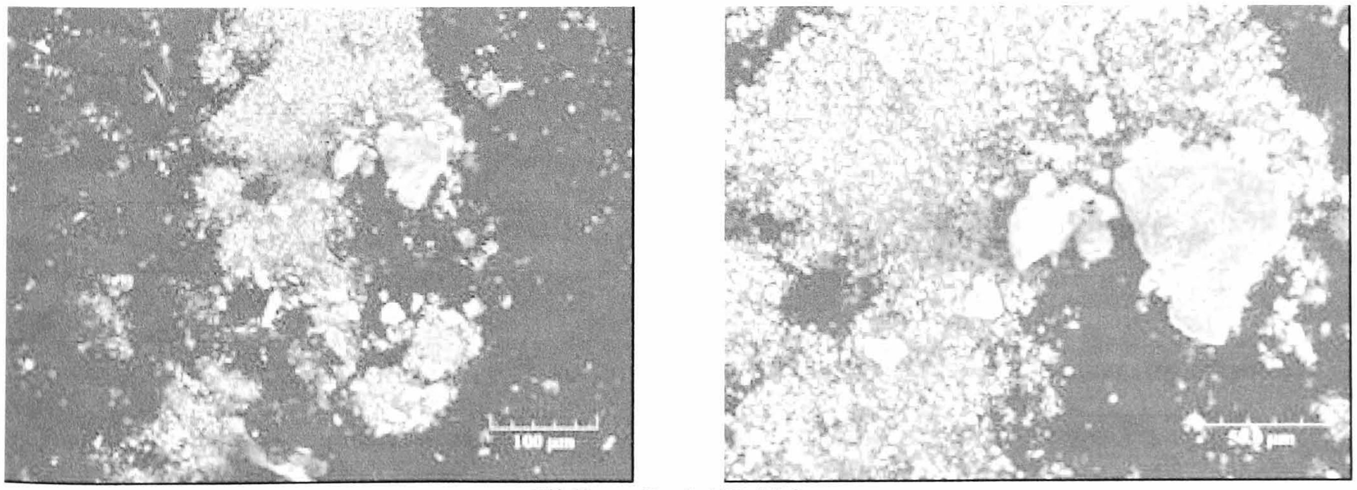

Sliding, *B*=1.1T 45deg

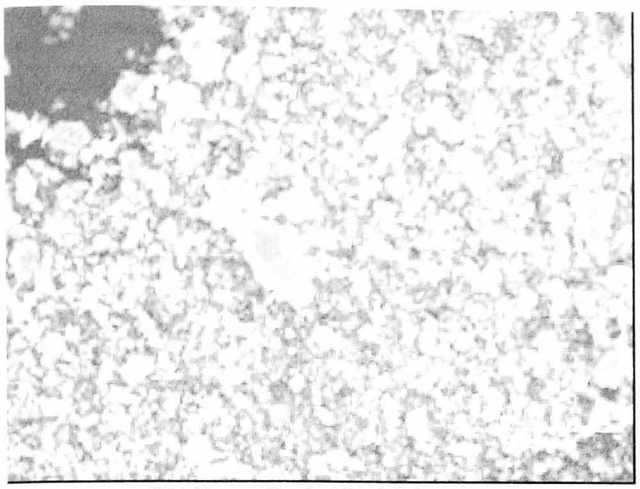

Sliding, B=1.1T 45deg

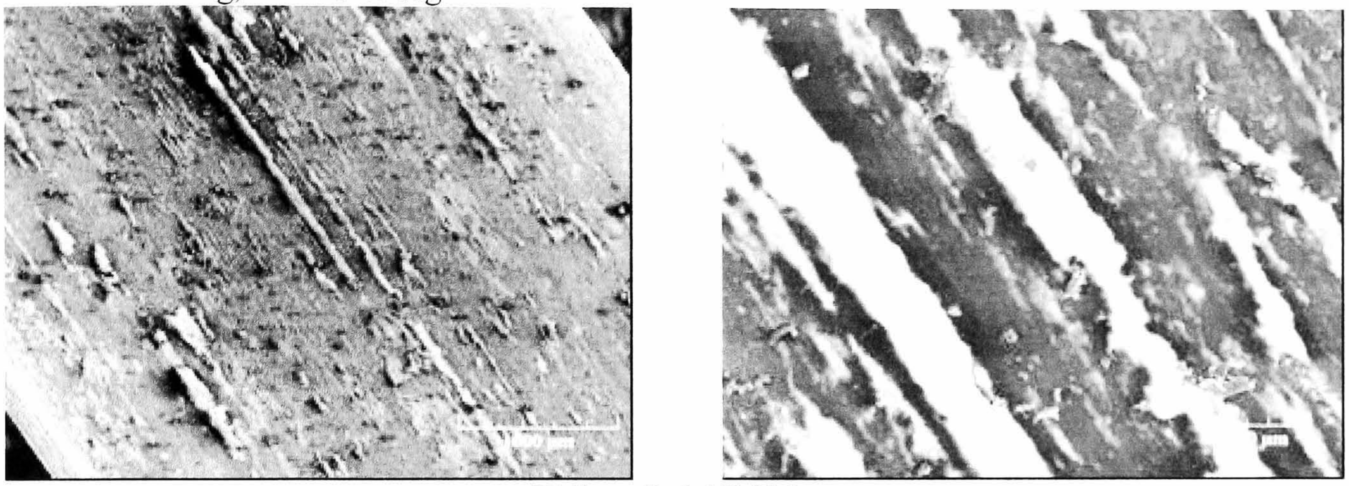

Sliding, B=1.1T 90deg

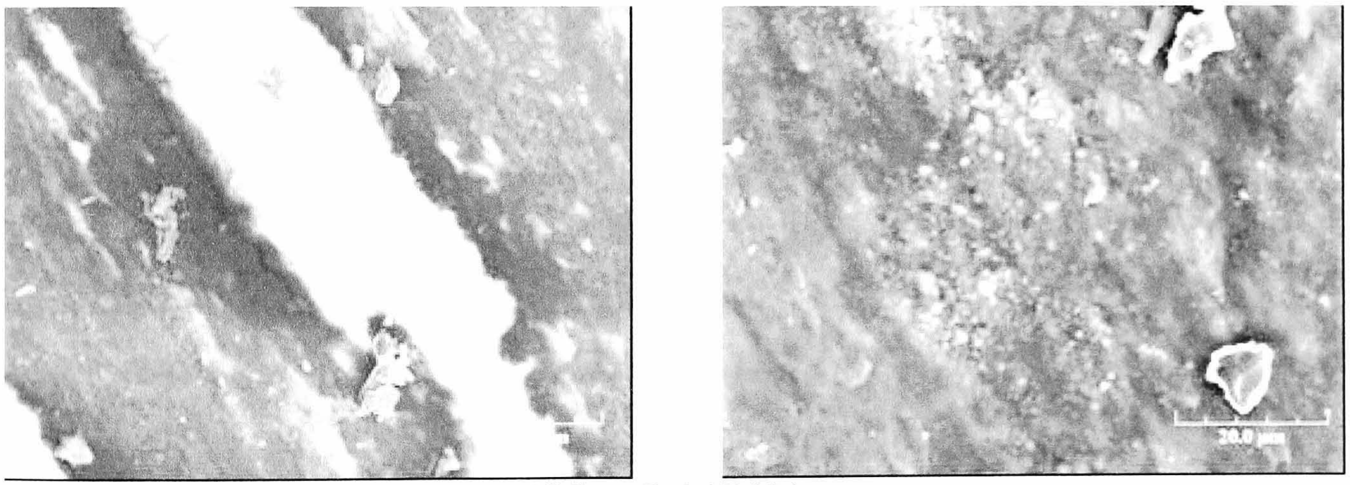

Sliding, B=1.1T 90deg

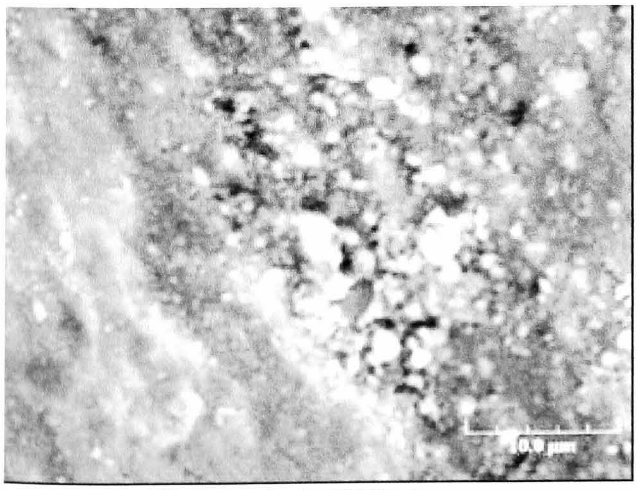

Sliding, B=1.1T 90deg

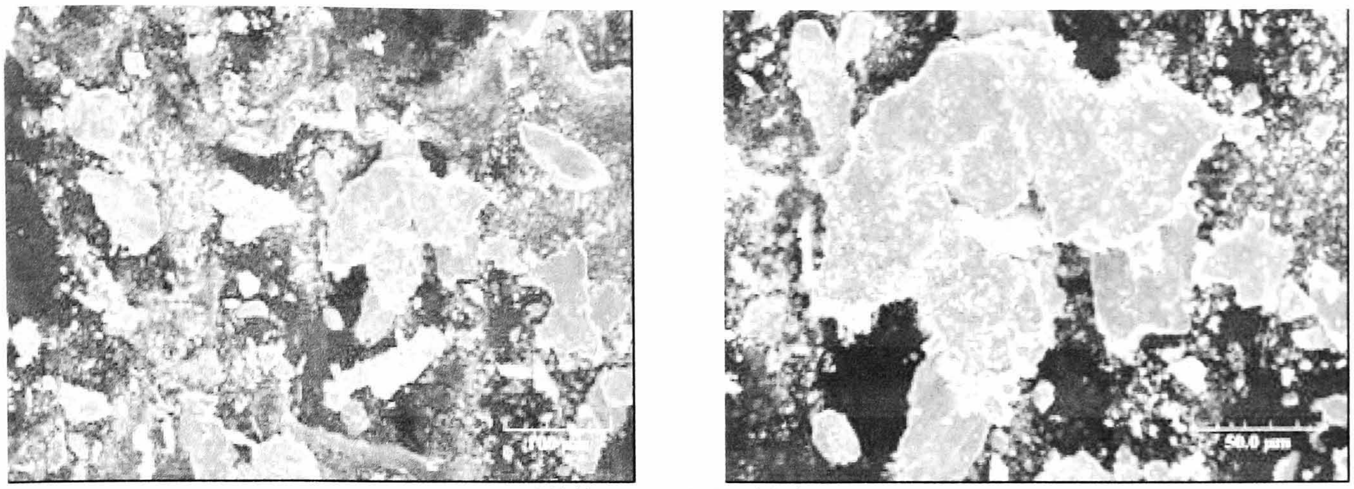

Sliding, B=1.1T 90deg

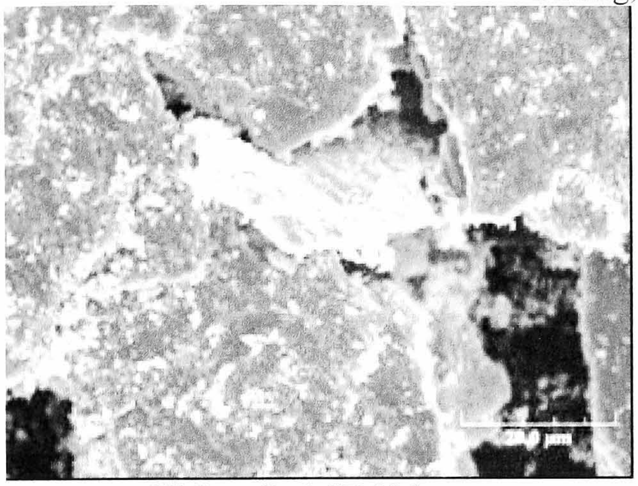

Sliding, B=1.1T 90deg

Appendix D Stress Distributions Produced by FE Analysis

(1) Pure rolling

(a) μ=0 σ_0=267 MPa (b) μ=0.1 σ_0=266 MPa

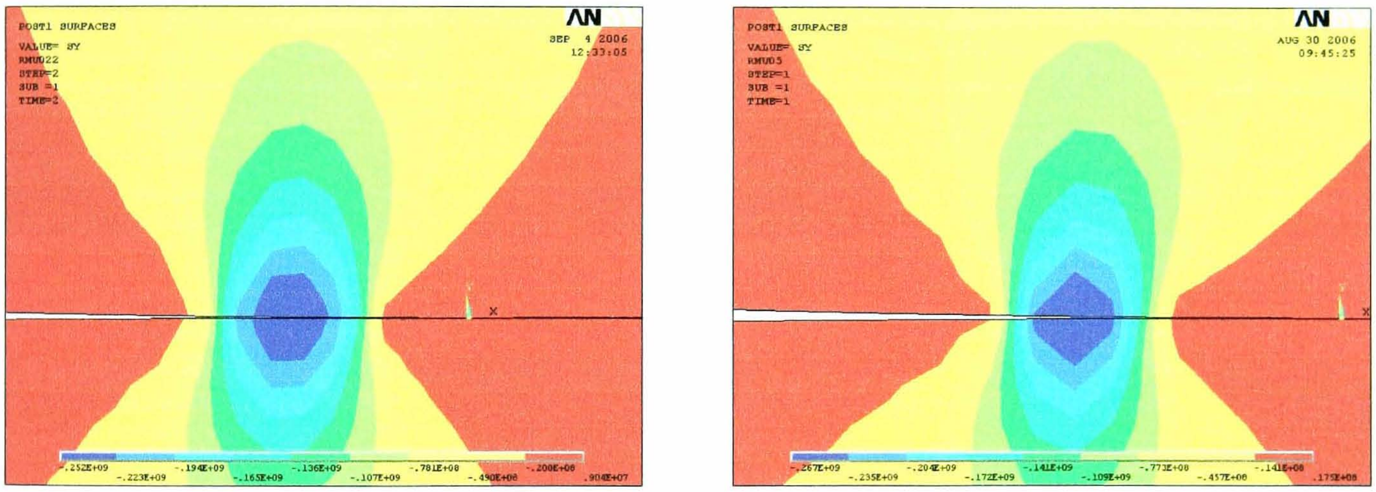

(c) μ=0.2 σ_0=262 MPa (d) μ=0.3 σ_0=265 MPa

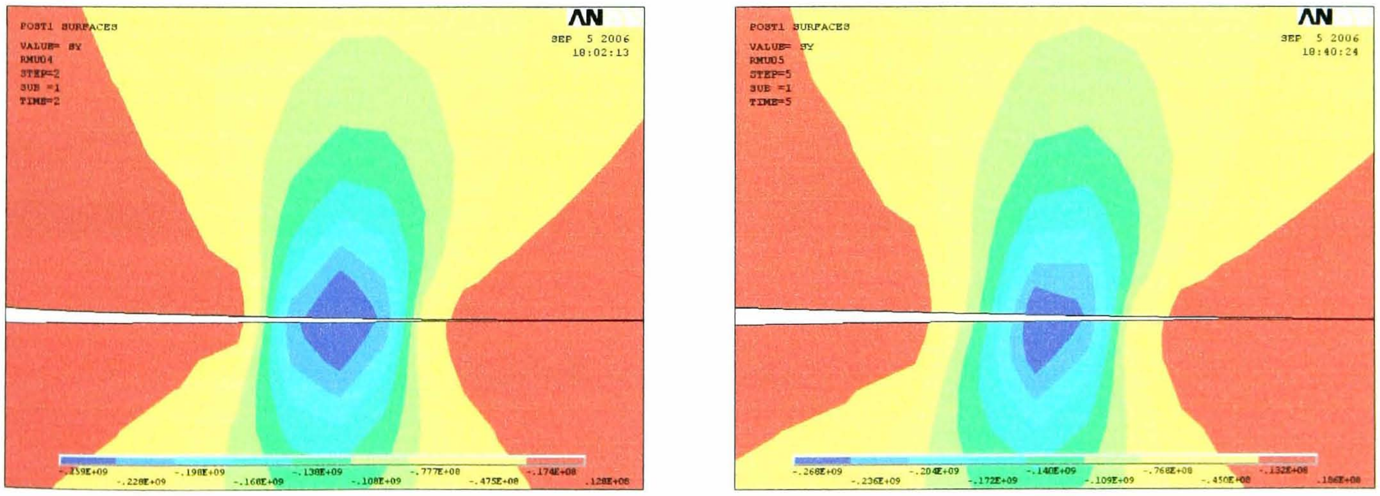

(e) μ=0.4 σ_0=267 MPa (f) μ=0.5 σ_0=266 MPa

Figure D-1 Contact pressure distributions $p(x)$ in different μ

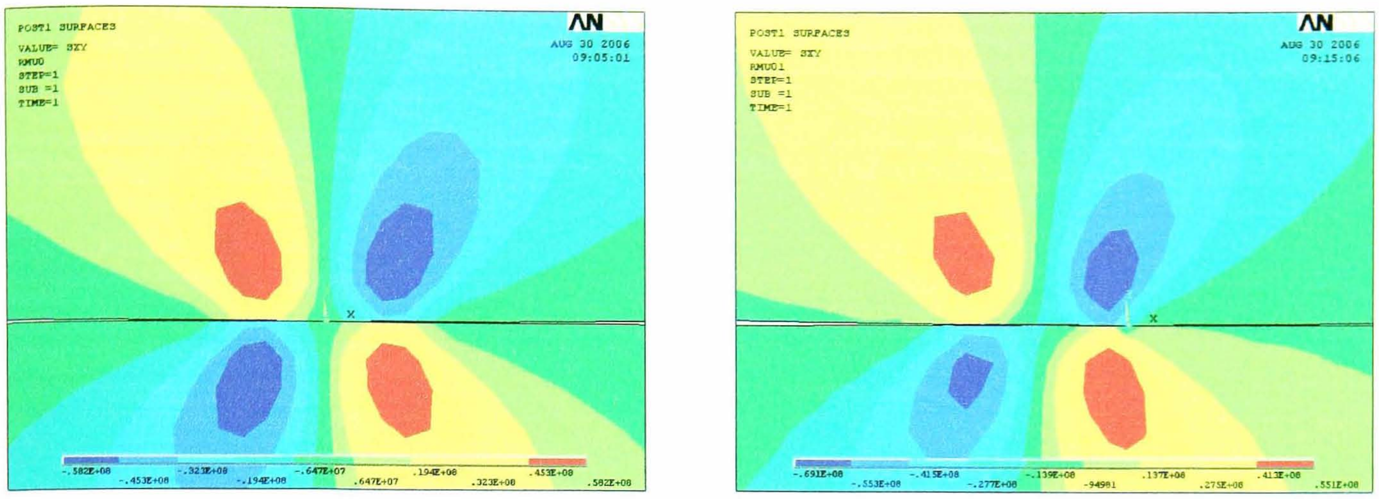

(a) μ=0 τ_{zxmax}=58.2 MPa (b) μ=0.1 τ_{zxmax}=69.1 MPa

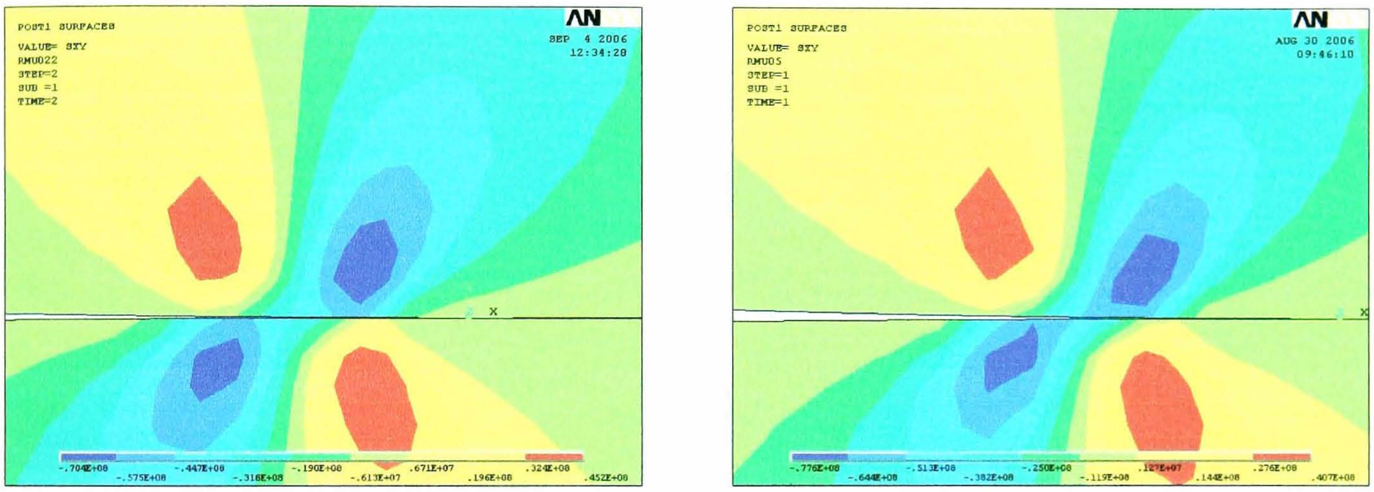

(c) μ=0.2 τ_{zxmax}=70.4 MPa (d) μ=0.3 τ_{zxmax}=77.6 MPa

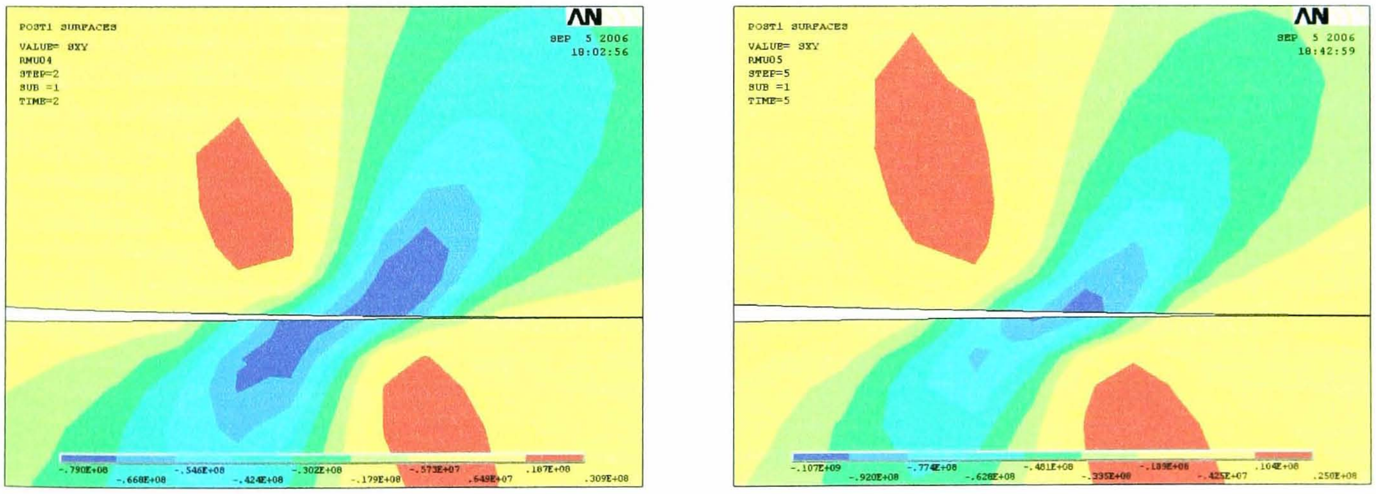

(e) μ=0.4 τ_{zxmax}=79.0 MPa (f) μ=0.5 τ_{zxmax}=96.0 MPa

Figure D-2 Shear stress distributions $p(x)$ in different μ

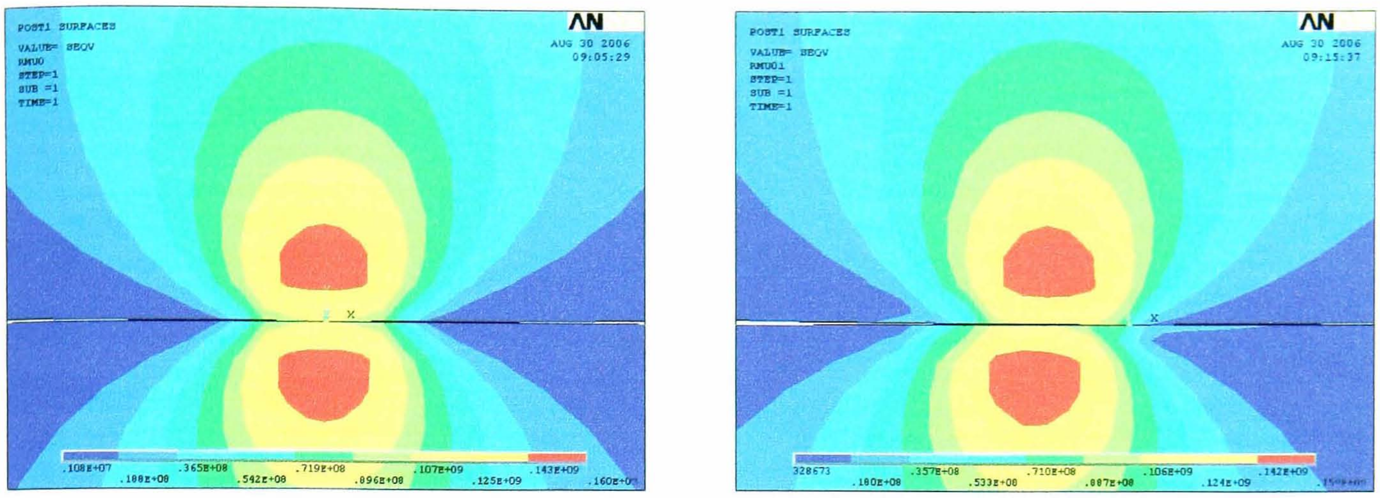

(a) μ=0 τ_{Rmax}=91.3MPa (b) μ=0.1 τ_{Rmax}=91.8MPa

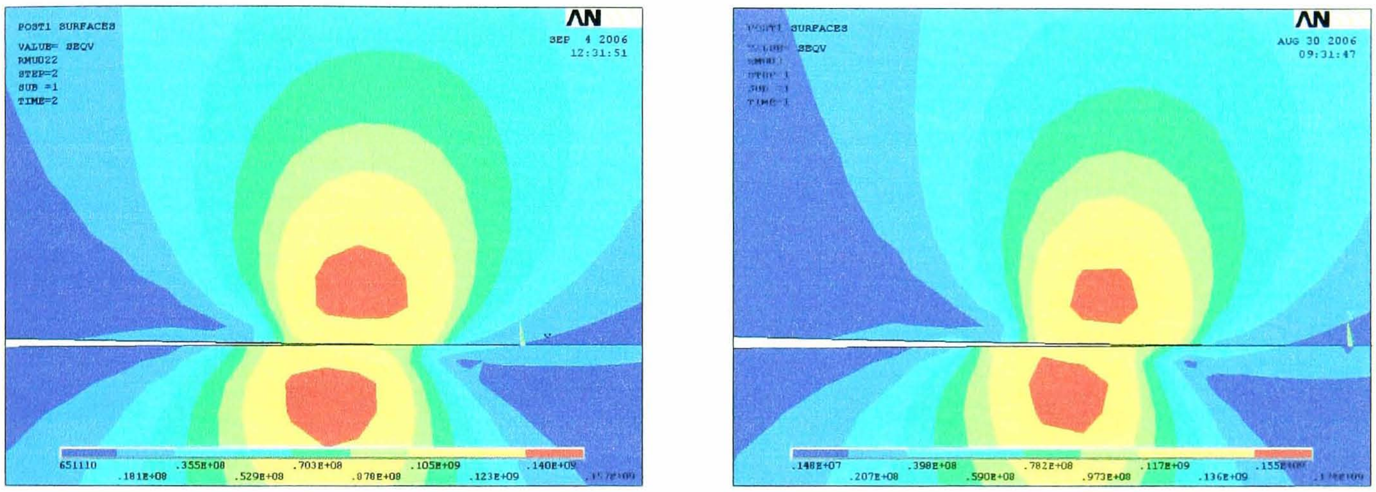

(c) μ=0.2 τ_{Rmax}=91.2MPa (d) μ=0.3 τ_{Rmax}=95.6MPa

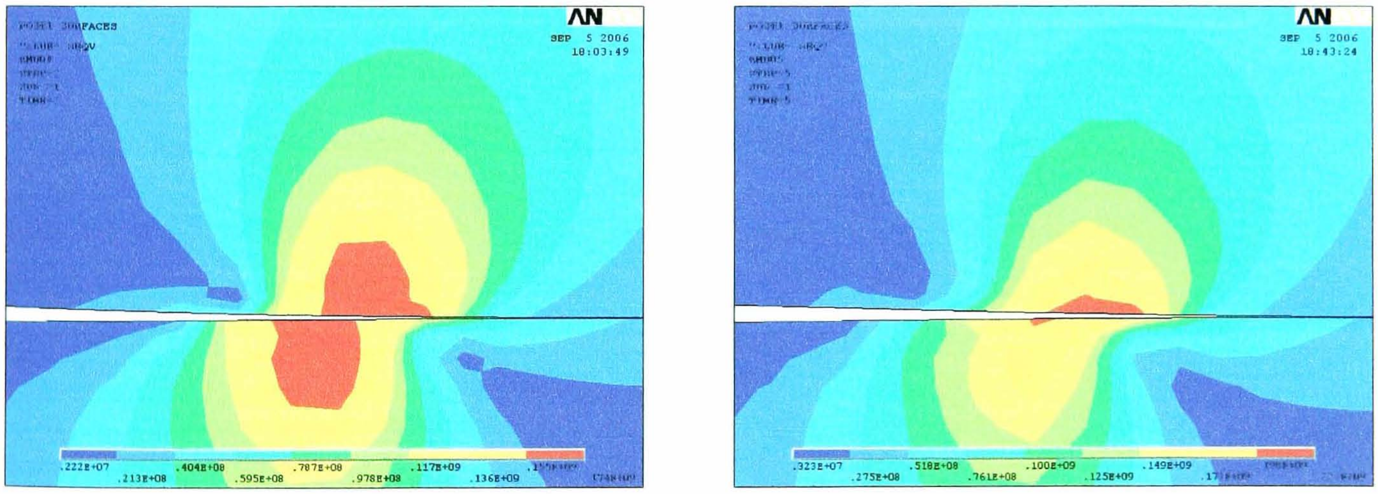

(e) μ=0.4 τ_{Rmax}=99.5MPa (f) μ=0.5 τ_{Rmax}=121.0MPa

Figure D-3 Von Mises' stress distributions $p(x)$ in different μ

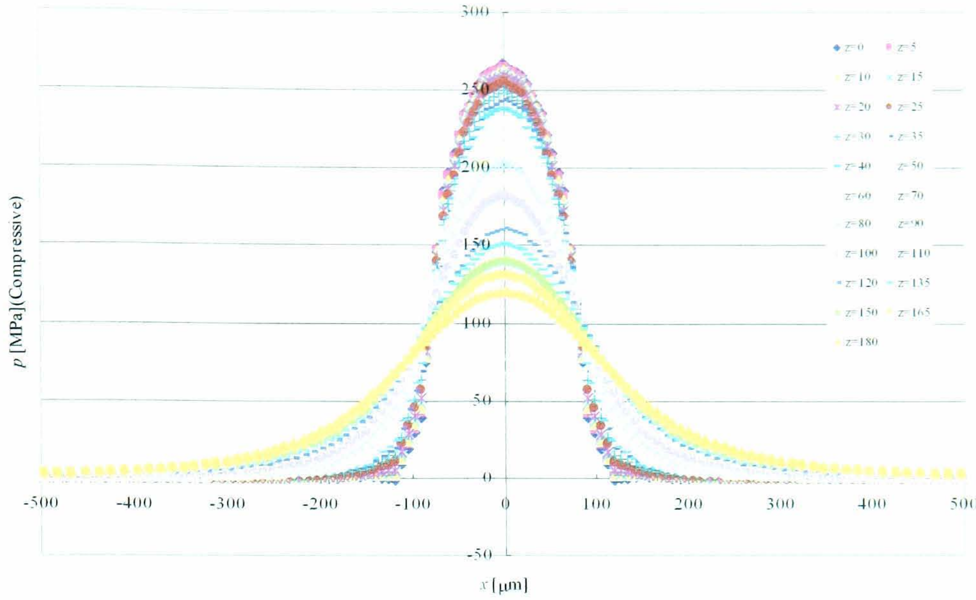

Figure D-4 Contact pressure distributions $p(x)$ in the depth Z [μm] from the surface (Roll, μ=0)

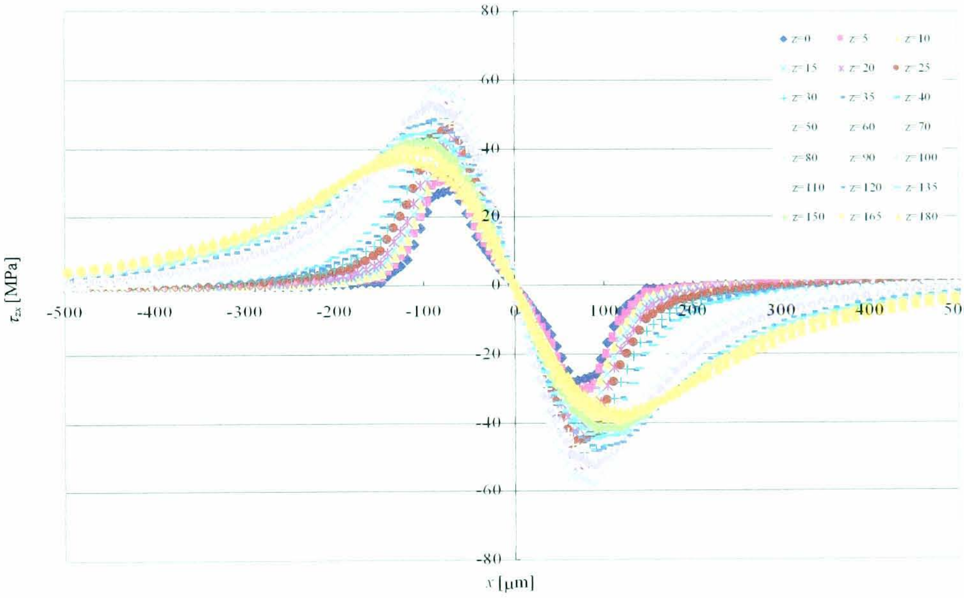

Figure D-5 Shear stress distributions τ_{zx} in the depth Z [μm] from the surface (Roll, μ=0)

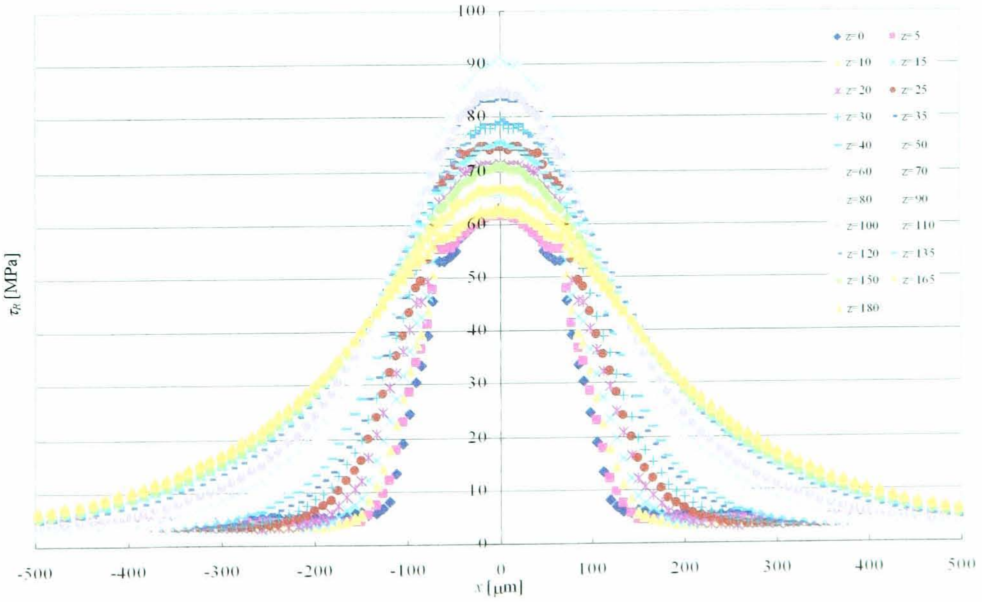

Figure D-6 Von Mises' stress distributions τ_R in the depth Z [μm] from the surface (Roll, μ=0)

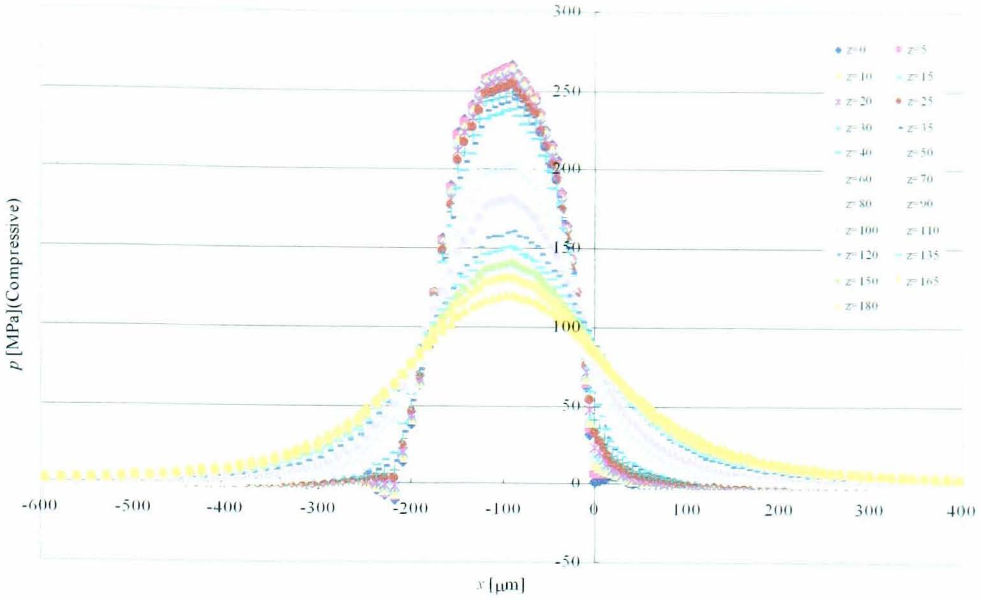

Figure D-7 Contact pressure distributions $p(x)$ in the depth Z [μm] from the surface (Roll, μ=0.1)

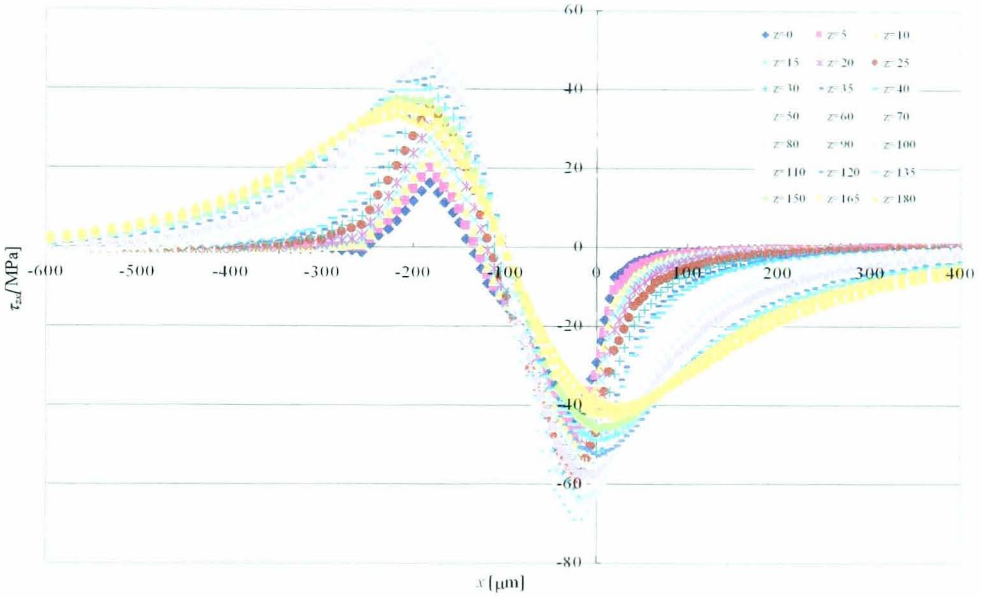

Figure D-8 Shear stress distributions τ_{zx} in the depth Z [μm] from the surface (Roll, μ=0.1)

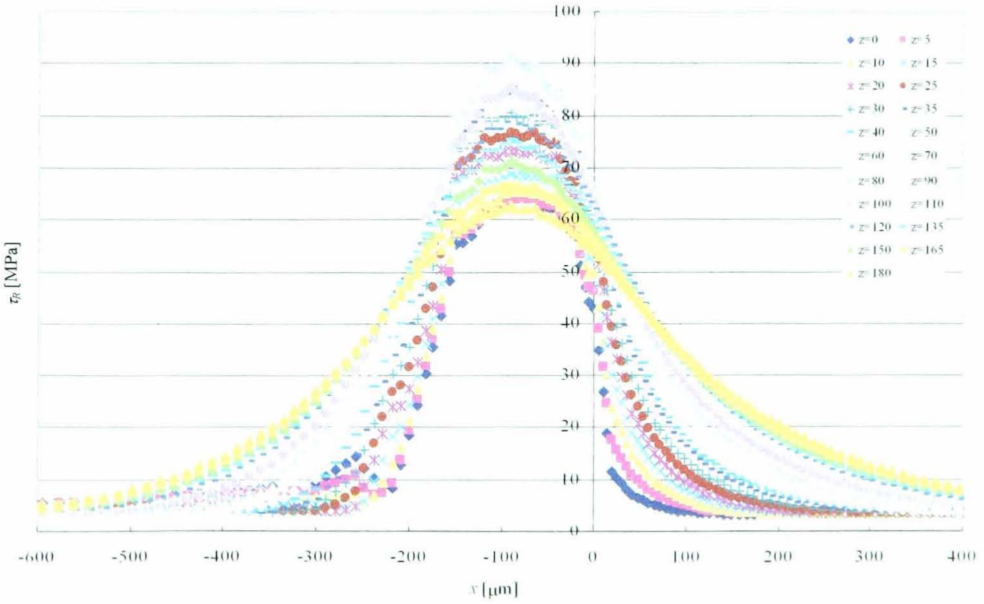

Figure D-9 Von Mises' stress distributions τ_R in the depth Z [μm] from the surface (Roll, μ=0.1)

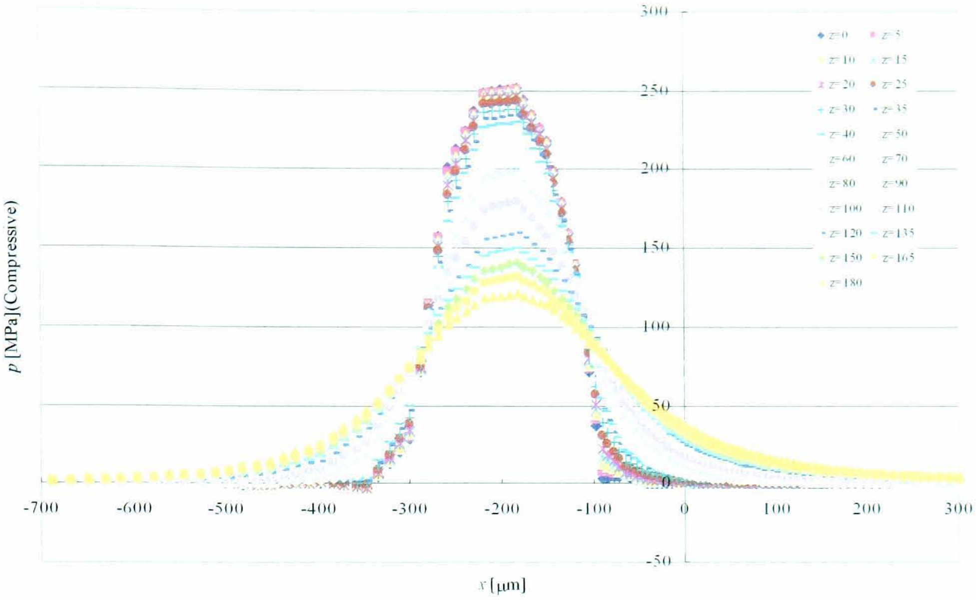

Figure D-10 Contact pressure distributions $p(x)$ in the depth Z [μm] from the surface (Roll, μ=0.2)

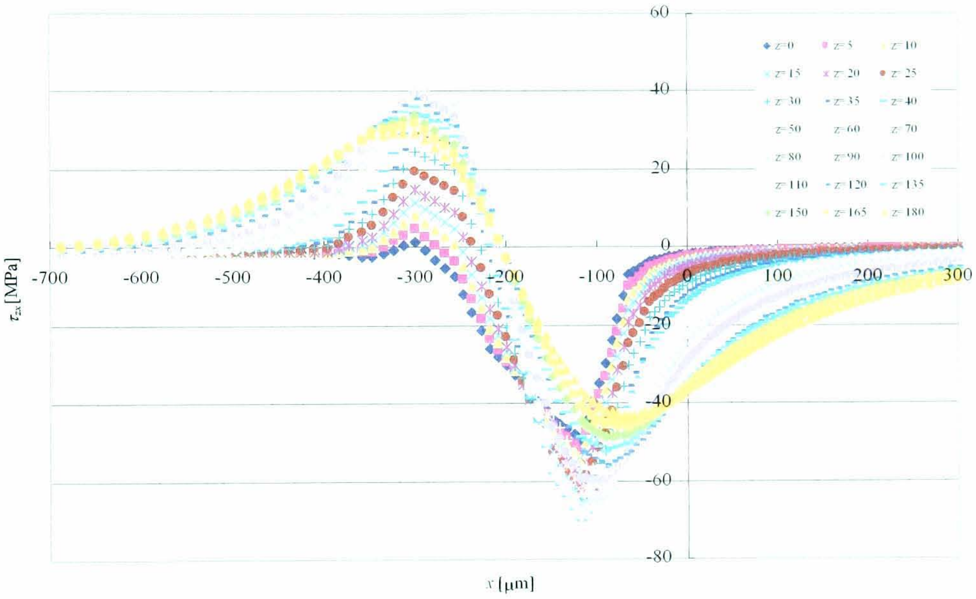

Figure D-11 Shear stress distributions τ_{zx} in the depth Z [μm] from the surface (Roll, μ=0.2)

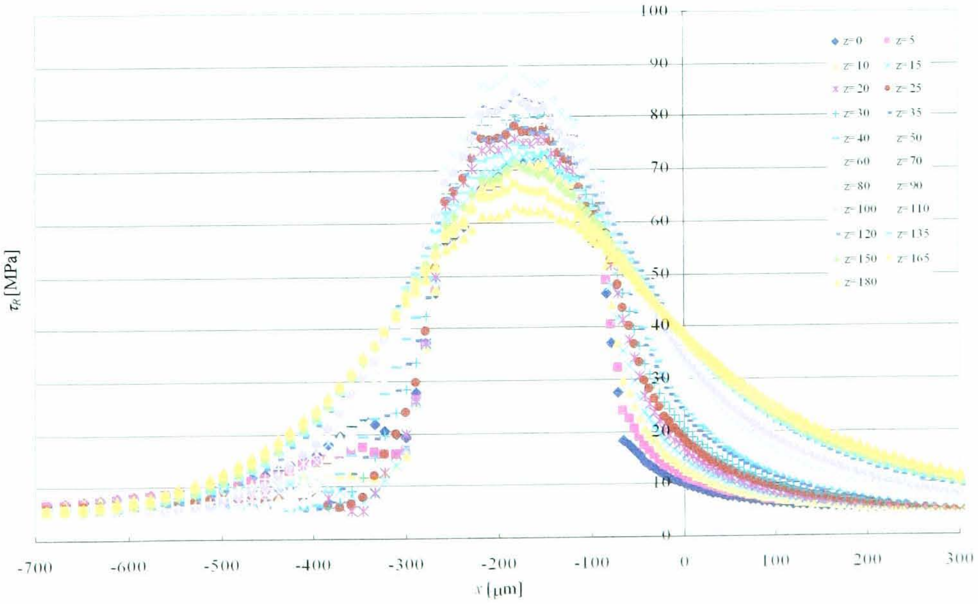

Figure D-12 Von Mises' stress distributions τ_R in the depth Z [μm] from the surface (Roll, μ=0.2)

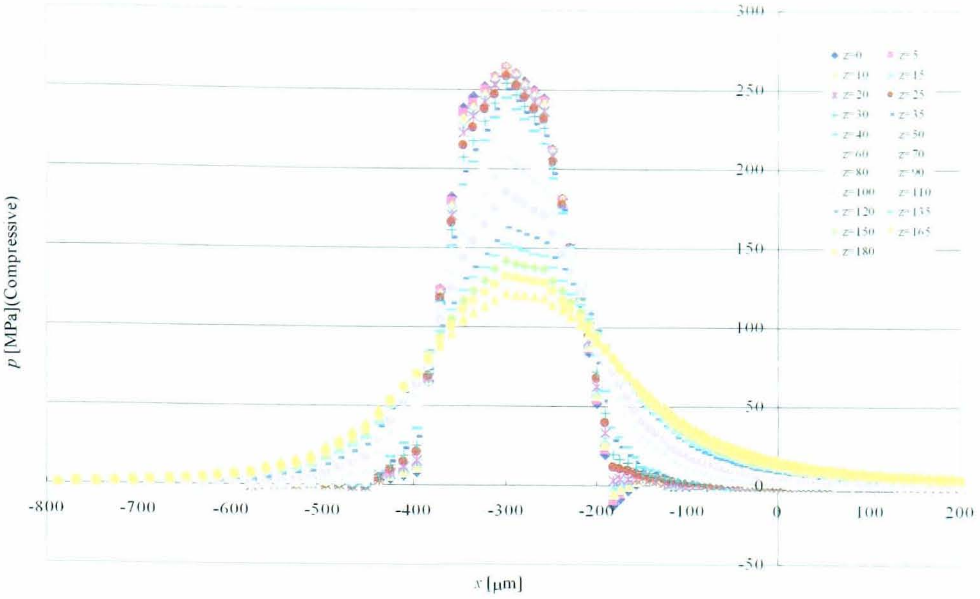

Figure D-13 Contact pressure distributions $p(x)$ in the depth Z [μm] from the surface (Roll, μ=0.3)

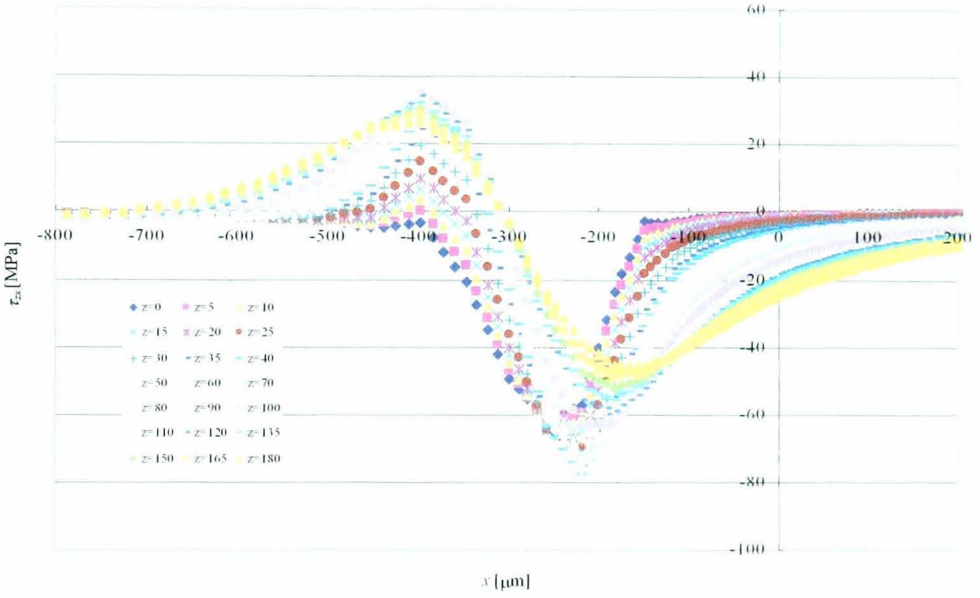

Figure D-14 Shear stress distributions τ_{zx} in the depth Z [μm] from the surface (Roll, μ=0.3)

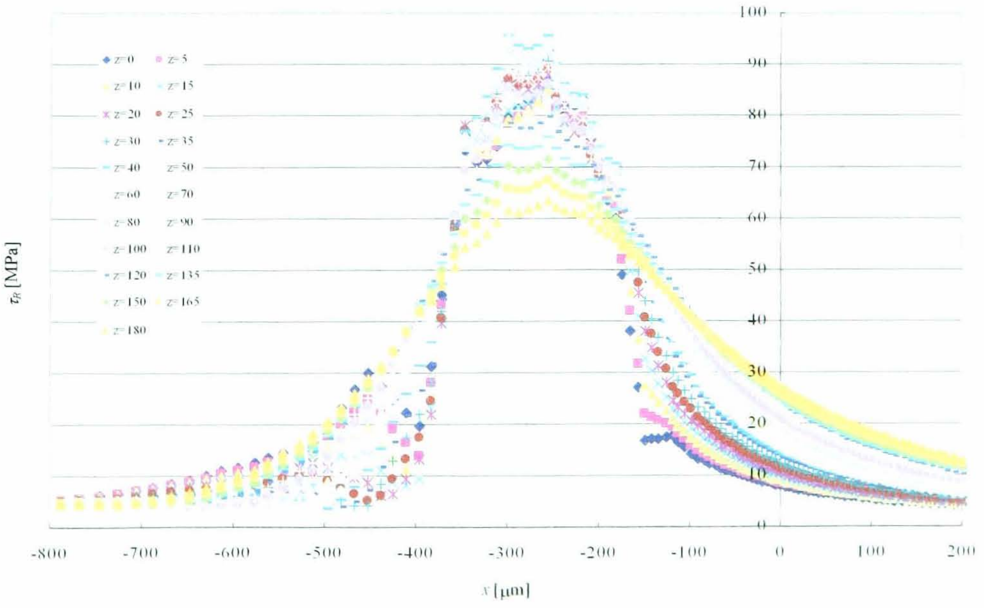

Figure D-15 Von Mises' stress distributions τ_R in the depth Z [μm] from the surface (Roll, μ=0.3)

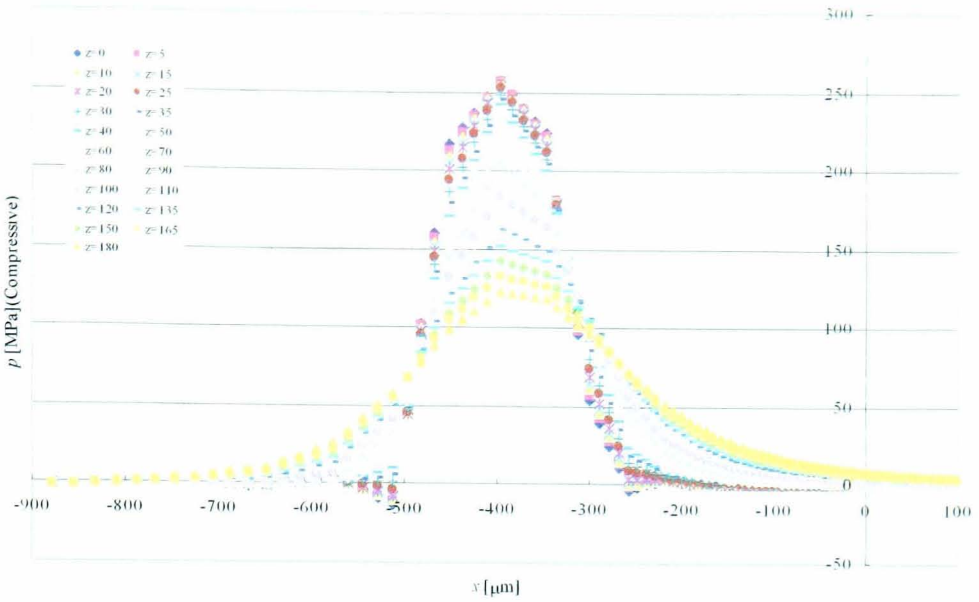

Figure D-16 Contact pressure distributions $p(x)$ in the depth Z [μm] from the surface (Roll, μ=0.4)

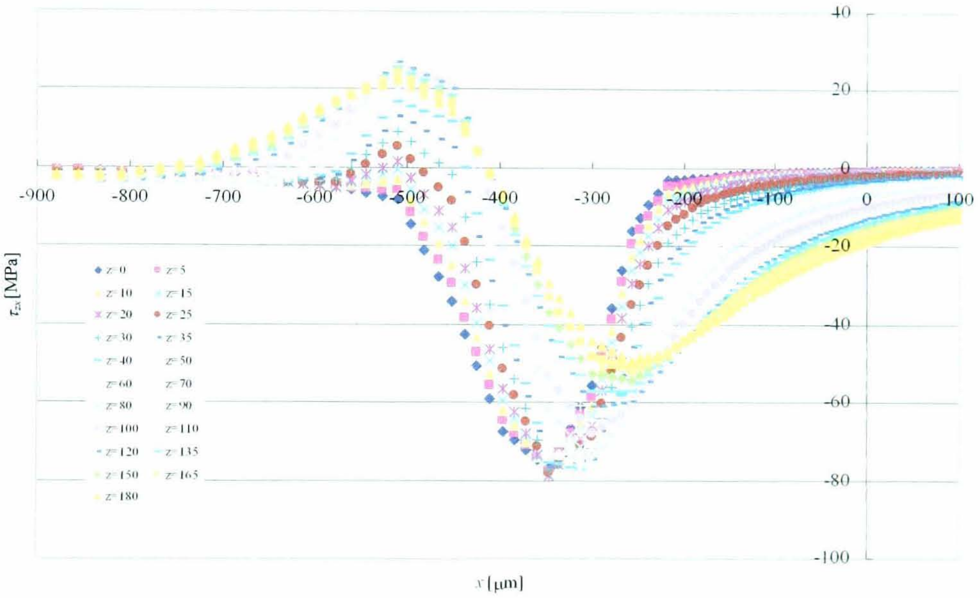

Figure D-17 Shear stress distributions τ_{zx} in the depth Z [μm] from the surface (Roll, μ=0.4)

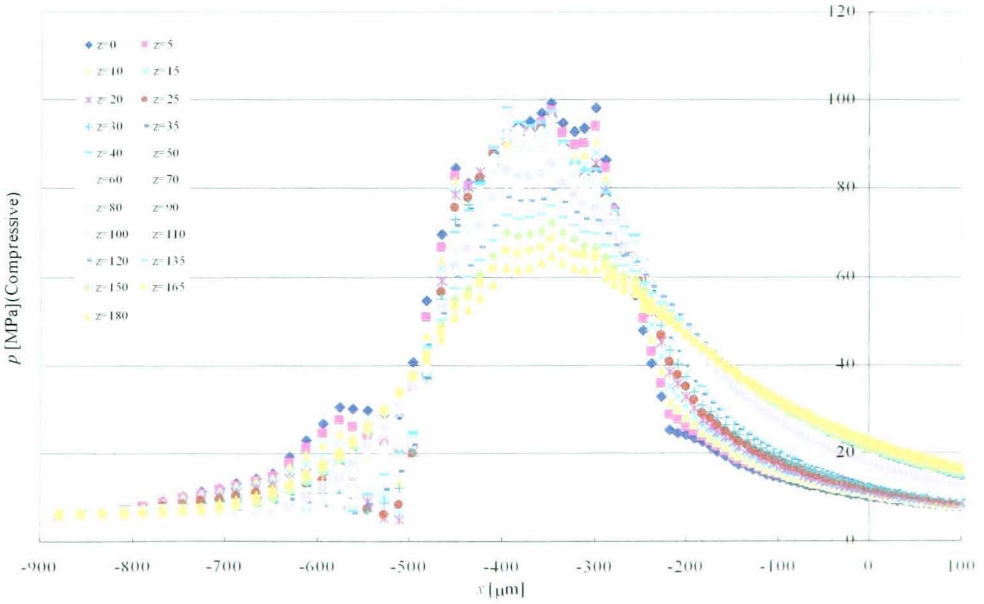

Figure D-18 Von Mises' stress distributions τ_R in the depth Z [μm] from the surface (Roll, μ=0.4)

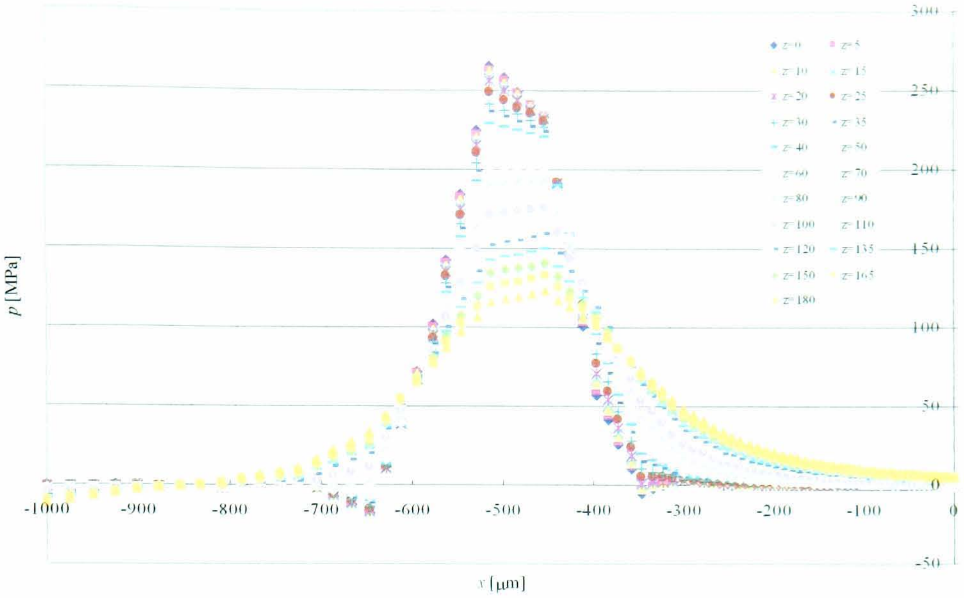

Figure D-19 Contact pressure distributions $p(x)$ in the depth Z [μm] from the surface (Roll, μ=0.5)

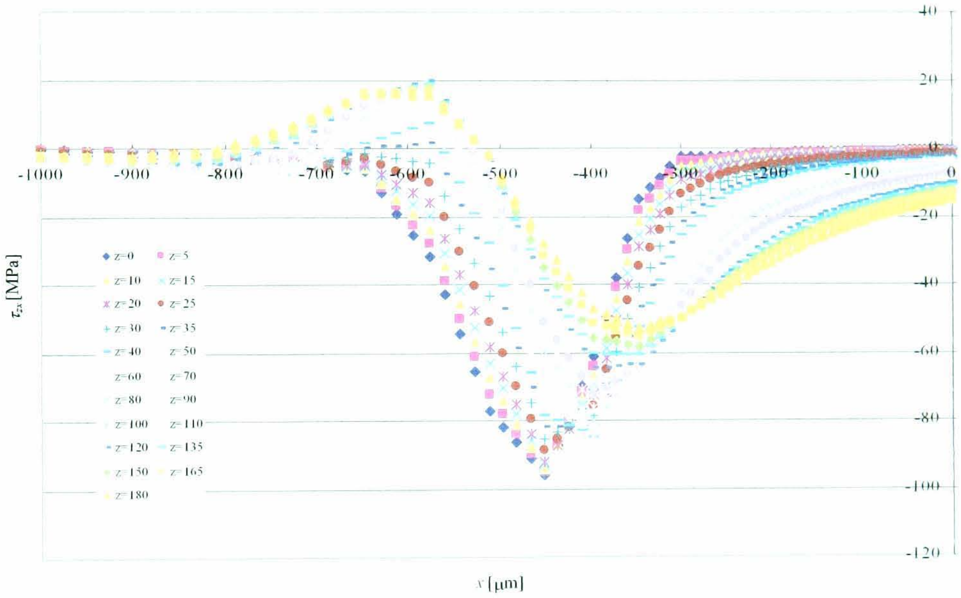

Figure D-20 Shear stress distributions τ_{zx} in the depth Z [μm] from the surface (Roll, μ=0.5)

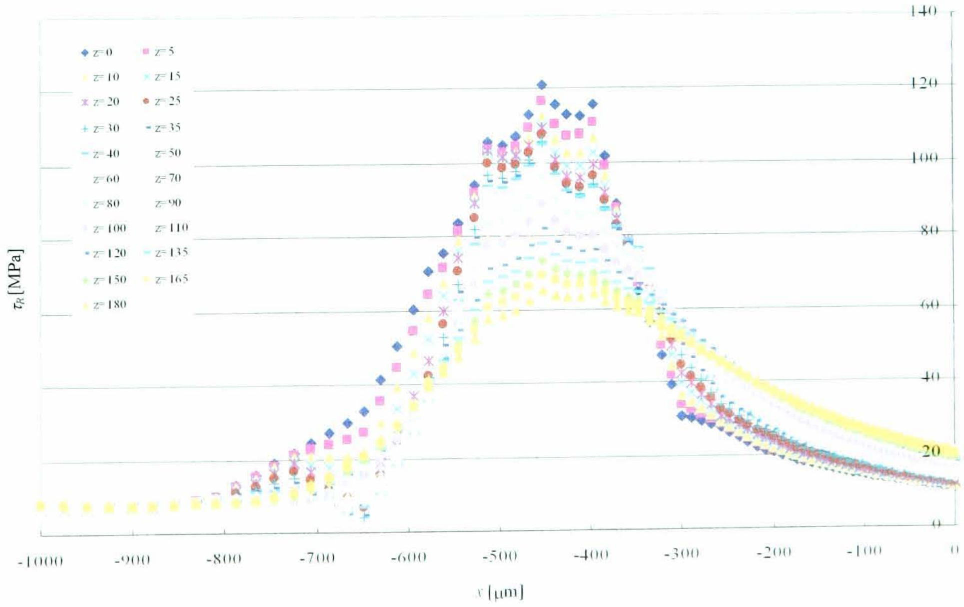

Figure D-21 Von Mises' stress distributions τ_R in the depth Z [μm] from the surface (Roll, μ=0.5)

(2) Rolling with Sliding

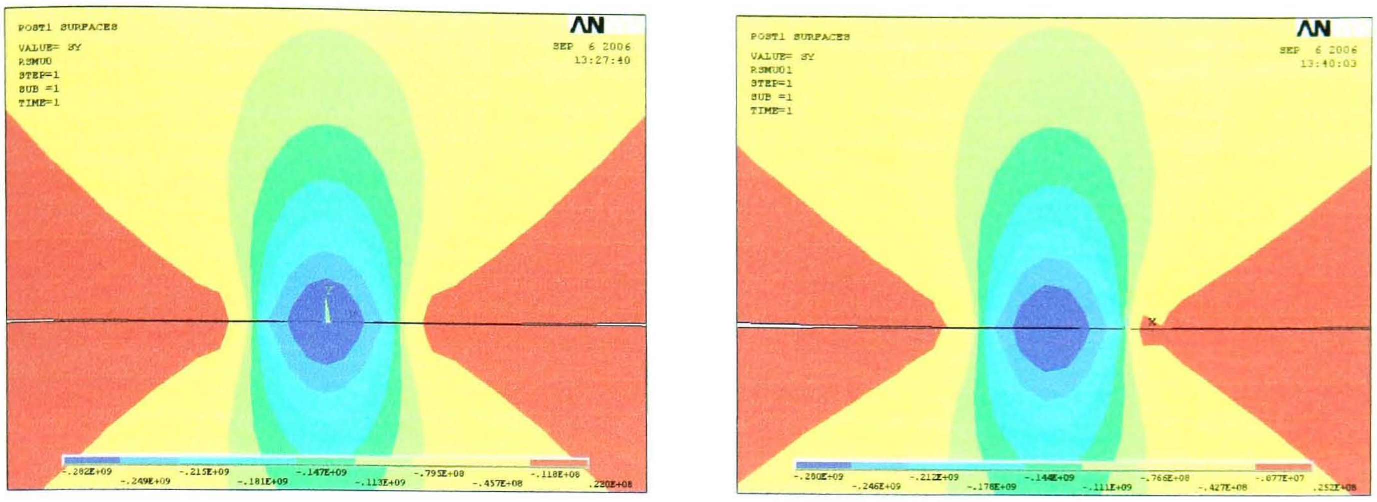

(a) μ=0 σ_0= 282 MPa

(b) μ=0.1 σ_0=280 MPa

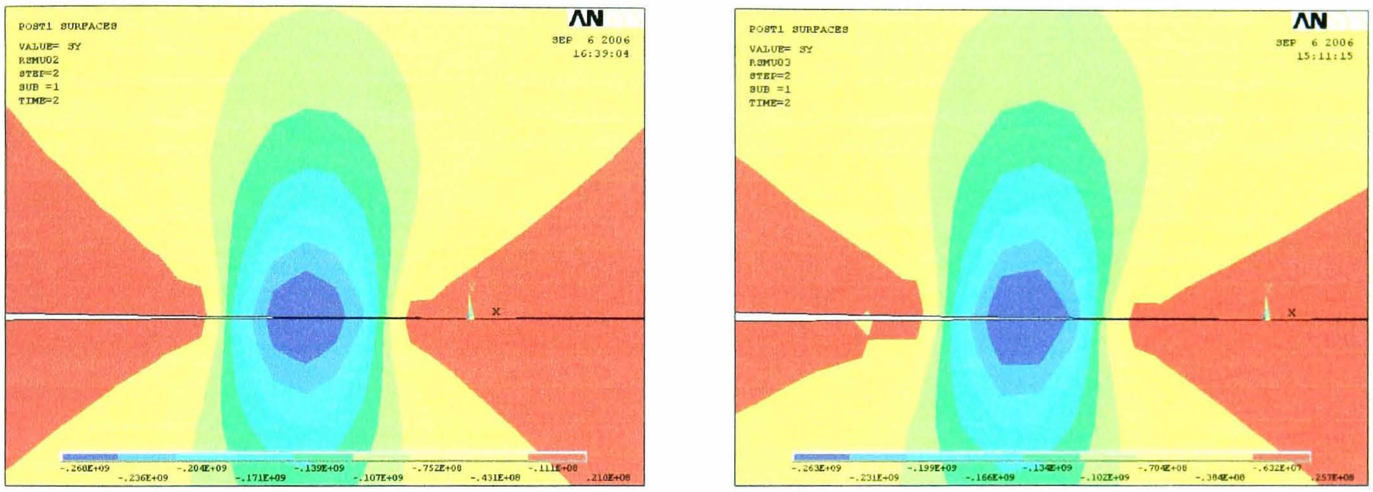

(c) μ=0.2 σ_0= 268 MPa

(d) μ=0.3 σ_0=263 MPa

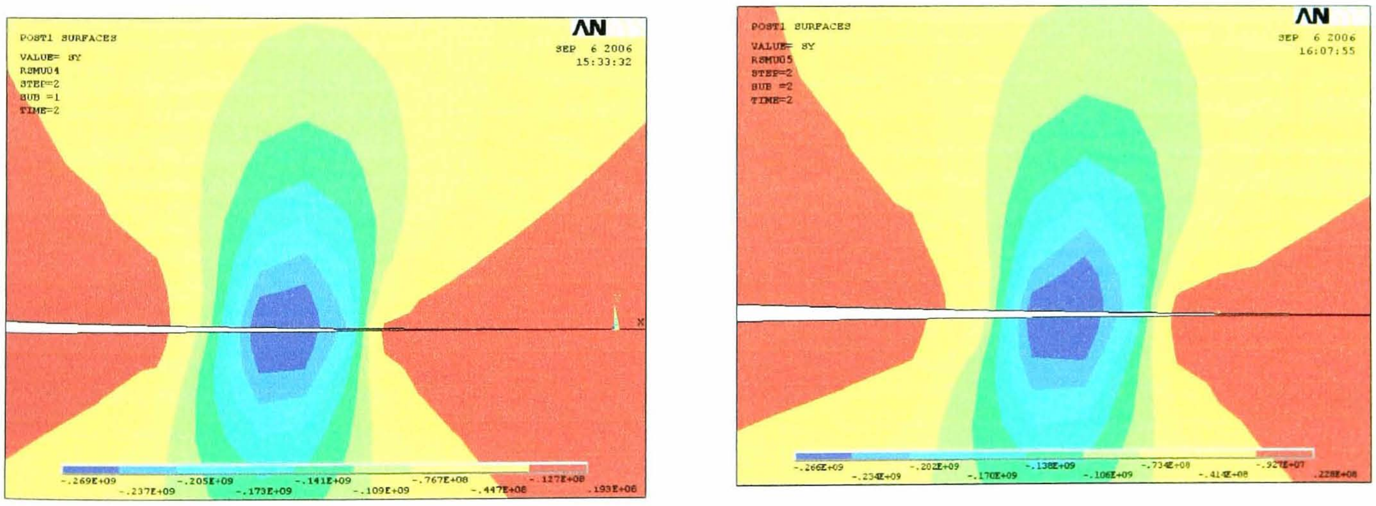

(e) μ=0.4 σ_0= 269 MPa

(f) μ=0.5 σ_0=264 MPa

Figure D-22 Contact pressure distributions $p(x)$ in different μ

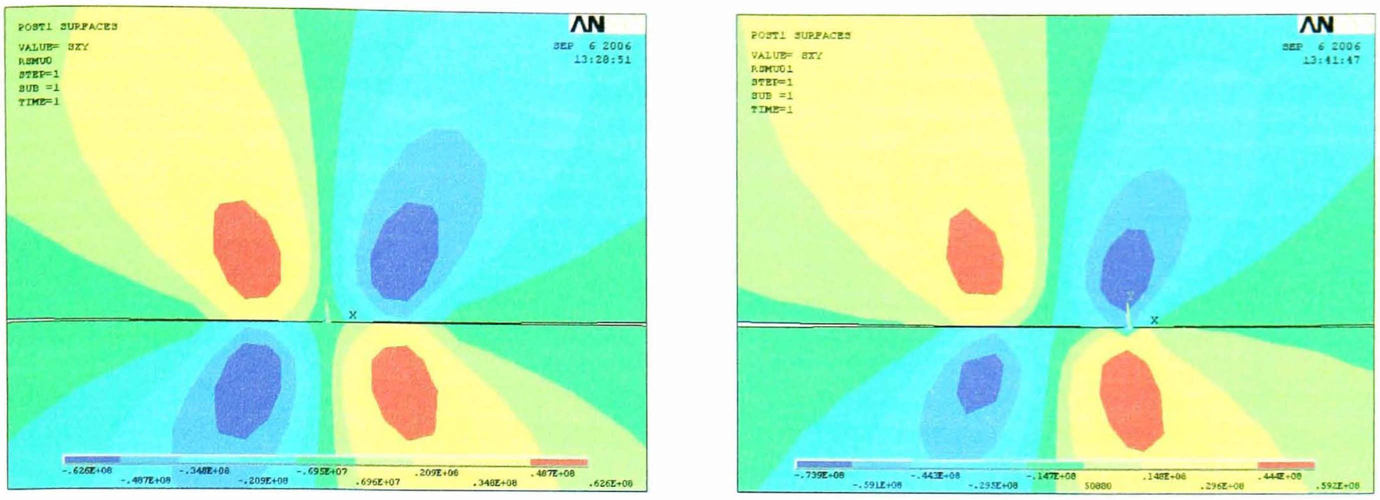

(a) μ=0 τ_{zxmax}=62.6 MPa (b) μ=0.1 τ_{zxmax}=73.9 MPa

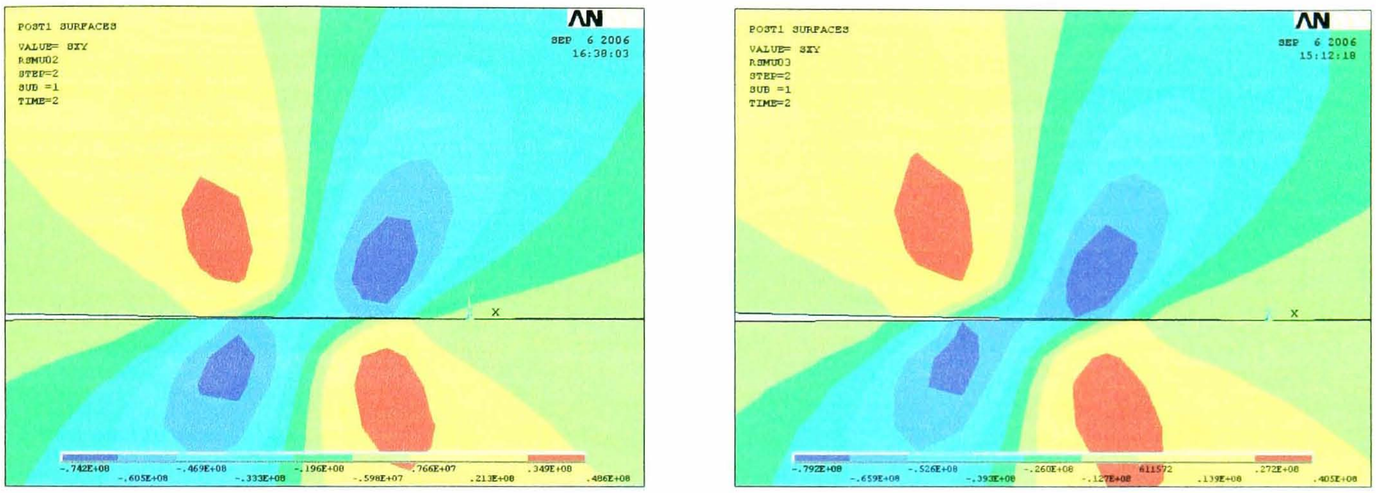

(c) μ=0.2 τ_{zxmax}=74.2 MPa (d) μ=0.4 τ_{zxmax}=79.2 MPa

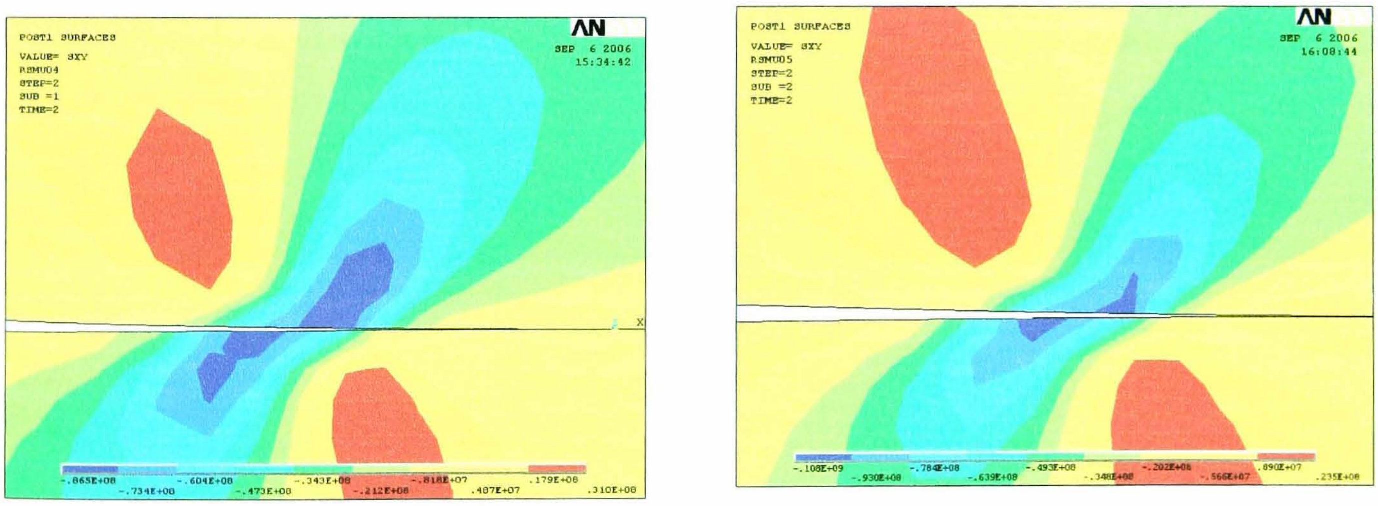

(e) μ=0.4 τ_{zxmax}=86.5 MPa (f) μ=0.5 τ_{zxmax}=95.5 MPa

Figure D-23 Shear stress distributions $p(x)$ in different μ

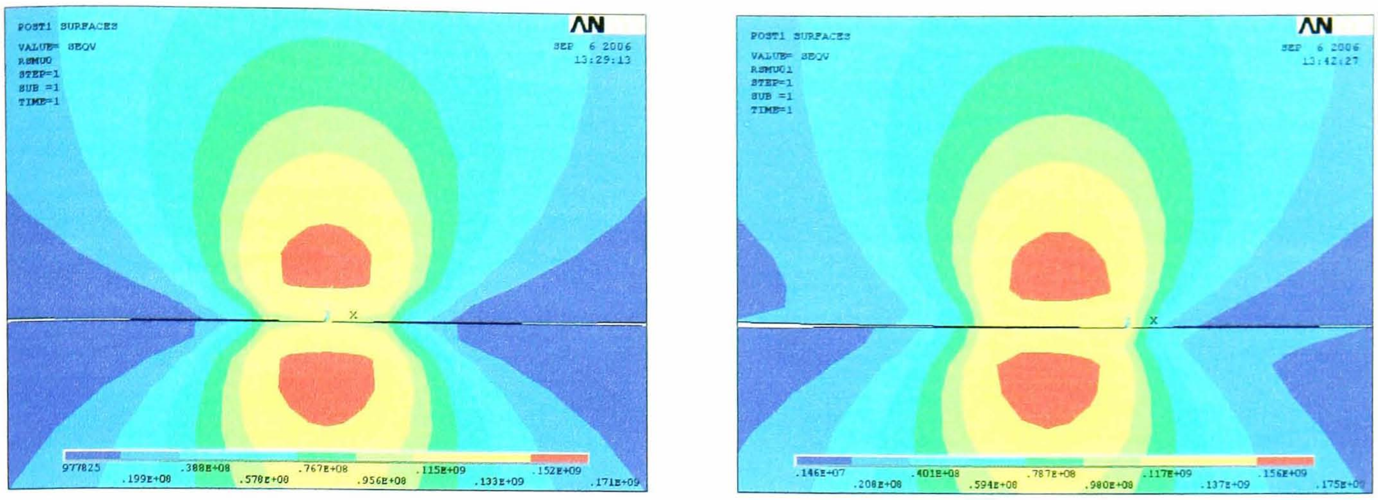

(a) μ=0 τ_{Rmax}=96.0 MPa (b) μ=0.1 τ_{Rmax}=96.8MPa

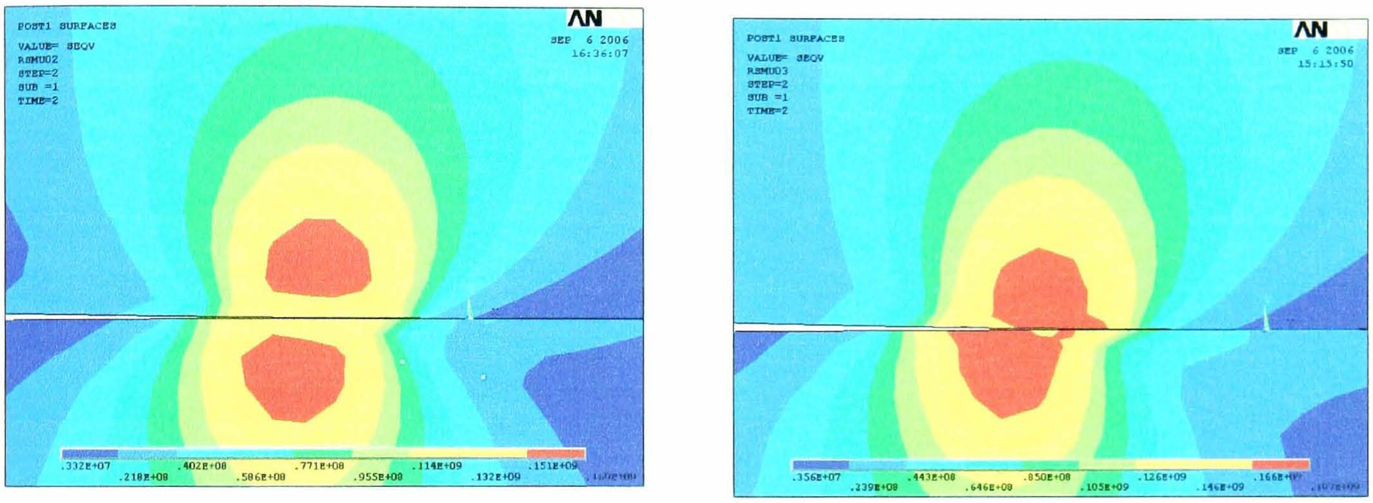

(c) μ=0.2 τ_{Rmax}=99.6MPa (d) μ=0.3 τ_{Rmax}=105.2 MPa

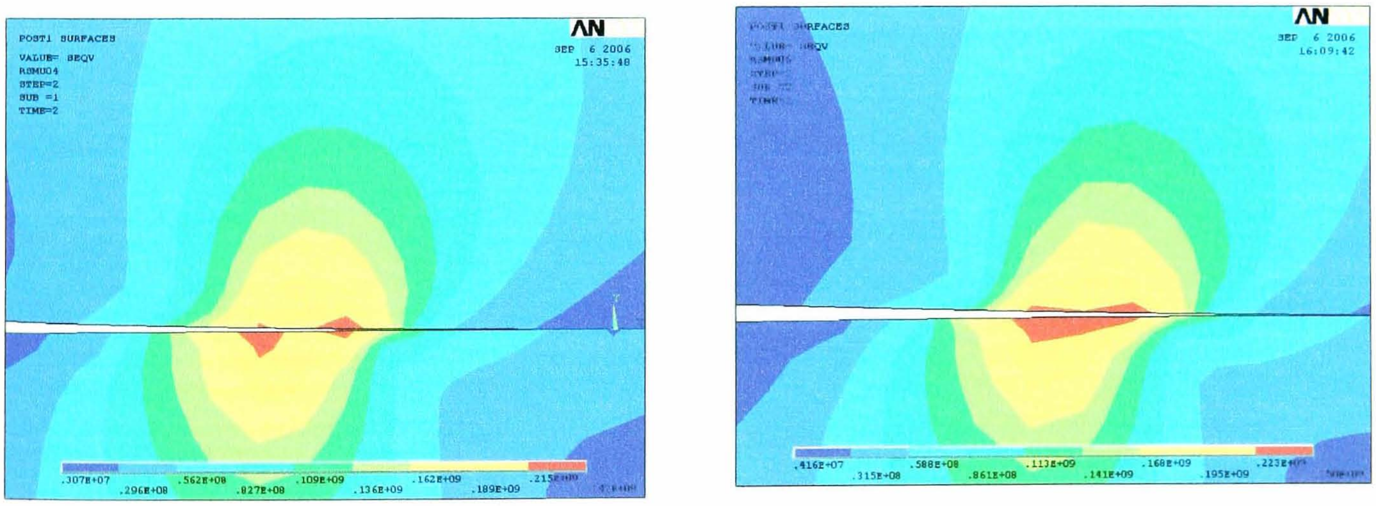

(e) μ=0.4 τ_{Rmax}=140.0MPa (f) μ=0.5 τ_{Rmax}=144.3MPa

Figure D-24 Von Mises' stress distributions $p(x)$ in different μ

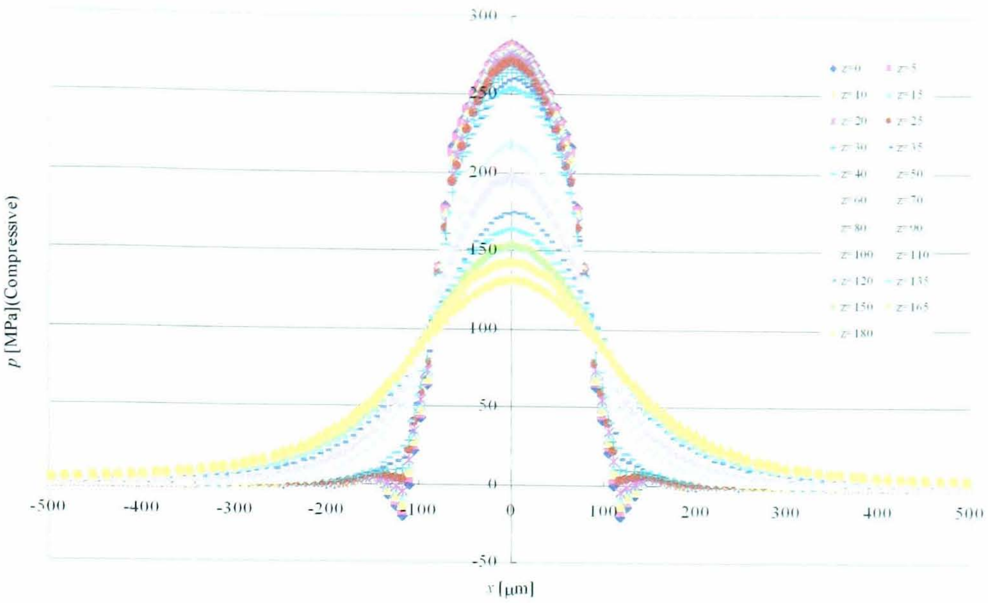

Figure D-25 Contact pressure distributions $p(x)$ in the depth Z [µm] from the surface (10% Slip, μ=0)

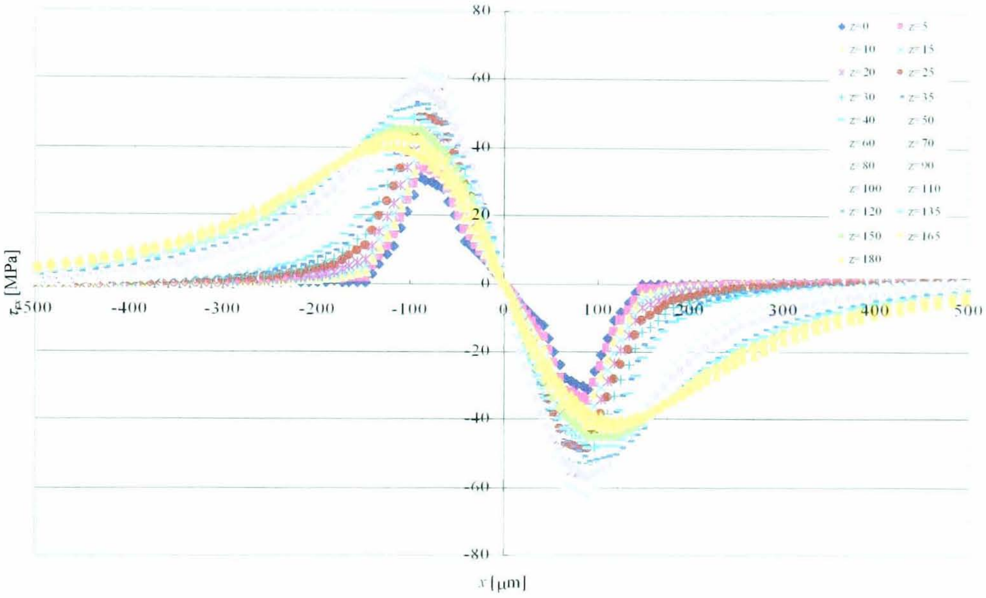

Figure D-26 Shear stress distributions τ_{zx} in the depth Z [µm] from the surface (10% Slip, μ=0)

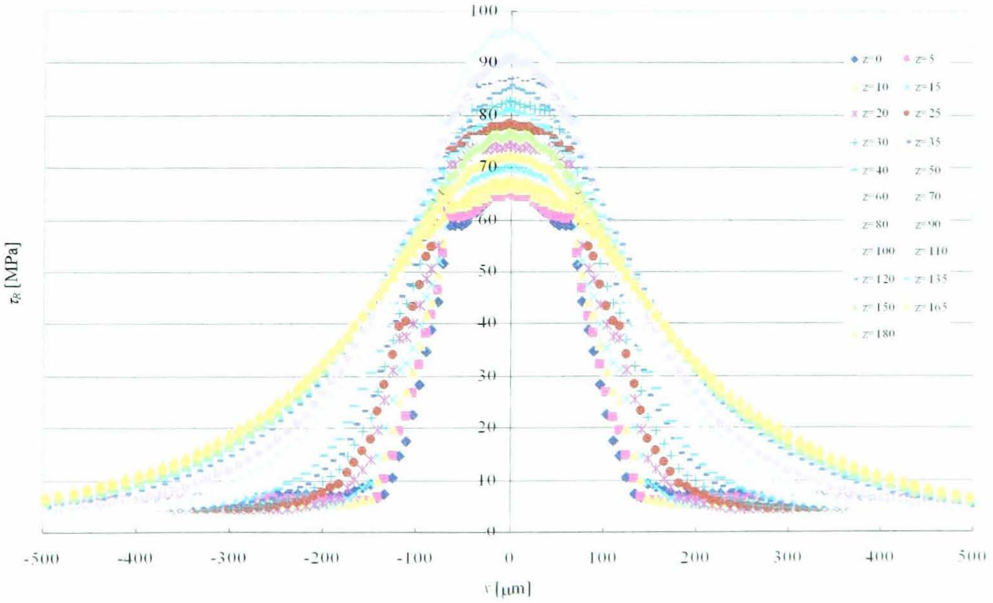

Figure D-27 Von Mises' stress distributions τ_R in the depth Z [µm] from the surface (10% Slip, μ=0)

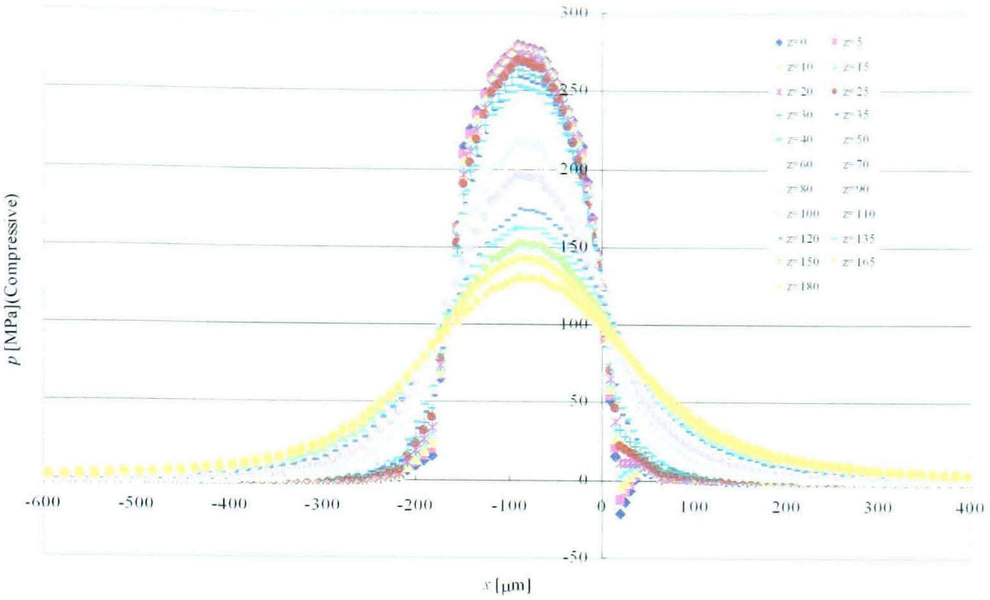

Figure D-28 Contact pressure distributions $p(x)$ in the depth Z [μm] from the surface (10% Slip, μ=0.1)

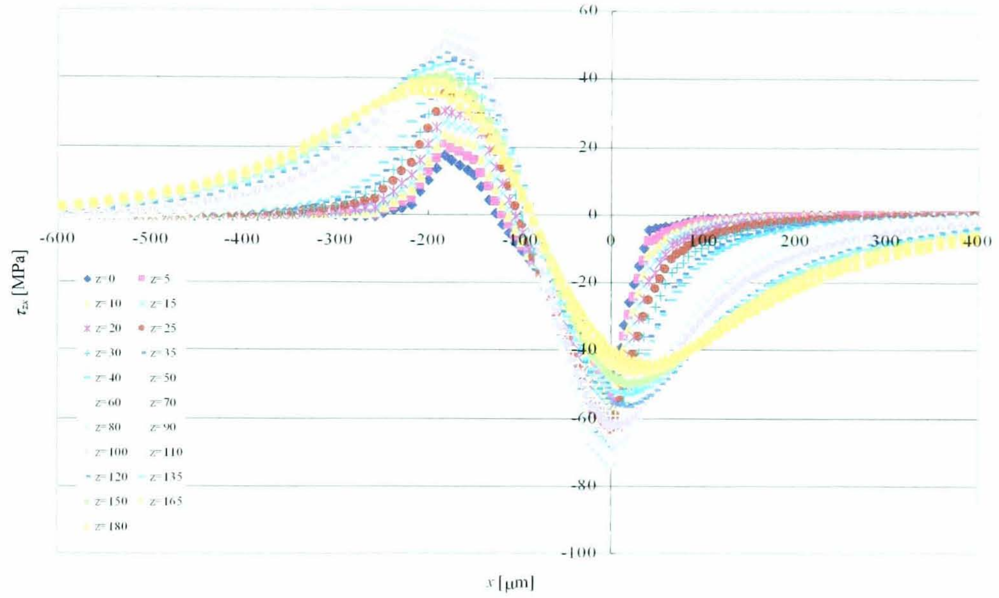

Figure D-29 Shear stress distributions τ_{zx} in the depth Z [μm] from the surface (10% Slip, μ=0.1)

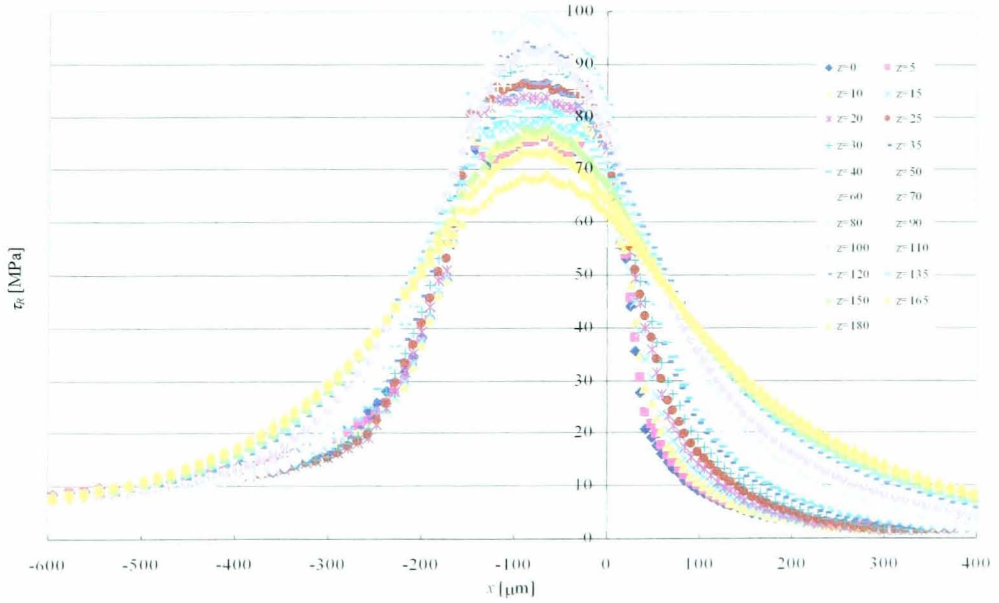

Figure D-30 Von Mises' stress distributions τ_R in the depth Z [μm] from the surface (10% Slip, μ=0.1)

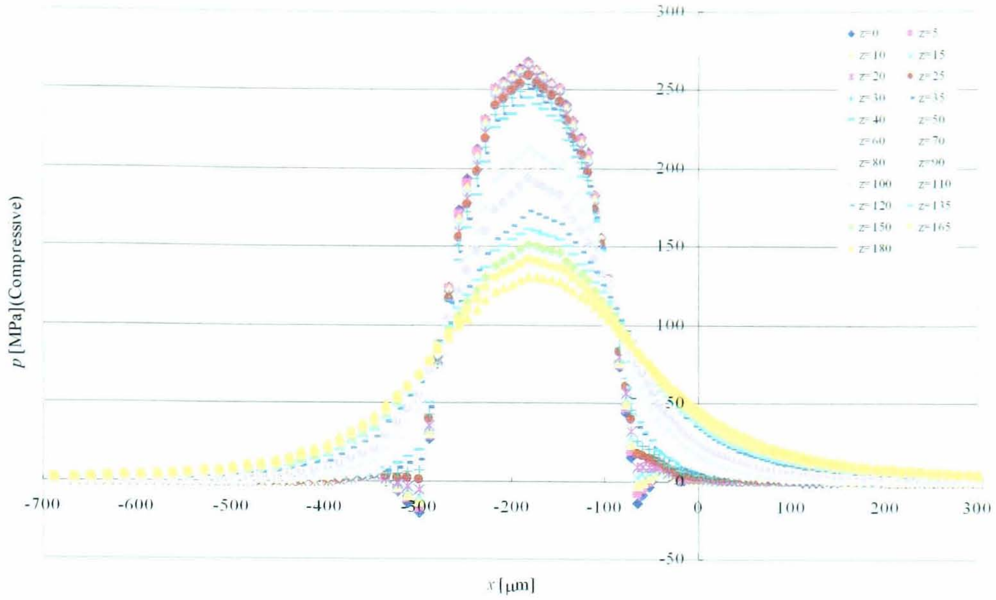

Figure D-31 Contact pressure distributions $p(x)$ in the depth Z [μm] from the surface (10% Slip, μ=0.2)

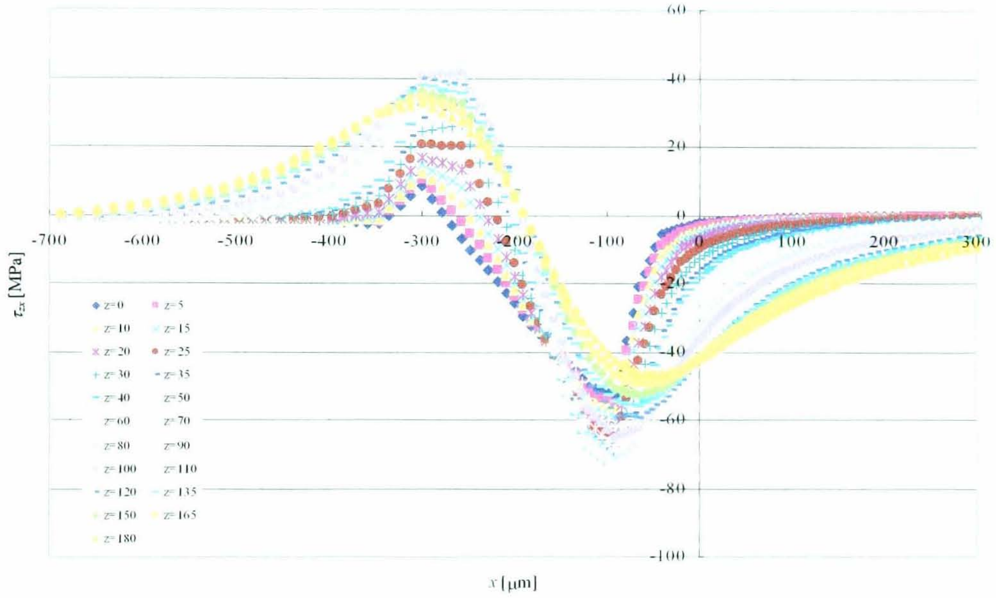

Figure D-32 Shear stress distributions τ_{zx} in the depth Z [μm] from the surface (10% Slip, μ=0)

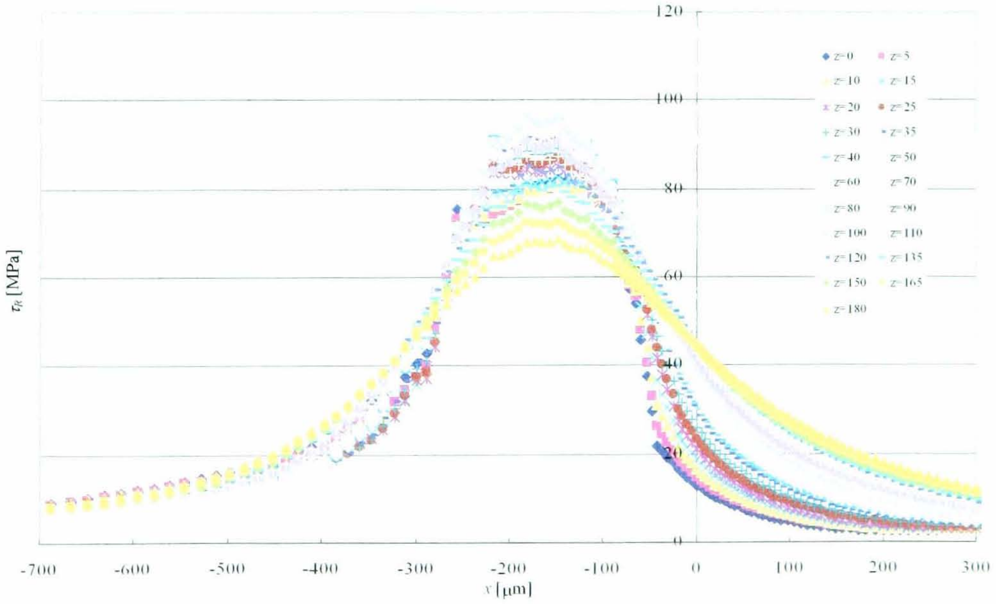

Figure D-33 Von Mises' stress distributions τ_R in the depth Z [μm] from the surface (10% Slip, μ=0.2)

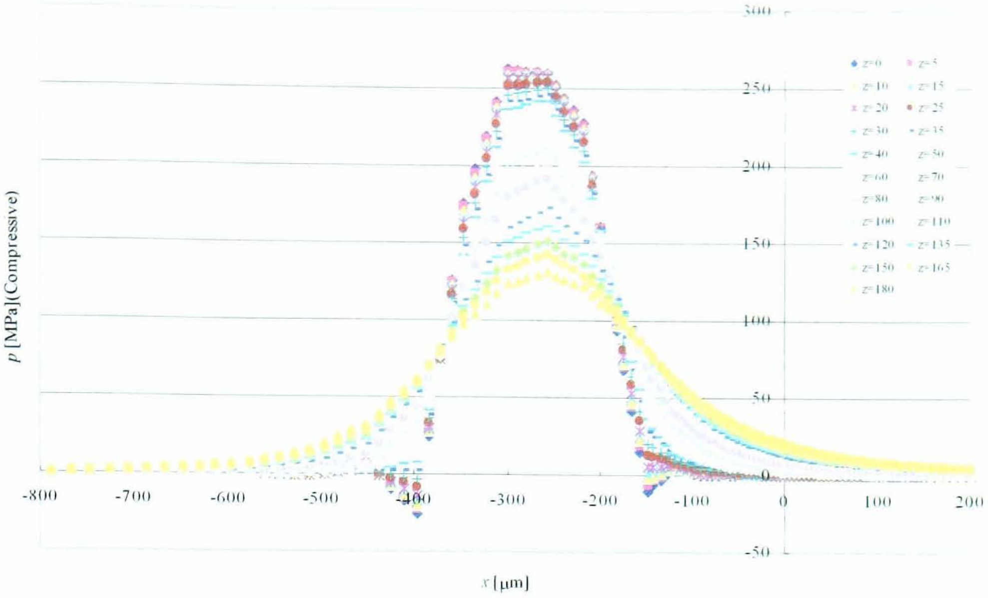

Figure D-34 Contact pressure distributions $p(x)$ in the depth Z [μm] from the surface (10% Slip, μ=0.3)

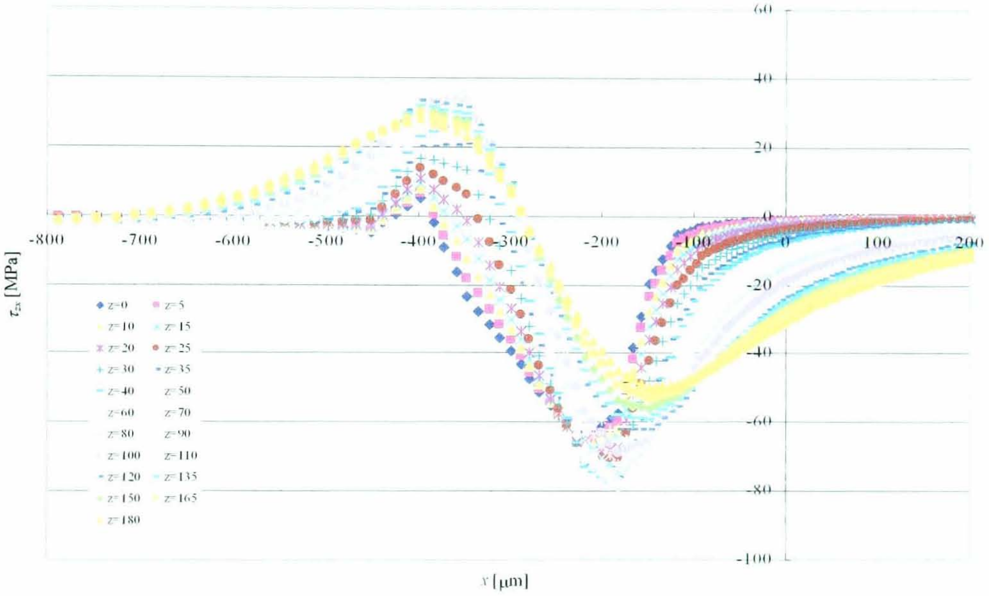

Figure D-35 Shear stress distributions τ_{zx} in the depth Z [μm] from the surface (10% Slip, μ=0.3)

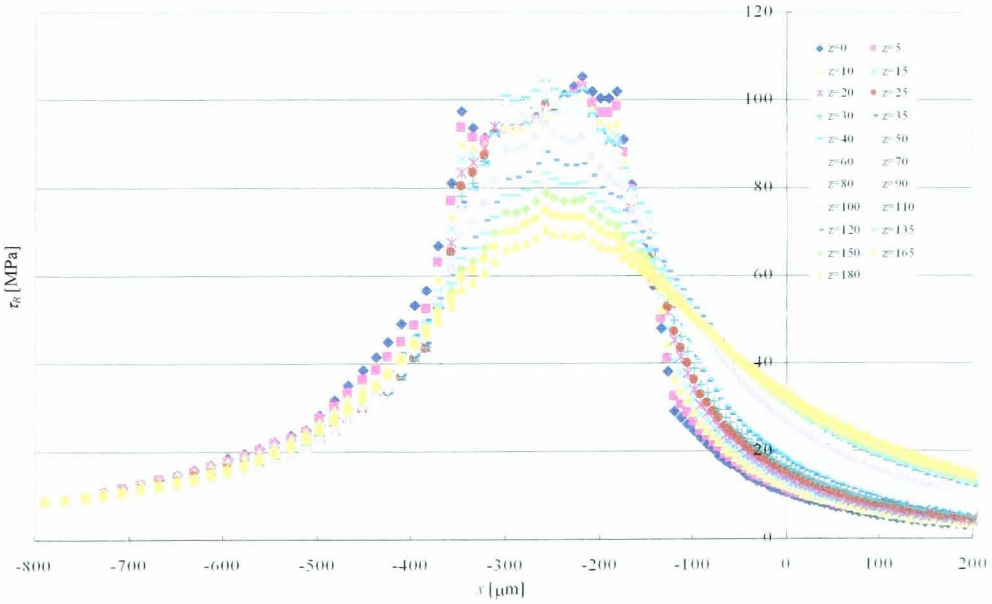

Figure D-36 Von Mises' stress distributions τ_R in the depth Z [μm] from the surface (10% Slip, μ=0.3)

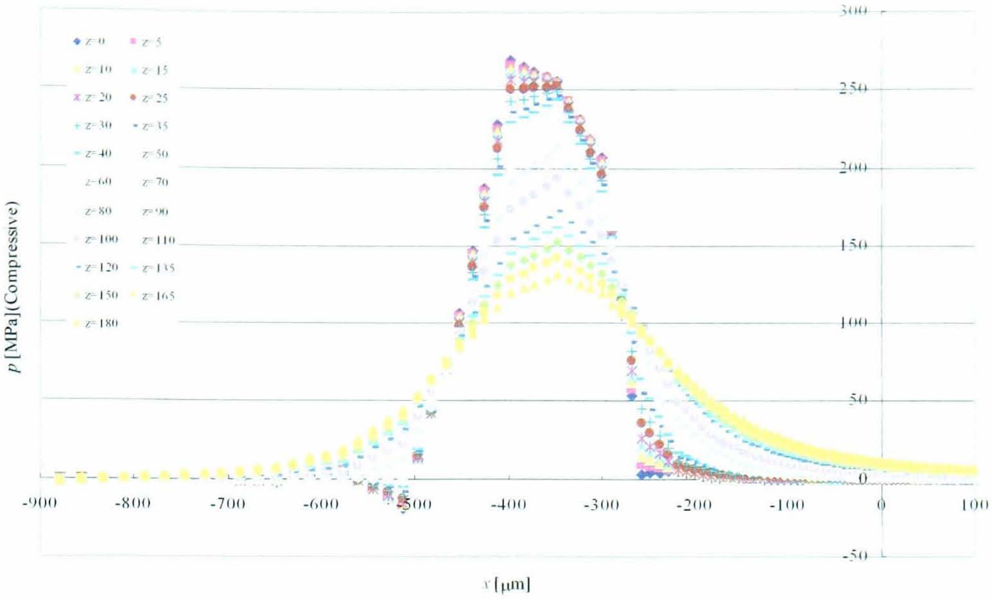

Figure D-37 Contact pressure distributions $p(x)$ in the depth Z [μm] from the surface (10% Slip, μ=0.4)

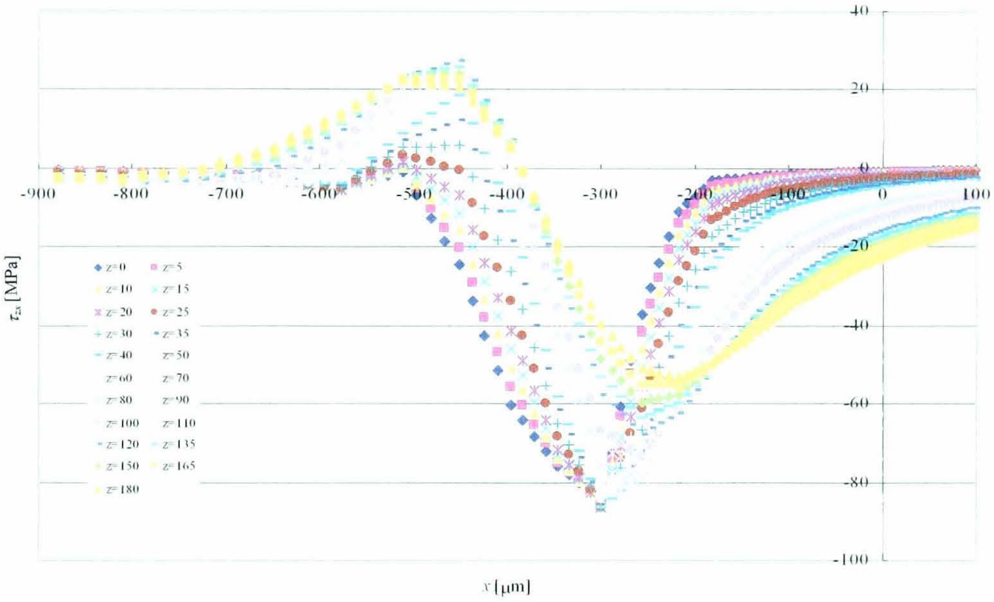

Figure D-38 Shear stress distributions τ_{zx} in the depth Z [μm] from the surface (10% Slip, μ=0.4)

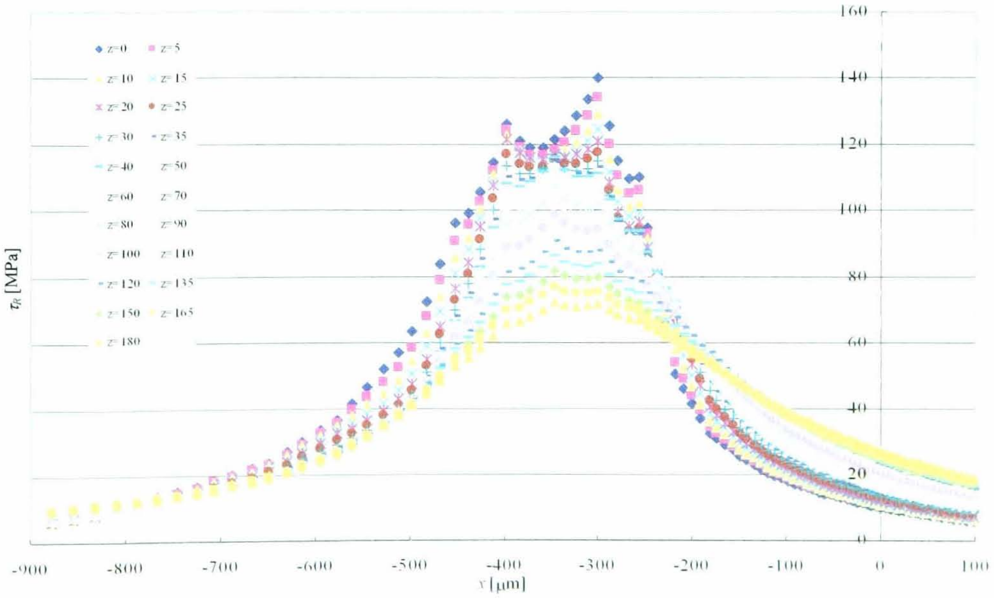

Figure D-39 Von Mises' stress distributions τ_R in the depth Z [μm] from the surface (10% Slip, μ=0.4)

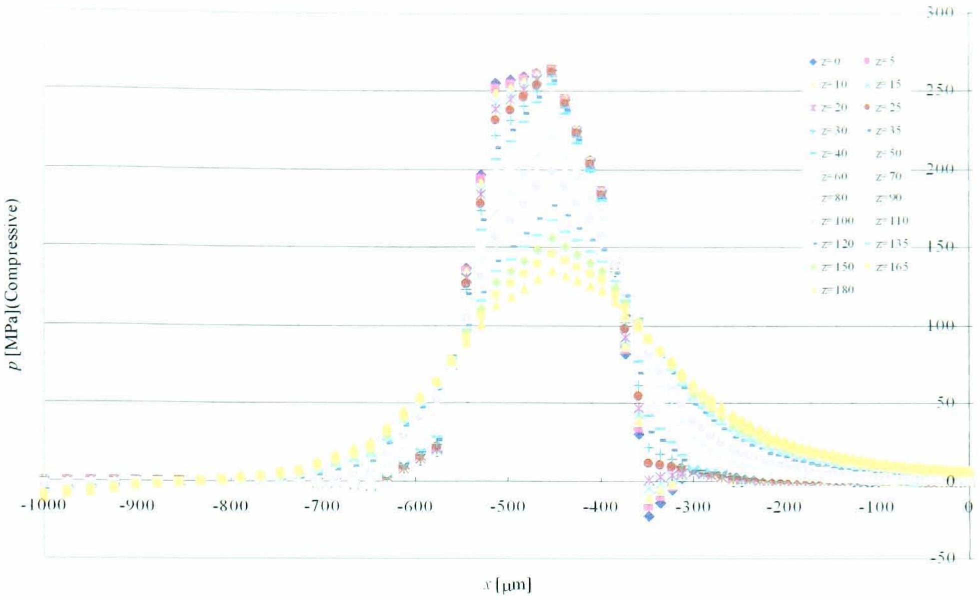

Figure D-40 Contact pressure distributions $p(x)$ in the depth Z [μm] from the surface (10% Slip, μ=0.5)

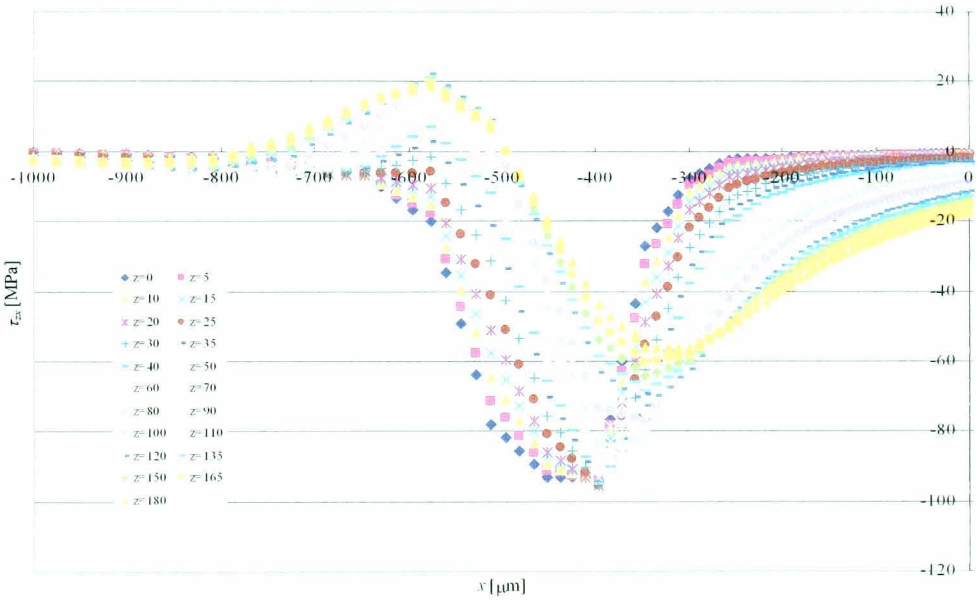

Figure D-41 Shear stress distributions τ_{zx} in the depth Z [μm] from the surface (10% Slip, μ=0.5)

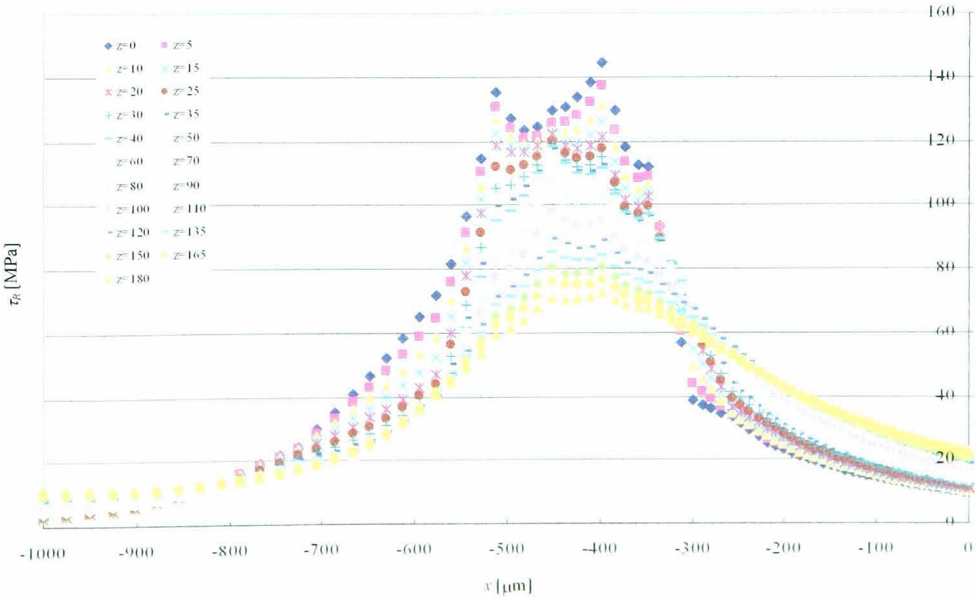

Figure D-42 Von Mises' stress distributions τ_R in the depth Z [μm] from the surface (10% Slip, μ=0.5)